

# **Treatment of Solid Cancerous Tumours Using Ultrasound-targeted Microbubble Destruction**



**Thomas McKaig BSc (Hons)**

Faculty of Life and Health Sciences

Ulster University

Thesis submitted for the degree of

Doctor of Philosophy

January 2023

I confirm that the word count of this thesis is less than 100,000 words.

## **Declaration**

I hereby declare that with effect from the date on which the thesis is deposited in Ulster University Doctoral College, I permit

1. The Librarian of the University to allow the thesis to be copied in whole or in part without reference to me on the understanding that such authority applies to the provision of single copies made for study purposes or for inclusion within the stock of another library.

2. The thesis to be made available through the Ulster Institutional Repository and/or EThOS under the terms of the Ulster eTheses Deposit Agreement which I have signed.

IT IS A CONDITION OF USE OF THIS THESIS THAT ANYONE WHO CONSULTS IT MUST RECOGNISE THAT THE COPYRIGHT RESTS WITH THE AUTHOR AND THAT NO QUOTATION FROM THE THESIS AND NO INFORMATION DERIVED FROM IT MAY BE PUBLISHED UNLESS THE SOURCE IS PROPERLY ACKNOWLEDGED.

## **Acknowledgements**

Thank you to my supervisory team - Prof. John Callan, Prof. Tony McHale and Dr Bridgeen Callan. I would like to give a special acknowledgement to my primary supervisor Prof. John Callan for the support and guidance you have given me over the course of my PhD and the opportunity to undertake it. I would especially like to thank you for the guidance and patience during the thesis writing aspect of this project.

I would like to thank my colleagues from the combined Callan/McHale laboratory for the friendship and mentoring I have received over the past few years. This made PhD life a much more enjoyable experience. Thank you to Dr Heather Nesbitt, Dr Keiran Logan, Dr Dean Nicholas, Dr Sukanta Kamila, Dr Federica Foglietta, Dr Simanpreet Kaur, Dr Jinhui Gao, Dr Nahid Khan, Sian Farrell, Chloe McClenaghan, Tierna Gillan, Jack Wright, Eoin McMullan and Poulette Odour. I want to wish you all a successful future in whatever path life takes you!

I would also like to acknowledge and give a huge thank you to my family. To my parents, thank you for providing me with the opportunities you did not have, and encouraging me to do what I wanted to do with my life. The love and support from mum hounding me with the transfer test through to my dad ensuring I was 'revising' for my PhD is one of the defining factors of achieving everything I have so far! I would also like to thank my brothers for the friendship and encouragement they have provided from the day they graced me with their presence... I really appreciate you all and thanks again!

To my wife, it wasn't long ago I was encouraging you through the writing of your thesis, it isn't as fun when the tables are turned. However, the support and love you have provided me with has made the unbearable, bearable. I appreciate that I am hard work enough without having to encourage me through writing my thesis so know how deeply grateful I am to have had you by my side through this process.

## Abstract

The main aim of the work undertaken in this thesis was to investigate the potential of ultrasound-targeted microbubble destruction (UTMD) mediated chemo-sonodynamic therapy (chemo-SDT) for the treatment of prostate cancer (PCa). Chapter 1 provides an introductory overview to the challenges associated with PCa, current treatments / limitations, SDT and the potential for combining SDT with UTMD. Chapter 2 details the methods used in chapters 3-6. Chapter 3 (the first results chapter) describes how the sonosensitiser Rose Bengal (RB) can be loaded onto microbubbles (MBs) using the avidin-biotin interaction with docetaxel (DTX) incorporated in the core to produce DTX-MB-RB that were subsequently tested for UTMD mediated efficacy in 3D spheroid and murine models PCa. This treatment produced improved efficacy when compared to standard DTX monotherapy. Chapter 4 aimed to address some of the shortcomings associated with the preparation of DTX-MB-RB in chapter 3. In particular, the requirement for the avidin-biotin linkage was eliminated and RB loading was achieved by synthesising a RB modified lipid which was used as a constituent lipid of the MB shell. This approach enabled the preparation of DTX-MB-RB in a single step from a pre-MB suspension following activation for 45 sec using a VialMix® shaker. The pre-MB suspension displayed good stability when stored for 3 months at 5 °C and these DTX-MB-RB were used in the efficacy experiments undertaken in Chapter 5. This involved testing the DTX-MB-RB in DU145 and LNCaP 3D spheroid models as well as PC3 (androgen resistant) and 22Rv1 (androgen dependent) murine models of PCa. The results demonstrated the effectiveness of UTMD mediated chemo-SDT in all the models tested and was more effective than UTMD mediated DTX-MB or MB-RB treatment in the 3D spheroid models and DTX monotherapy in the murine models. Chapter 6 involved the preparation of two new drug functionalised lipids: one functionalised with 5-fluoruridine (5-FUR) and the second with irinotecan (IRIN). These lipids were used to manufacture MBs carrying the drug payloads which were investigated for efficacy in 3D DU145 3D spheroid model of PCa. While these chemotherapies are not normally used in the treatment of PCa, the results demonstrated the potential of UTMD mediated 5FUR-MB-IRIN as the cell viability was reduced by 91.32%. Final conclusions and a future outlook are provided in Chapter 7.

## Tables and figures

Table 1.1 Summary of hallmarks of cancer and their respective treatment strategy	3
Figure 1.1 Location of the prostate	4
Table 1.2 Genes associated with hereditary PCa and their functions	8
Table 1.3 Genes associated with sporadic PCa and their functions	9
Table 1.4 Prostate cancer stage characterised by the TNM staging	13
Figure 1.2 Graphical Depiction of Treatment Options for Prostate Cancer	14
Table 1.5 Outline of the EAU-EANM-ESTRO-ESUR-SIOG prostate cancer guidelines panel's risk grouping based on the characteristics of a patients BCR	16
Figure 1.3 Chemical structure of DTX	22
Table 1.6 Description of the main classes of targeted drug cancer therapies	24
Figure 1.4 Mechanism of type I and II PDT	26
Figure 1.5 Proposed mechanisms of SDT	27
Figure 1.6 Chemical structure of Rose Bengal	28
Figure 1.7 MB shell formulated with different compositions i) lipid, ii) protein and iii) polymer	29
Figure 1.8 Sonograms using MB contrast agents a) traditional gray-scale image with no MB contrast agent, b) the image 8 seconds after administration of MBs, c) the image 35 seconds after MB administration and d) the image 2 min after MB administration	31
Table 1.7 Commercially available MB contrast agents for ultrasonic imaging	32
Figure 1.9 Compression and rarefaction of a soundwave in tissue	33
Figure 1.10 Mechanisms of MB induced sonoporation caused by stable and inertial cavitation	34
Figure 1.11 Ultrasound targeted drug delivery via non-destructive mechanisms	35
Figure 3.1 Confocal laser scanning microscope micrographs of tissue from PC3 tumours excised from mice. The tumours were stained with DAPI, fluorescence of DAPI and DOX	

were imaged, differential interference contrast micrographs were taken and a merged image was created. The mice received a tail vein injection of MBs with DOX and subsequent US for a) 5 mins, b) 10 mins and c) 15 mins [204].	57
Scheme 3.1 Synthetic procedure of Rose Bengal Biotin	60
Figure 3.2 $^1\text{H}$ -NMR of RB-biotin in DMSO-d <sub>6</sub>	62
Figure 3.3 $^{13}\text{C}$ -NMR of RB-biotin in DMSO-d <sub>6</sub>	63
Figure 3.4 The ESI-MS spectrum of RB-biotin in methanol (positive mode)	64
Figure 3.5 Schematic depicting DTX, and RB loaded MBs	65
Figure 3.6 (a) UV-vis spectra for concentrations of RB (b) Plot of absorbance against concentration of RB (mg/mL) (absorbance 565nm)	67
Figure 3.7 (a) HPLC chromatogram of DTX (b) Plot of peak area against concentration of DTX (mg/mL) (absorbance 231nm) (n=2)	68
Figure 3.8 (a) Optical microscope image at 40x objective lens magnification of DTX-MB-RB after 1 in 25 dilution in Unger's solution. (b) size distribution of DTX-MB-RB obtained from optical microscope images through MATLAB software	69
Table 3.1 Mean bubble count (number/mL), bubble size ( $\mu\text{m}$ ), RB loading concentration ( $\mu\text{M}$ ) and DTX loading concentration (mg/mL) batches of DTX-MB-RB (n=3).	70
Figure 3.9 DTX loadings for MBs prepared with 2.5, 5 or 10mg DTX, determined using HPLC (n=6) nsP>0.05, *P<0.05.	71
Table 3.2 Mean bubble count (bubbles/mL) and bubble size ( $\mu\text{m}$ ), for MBs prepared with 2.5, 5 or 10 mg of DTX.	72
Figure 3.10 RB loadings for MBs prepared with 2.5, 5 or 10mg DTX, determined using UV/vis spectrophotometry (n=4) nsP>0.05.	73
Figure 3.11 Plot of percentage bubble number (%) of DTX MB RBs prepared with 2.5, 5.0 or 10.0 mg DTX over a period of 90 min. *P>0.05.	74

Figure 3.12 Cell viability of LNCaP-Luc spheroids treated with i) Untreated ii) US only (iii) MB (iv) MB + US (v) MB-RB (vi) MB-RB + US (vii) DTX-MB (viii) DTX-MB + US (ix) DTX-MB-RB (x) DTX-MB-RB + US. [DTX] in all cases is 6.2μM. [RB] in all cases is 30μM. **P<0.01, ***P<0.001 and ****P<0.0001. Error bars show ± SEM (n=4).	76
Figure 3.13 Plot of percentage tumour growth in SCID mice bearing PC3 prostate tumours that received (i) no treatment (n=3) (ii) IP injection of DTX (10mg/kg) (n=4) (iii) IV injection of DTX-MB-RB – US (n=4) and (iv) IV injection of DTX-MB-RB + US (n=4). Treated on days 0, 4, 7, 10, 14, 18 and 21. ** P ≤ 0.01.	79
Figure 3.14 Plot of mice weights over 21 days as percentage weight change of day 0 weights. Mice received (i) no treatment (ii) IP injection of DTX (10mg/kg) (iii) IV injection of DTX-MB-RB – US and (iv) IV injection of DTX-MB-RB + US. *P>0.05 (n=4)	80
Figure 4.1 SonoVue® (Bracco) vial with powder form MBs (left), MiniSpike (middle) and saline filled syringe (right).	84
Figure 4.2 a) DEFINITY Vialmix shaker, shakes vial for 45s. b) The MBs are produced within the vial to be removed via a needle for administration.	85
Scheme 4.1 Synthetic scheme for the manufacture of RB-DSPE.	87
Figure 4.3 Stacked <sup>1</sup> H-NMR for RB-DSPE.	89
Figure 4.4 <sup>13</sup> C-NMR for RB-COOH (top) and RB-DSPE (bottom).	90
Figure 4.5 The MALDI-TOF spectrum of RB-DSPE.	91
Figure 4.6 Production of DTX-MB-RB using the revised VialMix® method.	93
Table 4.1 Composition of components (mol%) for formulations a-g.	94
Figure 4.7 Formulations a-g with i) size distribution, b) optical micrograph (40x objective lens) and iii) sample image of MB cake in vial.	94-96

Table 4.2 The bubble size ( $\mu\text{m}$ ), bubble number ( $\times 10^9/\text{mL}$ ) and flowability ranked 1-3. 1 = Not flowable, 2 = somewhat flowable and 3 = freely flowable.	97
Figure 4.8 Images of pre-MB colloidal formulation a) formulation F and b) formulation G.	97
Figure 4.9 Images of a) pre-MB suspension for vials stored at i) room temperature and ii) in the fridge. The corresponding MB cakes for the pre-MB suspensions stored at b) room temperature and c) in the fridge and i) representative size distribution and ii) 40x optical micrograph and iii) MB cake in the vial.	98-99
Table 4.3 The bubble size ( $\mu\text{m}$ ), bubble number ( $\times 10^9/\text{mL}$ ), pre-MB suspension clearness (clear or cloudy) and flowability ranked 1-3. 1 = Not flowable, 2 = somewhat flowable and 3 = freely flowable of MBs and pre-MB suspension produced after room temperature and fridge storage.	99
Figure 4.10 The bubble numbers for the batches stored at room temperature and fridge temperature.	100
Figure 4.11 Image of the vial after formulation 6 scale up batch was sonicated.	101
Figure 4.12 Image of vials rehydrated at $90^\circ\text{C}$ for 60 mins. Pre-MB suspension 1 & 2 and the corresponding MB cakes 3 & 4	101
Figure 4.13 Size distributions and optical micrographs for each repeat of the scaled batch.	102
Figure 4.14 Size of liposomes after 3-month fridge storage.	104
Figure 4.15 Effect on liposome size determined by DLS analysis of the DTX-MB-RB after 3-month fridge storage ( $n=3$ ).	105
Figure 4.16 Figure 4.16 Optical micrographs i) and size distribution plots ii) of DTX-MB-RB generated from pre-MB suspensions stored for a) 0 months, b) 1 month, c) 2 months and d) 3 months.	105



Figure 4.17 The effect on bubble number on DTX-MB-RB after 3-month fridge storage (n=3).	106
Figure 4.18 The effect on bubble size on DTX-MB-RB after 3-month fridge storage (n=3).	106
Table 4.4 Composition of components (mol%) for formulations blank MBs, DTX-MBs and MB-RBs.	107
Figure 4.19 Effect on liposome size determined by DLS analysis of the DTX-MB-RB after 3-month fridge storage (n=3).	108
Table 4.5 MB size and MB number for control formulations blank MBs, DTX-MBs and MB-RBs.	108
Figure 4.20 Formulations blank MBs, DTX-MBs and MB-RBs with i) size distribution, b) optical micrograph (40x objective lens) and iii) sample image of MB cake in vial.	109
Figure 4.21 Plot of percentage bubble number (%) of blank MBs, MB-RB, DTX-MB and DTX-MB-RB over 90 min. (N=3)	110
Figure 5.1 Cell viability of LNCaP spheroids treated with i) Untreated ii) blank MBs + US (iii) MB-RB (iv) MB-RB + US (v) DTX-MB (vi) DTX-MB + US (vii) DTX-MB -RB (vii) DTX-MB-RB + US. For experiment a) [DTX] was 16.67 $\mu$ M, [RB] was 50 $\mu$ M. For experiment b) [DTX] was 8.33 $\mu$ M, [RB] was 25 $\mu$ M. *P<0.05, **P<0.01 and ***P<0.001. Error bars show $\pm$ SEM (n=4).	117
Figure 5.2 Cell viability of DU145 spheroids treated with i) Untreated ii) blank MBs + US (iii) MB-RB (iv) MB-RB + US (v) DTX-MB (vi) DTX-MB + US (vii) DTX-MB-RB (vii) DTX-MB-RB + US. For experiment a) [DTX] was 16.67 $\mu$ M, [RB] was 50 $\mu$ M. For experiment b) [DTX] was 8.33 $\mu$ M, [RB] was 25 $\mu$ M. **P<0.01 and ***P<0.001. Error bars show $\pm$ SEM (n=4).	119
Figure 5.3 Individual tumour growth delay plots for nude balb/c mice implanted with 22Rv1 tumours, treated with a) untreated, b) DTX (matched dose) + US, c) enzalutamide, d) DTX-MB-RB, e) DTX-MB-RB + US and f) DTX-MB-RB enzalutamide + US.	122
Figure 5.4 Plot of a) percentage tumour growth and b) and b) percentage weight change for nude balb/c mice bearing 22Rv1 tumours. The mice were treated with i) untreated, ii)	

DTX (matched dose) + US, iii) enzalutamide, iv) DTX-MB-RB, v) DTX-MB-RB + US and vii) DTX-MB-RB enzalutamide + US.  $^{**}P < 0.01$  (N=5) 123

Figure 5.5 Kaplan Meier survival plot for nude balb/c mice bearing 22Rv1 tumours, treated with i) untreated, ii) DTX (matched dose) + US, iii) enzalutamide, iv) DTX-MB-RB, v) DTX-MB-RB + US and vii) DTX-MB-RB enzalutamide + US. (N=5) 124

Figure 5.6 Mean survival for nude balb/c mice bearing 22Rv1 tumours, treated with i) untreated, ii) DTX (matched dose) + US, iii) enzalutamide, iv) DTX-MB-RB, v) DTX-MB-RB + US and vii) DTX-MB-RB enzalutamide + US.  $^{**}P < 0.01$  (N=5). 125

Figure 5.7 Individual tumour growth delay plots for nude CD-1 mice implanted with PC3, treated with a) untreated, b) DTX (matched dose) + US, c) DTX (standard dose + US), d) DTX-MB + US, e) MB-RB + US, f) DTX-MB-RB and g) DTX-MB-RB + US. 128

Figure 5.8 Plot of a) percentage tumour growth and b) and b) percentage weight change for nude CD-1 mice bearing PC3 tumours. The mice were treated with i) untreated, ii) DTX (matched dose) + US, iii) DTX (standard dose + US), iv) DTX-MB + US, v) MB-RB + US, vi) DTX-MB-RB and vii) DTX-MB-RB + US.  $^{*}P < 0.05$  and  $^{**}P < 0.001$  (N=5) 129

Figure 5.9 Kaplan Meier survival plot for nude CD-1 mice bearing PC3 tumours, treated with i) untreated, ii) DTX (matched dose) + US, iii) DTX (standard dose + US), iv) DTX-MB + US, v) MB-RB + US, vi) DTX-MB-RB and vii) DTX-MB-RB + US. (N=5) 130

Figure 5.10 Mean survival for nude CD-1 mice bearing PC3 tumours, treated with i) untreated, ii) DTX (matched dose) + US, iii) DTX (standard dose + US), iv) DTX-MB + US, v) MB-RB + US, vi) DTX-MB-RB and vii) DTX-MB-RB + US.  $^{***}P < 0.001$  (N=5) 131

Figure 5.11 Plot of percentage weight change for healthy non tumour bearing mice. The mice were treated with i) untreated, ii) DTX-MB-RB or iii) DTX (10 mg/kg). (N=8) 134

Figure 5.12 Safety study in healthy non tumour bearing mice where mice received i) remained untreated, ii) DTX MB RB + US or iii) DTX (standard dose). Where biological markers were used to determine the health of mice in a) the kidney (glomerular cellularity, glomerular basement membrane, tubular vacuolation, interstitial

inflammation, interstitial fibrosis and collecting system), b) the liver (portal inflammation, lobular inflammation and steatosis) and c) a range of blood biomarkers (urea, ALT, RBC, Hb, HCT, MCV, MCH, MCHC, platelets, WBC, neutrophils, lymphocytes, monocytes and eosinophils). (N=8). (\*P≤0.05). 135

Figure 5.13 a) IVIS images of mice bearing 22Rv1 tumours, that received i) IR780 loaded MBs without US (top images), or ii) IR780 loaded MBs with US (bottom images). The images were taken at 0 hours; before treatment (left images) or 3 hours post treatment; (right images). b) Plot of tumour/back radiance for each treatment and timepoint. (n=3) 136

Scheme 6.1 for synthesis of 5FUR-DSPE. 143

Figure 6.1 Stacked <sup>1</sup>H-NMR spectra of 5FUR-DSPE. 145

Figure 6.2 <sup>13</sup>C-NMR spectra of 5FUR-DSPE. 146

Figure 6.3 ESI-MS spectrum of 5FUR-DSPE (negative mode). 147

Scheme 6.2 for synthesis of IRIN-DSPE. 148

Figure 6.4 Stacked <sup>1</sup>H-NMR spectra of IRIN-DSPE. 150

Figure 6.5 <sup>13</sup>C-NMR spectra of IRIN-DSPE. 151

Figure 6.6 ESI-MS spectrum of IRIN-DSPE (negative mode). 152

Table 6.1 Formulation for 5FUR-MB-IRIN components. 153

Figure 6.7 5FUR-MB-IRIN produced to determine quality of bubble number and size, a) vial of 5FUR-IRIN liposomes, b) vial of 5FUR-MB-IRIN, c) 40x optical image of 5FUR-MB-IRIN, d) size distribution of 5FUR-MB-IRIN. 154

Figure 6.8 Stability of 5FUR-MB-IRIN at 37.5°C. 155

Figure 6.9 DU145 spheroids treated with (i) control, (ii) US only, (iii) blank MBs, (iv) blank MBs + US, (v) 5FUR-MB-IRIN 5µM, (vi) 5FUR-MB-IRIN 5µM + US, (vii) 5FUR-MB-IRIN 10µM, (viii) 5FUR-MB-IRIN 10µM + US, (ix) 5FUR-MB-IRIN 20µM and (x) 5FUR-MB-IRIN 20µM + US. N=4. \*\*\*p≥0.001. 157

Figure 9.1 (a) Optical microscope image at 40x objective lens magnification of blank MBs after 1 in 25 dilution in Unger's solution. (b) size distribution of blank MBs obtained from optical microscope images through MATLAB software.	191
Table 9.1 Mean bubble count (number/mL), bubble size ( $\mu\text{m}$ ) for blank bubbles (n=3)	192
Table 9.2 Mean bubble count (number/mL), bubble size ( $\mu\text{m}$ ), Rose Bengal loading concentration ( $\mu\text{M}$ ) batches of MB-RB (n=3).	193
Figure 9.2 (a) Optical microscope image at 40x objective lens magnification of MB-RB after 1 in 25 dilution in Unger's solution. (b) size distribution of DTX-MB-RB obtained from optical microscope images through MATLAB software.	194
Table 9.3 Mean bubble count (number/mL), bubble size ( $\mu\text{m}$ ), DTX loading concentration (mg/mL) batches of DTX-MB (n=3).	195
Figure 9.3 (a) Optical microscope image at 40x objective lens magnification of DTX-MB after 1 in 25 dilution in Unger's solution. (b) size distribution of DTX-MB obtained from optical microscope images through MATLAB software.	195

## **Table of contents**

Chapter 1 – General introduction	1
1.1 Cancer	2
1.2 Prostate cancer	4
1.2.1 The prostate	4
1.2.2 Incidence and mortality	5
1.2.3 Molecular pathway of prostate cancer	6
1.2.3.1 Hereditary prostate cancer	6
1.2.3.2 Sporadic prostate cancer	9
1.2.4 Prostate cancer diagnosis	11
1.2.4.1 Prostate specific antigen (PSA) and digital rectal examination (DRE)	11
1.2.4.2 Gleason scoring, biopsies and magnetic resonance imaging (MRI)	12
1.2.5 Prostate cancer staging and treatments	12
1.2.5.1 Localised prostate cancer therapies	14
1.2.5.2 Biochemical recurrence	15
1.2.5.3 Salvage therapies for BCR prostate cancer	17
1.2.5.3.1 Salvage external beam radiotherapy (EBRT)	17
1.2.5.3.2 Salvage brachytherapy (BT)	17
1.2.5.3.3 Cryotherapy	18
1.2.5.3.4 High-intensity focused ultrasound (HIFU)	19
1.2.5.4 Locally advanced prostate cancer	19
1.2.5.5 Metastatic prostate cancer	20
1.2.6 Androgen deprivation therapy (ADT)	20
1.2.7 Docetaxel (DTX)	21

1.2.7.1 Docetaxel side effects	22
1.3 Targeted cancer therapy	23
1.3.1 Photodynamic therapy (PDT)	25
1.3.2 Sonodynamic therapy (SDT)	27
1.3.2.3 Rose Bengal (RB)	28
1.4 Microbubbles (MB)	29
1.4.1 Clinically approved use of MBs	30
1.5 Properties of ultrasound	32
1.5.1 Ultrasound therapy	33
1.5.2 Ultrasound-targeted microbubble destruction (UTMD)	35
1.5.2.1 UTMD mediated chemo-sonodynamic therapy	36
1.6 Aims and objectives	37
1.6.1 Chapter 3	37
1.6.2 Chapter 4	37
1.6.3 Chapter 5	37
1.6.4 Chapter 6	38
Chapter 2 – Methodology	39
2.1 Materials and reagents	40
2.2 Synthesis of Rose Bengal – biotin	41
2.2.1 Synthesis of rose bengal amine (7) 2-Aminoethyl 2,3,4,5-tetrachloro-6-(6-hydroxy-2,4,5,7-tetraiodo-3-oxo-3H-xanthen-9-yl)benzoate	41
2.2.2 Synthesis of biotin rose bengal (8) 2-(5-(2-Oxohexahydro-1H-thieno[3,4- d]imidazol-4-yl)pentanamido)ethyl 2,3,4,5-tetrachloro-6-(6-hydroxy-2,4,5,7- tetraiodo-3-oxo-3H-xanthen-9-yl)benzoate	41
2.3 Synthesis of Rose Bengal – DSPE	42

2.3.1 Synthesis of 8-((2, 3, 4, 5-tetrachloro-6-(6-hydroxy-2, 4, 5, 7 -tetraiodo-3- oxo-3H-xanthen-9-yl)henzoyl)oxy)octanoic acid (8).	42
2.3.2 Synthesis of 3-((hydroxy(2-(8-((2,3,4,5-tetrachloro-6-(6-hydroxy- 2, 4, 5, 7-tetraiodo-3-oxo-3H-xanthen-9-yl)henzoyl)oxy)octanamido)ethoxy) phosphoryl)oxy) propane-1 ,2-diyl distearate (9).	42
2.4 Synthesis of Irinotecan – DSPE	43
2.4.1 Synthesis of (19S)-19-[(2-{{(tert-butoxy)carbonyl}amino}acetyl)oxy]-10,19-diethyl-14,18-dioxo-17-oxa-3,13-diazapentacyclo[11.8.0.02,11.04,9.015,20]henicosa-1(21),2,4,6,8,10,15(20)-heptaen-7-yl [1,4'-bipiperidine]-1'-carboxylate hydrochloride salt (IR-GLY-BOC)	43
2.4.2 Synthesis of (19S)-19-[(2-aminoacetyl)oxy]-10,19-diethyl-14,18-dioxo-17-oxa-3,13-diazapentacyclo[11.8.0.02,11.04,9.015,20]henicosa-1(21),2,4,6,8,10,15(20)-heptaen-7-yl [1,4'-bipiperidine]-1'-carboxylate mixed hydrochloride/trifluoroacetate salt (IR-GLY)	43
2.4.3 Synthesis of 3-[(2-{{(19S)-7-{{[1,4'-bipiperidine]-1'-carbonyloxy}}-10,19-diethyl-14,18-dioxo-17-oxa-3,13-diazapentacyclo[11.8.0.02,11.04,9.015,20]henicosa-1(21),2,4,6,8,10,15(20)-heptaen-19-yl]oxy}}-2-oxoethyl)carbamoyl]propanoic acid (IR-GLY-ACID)	44
2.4.4 Synthesis of (2-{{3-[(2-{{(19S)-7-{{[1,4'-bipiperidine]-1'-carbonyloxy}}-10,19-diethyl-14,18-dioxo-17-oxa-3,13-diazapentacyclo[11.8.0.02,11.04,9.015,20]henicosa-1(21),2,4,6,8,10,15(20)-heptaen-19-yl]oxy}}-2-oxoethyl)carbamoyl]propanamido}ethoxy)[(2R)-2,3-bis(octadecanoyloxy)propoxy] phosphinic acid (IRIN - DSPE)	44
2.5 Synthesis of 5-Fluorouradine – DSPE	45
2.5.1 Synthesis of 5-fluoro-1-[6-(hydroxymethyl)-2,2-dimethyl-tetrahydro-2H-furo[3,4-d][1,3]dioxol-4-yl]-1,2,3,4-tetrahydropyrimidine-2,4-dione (5FUR-Ketal)	45
2.5.2 Synthesis of 4-{{[6-(5-fluoro-2,4-dioxo-1,2,3,4-tetrahydropyrimidin-1-yl)-2,2-dimethyl-tetrahydro-2H-furo[3,4-d][1,3]dioxol-4-yl]methoxy}-4-oxobutanoic acid (5FUR-Ketal-ACID)	45

2.5.3 Synthesis of [(2R)-2,3-bis(octadecanoyloxy)propoxy][2-(4-{[6-(5-fluoro-2,4-dioxo-1,2,3,4-tetrahydropyrimidin-1-yl)-2,2-dimethyl-tetrahydro-2H-furo[3,4-d][1,3]dioxol-4-yl]methoxy}-4-oxobutanamido)ethoxy]phosphinic acid (5FUR-Ketal-DSPE)	46
2.5.4 Synthesis of [(2R)-2,3-bis(octadecanoyloxy)propoxy][2-(4-{[(2S,5S)-5-(5-fluoro-2,4-dioxo-1,2,3,4-tetrahydropyrimidin-1-yl)-3,4-dihydroxy-2,5-dimethyloxolan-2-yl]methoxy}-4-oxobutanamido)ethoxy]phosphinic acid (5FUR-DSPE)	47
2.6 Preparation of DTX and Rose Bengal – biotin loaded microbubbles (DTX-MB-RB)	47
2.6.1 Characterisation of drug loading of DTX-MB-RB	47
2.7 Preparation of DTX-MB-RB from a pre-MB colloidal liposomal suspension	48
2.8 Preparation of 5FUR-MB-IRIN from a pre-MB colloidal suspension	49
2.9 Characterization of MB number and size	49
2.10 Determination of MB stability at 37.5oC	49
2.11 Determination of pre-MB colloidal liposomal suspension stability at 2-8°C	50
2.12 Culture of LNCaP-Luc/LNCaP spheroids	50
2.13 Culture of DU145 spheroids	50
2.14 <i>In vitro</i> efficacy determination of LNCaP-Luc/LNCaP spheroids	50
2.15 <i>In vitro</i> efficacy determination of DU145 spheroids	51
2.16 <i>In vivo</i> efficacy determination in PC3 xenografts treated with DTX-MB-RB	52
2.17 <i>In vivo</i> efficacy determination in 22Rv1 xenografts treated with DTX-MB-RB	53
2.18 <i>In vivo</i> safety determination and blood analysis in healthy non tumour bearing mice	53
2.19 Preparation of IR780-MB-RB from a pre-MB colloidal suspension.	54
2.20 Localisation of IR780 labelled MB-RB in mice bearing 22Rv1 tumours.	54
Chapter 3 – Docetaxel and Rose Bengal loaded MBs for ultrasound activated chemosonodynamic therapy of prostate cancer	56
3.1 Introduction	57
3.2 Aims and objectives	59



3.3 Results and discussion	60
3.3.1 Synthesis of Rose Bengal – biotin	60
3.3.2 Preparation of DTX-MB-RB conjugates	65
3.3.2.1 Characterisation of DTX-MB-RB conjugates	66
3.3.2.2 Optimisation of DTX drug loading on DTX-MB-RB	70
3.3.2.3 Effect of increasing DTX content on RB loading	70
3.3.2.4 Effect of increasing DTX content on stability of DTX-MB-RB at 37°C	73
3.3.4 Efficacy of DTX-MB-RB in Spheroids.	74
3.3.5 Efficacy of MB mediated chemo-SDT therapy using the DTX-MB-RB conjugates in mice bearing subcutaneous PC3 tumours.	77
3.4 Conclusions	81
Chapter 4 – Development of a single-vial, pre-MB colloidal suspension of the rapid preparation of docetaxel and Rose Bengal loaded MBs	82
4.1 Introduction	83
4.2 Aims and objectives	86
4.3 Results and discussion	87
4.3.1 Synthesis and Characterisation of RB-DSPE	87
4.3.2 Preparation of a DTX-MB-RB from a pre-MB suspension	92
4.3.2.1 Determining optimum temperature for storage of the pre-MB colloidal suspension	98
4.3.3 Scaling up manufacture of Pre-MB colloidal suspension	100
4.3.4 Extended stability of the Pre-MB colloidal suspension at 5°C.	102
4.3.5 Preparation of Blank MB, DTX-MB and MB-RB formulations.	107
4.3.6 Stability of Blank MB, DTX MB, MB-RB and DTX-MB-RB at 37°C.	110
4.4 Conclusion	111

Chapter 5 – UTMD mediated chemo-SDT treatment of androgen sensitive and insensitive models of prostate cancer using DTX-MB-RB prepared from a pre-MB colloidal suspension	112
5.1 Introduction	113
5.2 Aims and objectives	114
5.3 Results and discussion	115
5.3.1 Efficacy of UTMD mediated chemo-SDT using DTX-MB-RB prepared from a pre-MB colloidal suspension in a LNCaP spheroid model of prostate cancer	115
5.3.2 Efficacy of UTMD mediated chemo-SDT using DTX-MB-RB prepared from a pre-MB colloidal suspension in a DU145 spheroid model of prostate cancer	118
5.3.3 Efficacy of UTMD mediated chemo-SDT using DTX-MB-RB prepared from a pre-MB colloidal suspension in murine model of prostate cancer bearing ectopic 22Rv1 tumours	120
5.3.4 Efficacy of UTMD mediated chemo-SDT using DTX-MB-RB prepared from a pre-MB colloidal suspension in a murine model of prostate cancer bearing ectopic PC3 tumours	126
5.3.5 Safety study of DTX-MB-RB prepared from a pre-MB colloidal suspension in healthy non tumour bearing mice	131
5.3.6 UTMD mediated localisation of MBs loaded with IR780 in a murine model of prostate cancer.	136
5.4 Conclusions	138
Chapter 6 – Development of a single vial, pre-MB colloidal suspension loaded with 5-fluorouradine and irinotecan for the treatment of prostate cancer	139
6.1 Introduction	140
6.2 Aims and objectives	142
6.3 Results and discussion	143
6.3.1 Synthesis of 5Fur-DSPE	143

6.3.2 Synthesis of IRIN-DSPE	148
6.3.3 Preparation of 5FUR-MB-IRIN	153
6.3.3.1 Characterisation of 5FUR-MB-IRIN	153
6.3.4 Determination of 37.5°C stability of 5FUR-MB-IRIN	155
6.3.5 Efficacy determination of 5FUR-MB-IRIN <i>in vitro</i> spheroidal DU145 prostate cancer model	156
6.4 Conclusion	158
Chapter 7 – Conclusions and future outlook	159
Chapter 8 – References	163
Chapter 9 – Appendices	190
9.1 Control formulations - blank MBs	191
9.2 Control formulations – MB-RB	192
9.3 Control formulations – DTX-MB	193
9.4 Publications and conferences	195
9.4.1 Publications	195
9.4.2 Publications resulting from thesis – under review	196
9.4.3 Conferences	196

[Drug]	Drug concentration
5-FU	5-Fluorouracil
5-FUR	5-Fluorouradine
ADT	Androgen depravation therapy
ALT	Alanine transaminase
AR	Androgen receptor
BCR	Biochemical recurrence
BT	Brachytherapy
CDMO	Contract development and manufacturing organization
CRPC	Castration resistant prostate cancer
DBPC	1,2-dibehenoyl-sn-glycero-3-phosphocholine
DCM	Dichloromethane
DHT	Dihydrotestosterone
DLS	Dynamic light scattering
DMF	Dimethylformamide
DNA	Deoxyribonucleic acid
DOX	Doxorubicin
DPTAP	1,2-dipalmitoyl-3-trimethylammonium-propane
DRE	Digital rectal examination
DSPC	1,2-distearoyl-sn-glycero-3-phosphocholine
DSPE	1,2-distearoyl-sn-glycero-3-phosphoethanolamine
DTX	Docetaxel
EBRT	External beam radiotherapy
Enz	Enzalutamide

ESI-MS	Electrospray ionisation mass spectrometry
FBS	Foetal bovine serum
GMP	Good manufacturing practice
HDR	High dose rate
HIFU	High-intensity focused ultrasound
IC50	Half maximal inhibitory concentration
IP	Intraperitoneal
IRIN	Irinotecan
IV	Intravenous
LDR	Low dose rate
MALDI-TOF	Matrix-assisted laser desorption ionisation – time of flight
MB(s)	Microbubble(s)
MeOH	Methanol
MHRA	Medicines and Healthcare products Regulatory Agency
miRNA	Micro ribonucleic acid
MRI	Magnetic resonance imaging
NMR	Nuclear magnetic resonance
OS	Overall survival
PBS	Phosphate buffered saline
PCa	Prostate cancer
PDT	Photodynamic therapy
PEG	Propylene glycol
PFB	Perfluorobutane
PFS	Progression free survival

PI	Propidium iodide
PNP	Peak negative pressure
PPP	Peak positive pressure
PRF	Pulse repetition frequency
PS	Photosensitiser
PSA	Prostate specific antigen
PTX	Paclitaxel
RB	Rose Bengal
ROS	Reactive oxygen species
RP	Radical prostatectomy
RPMI	Roswell Park Memorial Institution
SCID	Severe combined immunodeficiency
SDT	Sonodynamic therapy
SEM	Standard error of the mean
S <sub>N</sub> 2	Bi-molecular Nucleophilic Substitution
TFA	Trifluoroacetic acid
TLC	Thin-layer chromatography
US	Ultrasound
UTMD	Ultrasound-targeted microbubble destruction
UV	Ultraviolet

## **Chapter One:**

### **General Introduction**

## **1.1 Cancer**

Cancer is the second leading cause of death worldwide, resulting in approximately 9.6 million deaths in 2018 [1]. In the UK alone, 164,901 people died of cancer between 2015 and 2017, equating to 28% of all deaths in 2017 [2]. The likelihood of being diagnosed with cancer increases with age and is most prevalent in those aged over 65 or with a history of cancer in the family. Other lifestyle risks such as smoking, diet, body weight or ultraviolet (UV) light exposure can also increase a person's likelihood of developing cancer [3]. The most common forms of cancer are breast, lung, prostate and bowel [4].

Cancer can be classed as a disease formed by the abnormal proliferation of cells. Generally, it derives from a genetic mutation that causes abnormal cell proliferation or alters cellular differentiation or survival. These mutations may prove beneficial to the cancer cell if such a mutation enhances the rate of cell proliferation, the cells become more dominant and establish a tumour or they alter the ability of a cell to terminate itself through apoptosis. The cancer cells may then proliferate to the point they invade surrounding tissues, spreading outwards from the original tumour site causing a metastatic state of the disease [5].

There are 10 main processes that are commonly used as targets for cancer therapy. These are referred to as ten "hallmarks of cancer": (i) self-sufficiency for growth signalling, (ii) resistance to growth suppressors, (iii) evasion of apoptosis, (iv) limitless cellular replication, (v) increased angiogenesis, (vi) induction of metastasis, (vii) metabolic reprogramming, (viii) evasion of immune response, (ix) genome mutation and (x) tumour inflammation [6].



Table 1.1 Summary of hallmarks of cancer and their respective treatment strategy [7].

Hallmark of Cancer	Treatment
<b>Self-sufficiency for growth signalling</b>	EGFR inhibitors
<b>Resistance to growth suppressors</b>	Cyclin-dependent kinase inhibitors
<b>Evasion of apoptosis</b>	Proapoptotic BH3 mimetics
<b>Limitless cellular replication</b>	Telomerase inhibitors
<b>Increased angiogenesis</b>	Inhibitors of VEGF signalling
<b>Induction of metastasis</b>	Inhibitors of HGF/c-Met
<b>Metabolic reprogramming</b>	Aerobic glycolysis inhibitors
<b>Evasion of immune response</b>	Immune activating anti-CTLA-4 mAb
<b>Genome mutation</b>	PARP inhibitors
<b>Tumour inflammation</b>	Selective anti-inflammatory drugs

Targeting a single hallmark has proven in many cases to provide only a short duration of therapeutic effect before encountering resistance [8]. For example, resistance to anti-CTLA-4 drugs has been reported – these drugs act as a blockade for the CTLA-4 receptor on tumour cells that downregulate T-cell proliferation. It has been reported by Barreto et al that cells are able to downregulate the proliferation of T-cells by VISTA, a potent T-cell downregulation molecule [9,10]. This is due to the tumours adaptive ability to operate via different mechanisms and pathways to bypass the treatment against a specific targeted hallmark. This has led to an increasing trend in the field of utilising multiple treatments to target more than one hallmark, in a strategic combinatorial manner to increase therapeutic effect by stopping resistance pathways and encouraging drug synergism.

## 1.2 Prostate cancer

### 1.2.1 The prostate

The prostate is a small walnut sized gland found in front of the rectum, at the base of the bladder with the urethra passing through the centre from the bladder to the penis (Figure 1.1) [11]. The prostate is made up of three main zones, the central zone at the base of the prostate surrounding the ejaculatory ducts making up 5-8% of the prostate, the peripheral zone surrounds the distal urethra making up 75% of the prostate and the transition zone that surrounds the proximal urethra making up 20% of the prostate [12-13].

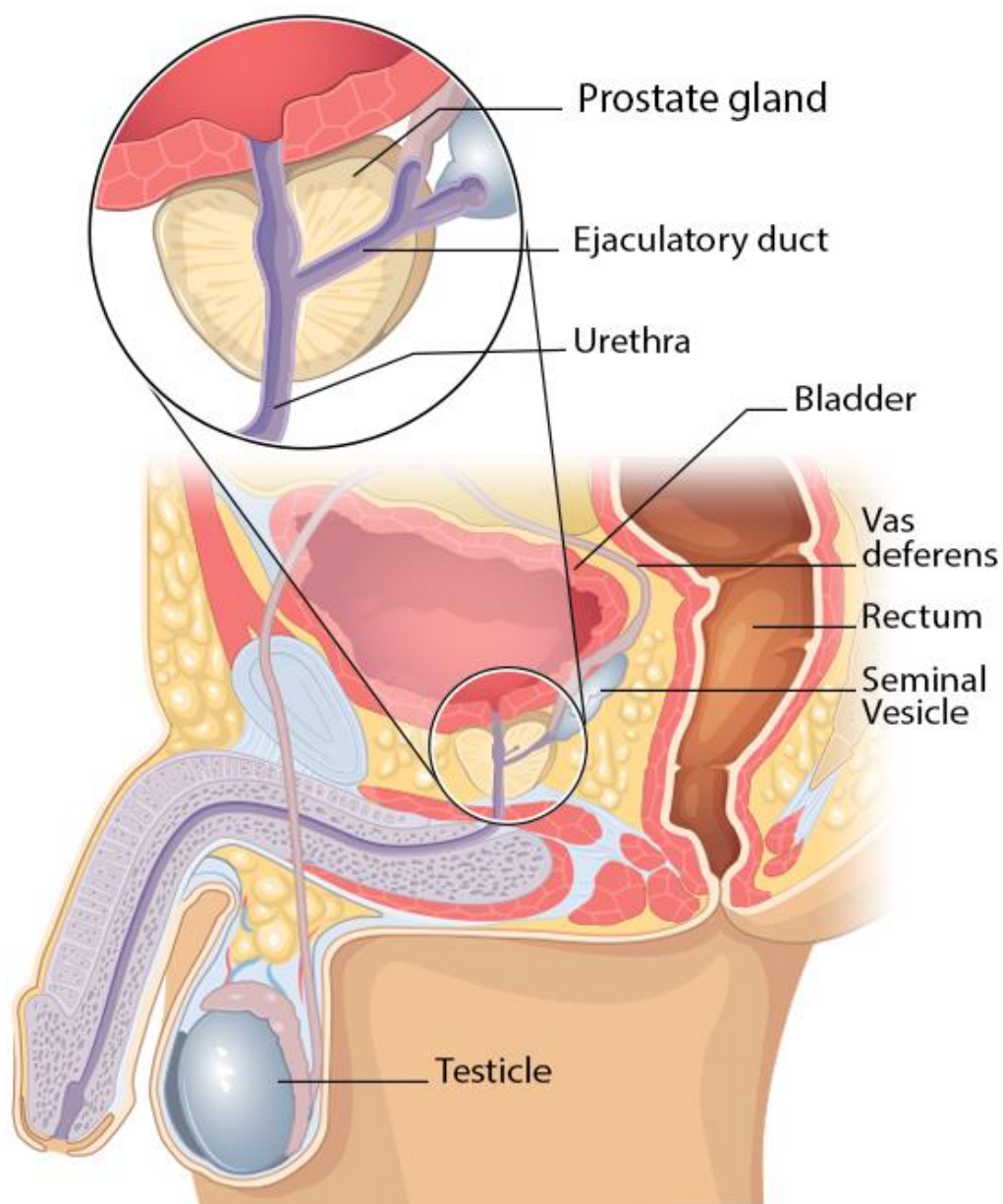


Figure 1.2 Location of the prostate. (Taken from [12]).

The prostate functions primarily as part of the reproductive system. It is responsible for the production of the fluidic component of semen which also comprises sperm cells from the testes. The prostate also functions to contract muscles involved during ejaculation and to convert testosterone into its more potent relative dihydrotestosterone (DHT), the deficiency of which is attributed to low sperm counts, low semen volume and semen coagulation [13].

### **1.2.2 Incidence and mortality**

In the UK, prostate cancer (PCa) is the most frequent form of cancer diagnosed in men. Approximately 48,500 cases are diagnosed each year, which is roughly 132 per day [14]. PCa has also become the third highest cause of cancer related death in the UK, surpassing deaths from breast cancer for the first time in 2015, with around 11,700 deaths, compared to 11,399 for breast cancer [14-15]. PCa is becoming a bigger killer due to increasing population age, this leads to more men being diagnosed with PCa as well as improvements in the treatment of breast cancer, highlighting that research is proving advantageous for new patients of these diseases. However, whilst extensive research has been undertaken into improving methods of diagnosis and treatment, in 2020 the charity PCUK stated that PCa deaths had exceeded 12,000 for the first time in a calendar year [16, 17].

PCa like many other cancers has a long list of risk factors. Some risk factors are non-lifestyle based such as age, race and family history [18]. Age is the most significant risk factor of men with PCa, it has been reported that more than half of all PCa diagnoses in the UK occur in men over the age of 70 [19]. Men of black Caribbean ethnicity show a much higher incidence rate of PCa than those of Caucasian ethnicity. In a study carried out by PRostate Cancer in Ethnic SubgroupS (PROCESS) between 1998 and 2001 it was reported that the age-adjusted incidence rate for white men in the UK was 56.4 per 100,000 compared to 173 per 100,00 and 139 per 100,000 for black Caribbean and black African ethnicities respectively [20]. While the incidence rate is higher when one or more close relatives has had PCa, there are numerous genes which may mutate to cause PCa. Work into the area of determining which mutated genes are most related to PCa is currently ongoing, which may aid the screening of PCa via diagnostic genetic testing [21]. Other risk factors for PCa may be lifestyle related. There is no defined set of lifestyle risk factors that are directly related to PCa incidence however there are some that show a correlation. These include diet, physical activeness, BMI, alcohol and tobacco usage. Other risk factors of PCa are disease related, a study carried out by Pacheo et al. (22) showed that patients with

a history of prostatitis made up 15% of PCa patients within their study, compared to the usual prevalence of 2-10% [22].

### **1.2.3 Molecular pathway of prostate cancer**

PCa development can either be 1) hereditary or 2) sporadic. Hereditary PCa is caused by inheritance of a gene that causes the disease, there are numerous genes that have been identified for both hereditary and sporadic PCa. However, it is not possible to distinguish between hereditary and sporadic gene mutations that lead to PCa development. This is because the genes that have been identified in hereditary PCa can also be identified in sporadic PCa. Some of the PCa associated hereditary genes identified are ELAC2, RNASEL, MSR1, NSB1, and CHEK2 [23]. Sporadic PCa can be caused by specific genes that increase the risk of the disease or by activation of PCa oncogenes. The genes that have been identified are TLR4, CDKN1B (p27) and the androgen receptor (AR) genes, CYP17 and SRD5A2. Identified PCa oncogenes are c-myc, bcl-2, c-Kit/tyrosine kinase receptor and STAT5 [23].

#### **1.2.3.1 Hereditary prostate cancer**

Mutations in the genes mentioned in Table 1.2 have been associated with hereditary PCa. ELAC2 was the first gene to be associated in cases of familial PCa, mutations in this gene have been determined to be responsible for <5% of PCa cases and there have been conflicting studies in determining the significance of this gene on PCa risk [24]. However, a meta-analysis carried out by Xu et al discovered that both polymorphisms of ELAC2 gene caused a significant increase in the risk of PCa [24]. Mutations in this gene are rare however, the mutations that can occur lead to either Ser217Leu which results in a structure alteration or Ala541Thr which reduces protein function [25]. The mechanism isn't completely understood but it is thought to aid driving cell cycle progression. However, *in vitro* studies carried out by Korver et al stated that overexpression of the gene causes a greater entry of cells in G2 phase and showed an interaction between ELAC2 and  $\gamma$ -tubulin, abnormalities in this process have been suggested to be a potential reason for uncontrolled cellular division [26].

Both RNASEL and MSR1 are genes that are activated in response to a viral infection. RNASEL as mentioned in Table 1.2, codes for RNase L which is a ribonuclease that operates by degrading uracil-rich single stranded RNA of either the infecting virus or the host cell initiating apoptosis [27]. RNASEL is considered a tumour suppressor gene due to its function in stress-mediated apoptosis. As is common amongst all hereditary PCa aetiology there have been conflicting studies determining the significance of risk associated with RNASEL deletion and PCa. A meta-analysis by Zuo et al confirmed this for the general population and that Hispanic Caucasians and Black Africans may be at a higher risk of PCa development due to RNASEL mutation [28].

MSR1 like RNASEL is also involved in immune response to pathogens, however, MSR1 codes for receptor proteins involved in recognition of foreign low-density lipoproteins via endocytosis. In PCa cells, the region that MSR1 gene is located (chromosome 8 p22) is deleted, suggesting that both RNASEL and MSR1 gene deletions may increase the risk of PCa due to inflammation caused by failure to carry out bacterial and viral RNA degradation [29].

NBS1 and CHEK2 are cell cycle checkpoint genes. NBS1, as mentioned in Table 1.2, is a gene that causes a recessive genetic condition known as Nijmegen breakage syndrome, a condition characterized by small head size, distinct facial features, immunodeficiencies and a greater susceptibility to cancers namely breast cancer, colorectal cancer and PCa [30 and 31]. NBS1 deletion impairs the ability of histone  $\gamma$ -H2AX to bind after DNA damage which leads to a delay in double stranded DNA re-joining post double stranded breakage [32].

CHEK2 is cell checkpoint inhibitor regulator involved in recognition and processing of DNA damage, cell cycle progression and apoptosis. It also stabilises tumour suppressor protein p53, which is involved in maintaining the cell cycle and responds to DNA-damage and oncogene activation by activating cell cycle arrest and apoptosis [33]. P53 protein irregularities may prevent damaged DNA repair and the ability to undergo apoptosis, or cell cycle arrest upon activation of oncogenes which cause the cell to replicate in a rapid uncontrolled manner [34].

Table 1.2 Genes associated with hereditary PCa and their functions.

<b>Gene</b>	<b>Function</b>	<b>References</b>
ELAC2	Codes for a protein that catalyses removal of 3' trailer on pre-tRNA. The protein can also interact with activated SMAD2 and FAST-1, lower expression may lead to suppression of transforming growth factor mediated cell cycle arrest.	[23, 24, 35, 36 and 37]
RNASEL	This gene codes for RNase L which is a ribonuclease that degrades the RNA of the cell and virus, inducing apoptosis of the virus infected cell.	[23, 38 and 39]
MSR1	MSR1 codes for macrophage scavenger receptors involved in activating endocytosis of low-density lipoproteins.	[23, 29 and 40]
NBS1	NBS is a recessive genetic disorder caused by mutation of NBS1, expression of the gene produces Nibrin, which operates as a cell cycle checkpoint protein. It aids in repair of double DNA strand damage.	[23, 41, 42 and 43]
CHEK2	Expression of this gene produces checkpoint kinase 2 which operates as a cell checkpoint regulator. It contains a forkhead-associated protein interaction domain, important in activation in response to DNA damage, it becomes phosphorylated and prevents cell from beginning mitosis. It has been shown to stabilise tumour suppressor protein p53.	[23, 44, 45 and 46]

### 1.2.3.2 Sporadic prostate cancer

Risk of sporadic PCa can be increased by mutation in certain genes including some mentioned in the hereditary prostate cancer section 1.2.3.1. However, other genes are also involved, and these are summarised in Table 1.3.

Table 1.3 Genes associated with sporadic PCa and their functions.

Gene	Function	References
TLR4	Member of toll-like receptor (TLR) family. Mediate cytokine production in response to gram-negative bacteria upon recognition of lipopolysaccharide (LPS).	[22, 47 and 48]
CDKN1B (p27)	Codes for protein p27, a cell cycle mediator, preventing the cell from replicating DNA stopping the cell from dividing too quickly.	[22, 49 and 50]
AR gene	Codes for the synthesis of the protein androgen receptor (AR). AR binds androgens such as testosterone, essential in male sexual development during puberty and proliferation of prostate cells.	[22, 51 and 52]
CYP17	Codes for P-450c17 $\alpha$ , this enzyme is responsible for the synthesis of testosterone.	[22, 53 and 54]
SRD5A2	Codes for the enzyme steroid 5-alpha reductase 2. It processes testosterone to DHT.	[22, 55 and 56]

Mutations of the TLR4 gene, a member of the toll-like receptor (TLR) family, have been associated with a small increase in PCa risk. The TLR4 receptor is found on the surface of cells and is responsible for recognising pathogen associated molecular patterns (PAMPs) from bacteria and fungi such as lipopolysaccharides (LPS) common within gram-negative bacteria and thus mediating cytokine production to regulate the innate immune response [57]. TLR4 receptors are expressed more on PCa cells compared to normal prostate cells. The increased number of TLR4 receptors lead to a more aggravated response to bacterial infection and a greater cytokine production with a greater pro-inflammatory induction [58]. Inflammation in the prostate from bacterial

infection including prostatitis are known to elevate the risk of PCa as mentioned in section 1.2.2 [59]. It has been shown that knockout of the TLR4 gene by transfection of TLR4 SiRNA into the PC3 cell line has shown reduced cellular migration and invasion [60].

CDKN1B, codes for p27, a protein involved in the mediation of the cell cycle. Competition for p27 by cyclin E/CDK complex and cyclin D/CDK is essential in driving cell cycle progression. p27 has a negative effect on cyclin E/CDK whereas it has a promotor effect on cyclin D/CDK complex [50]. In normal proliferating cells p27 expression is high, as it controls and mediates normal cell cycle progression and cellular proliferation, however in tumour tissue levels of p27 are almost non-existent [61]. Deletion of the gene or polymorphisms in critical regions such as the single polynucleotide polymorphism (SNP) 326T/G, which is most common in sporadic PCa cases than hereditary where the SNP -79C/T has a greater association according to a study carried out by Kibel et al [62]. It has been shown in a study by Sirma et al analysing over 4,000 patients that approximately 20% of cases show p27 expression loss [63].

The AR gene is responsible for the expression of AR in PCa cells. AR binds testosterone and DHT which stimulates male sexual development and prostate cell proliferation. Two main polymorphisms in the AR gene are CAG and GGN repeats in the gene. The number of CAG repeats influences the transcriptional rate in prostate cells, usually between 10 to 35, with variation amongst different ethnicities. Repeats of over 40 have shown a downregulation on transcription whereas a lower number of CAG repeats have shown an upregulation of transcription and greater risk of prostate carcinogenesis [64]. Whilst the length of the CAG sequence has shown conflicting risk on PCa, it has been noted that it poses a risk of earlier development of the disease rather than an overall increased risk. [65]. The GGN repeats are usually from 10 to 30, shorter GGN repeats have shown to increase transcriptional activity and thus aid in development of PCa. A retrospective analysis carried out in 2017 by H Weng et al, showed that shorter CAG (<22) and GGN (<16) compared to longer CAG ( $\geq 22$ ) and GGN repeats ( $\geq 16$ ) showed an increase PCa risk of 1.31 and 1.38-fold respectively [64].



CYP17 gene codes for the enzyme P-450c17 $\alpha$ , which is responsible for the synthesis of testosterone and DHT from less potent precursor androgens which drives prostate cell proliferation [66]. Mutation of this gene has been known to increase transcription of the gene leading to greater testosterone production, via a mutation in the promoter site known as the A2 allele [67]. It has been suggested that men who have heterozygous CYP17 A1/A2 gene or have homozygous CYP17 A2/A2 gene have a slightly greater risk than those with homozygous CYP17 A1/A1 gene. Haiman et al demonstrated that patients who are A1/A2 or A2/A2 have odds ratios of developing PCa of 1.26 and 1.17 respectively, compared to those who were A1/A1 [68].

#### **1.2.4 Prostate cancer diagnosis**

##### **1.2.4.1 Prostate specific antigen (PSA) and digital rectal examination (DRE)**

In the UK there is currently no screening programme for PCa, this is partially due to the unreliability of PCa testing. The current gold standard test for PCa, available in the UK for men over 50, consists of the digital rectal examination (DRE) and prostate-specific antigen (PSA) blood test [69]. The DRE test consists of a doctor feeling the abdomen and the rectum for signs of irregularity such as lumps and non-uniformly enlarged prostates that are not age-appropriate in size [70]. PSA testing is a blood test that checks for blood levels of the protein PSA. As PSA is produced in the prostate, levels of PSA that are considered abnormal for the patients age indicates possible cancerous growth due to the presence of more cells [71]. The importance of both tests has been extensively researched due to the invasive nature of the DRE test, however, retrospective analysis studies such as that carried out by Walsh et al in 2015 concluded that the DRE was an essential complementary test to PSA testing, due to the ability of DRE to detect PCa in the setting of a normal PSA level [69]. However, PCa screening remains a controversial issue due to PSA testing increasing prostate cancer diagnosis whilst having zero impact of PCa mortality [72]. The CAP randomized clinical trial concluded single PSA testing as a PCa screening system was not accurate. They reported that 189,386 men aged 50-69 attended a PSA testing clinic with 4.3% diagnosis rate (intervention group) compared to 219,439 men in the same age bracket who did not undergo PSA testing had a diagnosis rate of 3.6% (control group). Despite the increased diagnosis rate the difference in 10-year mortality rate was not significant,

the intervention group recorded a mortality rate of 0.30 per 1000 person-years compared to the control group with 0.31 per 1000 person-years [72].

#### **1.2.4.2 Gleason scoring, biopsies and magnetic resonance imaging (MRI)**

PCa is graded using the Gleason scoring system, a grading system developed by Donald Gleason in the 1960s and 1970s [73]. The Gleason grading system currently operates by analysis of biopsy samples under microscopy to determine the differentiation of the cells within the prostate. The scale uses 5 grades depending on the score assigned, grade 1 (Gleason score  $\geq 6$ ), grade 2 (Gleason score  $3 + 4 = 7$ ), grade 3 (Gleason score  $4 + 3 = 7$ ), grade 4 (Gleason score 8) and grade 5 (Gleason score 9-10) [74]. Grade 1 being considered well differentiated with 5 being poorly differentiated. Gleason scores of 7 are split to signify a grade where there are differing prognoses. A Gleason score  $3 + 4 = 7$  refers to most of the tumour cells being a grade 3 with some being a grade 4. The opposite is true for Gleason score  $4 + 3 = 7$  where most of the tumour is grade 4 and some grade 3. Patients with a  $4 + 3$  diagnosis tend to have a more aggressive cancer [75]. Higher Gleason score grading leads to a higher prevalence of cancers more likely to metastasise and a higher rate of biochemical recurrence (BCR) [76]. Magnetic resonance imaging (MRI) is used in two different stages of PCa diagnosis. The first example of MRI usage is in post biopsy, to determine the spread of the tumour [77]. Multi-parametric (mp) MRI is another example which combines a series of imaging techniques such as T2 weighted image (T2WI) with diffusion weighted imaging (DWI) to produce a more detailed view of the prostate, any cancer within the prostate and an exact target for biopsy. [78].

#### **1.2.5 Prostate cancer staging and treatments**

A PCa patients' treatment is determined by the classification of their disease. The gold standard method of classifying prostate cancer is the TNM staging system which stands for tumour, node and metastasis. The tumour description progresses through four stages which have subcategorizations, node refers to any spread into the lymph nodes and metastasis describes the presence of distant disease (Table 1.4) [79, 80]. These detailed staging characterisations aid physicians to decide the best treatment regimen for the

patient. This varies from early-stage disease where treatment is with curative intent or later stage palliative treatment.

Table 1.4 Prostate cancer stage characterised by TNM staging [80, 81].

<b>Tumour</b>	
T1	Cancer undetectable on scans or through DRE testing
T1a	Sample contains < 5% cancerous cells, incidentally, found during sampling or surgery for other condition
T1b	Sample contains > 5% cancerous cells, incidentally, found during sampling or surgery for other condition
T1c	Found after biopsy following PSA testing
T2	Cancer found completely within the prostate
T2a	Found within half of one side of the prostate
T2b	Found within more than half of one side of the prostate
T2c	Found within both sides of the prostate
T3	Tumour advancing through the prostatic capsule
T3a	Advancement into the bladder neck
T3b	Advancement into the seminal vesicles
T4	Advancement into surrounding tissue such as the pelvic wall, rectum or bladder
<b>Node</b>	
N0	No advancement of cancerous cells into local lymph nodes
N1	Advancement of cancerous cells into local lymph nodes
<b>Metastasis</b>	
M0	No metastatic spread to non-regional organs
M1	Metastatic spread to non-regional organs
M1a	Cancerous cells found in non-regional lymph nodes
M1b	Cancerous cells found in the bones
M1c	Cancerous cells found in other distant tissue

### 1.2.5.1 Localised prostate cancer therapies

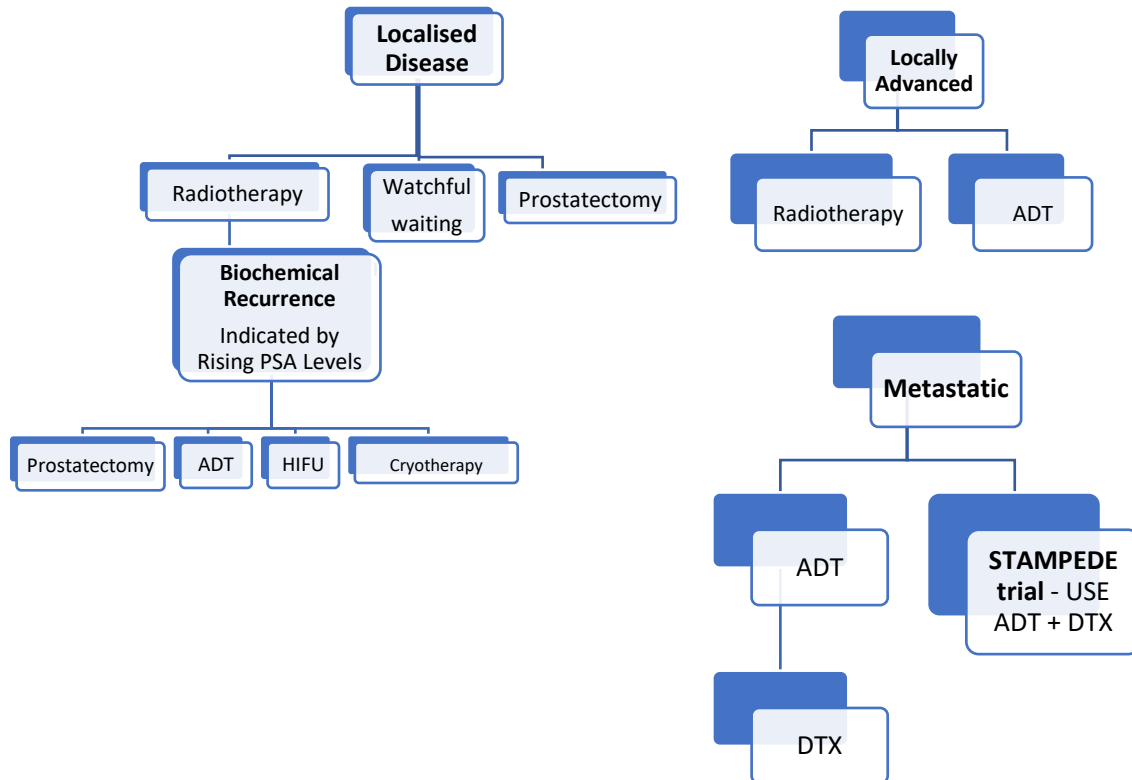


Figure 1.2 Graphical Depiction of Treatment Options for Prostate Cancer

Figure 1.2 summarises the disease stages of PCa and the possible treatments for each stage. Localised disease is the earliest treatable disease state of PCa, it is characterised by the entirety of the tumour remaining within the prostatic capsule. If the patient's disease has not metastasised or causing symptoms a clinician may recommend watchful waiting or active surveillance. Watchful waiting uses less invasive techniques of screening than active surveillance which is carried out by periodical biopsies. The use of these methods can prevent the need for patients to undergo unnecessary treatments that have severe side effects and can impact the rest of a PCa patients' life [82, 83]. Loeb et al has shown active surveillance to have a more beneficial outcome on patient survival and metastatic spread than watchful waiting. Patients that undertake watchful waiting had a lifetime risk of PCa death and metastasis of 8.72% and 10.30% respectively, compared to patients that received active surveillance with 5.42% and 6.50% [84]. The two main treatment options for localised PCa are radical

prostatectomy (RP) or external beam radiotherapy (EBRT) [85]. RP is the primary treatment for PCa patients, which involves total surgical removal of the prostate gland and some surrounding tissue. Despite this being the primary treatment option the rates of BCR are between 20-40% and the side effects of this treatment tend to be severe [86]. The most common side effects of RP in the long term after surgery include urinary incontinence and, erectile dysfunction if certain nerves are damaged during surgery. Other more severe side effects include loss of fertility due to the prostate no longer being able to provide the fluidic component of semen, therefore banking sperm may be suitable for the patient prior to operation [87-89]. EBRT is the other main treatment option for patients with localised PCa, which involves irradiating cancer cells with ionizing radiation causing alterations in the DNA of the cells that result in cell death [90]. The BCR of EBRT for localised PCa is between 30-50% [91]. These high rates of BCR for RP and EBRT highlight the complex nature of the disease and requirement for salvage treatments.

#### **1.2.5.2 Biochemical recurrence**

Cancer recurrence refers to the return of the disease after a treatment regimen ends [92]. BCR specifically refers to the detection of a rising PSA level after PSA blood testing, indicating the presence of remaining PCa cells post treatment. Despite the high levels of BCR in patients who received initial RP (20-40%) and EBRT (30-50%) [91, 93], it is widely accepted that most patients who have BCR tend to die of other causes than PCa itself [94]. There is current research into forming guidelines to suggest the best treatment regimen and the timing of salvage therapy initiation on an individual patient basis.

A systematic review carried out by the European Association of Urology (EAU)-European Association of Nuclear Medicine (EANM)-European Society for Radiotherapy and Oncology (ESTRO)-European Society of Urogenital Radiology (ESUR) and International Society of Geriatric Oncology (SIOG) (EAU-EANM-ESTRO-ESUR-SIOG prostate cancer guidelines panel) recommended the stratification of BCR PCa patients into severity-based groups. The severity-based groups displayed in Table 1.5 indicate the characteristics of BCR PCa that outline the risk group of the patient in developing a possibly life threatening from of the disease. Patients that

received initial RP are considered low-risk BCR if the PSA level doubling time is greater than 1 year and have a pathological Gleason scoring of less than 8 - the recommendation is that these patients can safely delay salvage EBRT. Patients are considered to have high-risk BCR if the PSA level doubling time is less than or equal to 1 year or have a pathological Gleason scoring of 8-10 - it is recommended that these patients receive early salvage radiotherapy. Patients that received initial EBRT are considered to have low-risk BCR if they have an interval from treatment to BCR of greater than 18 months and a biopsy Gleason score of less than 8- again it is recommended that these patients are offered a delayed salvage treatment. Patients are considered to be high-risk if the interval from treatment to BCR is less than or equal to 18 months and the biopsy Gleason score is between 8-10. These patients may benefit from early salvage therapies such as androgen deprivation therapy (ADT) [95]. Salvage therapies for BCR PCa include EBRT for patients who initially received RP, brachytherapy for patients who initially received EBRT, cryotherapy, high intensity focused ultrasound (HIFU), ADT or RP for patients who initially received EBRT [96].

Table 1.5 Outline of the EAU-EANM-ESTRO-ESUR-SIOG prostate cancer guidelines panel's risk grouping based on the characteristics of a patients BCR (Taken from [96]).

Risk Group	Characteristics
BCR after radical prostatectomy	
Low-risk BCR	PSA-DT >1 yr and pGS <8 (ISUP grade <4)
High-risk BCR	PSA-DT $\leq$ 1 yr or pGS 8-10 (ISUP grade 4-5)
BCR after radiation therapy	
Low-risk BCR	IBF >18 mo and bGS <8 (ISUP grade <4)
High-risk BCR	IBF $\leq$ 18 mo or bGS $\geq$ 8 (ISUP grade 4-5)

*BCR = biochemical recurrence; PSA-DT = prostate-specific antigen doubling time; pGS = pathological Gleason score; ISUP = International Society of Urological Pathology; IBF = Interval from primary therapy to biochemical failure; bGS = biopsy Gleason score.*

### **1.2.5.3 Salvage therapies for BCR prostate cancer**

#### **1.2.5.3.1 Salvage external beam radiotherapy (EBRT)**

Salvage EBRT is offered to BCR PCa patients based on several conditions, firstly they must have received initial RP. It has also been suggested that patients with an estimated life expectancy of less than 10 years may not benefit from salvage EBRT [97-99]. Due to the emergence of other salvage therapies clinical trials have been undertaken to determine the effects of salvage EBRT vs adjuvant EBRT on recurrence and survival-based outcomes. Salvage EBRT is classified as a radiotherapeutic regimen applied after the detection of BCR, adjuvant EBRT is classified as a radiotherapeutic regimen applied within 5 months of the initial RP [100]. The three clinical trials designed to determine the outcomes of these treatments were European Organisation for Research and Treatment of Cancer (EORTC) 22,911, Southwest Oncology Group (SWOG) 8794 and ARO 96-02 trial [101, 99]. The ARO 96-02 trial concluded that men who received adjuvant EBRT had a significantly reduced risk of BCR with a median disease recurrence at 13.8 years compared to the observation only group with 9.9 years. However, there was no significant benefit on overall survival (OS) with the adjuvant EBRT group having a median survival of 14.7 years vs the observation group with 13.8 years [101]. The EORTC 22,911 trial supported the finding of the ARO 96-02 trial. It found that the biochemical progression-free survival was 39.4% for the adjuvant EBRT compared with 61.8% in the observation group [101]. The SWOG 8794 showed a different outcome on survival showing that adjuvant EBRT improved median (OS) (15.2 years) compared to the observation group (13.3 years) [99]. Evidence from these trials would suggest utilising EBRT in the immediate post-operative timeframe rather than allowing the usual observation period before beginning salvage EBRT on the BCR PCa patient.

#### **1.2.5.3.2 Salvage brachytherapy (BT)**

Brachytherapy (BT) is defined by the implantation of radioactive seeds into the prostate to irradiate the tumour and can be a salvage therapy for PCa patients that received initial EBRT [102]. BT comes in low dose rate (LDR) and high dose rate (HDR), LDR-BT uses the isotopes I-125, Pd-103 and Cs-131 while HDR-BT uses the isotope Ir-192 [103]. The main issues with salvage therapies such as ADT, cryotherapy and HIFU is

their high levels of side effects. Brachytherapy benefits from reduced side effects presented by other salvage therapies. LDR-BT generally does not cause toxicity to other surrounding tissues and HDR-BT is only applied for a matter of min [104]. Limited data exists on the success of salvage BT on BCR PCa patients. One meta-analysis by J. Zhong et al in 2021 looked at 12 LDR-BT studies and determined 2- and 5-year BCR free survival rates of 71% and 52.5% respectively while 11 HDR-BT studies showed 2- and 5-year BCR free survival rates of 74% and 51% respectively. The meta-analysis also showed acceptable toxicity levels for LDR-BT and HDR-BT showing mean grade 3 or higher toxicities of 2 and 1.8% respectively. However, they highlighted some issues with their data that included differences in patient demographics, some BT treatments were salvage, and some were primary treatments as well as some studies using combined ADT. These limitations were attributed to inconsistencies in the reported data [105].

#### **1.2.5.3.3 Cryotherapy**

Cryotherapy is a salvage treatment that involves the freezing of the prostate to kill PCa cells. [106]. Advancements in the technology have improved specificity of the treatment which is referred to as focal cryotherapy [107]. The freezing was initially done using liquid nitrogen, more up-to-date methods utilise argon gas through a series of needles to freeze and helium gas to thaw the target area. The 5-year progression free survival (PFS) rates for cryotherapy in a data set in 1198 patients produced by Jones et al. (108) was 72.9% following the USAs phoenix definition of biochemical disease-free survival [107, 108]. The PFS of patients treated with focal cryotherapy was compared to those treated with whole gland cryotherapy by Tan et al in 2019 which investigated 385 men. They found that BCR following salvage cryotherapy was 22.2% for focal cryotherapy vs 21.5% for whole gland cryotherapy suggesting that both techniques are effective salvage treatments. However, they did not find a significantly different reduction in rates of impotence for focal and whole gland cryotherapy (52.6% and 59.6% respectively), or urinary function rates (9.3% and 15.1% respectively) within 12 months of treatment [109].



#### **1.2.5.3.4 High-intensity focused ultrasound (HIFU)**

HIFU is a relatively new form of BCR PCa salvage therapy that involves the use of directed high frequency ultrasound (US) to cause necrosis of the target PCa tissue by means of thermal ablation and acoustic cavitation [110, 111]. HIFU is only available to patients as part of a clinical trial, it has not been approved for widespread use due to the lack of safety data associated with the novel technology [112]. The first clinical study looking at long term outcome of patients treated with HIFU salvage treatment determined the 5-year disease-free survival rate with and without ADT - the rates were 87% and 86% respectively [113, 114].

HIFU has recently been identified as being an immunostimulant. The ablative nature of HIFU can cause tissue fractionation resulting in tumour specific antigens entering the lymphatic system where a T-cell mediated immune response can be initiated. Such a response would result in an immune system related anti-cancer effect at non-HIFU treated sites, a process that has been referred to as the “abscopal effect” [115, 116]. Pre-clinical studies have investigated the possibility of using PD-1 and CTLA-4 checkpoint inhibitors to compliment HIFU treatment [117]. In an *in vivo* murine study carried out by Orrason et al. (118), a small portion of the tumour was treated with HIFU rather than the whole tumour to limit vascular damage of the prostate enabling maximum blood flow to the target site and enable the newly generated antigens to enter circulation. The treated mice then received CTLA-4 and PDL-1 inhibitors and the results showed OS at 300 days was 62.5% compared to 0% for the other control groups. They also rechallenged the mice with the same cell-line to determine the effect of memory effector cells and determined that no tumour growth occurred up to 75 days after the rechallenge [118].

#### **1.2.5.4 Locally advanced prostate cancer**

Locally advanced PCa is defined as tumours that extend beyond the prostate boundaries but is not yet metastatic [119]. Patients with locally advanced prostate cancer who are considered low-risk of metastatic spread may be offered radical prostatectomy leading to 15-year survival rates of 74%. Patients considered higher risk of locally advanced prostate cancer may be offered EBRT and/or ADT [19, 120]. Neoadjuvant ADT is commonly utilised prior to EBRT and has been shown in the RTOG 86-10 trial to be

more beneficial than radiotherapy alone with OS of 50.5 and 41% respectively, however this was not statistically significant. However, for PCa patients with Gleason score 2-6 the difference was statistically significant (66.2% and 41.4%) for neoadjuvant ADT plus EBRT compared to EBRT alone. The proposed theory for the difference between these groups of patients was the greater levels of oxygenation which is known to increase the therapeutic outcomes of radiotherapy [121].

#### **1.2.5.5 Metastatic prostate cancer**

Metastatic PCa is described as the spread of the PCa primary tumour beyond the local area surrounding the prostate and into distant sites. The most common PCa metastases were identified in a 74,826-patient review which showed bone to be the most common at 84%, lymph nodes 10.6%, liver 10.2% and thorax 9.1% [123]. The NICE guidelines for metastatic PCa options was informed by two major clinical trials: ChemoHormonal Therapy versus Androgen Ablation Randomized Trial for Extensive Disease (CHAARTED) and Systemic Therapy in Advancing or Metastatic Prostate Cancer: Evaluation of Drug Efficacy (STAMPEDE) [124, 125]. The CHAARTED trial compared the median OS of a total of 790 patients who were treated with either a combination of ADT and DTX or ADT alone, they observed median OS for these groups to be 57.6 months and 44.0 months respectively [125]. The STAMPEDE trial aimed to determine if any benefit could be obtained by combining the standard of care (SOC) ADT, with either DTX or zoledronic acid (ZA). The results demonstrated that SOC + ZA produced no statistical difference in 5-year survival (57%) compared to SOC only (55%). However, the SOC + DTX group did produce a survival benefit when compared to SOC with a 5-year survival of 63% vs 55% and a overall median survival of 81 months vs 71 months [126].

#### **1.2.6 Androgen deprivation therapy (ADT)**

ADT is defined as surgical or medical castration to prevent androgen stimulated prostate growth [127]. ADT was first used to treat PCa by surgically removing the testes or through administration of oestrogen, to suppress testosterone production, which is known to advance growth in PCa. In patients surgically castrated via removal of the

testes the growth of the prostate was inhibited but not stopped, this was due to androgen production in the adrenal glands [128]. Advancements in ADT in the 60s and 70s led to the development of a class of antiandrogen drugs that compete for the AR with the androgens [129]. Antiandrogens block androgen function by preventing the AR undergoing nuclear translocation [130]. First-generation antiandrogens included flutamide, bicalutamide and nilutamide [131]. Second-generation antiandrogens such as enzalutamide (Enz) differ to first-generation antiandrogens due to their higher affinity for the AR. This is evidenced by clinical trials such as the Safety and Efficacy Study of Enzalutamide Versus Bicalutamide in Men with Prostate Cancer (STRIVE) trial. The STRIVE trial compared nonmetastatic and metastatic castration resistant PCa patients and observed a higher median OS of 19.4 months versus 5.7 months for the Enz second-generation antiandrogen vs the first generation bicalutamide [132].

### **1.2.7 Docetaxel (DTX)**

Docetaxel (DTX) is an antimicrotubular taxane which was developed and licensed as Taxotere and was given Food and Drug Administration (FDA) approval in 1996 for the treatment of breast cancer, before being approved for PCa in 2004 [133-135]. DTX is derived via a semi-synthetic pathway from compounds extracted from the needles of the European yew tree *Taxus baccata* [136, 137]. Today, DTX is a mainstay treatment for breast and metastatic PCa, as well as stomach, lung, and head and neck cancer [138]. Prior to the approval of DTX in 2004 by the FDA for PCa treatment, the most common chemotherapy for metastatic PCa was mitoxantrone. Clinical trials undertaken between 2000 and 2002 involving 1006 men determined that mitoxantrone plus prednisone was less effective in treating PCa patients than DTX every three weeks with median OS of 16.5 months and 18.9 months respectively [139].

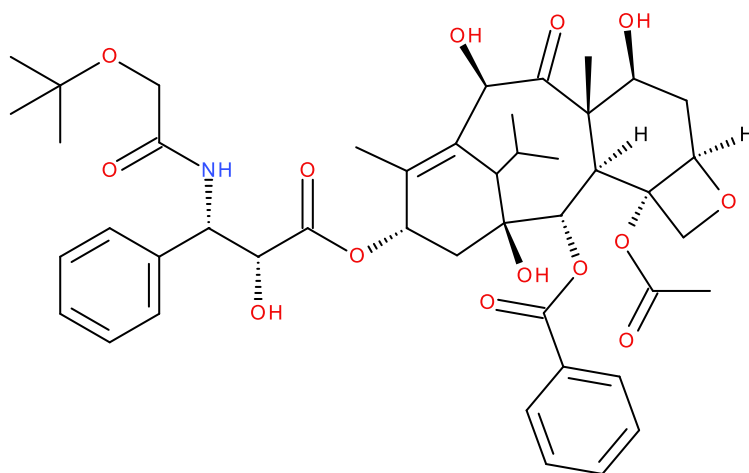


Figure 1.3 Chemical structure of DTX

DTX is as an antimicrotubule agent.  $\alpha$ -tubulin and  $\beta$ -tubulin form a heterodimer subunit of the microtubule polymer which is an essential step in G2 phase of the cell cycle [140]. DTX binds to  $\beta$ -tubulin which stabilises the microtubule polymer, preventing depolymerization and in turn halting mitosis [141, 142]. A second mechanism of action for DTX is to downregulate the expression of B-cell lymphoma 2 (Bcl-2), which is an apoptosis regulation protein, the expression of Bcl-2 can prevent apoptosis [143]. Bcl-2 is more highly expressed in PCa cells, therefore treatment with DTX can make PCa more susceptible to apoptosis [144, 145].

#### 1.2.7.1 Docetaxel side effects

DTX treatment like many chemotherapies has numerous side effects. Despite having a slightly better aqueous solubility than its taxane counterpart paclitaxel (PTX), it is still extremely hydrophobic. Taxotere, the commercial name for DTX, is formulated in polysorbate 80 (Tween 80) and ethanol to combat its poor aqueous solubility [146]. Polysorbate 80 has both systematic side effects (hypersensitivity, nonallergic anaphylaxis and rashes) as well as effects at the infusion site (pain, erythema, and thrombophlebitis) [147]. The drug itself is also known to have extensive side effects including increased infection risk due to white blood cell counts dropping, bruising, bleeding, lethargy, nausea, hair loss, anaemia, loss of appetite, mouth ulceration, diarrhoea, constipation, skin problems (dryness, rashes or itching), slower more brittle

nail growth, conjunctivitis, blurred vision, muscle and joint pain, lung problems (wheezing cough, fever and breathlessness), fluid build-up in limbs, chest pain and heart arrhythmia [148, 149]. The reason these side effects are so prevalent are because DTX chemotherapy is not targeted. This is further compounded as most patients diagnosed with prostate cancer are elderly men, many with other co-morbidities. Therefore, better targeted treatments and delivery systems are required which increase the amount of drug reaching the tumour but limiting systemic exposure.

### **1.3 Targeted cancer therapy**

Targeted cancer therapies differ from systemic cancer therapies such as DTX as they are designed to specifically be delivered or activated at the target site after administration. The goal of this is to maintain or improve therapeutic outcomes of a disease whilst reducing the severity of systemic side effects [150]. The first known targeted therapy was tamoxifen. First synthesised in 1962, tamoxifen was developed to inhibit oestrogen binding to the oestrogen receptor in oestrogen sensitive breast cancer and is now one of the best-selling breast cancer therapies worldwide [151, 152]. Since then, the field of targeted cancer therapies have developed massively with a wide variety of drug classes including hormone therapies such as tamoxifen and the antiandrogens described for PCa treatment, signal transduction inhibitors, gene expression modulators, apoptosis inducers, angiogenesis inhibitors, immunotherapies and drug conjugated monoclonal antibodies (Table 1.6) [153]. It is widely accepted that targeted drug therapies are the most important aspect of cancer therapy research for improving the therapeutic outcomes of cancer therapy and reducing the toxicity of traditional methods of cancer treatments.

Table 1.6 Description of the main classes of targeted drug cancer therapies [153-160].

<b>Class of target cancer therapy</b>	<b>Description</b>	<b>References</b>
<b>Hormone therapy</b>	Treatment of hormone sensitive cancers such as breast, cervical and prostate cancer using hormone blockades and hormone synthesis suppressants.	[154]
<b>Signal transduction inhibitors</b>	Blocks signal pathways that are utilised by cancer cells to promote cancerous growth leading to cell death.	[155]
<b>Gene expression modulators</b>	Protein based drugs that modulate the expression of genes by targeting the activity of transcription factors. These transcription factors could cause upregulation of genes that protect or promote cancerous growth.	[156]
<b>Apoptosis inducers</b>	Target apoptosis related proteins to cause the cell to undergo controlled cell death – apoptosis.	[157]
<b>Angiogenesis inhibitors</b>	Inhibition of angiogenesis (the formation of new blood vessels in the tumour microenvironment) preventing the ability of the tumour to increase circulation to the tumour.	[168]
<b>Immunotherapy</b>	Stimulation of the immune system to recognise tumour antigens and overcome cancerous evasion of the immune system.	[159]
<b>Antibody-drug conjugates</b>	Immunoconjugates comprised of monoclonal antibodies conjugated to an anticancer therapy, to deliver a drug payload after the monoclonal antibody binds to a tumour specific receptor.	[160]

### 1.3.1 Photodynamic therapy (PDT)

Outside the major classifications of targeted cancer therapy there are other more nuanced technologies available such as photodynamic therapy (PDT). PDT requires the use of photosensitiser (PS) administered topically or parenterally to the tumour, which is then irradiated by light of an appropriate wavelength activating the PS, causing the production of reactive oxygen species (ROS) and causing tumour specific cytotoxicity. As the sensitiser remains inactivated until exposed to light, the ability of PDT to cause cytotoxicity in a site-specific manner overcomes the major problem with traditional chemotherapy [161]. The ideal PS should be non-toxic until activated and produce enough ROS upon activation at a clinically suitable wavelength. Clinically suitable wavelengths refer to a wavelength of light that can penetrate tissue to the maximum extent possible. As a result, sensitisers that absorb in the red region of the visible spectrum or near infrared (NIR) spectrum are desired as these wavelengths penetrate deepest into human tissue [162].

The mechanism of PDT operates by excitation of an electron in the PS from a singlet ground state ( $S_0$ ) to a singlet excited state ( $S_1$ ) upon absorption of a photon of light. The  $S_0$  electron can either return to  $S_0$  via the production of light through fluorescence or it can undergo a process known as intersystem crossing. Intersystem crossing involves the  $S_1$  electron changing its spin-state to form a triplet excited state ( $T_1$ ).  $T_1$  has a longer lifetime, opening up the possibility for other non-radiative processes. A Type I photodynamic process involves a redox reaction where the  $T_1$  electron of the PS is transferred to an appropriate substrate to form free radicals such as hydroxyl radicals ( $OH\bullet$ ). A Type II photodynamic process involves the transfer of the  $T_1$  excited state energy to ground state molecular oxygen, which has an uncharacteristic triplet ground state, to form singlet excited state oxygen ( $O_2^{\bullet}$ ) (Figure 1.4) [163].

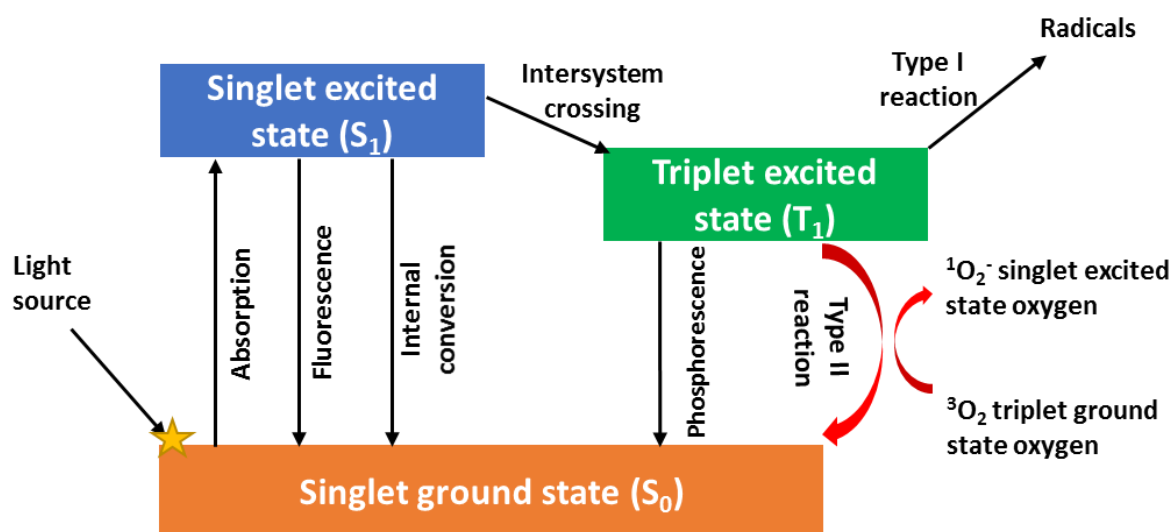


Figure 1.4 Mechanism of type I and II PDT

The ROS generated by the Type I and II photodynamic processes cause cytotoxicity by several pathways. One pathway involves the oxidation of proteins involved in key cellular functions such as enzymes and growth factors. These proteins are susceptible to oxidation particularly in cysteine and methionine rich amino acid chains [164, 165]. ROS can also cause cytotoxicity via the peroxidation of lipids that form the cell membrane leading to apoptosis upon the release of ceramide. The oxidation of DNA can also occur leading to DNA strand breakage which in turn leads to cellular necrosis [166, 167]. This variety of mechanisms that can cause cell death means it is difficult for cancer cells to generate resistance to PDT.

PDT is also known to have immunostimulatory effects. This is attributed to the inflammatory damage caused by PDT that causes an influx of dendritic cells, monocytes, macrophages, neutrophils and mast cells to the treatment site. As a result, PDT has been shown to stimulate the immune response by recruitment of B and T cells. Consequently, PDT has been combined with emerging immunotherapies to determine if the immune response caused by PDT can be complimented by these immunotherapies. In addition, this opens the potential for PDT, which has largely been viewed as a localised treatment to also be used in the treatment of systemic disease. [168].



A major drawback of PDT that has limited its clinical utility is the inability of light to penetrate deeply into tissue. Even light in the phototherapeutic window (600-850nm) can only penetrate tissue to depths of approximately 5 mm. This has restricted the use of PDT to the treatment of superficial lesions and limited its application in the treatment of larger deeper-seated solid tumours. The use of interstitial fibreoptic light delivery has provided moderate success in overcoming this limitation but this is a relatively complicated procedure with limited possibility of widespread clinical use [169].

### 1.3.2 Sonodynamic therapy (SDT)

Sonodynamic therapy (SDT) shares many similarities with PDT, but low-intensity ultrasound (US) is used instead of light to activate the sensitizer. The major benefit of SDT is that US can permeate tissue to depths of tens of centimetres depending on the frequency used. This is evident during the use of US in sonography for the detection of solid cancerous tumours and the imaging of foetuses during pregnancy [170].

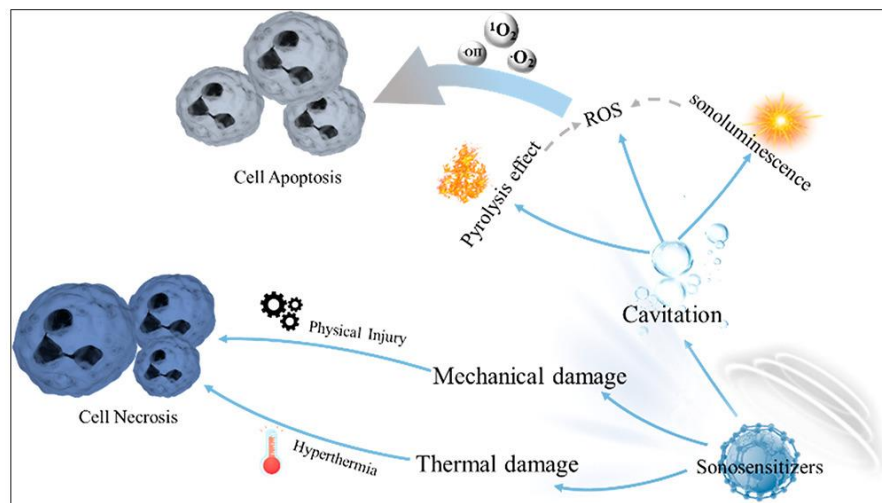


Figure 1.5 Proposed mechanisms of SDT (taken from [171]).

The US conditions used in SDT does not cause cellular damage itself but instead activates the sonosensitizer which is responsible for the observed cytotoxic effect. This is distinctly different to HIFU (section 1.2.5.3.4), which causes cellular necrosis by thermal ablation [172]. Two mechanisms have been proposed for the cytotoxic effect generated by SDT. The first is pyrolysis where the ultrasound generates microbubbles (MBs) which rapidly expand and collapse (inertial cavitation) producing extremely

high localised temperatures and pressures up to 10,000 °K and 81 MPa, respectively. These extreme localised conditions can cause pyrolysis of the sensitiser into radical fragments and / or ROS [173-175]. The second mechanism involves sonoluminescence. In this mechanism, inertial cavitation leads to the release of light photons which activate the sensitiser as in PDT [176]. The detection of light within a US frequency relevant to SDT (1.93 MHz) was reported by Umemura et al who observed broadband sonoluminescence over 250-650 nm, with a peak intensity detected between 400-450 nm [177]. Further evidence was provided by Beguin et al. (178) who demonstrated the activation of Rose Bengal (RB) by sonoluminescence resulting in singlet oxygen detected using the by singlet oxygen sensor green (SOSG). While some debate still exists as to the exact mechanism of SDT mediated cytotoxicity, it opens the potential for the targeted treatment of more deep-seated tumours, such as those localised in the prostate [178].

### 1.3.2.3 Rose Bengal (RB)

Rose Bengal (RB) is a xanthene dye, used medically for detecting ocular dryness by staining dead and damaged cells, but not healthy cells [179, 180].

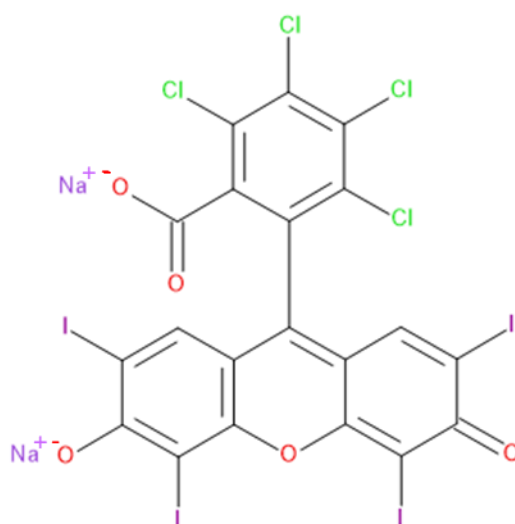


Figure 1.6 Chemical structure of Rose Bengal.

It has also been demonstrated to be an effective PS for PDT and SS for SDT. RB is weakly fluorescent and has excitation and emission maxima of 550nm and 572nm respectively [181]. McEwan et al have tested the PDT and SDT effectiveness of RB in

RIF-1, HeLa and B16 melanoma cell lines. The PDT and SDT mediated toxicity were comparable in the RIF-1 and HeLa cell lines. However, in the highly pigmented B16 melanoma cell line, SDT was significantly better than PDT with cell viabilities of 60% and 82% respectively at the same RB concentration. In addition, SDT treated B16 melanoma tumours in mice were 380% smaller than their PDT counterparts 4 days after treatment. This difference was attributed to the highly pigmented melanin acting as a filter for the excitation light that reduces PDT efficacy. The use of ultrasound circumvents this problem in SDT [182].

#### 1.4 Microbubbles (MBs)

MBs comprise a gas filled core stabilised by an outer shell of phospholipids, polymers or proteins. The main clinical application of MBs are as contrast agents for ultrasonic imaging. The shell stabilises the MB which would otherwise be unstable due to the surface tension effects of bubbles in the micro size range. Backscatter for ultrasonic imaging is provided by the gas core which improves the quality of the image the sonographer receives [183].

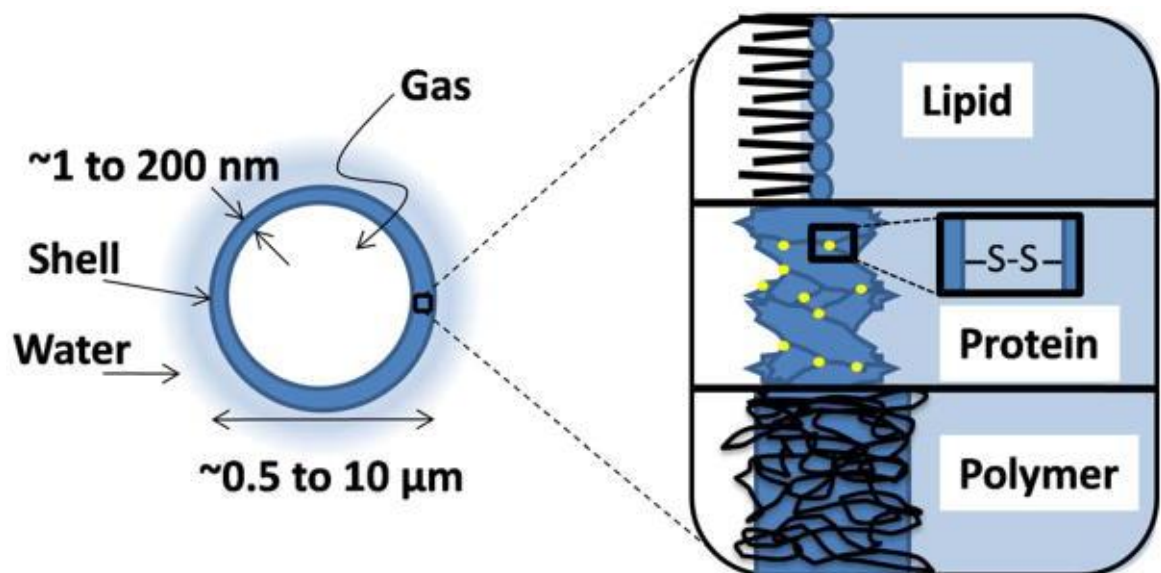


Figure 1.7 MB shell formulated with different compositions i) lipid, ii) protein and iii) polymer. (Taken from [183])

The most common production methods for MBs are mechanical agitation or sonication. Upon production and dispersion in aqueous media, two forms of bubbles are identified

and can be observed separating by size. The first are smaller singular bubbles with high flowability and with a greater ability to remain in suspension, generally found at the bottom of the dispersion. The second are larger interlinked polyhedral MBs which are more static in terms of flowability, this is also considered the foam layer which is generally disposed of [184].

#### **1.4.1 Clinically approved use of MBs**

MBs are currently clinically approved as contrast agents for use in ultrasonic imaging. The MBs oscillate when US is applied, they produce acoustic scattering that provides an US impedance that is distinguishable from the surrounding tissue. Figure 1.8 illustrates the ability of MBs to scatter US and produce a contrast over time to reduce background noise from surrounding tissue and produce total image washout allowing for the tumour mass to be seen clearly. Figure 1.8 a) shows traditional gray-scale ultrasound image showing a mass in the centre of the image, b) shows a small improvement of the image 8 seconds post MB administration, c) at 35 seconds there is washout of the mass in the centre and d) shows that after 2 min the mass appears completely black with total washout of the image, where the images are providing enough contrast to completely distinguish the central mass from the surrounding tissue [185-187].

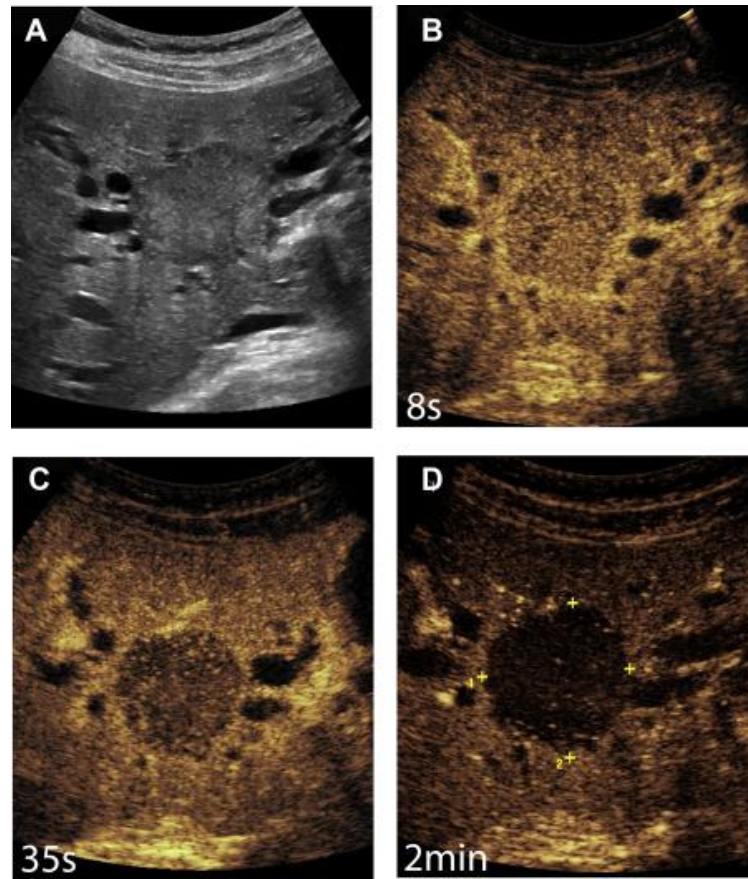


Figure 1.8 Sonograms using MB contrast agents a) traditional gray-scale image with no MB contrast agent, b) the image 8 seconds after administration of MBs, c) the image 35 seconds after MB administration and d) the image 2 min after MB administration. (Reproduced from [185])

There are several commercially available MBs used as contrast agents that comprise various types of shell and internal gas compositions. Table 1.7 displays the commercially available MB contrast agents; the list highlights the fact that lipid shells are the most common [188]. Lipid shells are reported to be advantageous for MB production due to the ability of phospholipids to self-assemble. Phospholipids comprise of hydrophobic acyl tails and hydrophilic phosphate heads; this aids the phospholipids to spontaneously form into a monolayer with the acyl layer orientating towards the core of the MB. The acyl tail undergoes lateral compression allowing them to form a low surface tension below their phase transition temperature, this in turn maintains stability of the gaseous core [189].

Table 1.71 Commercially available MB contrast agents for ultrasonic imaging, (reproduced from [188]).

<i>Name</i>	<i>Shell composition</i>	<i>Core gas</i>	<i>Mean diameter (<math>\mu\text{m}</math>)</i>
<i>Levovist</i>	Galactose/palmitic acid	Air	2-8
<i>Optison</i>	Human albumin	Octafluoropropane	1-2.25
<i>SonoVue</i>	Lipid	Sulfur hexafluoride	3
<i>Definity</i>	Lipid	Octafluoropropane	2.5
<i>Sonazoid</i>	Lipid	Perfluorobutane	3.2

### 1.5 Properties of ultrasound

Ultrasound is a form of mechanical sound energy that is inaudible to humans with a frequency of greater than 20 Hz [190]. The speed in which ultrasound travels through a medium is known as propagation. Propagation occurs when US travels through a medium such as human tissue where the alternating pressures of the oscillating soundwave cause mechanical vibration of particles as the soundwave travels. As ultrasound propagates through tissue it loses energy through attenuation. This is when the ultrasonic waves are absorbed and released as heat rather than as sound [191-193]. Ultrasound comprises two types of waves i) longitudinal waves and ii) transverse waves. Longitudinal waves correspond to a high-pressure portion where the particles are compressed. Transverse waves correspond to a low-pressure portion where the particles are scattered, known as rarefaction (Figure 6) [194].

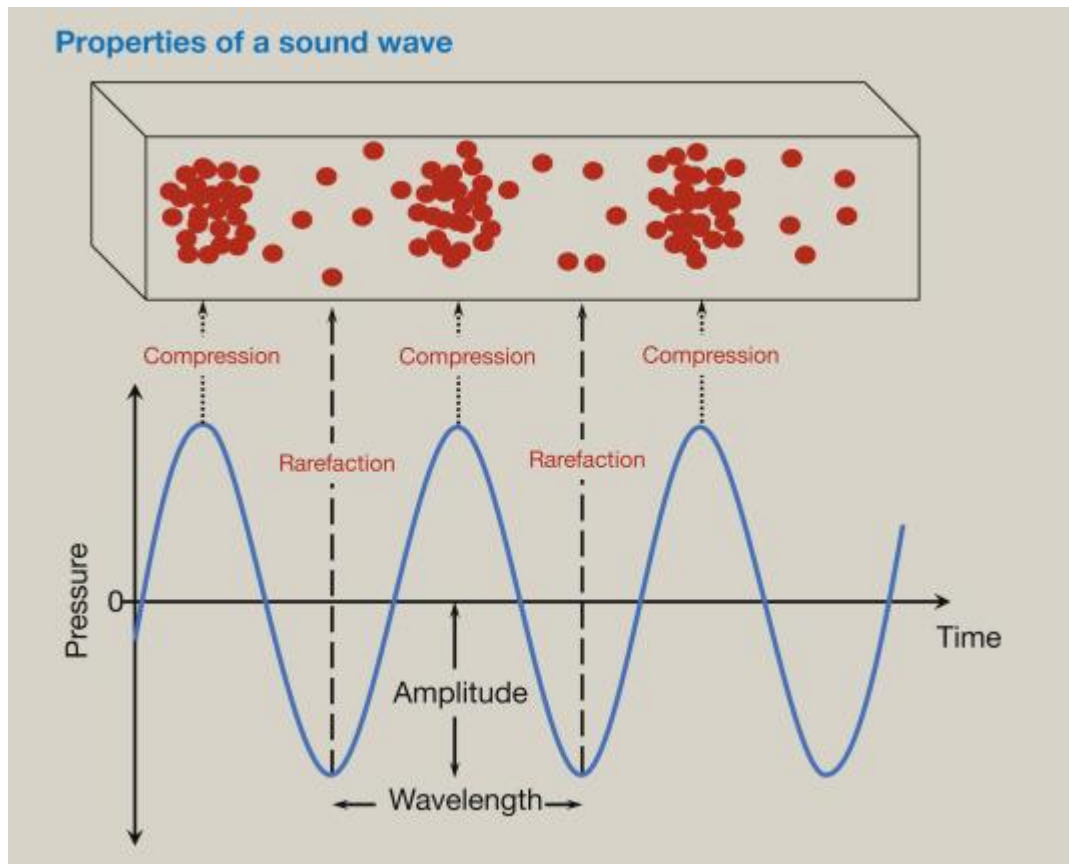


Figure 1.9 Compression and rarefaction of a soundwave in tissue (reproduced from [194]).

### 1.5.1 Ultrasound therapy

US forms a component part of several therapeutic and drug delivery strategies: i) HIFU, ii) SDT, iii) sonoporation and iv) gene transfer [195]. HIFU and SDT have been described in Sections 1.2.5.3.4 and 1.3.2 respectively.

Sonoporation involves the application of US during drug delivery to cause the formation of transient pores in the cell membrane of target tissue to improve drug uptake. This pore formation is facilitated by the MB cavitation local to the target tissue. Wang et al. (196) investigated the potential of sonoporation-induced cell membrane permeabilization using exogenous MBs. They used propidium iodide (PI) as a drug surrogate and the effect of MB cavitation on the uptake of PI into the cells was investigated. Cells that had MBs adjacent showed an uptake of PI over time, whereas cells with no adjacent MBs showed no change [196]. Two mechanisms of this have been postulated, the first is due to inertial cavitation of MBs under US near a tissue



boundary which causes deformities in the pattern of cavitation of the MB, the energy of which causes a liquid jet to extend through the internal portion of the MB. This jet can place large amounts of energy on the impact site causing pores to form in the target tissue. If the MB collapses shockwaves can be formed causing damage to the target tissue also. The second mechanism operates by the ‘pushing and pulling’ of the cell membrane during stable cavitation. MBs adjacent to tissue push on the cell membrane as they expand causing it to open and pulling in on the cell membrane as the MB shrinks (Figure 1.10) [197, 198]. Gene transfer utilises sonoporation to deposit DNA or RNA into a cell using the mechanisms described above. It is a non-viral method of gene transfer that provides a less toxic alternative to traditional viral vectors for gene transfer. [199].

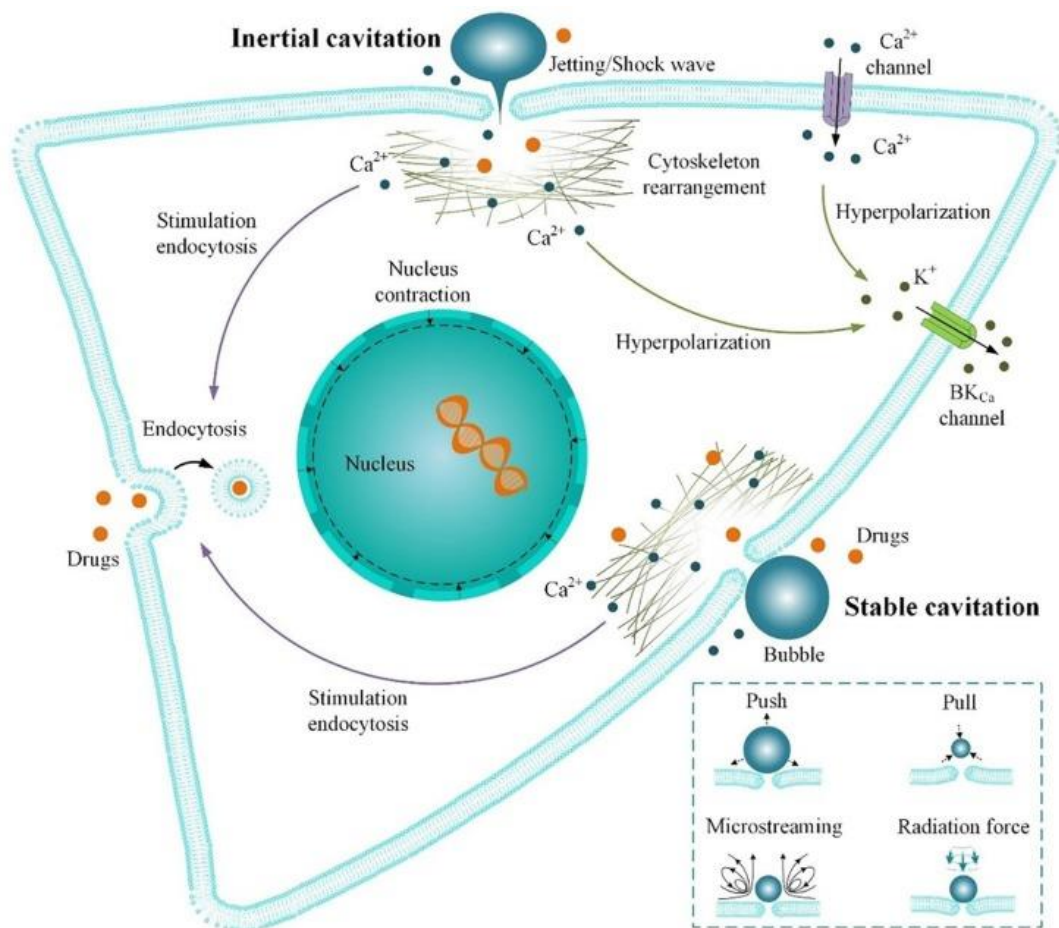


Figure 1.10 Mechanisms of MB induced sonoporation caused by stable and inertial cavitation (reproduced from [198]).



### 1.5.2 Ultrasound-targeted microbubble destruction (UTMD)

MBs provide the ability to deliver drugs directly to a specific site. MBs are administered systemically via intravenous infusion, US is immediately applied to the target site such as a tumour. The US focused on the tumour causes MBs to oscillate, if the US is at a high enough intensity the MBs will undergo inertial cavitation causing MB collapse. The collapse of the MB in the vicinity of the tumour increases the uptake of the drug in the surrounding tissue. Further uptake is driven by processes such as sonoporation, microjetting and microstreaming. The MBs can also be loaded with drugs themselves when the shrinking, expanding and liquid jetting causes the leakage of drugs from the MB into the target tissue that has been permeated by the mechanical effects of the MBs (Figure 1.11) [200]. The ability of UTMD to deliver drugs directly to the intended site both allows for much lower doses of toxic drugs to be used which can have the same therapeutic effect as high dose standard treatments. The other benefit is reduced systemic release of toxic chemotherapies reducing harmful side effects [201]. As described before, the main chemotherapy used in the treatment of PCa is DTX despite the severity of observed side effects. These side effects could be reduced by incorporation within a US targeted MB drug delivery system.

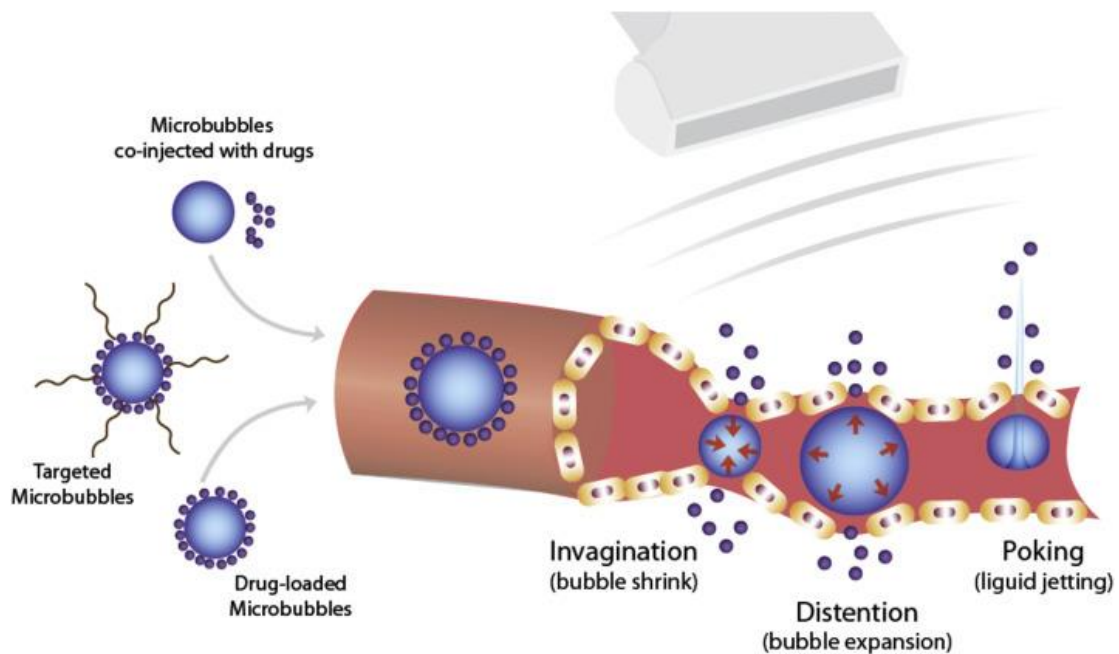


Figure 1.11 Ultrasound targeted drug delivery via non-destructive mechanisms (taken from [200]).

### **1.5.2.1 UTMD mediated chemo-sonodynamic therapy**

Chemo-SDT combines conventional chemotherapy with SDT. MB have commonly been used to deliver both the chemotherapy and SDT sensitiser, with the US conditions used to cause MB cavitation also activating the sensitiser. McEwan et al. (202, 204) first described the potential of UTMD mediated chemo-SDT using lipid stabilised MBs attached to the antimetabolite 5-FU and Rose Bengal. The MBs were shown to target delivery of the drug payloads to pancreatic tumours in mice and combined chemo-SDT was significantly more effective than chemotherapy or SDT alone. Interestingly, the amount of chemotherapy used was a fraction of a normal dose used in mice and as a result the treatment was well tolerated. Since this study, the same group has investigated other chemotherapies in combination with Rose Bengal, such as gemcitabine, doxorubicin and paclitaxel [202, 204]. Various methods have also been adopted for incorporation of the drugs within the MB. This includes use of the biotin-avidin-biotin interaction, covalent attachment of the drugs to the lipid, or hydrophobic incorporation of drugs in the hydrocarbon component of the MB shell. More detail on these studies will be provided in the chapter introductions.

## **1.6 Aims and objectives**

The main aims of the work described in this thesis were to investigate the potential of UTMD mediated chemo-SDT therapy as a treatment for prostate cancer. The specific objective of the work undertaken in each result chapter is provided below.

### **1.6.1 Chapter 3**

Chapter 3 outlines the development of a UTMD chemo-SDT formulation utilising the thin-film, sonication production of MBs loaded with DTX in the core and RB-biotin attached to the shell via the avidin-biotin linkage. The loading of DTX was optimised whilst maintaining the MB size, number, stability, and RB loading. The effectiveness of this formulation to treat PCa was determined in a 3D LNCaP spheroid model, as well as a PC3 murine model.

### **1.6.2 Chapter 4**

While the results obtained in Chapter 3 were promising, the method used for the preparation of drug loaded MB presented challenges when considering potential clinical translation of the technology. In particular, the requirement to use the biotin-avidin-biotin interaction to load RB would require several steps to be undertaken in a hospital pharmacy prior to administration. Therefore, chapter 4 describes the synthesis of a RB modified lipid and the development of a method for its incorporation with DTX into a pre-MB suspension that can generate drug-loaded MBs in a single mixing step.

### **1.6.3 Chapter 5**

In Chapter 5, the DTX/RB loaded MBs generated in Chapter 4 were tested for efficacy in a range of *in vitro/ in vivo* models of Pca. Specifically, 3D DU145 and LNCaP spheroid models were employed to determine the efficacy in both castration resistant and androgen sensitive cell lines of Pca. In addition, castrate resistant (PC3) and androgen sensitive (22Rv1) murine models were also employed. The efficacy was compared to MBs loaded with either RB or DTX alone and the free drugs (i.e., non-MB bound) DTX and enzalutamide.

#### **1.6.4 Chapter 6**

Chapter 6 differed slightly from Chapters 3-5 as it did not comprise a SDT component. The combination of 5-FU and IRIN in regimens has proven effective in colorectal cancer but is associated with significant off target toxicity. By utilising UTMD as a delivery mechanism this toxicity could be reduced. Chapter 6 therefore explored the development of MBs loaded with combined 5-FUR and IRIN and their efficacy in a 3D DU145 spheroid model of Pca.

## **Chapter 2:**

### **Methodology**

## 2.1 Materials and reagents

Chemicals were purchased from commercial sources at the highest possible grade. PC3, RM-1, DU145, LNCaP and 22Rv1 cells were obtained from the American Type Culture Collection (ATCC) (Manassas, VA, USA) and Matrigel from BS sciences (San Jose, CA, USA). SCID mice, nu/nu balb/c and C-57 mice were bred in house, nu/nu CD-1 mice were obtained from Axis BioServices (Coleraine, UK). Phospholipids were purchased from Avanti Polar Lipids (Alabaster, AL, USA). Rose Bengal, biotin, and cholesterol were purchased from Sigma Aldrich (St. Louis, MO, USA). Docetaxel was purchased from XABC (Shaanxi, China). Avidin from egg white was purchased from Thermo Fisher (Waltham, MA, USA). MBs were formed using a Microson ultrasonic cell disruptor, 100 W, 22.5 kHz, from Misonix Inc. (Farmingdale, NY, USA). Optical microscope images were obtained using an AmScope 40x-2000x Lab Trinocular Lab Microscope from AmScope (Irvine, CA, USA). Analysis of MB size and concentration was determined using a bespoke MATLAB algorithm (2010B, MathWorks, Natick, MA, USA). UV-Vis spectra were recorded with a Varian Cary spectrophotometer (Palo Alto, CA, USA), using quartz cells (path length = 1 cm). UV absorbance of MTT was analysed using a Fluostar Omega plate reader (BMG Labtech, Ortenberg, Germany). NMR spectra were obtained on Varian 500 MHz instrument at  $25.0 \pm 1$  °C (Palo Alto, CA, USA) and processed using TopSpin software (Bruker, Billerica, MA, USA). ESI-MS were obtained using a Finnegan LCQ-MS instrument (San Jose, CA, USA). HPLC analysis was carried out on a Shimadzu LC-8 preparative pump system (Shimadzu Corp., Kyoto, Japan). Dynamic light scattering (DLS) analysis was carried out on a Malvern Zetasizer 3000HSA (Malvern, Worcestershire, UK). Fluorescent IVIS images were obtained using a IVIS Spectrum *In Vivo* Imaging System from PerkinElmer (Waltham, MA, USA). Error in experimental data was displayed as standard error of the mean (SEM), while statistical analysis was carried out using either a 2-tailed students t-test or one-way ANOVA, on Prism GraphPad software v5.01 (GraphPad, San Diego, CA, USA). Power calculations were carried out to provide the sample size to inform the grant in which the work in this thesis was funded from. The sample size was determined based on a 25% change between each group at the experimental end point, with a SD of 10% at 90% power with a significance level of 0.05. These metrics yielded a sample size per group of 4.

## 2.2 Synthesis of rose bengal – biotin

### 2.2.1 Synthesis of 2-Aminoethyl 2,3,4,5-tetrachloro-6-(6- hydroxy-2,4,5,7-tetraiodo-3-oxo-3H-xanthen-9-yl)benzoate (rose bengal - amine)

To a stirred solution of rose bengal disodium (1.0 g, 1.0 mmol) in anhydrous DMF (10 mL) was added 2-bromoethylamine (0.32 g, 1.5 mmol). The resultant mixture was stirred at 80°C for 7 hours. The DMF was then removed under reduced pressure and the residue stirred for 18 hours in diethyl ether (200 mL). The solution was filtered, and the resulting solid stirred in water (200 mL) for 18 hours. The suspension was filtered, the solid residue was recrystallised from methanol, the product obtained was a dark red solid. <sup>1</sup>H-NMR (500 MHz, DMSO-d<sub>6</sub>): 2.42 (t, CH<sub>2</sub>, 2H), 3.80 (t, OCH<sub>2</sub>, 2H), 7.26 (s, ArH, 2H), 7.60 (s, NH<sub>2</sub>, 2H). <sup>13</sup>C-NMR (500 MHz, DMSO-d<sub>6</sub>): 19.0, 37.5, 49.3, 56.5, 62.7, 76.6, 97.9, 129.6, 130.6, 132.4, 133.4, 10.6, 110.9, 134.7, 135.7, 136.4, 137.0, 139.6, 157.5, 163.2, 172.3. ESI-MS: calculated for C<sub>22</sub>H<sub>9</sub>C<sub>14</sub>I<sub>4</sub>NO<sub>2</sub> = 1016.53, found 1016.13

### 2.2.2 Synthesis of 2-(5-(2-Oxohexahydro-1H-thieno[3,4- d]imidazol-4-yl)pentanamido)ethyl 2,3,4,5-tetrachloro-6-(6-hydroxy-2,4,5,7- tetraiodo-3-oxo-3H-xanthen-9-yl)benzoate (rose bengal - biotin)

To a solution of rose bengal - amine (74 mg, 74 μmol) in DMF (2 mL), was added biotin-N-hydroxysuccinimide ester (25 mg, 74 μmol) dissolved in DMF (2mL). Triethylamine (TEA, 10 μl, 0.71 μmol) was subsequently added to the mixture and then stirred at room temperature for 12 hours. The resulting solution was added to a solution of hexane: chloroform (200 ml, 4:1) and stirred for 24 hours at room temperature. The solution filtered and the filtrate retained which was washed three times with diethyl ether and dried in a vacuum oven to yield biotin rose bengal as a red powder (14 mg, 10% yield). <sup>1</sup>H-NMR(500 MHz, DMSO-d<sub>6</sub>): 1.40 (m, CH<sub>2</sub>, 2H), 1.65 (m, CH<sub>2</sub> x2, 4H), 2.05(m, CH<sub>2</sub>, 2H), 2.85 (t, CH<sub>2</sub>, 2H), 2.90 (q, CH<sub>2</sub>, 2H), 3.15 (m, CH,1H), 4.00 (t, OCH<sub>2</sub>, 2H), 4.15 (t, CH, 1H), 4.30 (m, CH, 1H), 6.35 (s, NH, 1H), 6.40 (s, NH, 1H), 7.45 (s, ArH, 2H). <sup>13</sup>C-NMR (125 MHz, DMSO-d<sub>6</sub>): 8.98, 9.03, 25.52, 28.57, 29.45, 31.72, 35.52, 37.34, 46.07, 53.13, 55.86, 59.66, 61.48, 64.65, 76.50, 97.69, 110.56, 124.271, 129.37, 130.48, 132.34, 134.79, 135.50, 136.41, 139.79, 157.42, 163.13, 163.57, 172.23, 172.68, 228.31, 230.86. ESI-MS (-ve mode): calculated for C<sub>32</sub>H<sub>23</sub>Cl<sub>4</sub>I<sub>4</sub>N<sub>3</sub>O<sub>7</sub>S = 1242.15 found = 1241.13

## 2.3 Synthesis of rose bengal – DSPE

### 2.3.1 Synthesis of 8-((2, 3, 4, 5-tetrachloro-6-(6-hydroxy-2, 4, 5, 7-tetraiodo-3-oxo-3H-xanthen-9-yl)henzoyl)oxy)octanoic acid (rose bengal – carboxylic acid).

To a stirred solution of Rose Bengal disodium salt (10.00 g, 9.80 mmol) in anhydrous DMF (100 mL) was added 8-bromooctanoic acid (2.20 g, 9.80 mmol) and the solution was stirred at 80°C for 8 hours or until no starting material was visible by TLC (CHCl<sub>3</sub>:CH<sub>3</sub>OH 8:2 v/v). Following completion of the reaction, the solvent was removed under reduced pressure and the residue was stirred in diethyl ether (200 mL) for 24 hours after which time the suspension was filtered and the solids were stirred in distilled water (200 mL) for 24 hours. This suspension was then filtered and dried to afford the carboxylic acid derivative 8 as a deep purple powder (8.70 g, 80%). <sup>1</sup>H-NMR (DMSO-d<sub>6</sub>) : 7.49 (s, 2H, Aromatic-CH X2), 3.89 (brs, 2H, O-CH<sub>2</sub>-), 2.09 (brs, 2H, -CH<sub>2</sub>-COOH), 1.39 (brs, 2H, -CH<sub>2</sub>-), 1.21-1.12(m, 6H, -CH<sub>2</sub>- X 3), 0.89 (brs, 2H, -CH<sub>2</sub>-). ESI-MS: 1114.47 (-ve mode).

### 2.3.2 Synthesis of 3-((hydroxy(2-(8-((2,3,4,5-tetrachloro-6-(6-hydroxy-2, 4, 5, 7-tetraiodo-3-oxo-3H-xanthen-9-yl)henzoyl)oxy)octanamido)ethoxy)phosphoryl)oxy)propane-1,2-diyl distearate (rose bengal – DSPE)

To a stirred solution of DSPE (0.50 g, 0.60 mmol), 8 (0.90 g, 0.80 mmol) and HBTU (0.30 g, 0.8 mmol) in CHCl<sub>3</sub>:CH<sub>3</sub>OH:H<sub>2</sub>O (65:35:8 v/v) was added DIPEA (0.43 g, 3.3 mmol) and the solution was stirred at room temperature for 24 hours or until no starting material was visible by TLC (CHCl<sub>3</sub>:CH<sub>3</sub>OH 8:2 v/v). After completion of the reaction the solvent was removed under reduced pressure and the resultant crude product was purified using column chromatography (CHCl<sub>3</sub>:CH<sub>3</sub>OH 8:2 v/v) to afford 9 as a deep purple powder (0.63 g, 43%). <sup>1</sup>H-NMR (CDCl<sub>3</sub>:MeOH, 2:1): 7.40 (s, Aromatic-CH X 2, 2H), 5.20 (m, -CH, 1H), 4.38 (m, OCH<sub>2</sub>, 2H), 4.25 (m, CH<sub>2</sub>, 2H), 3.85 (m, CH<sub>2</sub>, 2H), 3.42 (m, CH<sub>2</sub>, 2H), 3.31 (m, CH<sub>2</sub>, 2H), 2.28 (m, CH<sub>2</sub>, 2H), 2.19 (m, CH<sub>2</sub>, 2H), 1.58 (m, CH<sub>2</sub>, 2H), 1.51 (m, CH<sub>2</sub>, 2H), 1.25 (m, CH<sub>2</sub> x 28, 56H), 1.25 (m, CH<sub>2</sub>, 2H), 1.10 (m, CH<sub>2</sub>, 2H), 0.84 (m, CH<sub>2</sub>, 2H), 0.68 (m, CH<sub>2</sub>, 2H). <sup>13</sup>C-NMR (CDCl<sub>3</sub>:MeOH, 2:1): 175.8(CO), 173.9 (CO), 173.5 (CO), 173.2 (C), 163.3(CO), 157.8(CH), 150.8 (C), 141.5 (C), 136.8(C), 135.6 (C), 132.1 (C), 130.3 (C), 129.5 (C), 112.8(C), 101.6 (C), 96.2 (C), 80.1 (C), 79.3(C), 77.0 (CH<sub>2</sub>), 75.9 (CH<sub>2</sub>), 72.0 (CH<sub>2</sub>), 49.4(CH<sub>2</sub>), 49.0 (CH<sub>2</sub>), 40.0(CH<sub>2</sub>), 36.0(CH<sub>2</sub>), 34.1(CH<sub>2</sub>), 33.9(CH<sub>2</sub>), 31.7(CH<sub>2</sub>), 31.3(CH<sub>2</sub>).



29.5(CH<sub>2</sub>), 29.2(CH<sub>2</sub>), 29.0(CH<sub>2</sub>), 28.6(CH<sub>2</sub>), 28.0(CH<sub>2</sub>), 25.0(CH<sub>2</sub>), 24.7(CH<sub>2</sub>), 22.5(CH<sub>2</sub>), 13.7(CH<sub>3</sub>). MALDI-TOF-MS: 1844.31 (-ve mode).

## 2.4 Synthesis of Irinotecan – DSPE

### 2.4.1 Synthesis of (19S)-19-[(2-{{(tert-butoxy)carbonyl}amino}acetyl)oxy]-10,19-diethyl-14,18-dioxo-17-oxa-3,13-diazapentacyclo[11.8.0.0<sup>2,11</sup>.0<sup>4,9</sup>.0<sup>15,20</sup>]henicosa-1(21),2,4,6,8,10,15(20)-heptaen-7-yl [1,4'-bipiperidine]-1'-carboxylate hydrochloride salt (IR-GLY-BOC)

Irinotecan hydrochloride trihydrate (800 mg, 1.18 mmol equivalent to 736 mg of anhydrous irinotecan hydrochloride) was dissolved in DMF (20 mL) and evaporated to dryness at 60°C under reduced pressure. The resulting residue was dissolved in anhydrous DCM (20 mL) and *N*-(tert-Butoxycarbonyl)glycine (270 mg, 1.54 mmol), 4-Dimethylaminopyridine (16 mg, 0.13 mmol) and *N,N'*-Dicyclohexylcarbodiimide (397 mg, 1.93 mmol) were added and the solution was stirred overnight at 20°C under an atmosphere of N<sub>2</sub>. The resulting suspension was filtered, and the filtrate was reduced *in vacuo* followed by the addition of isopropanol (100 mL). This solution was then reduced in vacuo to approximately 15 mL total volume. Heptane (150 mL) was then added, and the suspension was stirred for 15 mins and then filtered and washed twice with heptane (15 mL) to yield a pale-yellow solid which was used in the next step without further purification (950 mg, 95% yield). <sup>1</sup>H-NMR(500 MHz, DMSO-d<sub>6</sub>): 0.90 (m, CH<sub>3</sub>, 3H), 1.28 (m, CH<sub>3</sub>, 3H), 1.40 (m, CH<sub>2</sub>, 2H), 1.49 (m, CH<sub>3</sub>, 3H), 1.82 (m, CH<sub>2</sub> X 4, 8H), 2.19 (m, CH<sub>2</sub>, 4H), 3.18 (m, CH<sub>2</sub> X5, 10H), 3.85 (d, CH<sub>2</sub>, 2H), 5.39 (m, CH<sub>2</sub>N, 2H), 5.58 (m, CH<sub>2</sub>O, 2H), 7.24 (s, ArH, 1H), 7.42 (s, ArH, 1H), 7.64 (d, ArH, 1H), 7.98 (d, ArH, 1H), 8.42 (m, NH, 1H). ESI-MS: 744.3 (+ve mode)

### 2.4.2 Synthesis of (19S)-19-[(2-aminoacetyl)oxy]-10,19-diethyl-14,18-dioxo-17-oxa-3,13-diazapentacyclo[11.8.0.0<sup>2,11</sup>.0<sup>4,9</sup>.0<sup>15,20</sup>]henicosa-1(21),2,4,6,8,10,15(20)-heptaen-7-yl [1,4'-bipiperidine]-1'-carboxylate mixed hydrochloride/trifluoroacetate salt (IR-GLY)

To a stirred ice-cold solution of IR-GLY-BOC (950 mg, 1.22 mmol) in DCM (10 mL) was added trifluoroacetic acid (2 mL). The resulting bright yellow solution was stirred at 20°C for 3 hours before the solvent was removed in vacuo and replaced with acetonitrile (50 mL). The resulting solution was then reduced in vacuo to approx. 15 mL total volume and diethyl ether

(150 mL) was added, and the suspension was stirred for 15 mins before filtering and washing with diethyl ether (15 mL) to yield a mixed TFA/HCl salt which was used in the next step without further purification (700 mg, ~96% yield). <sup>1</sup>H-NMR(500 MHz, DMSO-d<sub>6</sub>): 0.93 (m, CH<sub>3</sub>, 3H), 1.25 (m, CH<sub>3</sub>, 3H), 1.42 (m, CH<sub>2</sub>, 2H), 1.81 (m, CH<sub>2</sub> X 4, 8H), 2.19 (m, CH<sub>2</sub> X2, 4H), 2.90 – 3.41 (m, CH<sub>2</sub> X5, 10H), 3.90 (d, CH<sub>2</sub>, 2H), 5.39 (m, CH<sub>2</sub>N, 2H), 5.58 (m, CH<sub>2</sub>O, 2H), 7.22 (s, ArH, 1H), 7.48 (s, ArH, 1H), 8.01 (d, ArH, 1H), 8.17 (d, ArH, 1H), 8.41 (m, NH<sub>3</sub><sup>+</sup>, 3H), 10.03 (brs, NH, 1H). ESI-MS: 643.73 (+ve mode)

#### **2.4.3 Synthesis of 3-[(2-{[(19S)-7-{[1,4'-bipiperidine]-1'-carbonyloxy}-10,19-diethyl-14,18-dioxo-17-oxa-3,13-diazapentacyclo[11.8.0.0<sup>2,11</sup>.0<sup>4,9</sup>.0<sup>15,20</sup>]henicosa-1(21),2,4,6,8,10,15(20)-heptaen-19-yl]oxy}-2-oxoethyl)carbamoyl]propanoic acid (IR-GLY-ACID)**

To a stirred solution of IR-GLY (700 mg, 0.88 mmol) in anhydrous DCM (20 mL) was added succinic anhydride (176 mg, 1.76 mmol) and triethylamine (568 mg, 5.6 mmol). The resulting solution was stirred at 25°C for 24 hours under an atmosphere of N<sub>2</sub> followed by removal of the solvent in vacuo. To the resulting residue was added isopropanol (100 mL) and the solvent was reduced by 50% of the total volume. The resulting suspension was then filtered and washed with ice cold isopropanol (2 x 20 mL) to yield a pale-yellow powder which was used in the next step without further purification (340 mg, 51% yield). <sup>1</sup>H-NMR(500 MHz, DMSO-d<sub>6</sub>): 0.94 (m, CH<sub>3</sub>, 3H), 1.23 (m, CH<sub>3</sub>, 3H), 1.42 (m, CH<sub>2</sub>, 2H), 1.78 (m, CH<sub>2</sub> X 4, 8H), 1.81-2.10 (m, CH<sub>2</sub> X2, 4H), 2.39 (d, CH<sub>2</sub>, 4H), 2.60 – 3.23 (m, CH<sub>2</sub> X5, 10H), 4.04 (d, CH<sub>2</sub>, 2H), 5.38 (m, CH<sub>2</sub>N, 2H), 5.50 (m, CH<sub>2</sub>O, 2H), 7.11 (s, ArH, 1H), 7.62 (s, ArH, 1H), 7.99 (d, ArH, 1H), 8.19 (d, ArH, 1H), 8.43 (m, NH, 1H). ESI-MS: 743.32 (+ve mode)

#### **2.4.4 Synthesis of (2-{3-[(2-{[(19S)-7-{[1,4'-bipiperidine]-1'-carbonyloxy}-10,19-diethyl-14,18-dioxo-17-oxa-3,13-diazapentacyclo[11.8.0.0<sup>2,11</sup>.0<sup>4,9</sup>.0<sup>15,20</sup>]henicosa-1(21),2,4,6,8,10,15(20)-heptaen-19-yl]oxy}-2-oxoethyl)carbamoyl]propanamido}ethoxy)](2R)-2,3-bis(octadecanoyloxy)propoxy]phosphinic acid (IRIN-DSPE)**

To a stirred solution of IR-GLY-ACID (340 mg, 0.46 mmol), HATU (197 mg, 0.52 mmol), and diisopropylamine (196 mg, 1.52 mmol) in anhydrous DCM (30 mL) was added DSPE (283

mg, 0.38 mmol) and the suspension was stirred at 45°C for 30 mins under an atmosphere of N<sub>2</sub>. Following complete dissolution of the starting materials, the temperature was lowered to 25°C and stirring was continued for a further 3 hours. The solvent was then removed in vacuo and to the residue was added acetonitrile (100 mL). The resulting suspension was stirred for 30 mins and then filtered and washed with ice cold acetonitrile (2 x 20 mL). The crude product was purified by flash column chromatography (DCM:MeOH 90:10 to 80:20 v/v) (350 mg, 54% yield). <sup>1</sup>H-NMR (CDCl<sub>3</sub>:MeOH, 2:1): 0.68 (m, CH<sub>3</sub> X 2, 6H), 0.98 (m, CH<sub>3</sub>, 3H), 1.50 (m, CH<sub>2</sub> X28, 56H), 1.54 (m, CH<sub>3</sub>, CH<sub>2</sub>, 5H), 2.02 (m, CH<sub>2</sub> X5, 10H), 2.18 (m, CH<sub>2</sub>, 2H), 2.29 (d, CH<sub>2</sub>, 2H), 3.09 (m, CH, CH<sub>2</sub>, 5H), 3.30 (d, CH<sub>2</sub> X3, 6H), 3.71 (m, CH<sub>2</sub>, 2H), 3.78 (m, CH<sub>2</sub>, 2H), 3.95 (m, CH<sub>2</sub>, 2H), 4.15-4.26 (d, CH<sub>2</sub>, 2H), 4.19 (m, CH<sub>2</sub>, 2H), 5.30 (m, CHO, 1H), 5.12 (d, CH<sub>2</sub> X2, 4H), 7.58 (s, ArH, 1H), 7.72 (s, ArH, 1H), 7.80 (d, ArH, 1H), 8.13 (d, ArH, 1H). <sup>13</sup>C-NMR (CDCl<sub>3</sub>:MeOH, 2:1): 11.0, 19.0, 26.7, 28.9, 33.8, 36.0, 38.1, 44.0, 45.1, 48.0, 54.0, 66.5, 67.8, 71.2, 74.2, 81.8, 100.9, 123.9, 131.8, 135.0, 150.5, 151.9, 154.3, 155.1, 157.9, 161.9, 171.8, 173.7, 177.9. ESI-MS: 1471.7 (-ve mode)

## 2.5 Synthesis of 5-Fluorouradine – DSPE

### 2.5.1 Synthesis of 5-fluoro-1-[6-(hydroxymethyl)-2,2-dimethyl-tetrahydro-2H-furo[3,4-d][1,3]dioxol-4-yl]-1,2,3,4-tetrahydropyrimidine-2,4-dione (5FUR-Ketal)

To a stirred, ice-cooled suspension of 5-fluorouridine (4.50 g, 17.16 mmol) in acetone (315 mL) was added concentrated sulfuric acid (4.1 g, 41.98 mmol) dropwise over 2 min. The reaction mixture was then warmed to 25°C and stirring was continued for a further 6 hours. The solvent was then removed in vacuo and the crude residue purified by recrystallisation from ethanol to yield a crystalline white powder (3.86 g, 74% yield). <sup>1</sup>H-NMR (DMSO-d<sub>6</sub>) 1.29 (s, CH<sub>3</sub>, 3H), 1.45 (s, CH<sub>3</sub>, 3H), 4.21 (m, CHO X3, 3H), 4.78 – 5.04 (d, CH<sub>2</sub>, 2H), 5.78 (m, CHO, 1H), 8.03 (s, ArH, 1H).

### 2.5.2 Synthesis of 4-{[6-(5-fluoro-2,4-dioxo-1,2,3,4-tetrahydropyrimidin-1-yl)-2,2-dimethyl-tetrahydro-2H-furo[3,4-d][1,3]dioxol-4-yl]methoxy}-4-oxobutanoic acid (5FUR-Ketal-ACID)

To a stirred solution of 5FUR-Ketal (3.86 g, 12.77 mmol) in anhydrous DCM (80 mL) was added succinic anhydride (1.53 g, 15.29 mmol) and 4-Dimethylaminopyridine (1.87 g, 15.31

mmol). The resulting solution was stirred at 25°C under nitrogen for 24 hours. The solvent was then removed in vacuo and the residue was taken up in sodium bicarbonate solution (10% w/v, 40 mL) and washed with DCM (2 x 20 mL). The pH of the aqueous phase was then adjusted to pH = 5 using HCl (2N) and the product extracted with ethyl acetate (4 x 100 mL). The combined organic extracts were dried with anhydrous sodium sulfate, filtered, and reduced in vacuo to yield a white crystalline solid (3.60 g, 70% yield). <sup>1</sup>H-NMR (DMSO-d<sub>6</sub>) 1.29 (s, CH<sub>3</sub>, 3H), 1.45 (s, CH<sub>3</sub>, 3H), 4.21 (m, CHO X3, CH<sub>3</sub>, 5H), 4.78 – 5.04 (d, CHO, 1H), 5.78 (m, ArH, 1H), 8.03 (s, COOH, 1H). <sup>13</sup>C-NMR (DMSO-d<sub>6</sub>): 24.9, 27.4, 29.1, 31.4, 40.2, 64.8, 80.3, 84.0, 84.3, 92.8, 114.0, 127.8, 139.9, 141.8, 149.9, 158.9, 172.8, 174.1.

### **2.5.3 Synthesis of [(2R)-2,3-bis(octadecanoyloxy)propoxy][2-(4-{[6-(5-fluoro-2,4-dioxo-1,2,3,4-tetrahydropyrimidin-1-yl)-2,2-dimethyl-tetrahydro-2H-furo[3,4-d][1,3]dioxol-4-yl]methoxy}-4-oxobutanamido)ethoxy]phosphinic acid (5FUR-Ketal-DSPE)**

DSPE (500 mg, 0.69 mmol) was added to a stirred solution of 5FUR-Ketal-ACID (300 mg, 0.75 mmol), HATU (254 mg, 1.34 mmol), and diisopropylamine (346 mg, 2.68 mmol) in anhydrous DCM (30 mL) and the suspension was stirred at 45°C for 30 mins under an atmosphere of N<sub>2</sub>. Following complete dissolution of the starting materials, the temperature was lowered to 25°C and stirring was continued for a further 3 hours. The reaction mixture was then washed with HCl (1N, 2x 10 mL), dried with sodium sulfate, filtered, and reduced in vacuo. To the residue was added acetonitrile (100 mL) and the resulting suspension was stirred for 30 mins, filtered and washed with ice cold acetonitrile (2 x 20 mL). The crude product was purified by flash column chromatography (DCM:MeOH 90:10 to 80:20 v/v) (469 mg, 60% yield). <sup>1</sup>H-NMR (CDCl<sub>3</sub>:MeOH, 2:1): 0.88 (m, CH<sub>3</sub> X2, 6H), 1.22 (m, CH<sub>2</sub> X28, 56H), 1.51 (m, CH<sub>2</sub>, 2H), 2.61 (m, CH<sub>2</sub>, 2H), 2.59 (m, CH<sub>2</sub>, 2H), 2.36 (m, CH<sub>2</sub>, 2H), 3.43 (d, CH<sub>2</sub>, 2H), 3.61 (m, CH<sub>2</sub>O, CHO X3, 5H), 3.91 (d, CH<sub>2</sub>, 2H), 3.99-4.40 (m, CH<sub>2</sub>, 2H), 4.40 (m, CH<sub>2</sub>, 2H), 5.01 (m, CH, 1H), 5.75 (s, OCHN, 1H), 7.72 (s, ArH, 1H).

#### **2.5.4 Synthesis of [(2R)-2,3-bis(octadecanoyloxy)propoxy][2-(4-[(2S,5S)-5-(5-fluoro-2,4-dioxo-1,2,3,4-tetrahydropyrimidin-1-yl)-3,4-dihydroxy-2,5-dimethyloxolan-2-yl]methoxy}-4-oxobutanamido)ethoxy]phosphinic acid (5FUR-DSPE)**

To a stirred solution of 5FUR-Ketal-DSPE (600 mg, 0.53 mmol) in DCM (6.5 mL) was added TFA (90% v/v (water), 300  $\mu$ L). The solution was stirred for 3 hours at 25°C followed by removal of the solvent in vacuo. To the resulting residue was added acetonitrile (20 mL) and the suspension was stirred for 30 min, filtered, and washed with acetonitrile (2 x 20 mL) to yield an off-white solid (534 mg, 90% yield). <sup>1</sup>H-NMR (CDCl<sub>3</sub>:MeOH, 2:1): 0.78 (m, CH<sub>3</sub> X2, 6H), 1.23 (m, CH<sub>2</sub> X28, 56H), 1.52 (m, CH<sub>2</sub>, 2H), 2.25 (m, CH<sub>2</sub>, 2H), 2.51 (m, CH<sub>2</sub> X2, 4H), 3.35 (d, CH<sub>2</sub>, 2H), 3.91 (d, CH<sub>2</sub>, 2H), 4.12 (m, CH<sub>2</sub>O, CHO X3, 5H), 4.25-4.40 (m, CH<sub>2</sub>, 2H), 4.30 (m, CH<sub>2</sub>, 2H), 5.30 (m, CH, 1H), 5.65 (s, OCHN, 1H), 7.782 (s, ArH, 1H). <sup>13</sup>C-NMR (CDCl<sub>3</sub>:MeOH): 18.0, 23.0, 25.0, 29.5, 32.0, 34.0, 40.0, 63.0, 64.0, 66.0, 66.5, 69.0, 69.5, 75.0, 82.0, 91.0, 125.0, 140.0, 143.0, 150.0, 158.0, 173.0, 174.0, 174.5. ESI-MS: 1090.3 (-ve mode).

#### **2.6 Preparation of DTX and Rose Bengal loaded microbubbles (DTX-MB-RB) using the avidin-biotin interaction to load Rose Bengal.**

DTX-MB-RB were prepared by dissolving 1,2-dibehenoyl-sn-glycero-3-phosphocholine (DBPC), 1,2-distearoyl-sn-glycero-3-phosphoethanolamine-N-[amino(polyethylene glycol)-2000] (DSPE-PEG(2000)) and DSPE-PEG(2000)-biotin in chloroform, molar ratio of 82:9:9, along with 5mg of DTX. The chloroform was evaporated at 40°C in a glass vial to leave a dried, lipid/drug film. The film was reconstituted in 2mL of Ungers' solution [PBS (pH 7.4  $\pm$  0.1), propylene glycol and glycerol (8:1:1 v/v)] the solution was heated at 80°C and stirred for 45 min. The resultant suspension was sonicated using a Microson ultrasonic cell disrupter at amplitude 22% for 60 seconds and again at amplitude of 90% under an atmosphere of perfluorobutane (PFB) gas for 30 seconds. The subsequent DTX-MBs were centrifuged at 700RPM for 5 min, the infranatant (below the MB cake) was removed and the bubbles were washed in 2mL of PBS (pH 7.4  $\pm$  0.1). The washing step was repeated a further two times and the PBS was removed by centrifugation. The MBs were dispersed in PBS (pH 7.4  $\pm$  0.1) (1 mL) and an avidin (10mg/mL) solution (1 mL) was added and the contents mixed on an orbital shaker for 5 min in an ice bath. The MBs were centrifuged at 700RPM for 5 mins, the infranatant removed and washed with PBS (pH 7.4  $\pm$  0.1) (2 mL) which was removed following centrifugation. The MBs were functionalised with RB-biotin by adding 1mL of PBS (pH 7.4  $\pm$

0.1) and 1mL of RB-biotin (5mg/mL) and mixed on an orbital shaker for 5 mins in an ice bath. The DTX-MB-RB were subsequently centrifuged at 700RPM for 5 mins and the infranatant removed. The MBs were washed twice to remove any excess RB-biotin and the final MB cake was reconstituted in 2mL of PBS (pH  $7.4 \pm 0.1$ ). When the MBs required an oxygen core for treatments, the MBs were sparged for 2 min with oxygen, to replace the PFB gas in the core of the MBs with oxygen gas.

### **2.6.1 Characterisation of drug loading of DTX-MB-RB**

To determine DTX loading, an aliquot of DTX-MB-RB was diluted in a solution of acetonitrile / water (6:4 v/v) and sonicated to rupture the MBs. The resulting sample was analysed by reverse phase HPLC. 50 $\mu$ L was injected onto a Phenomenex C<sub>18</sub> column (250 x 4.6mm, 5 $\mu$ m) and eluted using a mobile phase of acetonitrile and water (6:4 v/v), a flow rate of 1.5mL/min and UV/Vis detection (231nm). The loading of DTX was determined using the peak area on the chromatogram and the equation of the line for the DTX calibration curve.

The drug loading of RB-biotin was determined by taking an aliquot of the DTX-MB-RB and diluting with PBS (pH  $7.4 \pm 0.1$ ). The resulting sample was sonicated for 60 seconds to rupture the DTX-MB-RB and the absorbance recorded 560nm. The final RB loading was determined using the intensity of absorbance at 560 nm with reference to an RB calibration curve.

### **2.7 Preparation of DTX-MB-RB from a pre-MB colloidal suspension using RB-DSPE to load the Rose Bengal.**

A pre-MB colloidal suspension was prepared by dissolving DBPC, RB-DSPE, cholesterol, DSPE-PEG(2000) and DTX in a molar ratio of (30:37.5:10:10:12.5) to a total mass of 10mg of components, in 2mL of a chloroform/ethanol mixture (2:1) in a 5mL round bottom flask. The chloroform and ethanol were evaporated at 40°C under vacuum to form a dry, thin lipid/drug film. The film was reconstituted in 2mL of Ungers' solution and mixed at 90°C using a rotary evaporator. The drug/lipid solution was sonicated at an amplitude of 25% using a Microson ultrasonic cell disrupter to produce the pre-MB colloidal suspension. 1mL aliquots of the liposomal suspension were transferred to 2mL crimp vials. The vials were crimped after displacing the air atmosphere with PFB gas. The vials were stored at 2-8°C until required when

they were then activated by shaking for 45 seconds on a Vialmix® shaker to produce the DTX-MB-RB.

## **2.8 Preparation of 5FUR-MB-IRIN from a pre-MB colloidal suspension**

A pre-MB colloidal suspension was prepared by dissolving DBPC, 5FUR-DSPE, IRIN-DSPE, cholesterol and DSPE-PEG(2000) in a molar ratio of (30:25:25:10:10) to a total mass of 10mg of components, in 2mL of a chloroform/ethanol mixture (2:1) in a 5mL round bottom flask. The chloroform and ethanol were evaporated at 40°C under vacuum to form a dry, thin lipid/drug film. The film was reconstituted in 2mL of Ungers' solution and mixed at 90°C using a rotary evaporator. The drug/lipid solution was sonicated at an amplitude of 25% using a Microson ultrasonic cell disrupter to produce the pre-MB colloidal suspension. 1mL aliquots of the liposomal suspension were transferred to 2mL crimp vials. The vials were crimped after displacing the air atmosphere with PFB gas. The vials were stored at 2-8°C until required when they were then activated by shaking for 45 seconds on a Vialmix® shaker to produce the 5FUR-MB-IRIN.

## **2.9 Characterization of MB number and size**

The MB number and size were determined by taking an aliquot of the MBs and diluting them 1 : 25 in Ungers' solution. A sample of this suspension was loaded onto a haemocytometer and images (n=20) were taken using an optical microscope (x 40 objective). Size distribution and MB concentration (MB number/mL) were determined by analysis using a purpose-made algorithm on MATLAB software (MathWorks, Natick, MA, USA) (205).

## **2.10 Determination of MB stability at 37.5°C**

Where relevant, MBs were placed in an incubator at 37.5°C. Samples were taken at the timepoints 0, 30, 60, 90 mins. The samples were characterised in terms of MB number and size following method 2.9.

### **2.11 Determination of pre-MB colloidal suspension stability at 2-8°C**

The pre-MB colloidal liposomal suspension was produced following method 2.6. 15 vials in total were prepared and stored for a period of 3 months. At timepoints 0, 1, 2 and 3 months, 3 vials were activated using the Vialmix® shaker and characterised in terms of MB number and size following method 2.9. The remaining 3 vials were used to characterise the pre-MB suspension using DLS at the same timepoints.

### **2.12 Culture of LNCaP-Luc or LNCaP spheroids**

LNCaP-Luc/LNCaP cells were cultured using Roswell Park Memorial Institute (RPMI) culture media: 100 U/mL penicillin, 100 mg/mL streptomycin, and 20% foetal bovine serum (FBS) in a humidified 5% CO<sub>2</sub> atmosphere at 37°C. Spheroids were cultured in ultralow attachment (ULA) 96-well plates from Corning. The polystyrene coating ensures cells do not attach to the plate and the curved nature of each well allows gravity to pull the cells together where intracellular matrices is formed to allow cells to form in a 3D spherical fashion, rather than a 2D monolayer. Cells were seeded at 1,000 cells/well in 200µL of RPMI media. Media was replenished every 4 days by discarding 100µL from the well and replacing it with 100µL of fresh RPMI.

### **2.13 Culture of DU145 spheroids**

DU145 cells were cultured as described for LNCaP-Luc/LNCaP spheroids in 2.12 using the same plates. Cells were seeded at 5,000 cells/well in 200µL of RPMI media. Media was replenished every 3 days by discarded 100µL from the well and replacing it with 100µL of fresh RPMI.

### **2.14 *In vitro* efficacy determination of MB based treatments in LNCaP-Luc/LNCaP spheroids.**

LNCaP-Luc or LNCaP spheroids were used in Chapter 3 and Chapter 5 respectively. In chapter 3, spheroids were treated with: US only, blank MB, blank MB with US, MB-RB, MB-RB + US, DTX-MB, DTX-MB + US, DTX-MB-RB and DTX-MB-RB + US. [DTX] = 6.2µM and [RB] = 30µM, [MB] = 2.88x10<sup>8</sup> MB/mL. Untreated spheroids served as a control.



In chapter 5 the groups were: untreated, MB with US, DTX-MB, DTX-MB + US, MB-RB, MB-RB + US, DTX-MB-RB and DTX-MB-RB + US. Two different treatment doses were used. In experiment 1: [DTX] = 8.33 $\mu$ M and [RB] = 25 $\mu$ M while in experiment 2 [DTX] = 16.67 $\mu$ M and [RB] = 50 $\mu$ M, in both cases [MB] = 3.56x10<sup>8</sup>/mL.

Where US was used, it was applied using a Sonidel SP100 sonoporator with US transmission gel and directly applying the probe to the bottom of each well with US for 1 second and for 30 seconds after 30 min (frequency – 1MHz, power density – 3.0 W/cm<sup>2</sup>, duty cycle – 30% and PRF – 100Hz). The MB treatments were diluted in RPMI to the appropriate concentration, 100 $\mu$ L of media was removed from the well and 100 $\mu$ L of MBs in RPMI was added. After 24 hours, 3 spheroids were collected in an Eppendorf (repeated 4 times for each condition). The spheroids were subsequently centrifuged, and the media removed. This was replaced with 200 $\mu$ L of MTT (5mg/mL) prepared in RPMI, the spheroids were destroyed mechanically by pipetting repeatedly and vigorously for 30 seconds each, they were then incubated for 3 hours, in a humidified 5% CO<sub>2</sub> atmosphere at 37°C. After incubation, media was removed and 100 $\mu$ L of DMSO was added, the contents of each Eppendorf were transferred to a 96-well plate. The absorption of each well was determined at 570nm using FLUOstar Omega microplate reader, and the data displayed as percentage cell viability against the untreated spheroids.

### **2.15 *In vitro* efficacy determination of MB based treatments in DU145 spheroids**

DU145 spheroids were used in Chapters 5 and 6. In chapter 5, the spheroids were treated with: untreated, blank MB + US, DTX-MB, DTX-MB + US, MB-RB, MB-RB + US, DTX-MB-RB and DTX-MB-RB + US. Two experiments were conducted: in experiment 1 [DTX] = 8.33 $\mu$ M and [RB] = 25 $\mu$ M while in experiment 2 [DTX] = 16.67 $\mu$ M and [RB] = 50 $\mu$ M. In both cases [MB] = 4.11x10<sup>8</sup>/mL.

In chapter 6, the spheroids were allocated into the groups: untreated, US only, blank MB, blank MB + US, 5FUR-MB-IRIN and 5FUR-MB-IRIN + US. 3 experiments were undertaken where [IRIN and 5-FUR] = 5, 10 and 20 $\mu$ M. [MB] = 7.02x10<sup>8</sup>/mL.

Where appropriate, US was applied using a Sonidel SP100 sonoporator with US transmission gel and directly applying the probe to the bottom of each well with US for 1 second immediately and for 30 seconds after 30 min (frequency – 1MHz, power density – 3.0 W/cm<sup>2</sup>, duty cycle – 30% and PRF – 100Hz). MB treatments were diluted in RPMI to the appropriate

concentration, 100µL of media was removed from the well and 100µL of MBs in RPMI was added. After 24 hours, 3 spheroids were collected in an Eppendorf (repeated 4 times for each condition). The spheroids were subsequently centrifuged, and the media removed. This was replaced with 200µL of MTT (5mg/mL) prepared in RPMI, the spheroids were destroyed mechanically by pipetting repeatedly and vigorously for 30 seconds each, they were then incubated for 3 hours. After incubation, media was removed and 100µL of DMSO was added, the contents of each Eppendorf were transferred to a 96-well plate. The absorption of each well was determined at 570nm using FLUOstar Omega microplate reader, and the data displayed as percentage cell viability against the untreated spheroids.

## **2.16 DTX-MB-RB treatment of mice bearing PC3 tumours.**

All animals employed in this study were treated in accordance with the licenced procedures under the UK Animals (Scientific Procedures) Act 1986. All murine in vivo studies were carried out under project license number 2835 and personal licence number 1979. For the experiment conducted in chapter 3, PC3 cells ( $5 \times 10^6$ ) in 100µL of Matrigel: PBS (50:50) were subcutaneously implanted into the rear dorsum of SCID mice (C.B-17/IcrHan®Hsd-Prkdcscid). For the experiment conducted in chapter 4 nu/nu SCID CD-1 mice were used. Palpable tumours were present after 2 weeks post implantation, and the tumour dimensions measured using Vernier callipers. Tumour volume was calculated according to the formula: length x height x width / 2.

Once the tumours reached a mean volume of 100mm<sup>3</sup> the animals were allocated to treatment groups (n=5). For the experiment outlined in chapter 3 the groups were: group 1 was untreated, group 2 received a 100µL intraperitoneal injection (IP) injection of DTX standard dose (10mg/kg), group 3 and 4 received a 100µL intravenous (IV) tail vein injection of DTX-MB-RB ([RB] = 1.34 mg/kg and [DTX] = 0.28 mg/kg) without US (group 3) or with US (group 4). Animals were treated on days 0, 4, 7, 10, 14, 18 and 21.

For the experiment outlined in chapter 5 the groups were: group 1 remained untreated, group 2 and 3 received a 100µL IV infusion of DTX-MB-RB ([RB] = 6.35 mg/kg and [DTX] = 0.94 mg/kg) without US (group 2) or with US (group 3), group 4 received a 100µL IV injection of DTX (matched dose [DTX] = 0.94 mg/kg) with US, group 5 received a 100µL IV injection of DTX (standard dose [DTX] = 10 mg/kg), group 6 received a 100µL IV injection of DTX-MB

with US ([DTX] = 0.94 mg/kg) and group 7 received a 100µL IV injection of MB-RB with US ([RB] = 6.35 mg/kg). These animals were treated on days 0, 4, 7, 11, 14, 19, 22, 26 and 29.

In both experiments, US was applied directly to the tumour using a Sonidel SP100 sonoprotector (3.5 W/cm<sup>2</sup>, 1 MHz, 30% duty cycle, and PRF = 100 Hz; PNP = 0.48MPa; M.I. = 0.48) using US gel to transmit US and provide contact.

### **2.17 DTX-MB-RB treatment of mice bearing 22Rv1 tumours.**

All animals employed in this study were treated in accordance with the licenced procedures under the UK Animals (Scientific Procedures) Act 1986. In the experiment conducted in chapter 5, 22Rv1 cells (5x10<sup>6</sup>) in 100µL of Matrigel: serum free media (50:50) were implanted subcutaneously into the rear dorsum of nu/nu SCID balb/c mice. Palpable tumours appeared after 2-3 weeks, once palpable were measured using Vernier callipers and the tumour volume calculated using the formula: length x height x width / 2.

Once the tumours reached a mean size of 80mm<sup>3</sup> the animals were allocated to treatment groups (n=5). Group 1 remained untreated, group 2 received a 100µL IV injection of DTX (matched dose) ([DTX] = 1.11 mg/kg), group 3 received a 100µL IP injection of enzalutamide (Enz) daily ([Enz] = 10 mg/kg), group 4, 5 and 6 received a 100µL IV injection of DTX-MB-RB ([RB] = 7.54 mg/kg and [DTX] = 1.11 mg/kg) without US (group 4), with US (group 5) or with US and a 100µL IP injection of Enz daily ([Enz] = 10 mg/kg). Mice were treated on days 0, 4, 6, 8, 10, 12, 14, 16, 18, 20, 22 and 24 unless culled due to tumour size earlier than the treatment day, Enz was administered daily.

US was administered directly to the tumour using a Sonidel SP100 sonoprotector (3.5 W/cm<sup>2</sup>, 1 MHz, 30% duty cycle, and PRF = 100 Hz; PNP = 0.48MPa; M.I. = 0.48) using US gel to transmit US and provide contact.

### **2.18 Safety study in healthy non tumour bearing mice**

Healthy non-tumour bearing CD-1 mice were separated into the groups (n=8): group 1 remained untreated, group 2 received a 100µL IV injection of DTX-MB-RB ([RB] = 7.60 mg/kg and [DTX] = 1.12 mg/kg) with US or a 100 µL IV injection of DTX (standard dose) ([DTX] = 10 mg/kg). The body weights of the mice were recorded every second day, blood

samples were taken before treatment, at day 10 and day 15 and analysed for urea and alanine aminotransferase (ALT). Blood smears were also taken and analysed for cell counts including red blood cells (RBC), haemoglobin (Hb), haematocrit level (HCT), mean corpuscular volume (MCV), mean corpuscular haemoglobin (MCH), mean corpuscular haemoglobin concentration (MCHC), platelets, white blood cell count (WBC), neutrophils, lymphocytes, monocytes, and eosinophils. Histological markers for glomerular cellularity, glomerular basement membrane, tubular vacuolation, interstitial inflammation, interstitial fibrosis, collecting system, portal inflammation, lobular inflammation and steatosis were also analysed. Blood smear analysis was carried out by the Veterinary Pathology Group (VPG) (Leeds, UK), the histological analysis of tissues was carried out by Paul Kelly and Declan O'Rourke at the Department of Pathology, Belfast Health and Social Care Trust (Belfast, UK).

### **2.19 Preparation of IR780-MB-RB from a pre-MB colloidal suspension.**

A pre-MB colloidal suspension was prepared by dissolving DBPC, RB-DSPE, cholesterol, DSPE-PEG(2000) and IR780 in a molar ratio of 30:37.5:10:10:12.5 to a total mass of 10mg of components, in 2mL of a chloroform/ethanol mixture (2:1) in a 5mL round bottom flask. The chloroform and ethanol were evaporated at 40°C under vacuum to form a dry, thin lipid/drug film. The film was reconstituted in 2mL of Ungers' solution and mixed at 90°C using a rotary evaporator. The drug/lipid solution was sonicated at an amplitude of 25% using a Microson ultrasonic cell disrupter to produce the pre-MB colloidal suspension. 1mL aliquots of the liposomal suspension were transferred to 2mL crimp vials. The vials were crimped after displacing the air atmosphere with PFB gas. The vials were stored at 2-8°C until required when they were then activated by shaking for 45 seconds on a Vialmix® shaker to produce the IR780-MB-RB.

### **2.20 Localisation of IR780 labelled MB-RB in mice bearing 22Rv1 tumours.**

22Rv1 tumours were implanted in 6 mice as describe in section 2.16. MB-RB, prepared with IR-780 in place of DTX (see 2.19). Once tumours reached  $\sim 500\text{mm}^3$  the animals were separated into 2 groups (n=3). Both groups 100 $\mu\text{L}$  injection of IR780 loaded MB-RB ([RB = 8.86 mg/mL and [IR780] = 0.89 mg/mL, [MB] =  $2.84 \times 10^9/\text{mL}$ ), with one group also receiving US during injection and for 3.5 min total (Sonidel SP100 sonoprotator (3.5 W/cm<sup>2</sup>, 1 MHz,

30% duty cycle, and PRF = 100 Hz; PNP = 0.48MPa; M.I. = 0.48) using US gel to transmit US and provide contact. The mice were imaged using an IVIS Spectrum *In Vivo* Imaging System before IV administration of the MBs and 3 hours later. Regions of Interest (ROI's) were identified on the tumour, and a secondary ROI was taken on the back to control for background radiance. Mice were imaged at time points 0 and 3 hours.

### **Chapter 3:**

## **Docetaxel and Rose Bengal Loaded Microbubbles for Ultrasound Activated Chemo-Sonodynamic Therapy of Prostate Cancer.**

### 3.1 Introduction

As described in section 1.5.2, UTMD has the potential to enhance drug uptake in tumours due to mechanisms such as cavitation, microstreaming, microjetting and sonoporation. This highlights the potential for using UTMD for the treatment of PCa where radical prostatectomy has not been attempted. The ability to increase drug uptake utilising UTMD within PCa was investigated by Lee et al. [204]. Mice bearing subcutaneous PC3 tumours received a tail vein IV injection of MBs loaded with doxorubicin (DOX). They received US for a) 5 min, b) 10 min and c) 15 min ( $2 \text{ w/cm}^2$ , 60% DC). Figure 3.1 shows that increasing the treatment time subsequently increased the fluorescent intensity of DOX within the sampled tumour tissue.

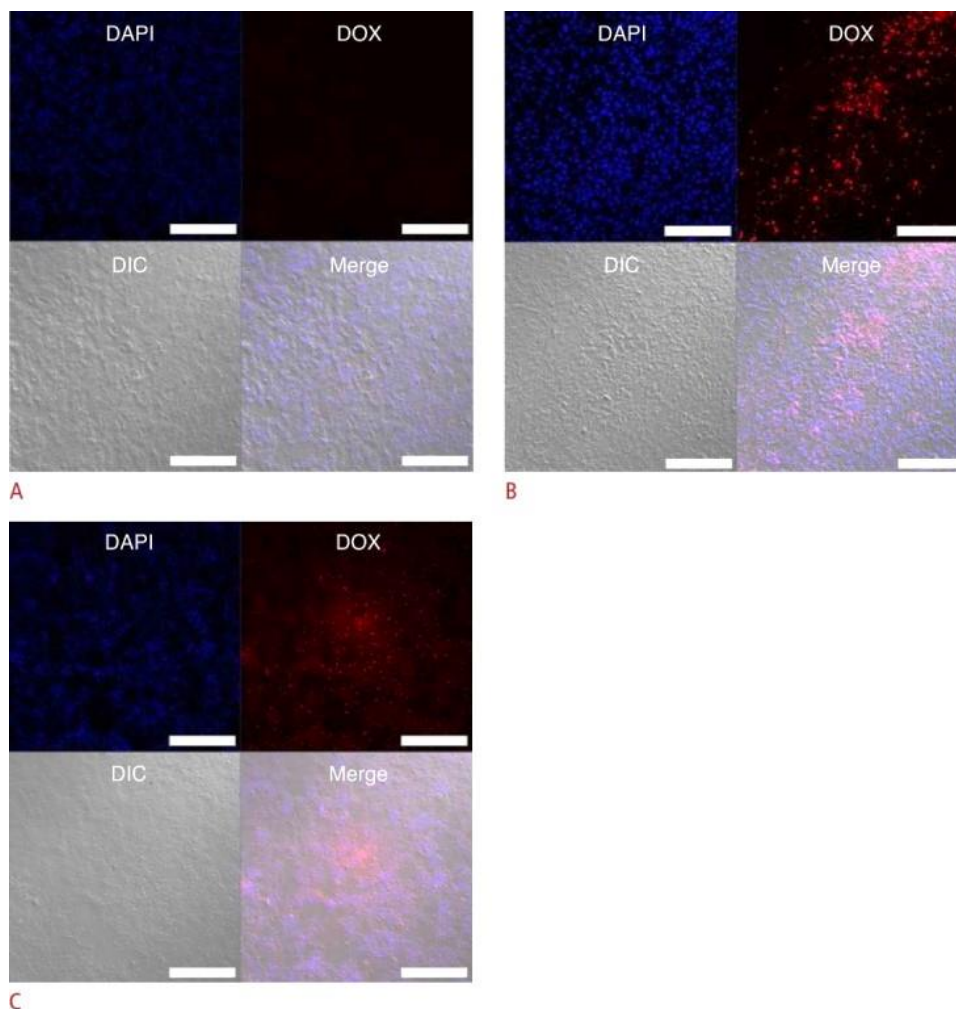


Figure 3.1 Confocal laser scanning microscope micrographs of tissue from PC3 tumours excised from mice. The tumours were stained with DAPI, fluorescence of DAPI and DOX were imaged, differential interference contrast micrographs were taken and a merged image was created. The mice received a tail vein injection of MBs with DOX and subsequent US for a) 5 mins, b) 10 mins and c) 15 mins. Taken from Lee et al. [204]

UTMD has also been investigated in the microRNA (miRNA) treatment of PCa. MiRNAs are small non-coding, ~22 nucleotide sequences that are transcribed from DNA. They are critical for several biological processes and in recent years their potential diagnostic (biomarkers) and therapeutic (regulation of gene expression) capability has been investigated [206]. Qin et al [207], investigated the potential of UTMD using the miRNA, miR-205 in the treatment of PCa. This involved UTMD using 1,2-distearoyl-3-trimethylammoniumpropane (DPTAP) and PEG-2000 stearate stabilised MBs combined with the miR-205. DU145 and PC3 cells were treated with cisplatin and transfected using UTMD mediated miR-205 UTMD. It was determined that UTMD-mediated miR-205 delivery promotes cisplatin-modulated apoptosis and scratch-assay results suggested that cells treated with cisplatin and UTMD-mediated delivery of miR-205 showed decreased cell migration and invasion compared to cells treated with either treatment separately [207]. The ability to increase both the uptake of chemotherapy and miRNA treatments using UTMD, highlights a possibility to increase the uptake of current chemotherapies such as DTX. However, loading the drug within the MBs, rather than administering alongside the MBs, may provide improved efficacy with reduced systemic overspill due to better targeting.

The main aim of the work carried out in this chapter was to prepare MBs loaded with RB and DTX to determine the potential of chemo-SDT as a treatment for prostate cancer. DTX was loaded hydrophobically into the acyl chain layer of the MB shell while a biotin derivative of RB was prepared to enable sensitiser attachment to the shell of the MB using the avidin-biotin interaction. The formulated MBs were tested for efficacy in a prostate LNCaP 3D spheroid model as well as PC3 and RM-1 murine models of the disease.



### 3.2 Aims and objectives:

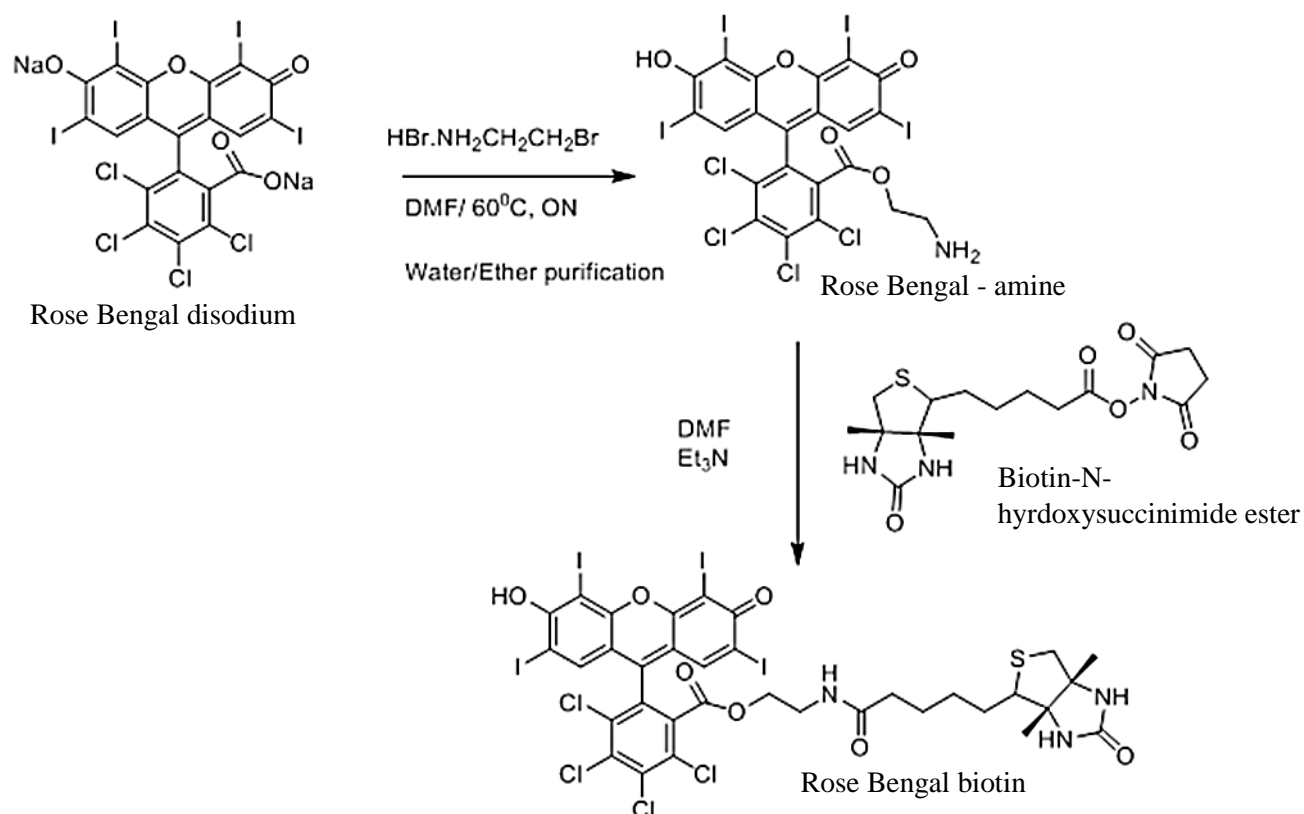
The main aim of the work reported in this chapter was to prepare a single MB formulation loaded with DTX and RB to determine the efficacy of UTMD mediated treatment using the MBs in *in vitro* and *in vivo* models of prostate cancer. The specific objectives were:

1. Synthesis and characterisation of a RB-biotin ligand suitable for the attachment to the surface of avidin functionalised lipid stabilised MBs.
2. Prepare DTX loaded avidin functionalised MBs (DTX-MB) and investigate the impact of DTX loading on the ability to attach RB-biotin ligand to produce DTX-MB-RB.
3. Determine efficacy of UTMD mediated chemo-SDT in 3D spheroid models of prostate cancer.
4. Determine efficacy of UTMD mediated chemo-SDT in SCID mice ectopically implanted with PC-3 and LNCaP tumours.
5. Determine efficacy of UTMD mediated chemo-SDT in C57 mice ectopically implanted with RM-1 tumours.

### 3.3 Results and discussion

#### 3.3.1 Synthesis of Rose Bengal – Biotin

The method chosen for attaching RB to the MBs was to utilise the biotin-avidin-biotin interaction. Therefore, it was necessary to derivatise Rose Bengal with biotin functionality. RB – Biotin was synthesised according to a literature protocol [208], following the scheme shown in Scheme 3.1.



Scheme 3.1 Synthetic procedure of Rose Bengal Biotin

The first step in the scheme is a  $\text{S}_{\text{N}}2$  reaction between Rose Bengal disodium and 2-bromoethylamine hydrobromide that connected both molecules together via an ester bond. The resulting amine functionalised (rose bengal – amine) was then reacted with the N-succinimidyl ester of biotin (Biotin-N-hydroxysuccinimide ester) via an amidation reaction resulting in the formation RB – Biotin.

The synthesis of target compound RB – Biotin was confirmed using  $^1\text{H}$ -NMR,  $^{13}\text{C}$ -NMR and ESI-MS displayed in Figures 3.2, 3.3 and 3.4 respectively. Figure 3.4 shows a base peak of 1241.7 Da, corresponding to the  $[\text{M}+\text{H}]^+$  ion peak. The  $^1\text{H}$ -NMR shown in Figure 3.2 shows a sharp singlet peak at 7.30 ppm corresponding to the two aromatic protons of RB (A) and two

resonances at 6.40 ppm and 6.30 ppm representing the urea protons of biotin. Six methylene protons closest to the biotin (**H,I,J**) appear on resonances grouped between 1.20 ppm and 1.70 ppm, while methylene protons **G** and **D**, adjacent to the amide group, were observed at 2.05 and 2.90 ppm respectively. The methine protons attached to the bridging carbons of the biotin ring (**B**) were observed on separate resonances at 4.30 and 4.15 ppm, while the methine proton **F** and methylene protons **E** of the biotin unit were observed at 3.05 and 2.85 ppm respectively.

<sup>13</sup>C-NMR analysis (Figure 3.3) revealed resonances between 20 ppm and 65 ppm that correspond to the aliphatic carbons of biotin and the linker group between RB and biotin. The remaining downfield resonances between 70 ppm and 200 ppm were assigned to the aromatic carbons of RB and the carbonyl carbons of the urea, amide, and ester groups. The combined analytical data obtained for RB – Biotin was consistent to that described in the literature and confirms successful synthesis of RB – Biotin.

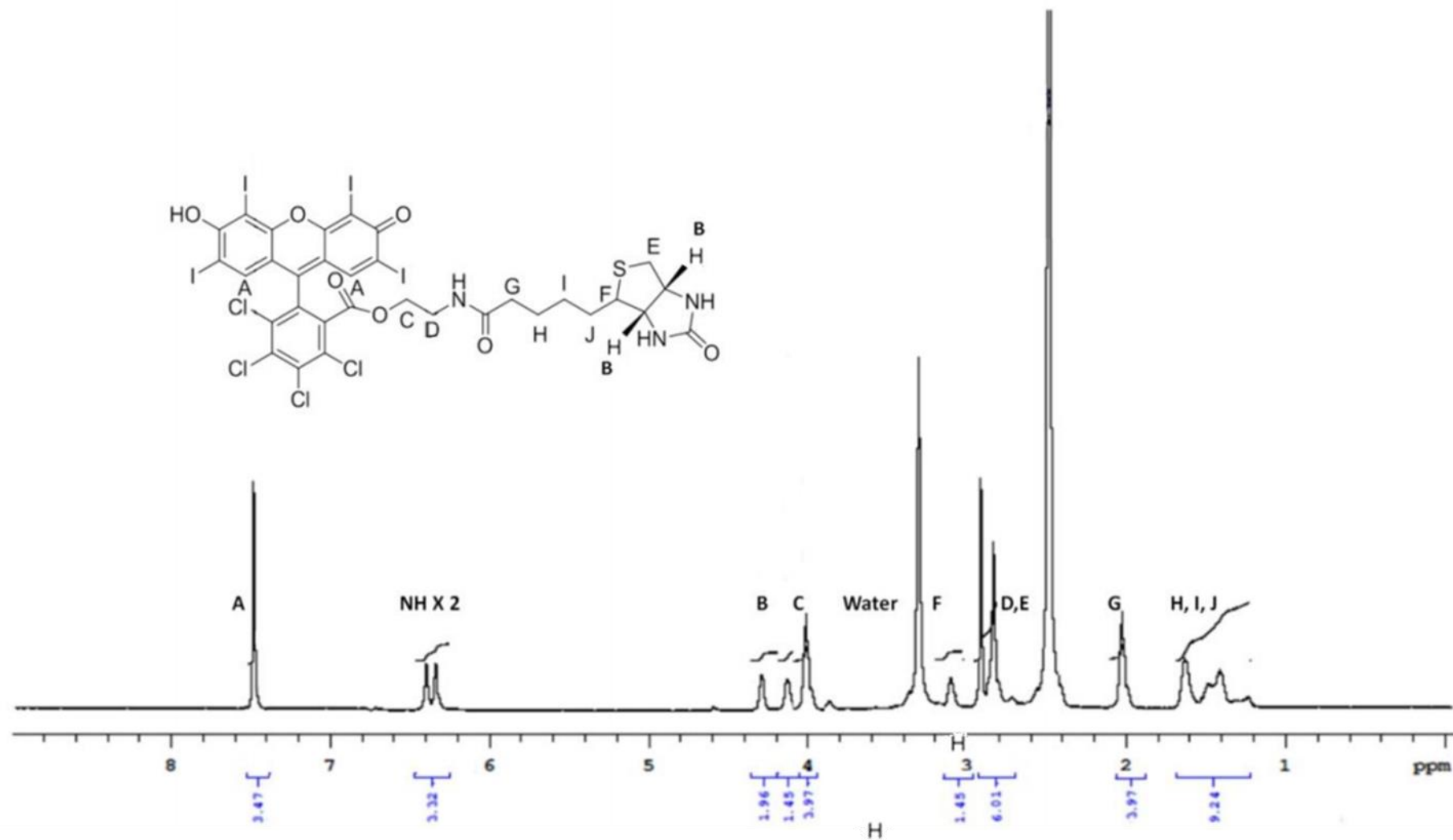


Figure 3.2 <sup>1</sup>H-NMR of RB – Biotin in DMSO-d<sub>6</sub>.

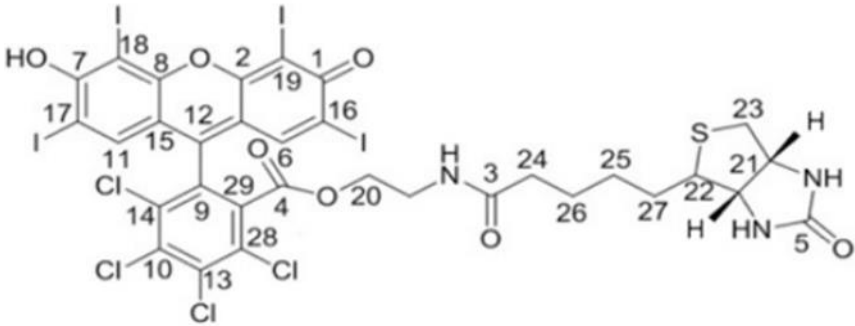


Figure 3.3  $^{13}\text{C}$ -NMR of RB – Biotin in DMSO-d<sub>6</sub>.

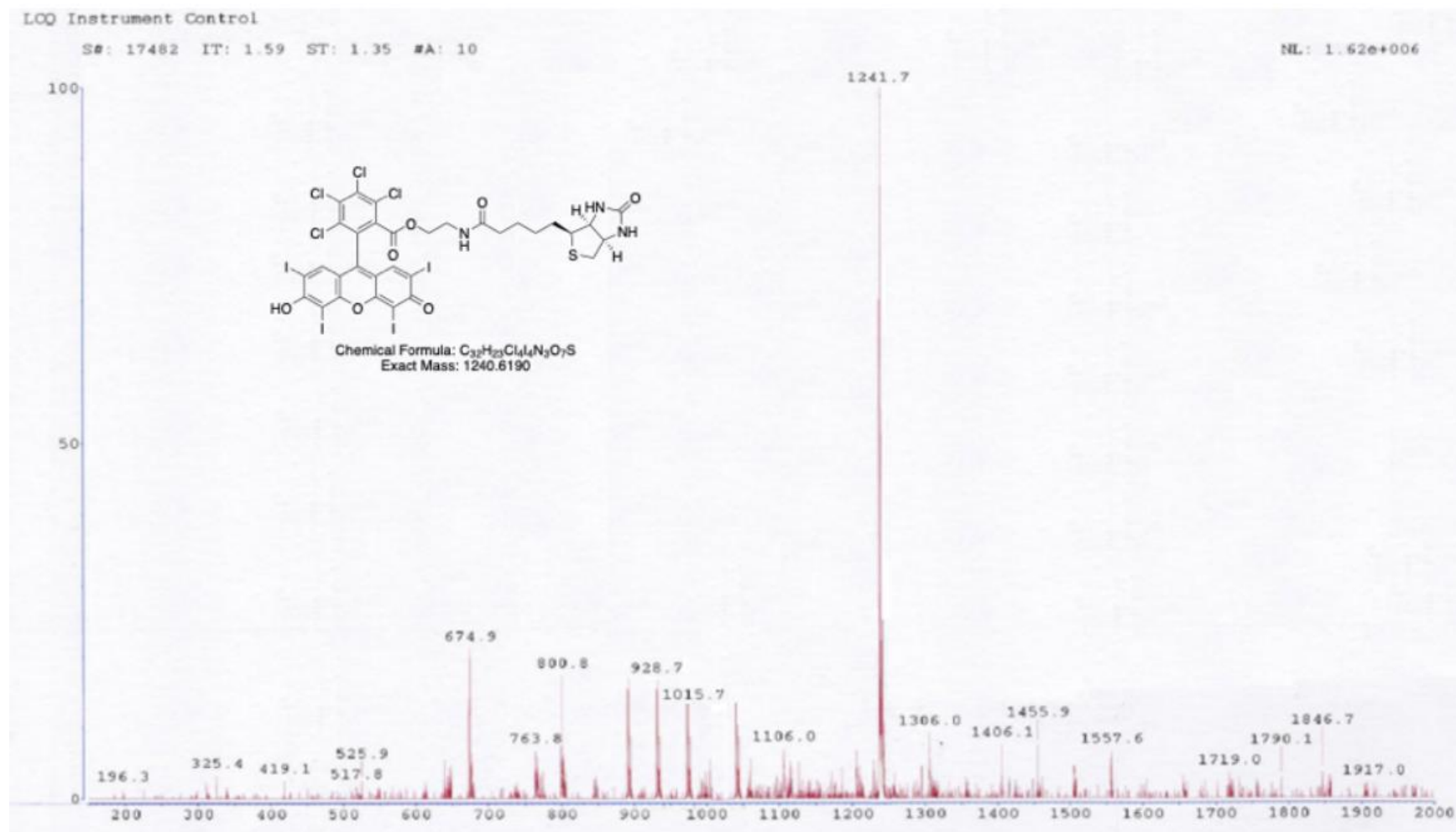


Figure 3.4 The ESI-MS spectrum of RB – Biotin in methanol (positive mode).

### 3.3.2 Preparation of DTX-MB-RB conjugates

The preparation of DTX-MB-RB first required preparing DTX loaded MB (DTX-MB) using the thin film hydration method. DTX is extremely hydrophobic and can be incorporated within the hydrophobic acyl chain layer of the MB shell using hydrophobic interactions, in a similar manner to that used previously for PTX. The first step involved dissolving the lipids and DTX in chloroform. The chloroform was then evaporated, and the resulting film hydrated in 2mL of Unger's solution (a mix PBS, glycerol, and propylene glycol (8:1:1)) and heated to 85°C for 45 min. The solution was then sonicated at low intensity using a Microson ultrasonic cell disruptor at 22% intensity for 30 seconds forming a suspension of liposomes with Ungers' solution in the core. MBs were then formed using a second higher intensity sonication at 89% intensity under an atmosphere of perfluorobutane (PFB) which is an extremely hydrophobic gas that helps stabilise MB formation. Excess non-incorporated lipids, DTX and other particulate matter were separated from the MB by low-speed centrifugation for 5 mins with MBs isolated as a concentrated cake floating on the infranatant solution. Avidin was then added to the DTX-MBs binding to the DPSE-PEG(2000)-Biotin component lipid of the DTX-MBs. Avidin contains four binding sites with a high affinity for biotin which can be utilised to conjugate the biotin functionalised RB [209]. The avidin functionalised DTX-MBs were then mixed with RB-biotin which binds to the avidin resulting in generation of the DTX-MB-RB conjugates. Full detail on the preparation of the DTX-MB-RB conjugate is provided in section 2.6.

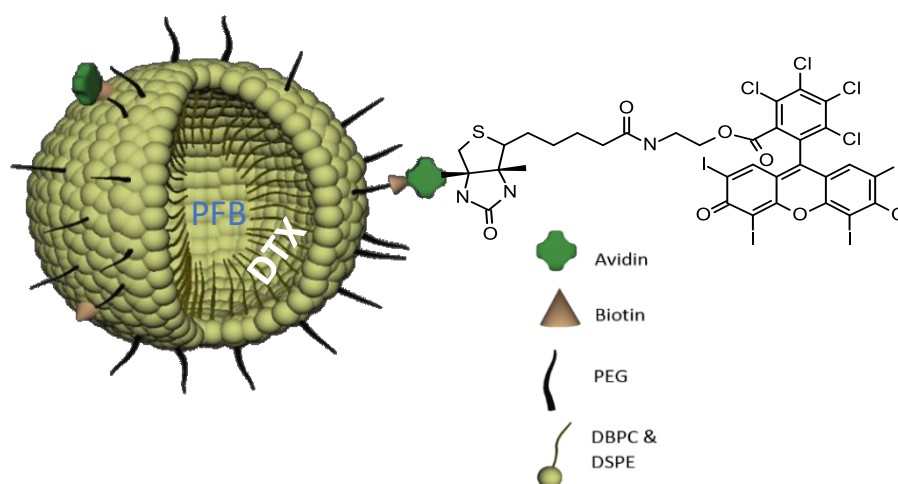


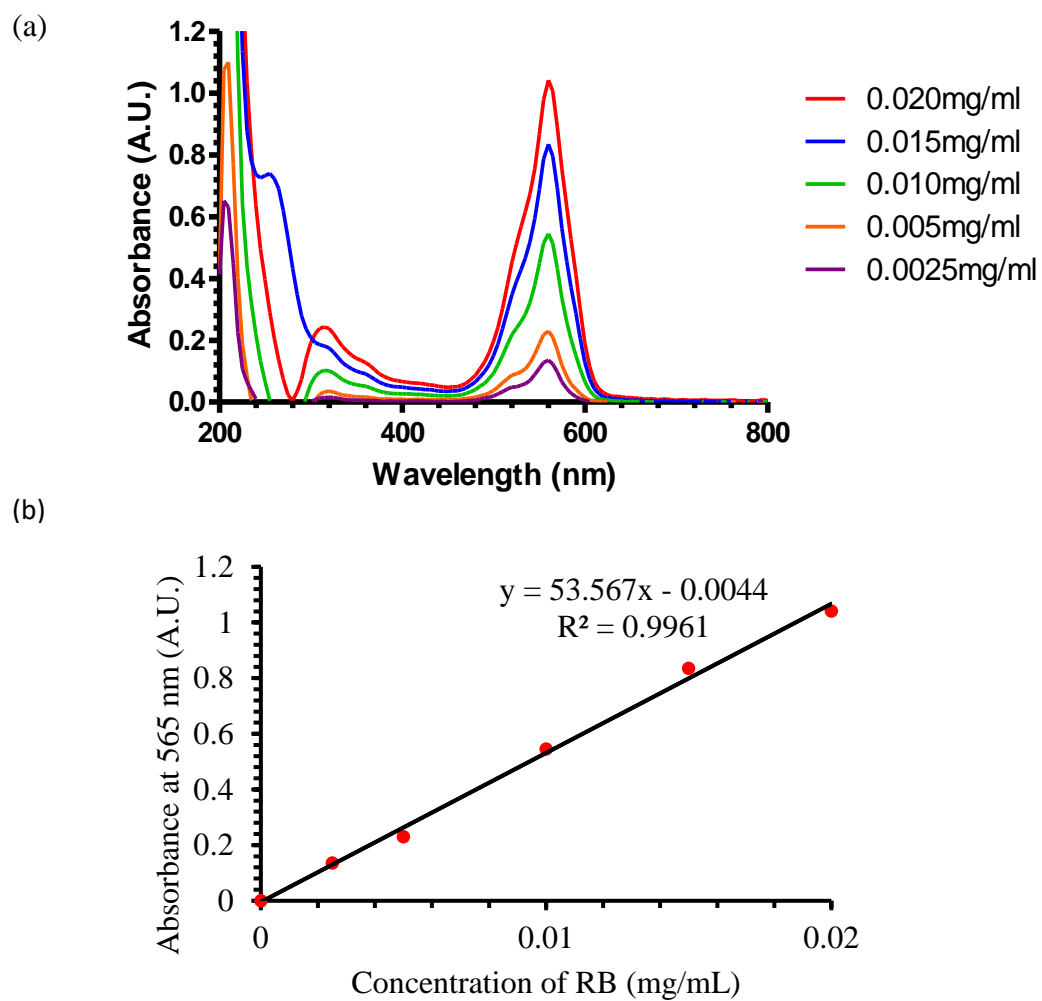
Figure 3.5 Schematic depicting DTX and RB loaded MBs.

### 3.3.2.1 Characterisation of DTX-MB-RB conjugates

Characterisation of DTX-MB-RB was essential to determine the drug loadings, MB concentration and sizes. Three batches of DTX-MB-RB conjugates were manufactured following the processes outlined 3.3.2. Samples of the MBs were collected for the determination of RB and DTX loadings. For the RB-biotin loading, a UV-vis spectrophotometry RB-biotin calibration curve was constructed following the methods described in section 2.6.1. Figure 3.5 (a) shows the spectra displaying increasing absorbance of RB – biotin between 0.0025 and 0.02mg/mL with a lambda max of 565nm. The corresponding calibration curve is shown in Figure 3.6 (b) and good linearity was detected in the 0-0.02 mg/mL range with an  $r^2$  of 0.9961. A sample of the DTX-MB-RB were then burst to release the RB-biotin into solution and analysed by UV-Vis spectrometry. The mean RB loading concentration was determined as  $10.143 \pm 0.655 \mu\text{g}/10^8 \text{ MBs}$  (Table 3.1).

DTX loading was determined using reverse phase HPLC following the method outlined in section 2.6.1. A calibration curve was constructed using standard solutions DTX between 0.025 and 0.1 mg / mL. DTX eluted at retention time of 4.5 min and chromatograms of the standard solutions are shown in Figure 3.6 (a) and increase in intensity at 4.5 min with increasing DTX concentration. A calibration curve of DTX constructed by plotting peak area at 4.5 min against concentration, and good linearity was observed over the concentration range tested ( $r^2 = 0.99$ ) (Figure 3.7b). A 100 $\mu\text{L}$  sample of the DTX-MB-RB were sonicated in 900 $\mu\text{L}$  of mobile phase (acetonitrile:water (60:40)). This was centrifuged at 5000RPM for 2 min to separate the DTX from the MB lipids. The pellet was reconstituted in a further 1mL of mobile phase and the centrifugation was repeated. The supernatants of both centrifugations were mixed and loaded onto the HPLC. The mean DTX loading for three batches of DTX-MB-RB was  $2.773 \pm 1.181 \mu\text{g}/10^8 \text{ MBs}$  (Table 3.1). A higher loading for RB was observed, this may be due to differences in the methods of drug loading. Where DTX was loaded hydrophobically within the acyl layer of the MB shell and RB was added via the avidin-biotin interaction to the surface of the MB shell.





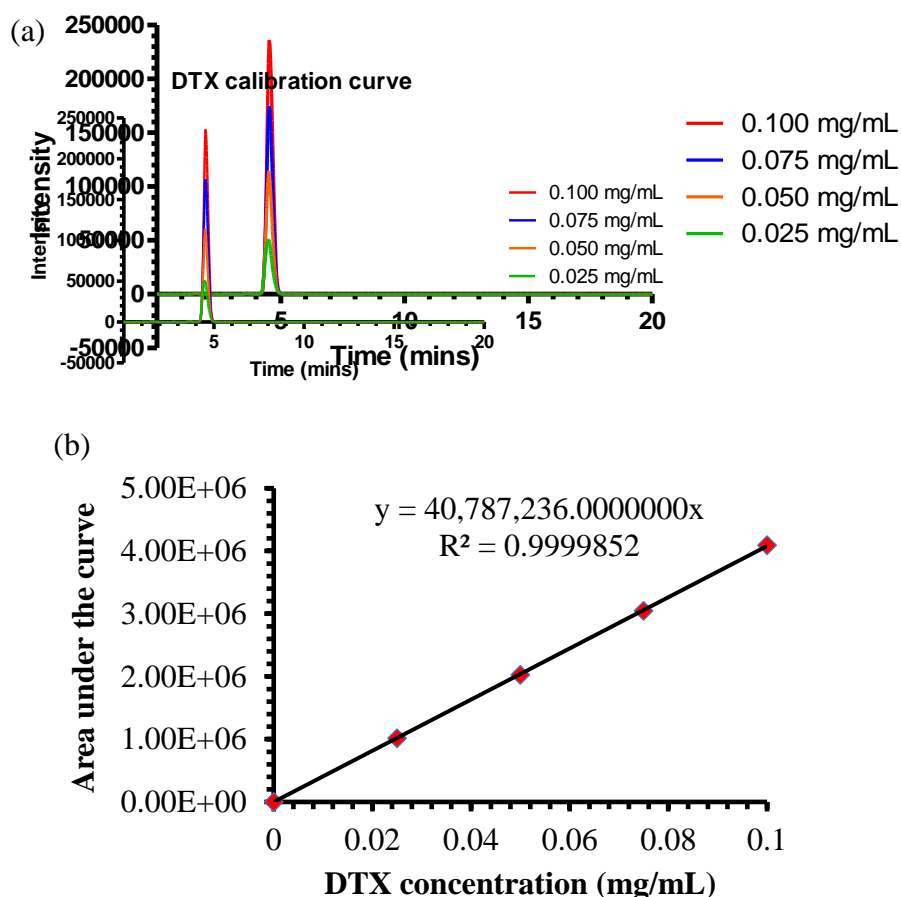
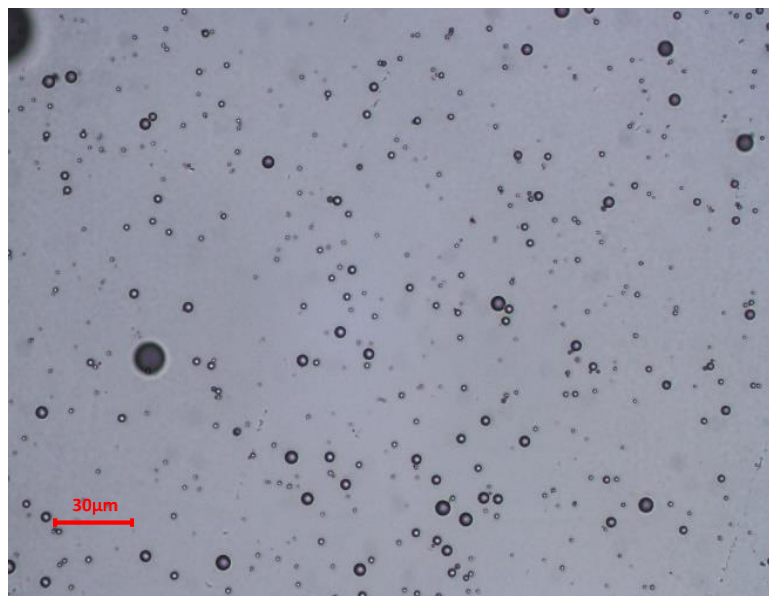


Figure 3.7 (a) HPLC chromatograms of DTX (b) Plot of peak area against concentration of DTX (mg/mL) (absorbance 231nm) (n=2).

The DTX-MB-RB formulation was also tested to determine MB number and size distribution. To facilitate this, optical micrographs of the DTX-MB-RB were taken, and the images analysed using a purpose-built MATLAB algorithm producing a size distribution curve. A representative image of the DTX-MB-RB is shown in Figure 3.8 (a) and reveal spherical particles with a mean diameter of  $1.65\mu\text{m} \pm 1.09\mu\text{m}$  (Figure 3.8 (b)). For three batches tested, the mean MB concentration was  $6.213 \times 10^9 \pm 0.707 \times 10^9/\text{mL}$  with a mean diameter of  $1.153\mu\text{m} \pm 0.750\mu\text{m}$ . These numbers are consistent with previous reports of MBs prepared using the thin-film hydration approach and suggest inclusion of DTX in the shell or RB to the surface does not impact the yield or size distribution of the MBs produced.

(a)



(b)

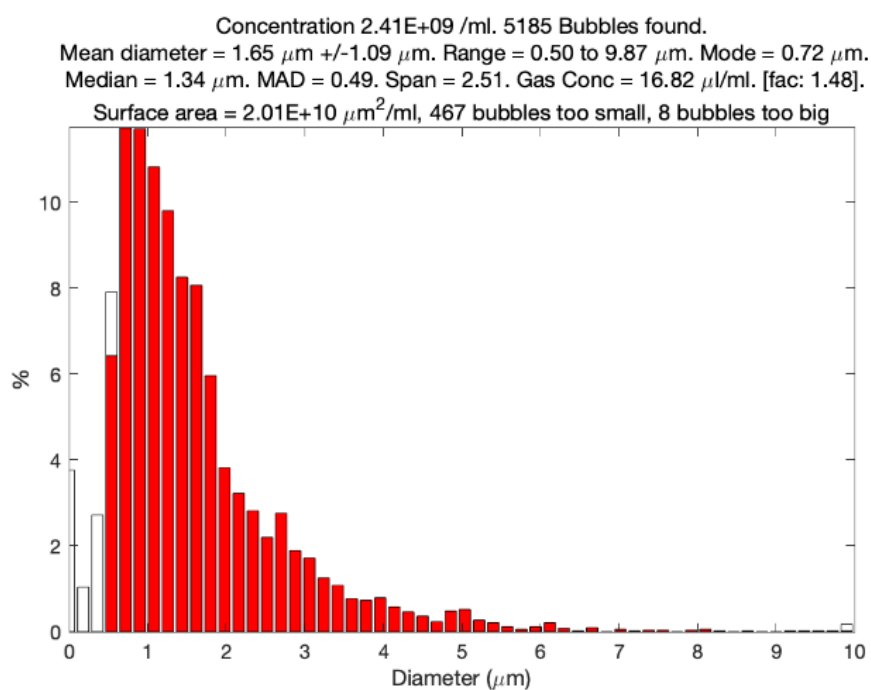


Figure 3.8 (a) Optical microscope image at 40x objective lens magnification of DTX-MB-RB after 1 in 25 dilution in Unger's solution. (b) size distribution of DTX-MB-RB obtained from optical microscope images through MATLAB software.

Table 3.1 Mean bubble count (number/mL), bubble size ( $\mu\text{m}$ ), RB loading concentration ( $\mu\text{M}$ ) and DTX loading concentration ( $\text{mg/mL}$ ) batches of DTX-MB-RB ( $n=3$ ).

	MB concentration (Number/mL) $\pm$ SD	MB Size ( $\mu\text{m}$ ) $\pm$ SD	RB Loading ( $\mu\text{g}/10^8$ MBs) $\pm$ SD	DTX Loading ( $\mu\text{g}/1 \times 10^8$ MBs) $\pm$ SD
Mean	$6.213 \times 10^9 \pm$ $0.707 \times 10^9$	$1.153 \pm 0.750$	$10.143 \pm 0.655$	$2.773 \pm 1.181$

### 3.3.2.2 Optimisation of DTX drug loading on DTX-MB-RB

After establishing a successful method of producing DTX-MB-RB conjugates, the next step was to determine the optimal starting mass of DTX to maximise the loaded DTX concentration within the MBs. Batches of DTX-MB-RB conjugates were prepared with increasing masses of DTX incorporated within the film of the MBs (2.5, 5 and 10mg). Following preparation, the amount of DTX incorporated in the MB shell was determined using RP-HPLC using the method described in 2.6.1. The results are displayed in Figure 3.9 and show a significant 117.5% increase in DTX content between the 2.5 and 5mg batches from  $1.699 \pm 0.67 \mu\text{g}/1 \times 10^8$  MBs to  $3.392 \pm 1.914 \mu\text{g}/1 \times 10^8$  ( $p \leq 0.05$ ). However, further increasing the DTX film content to 10mg produced a non-significant 15.4% increase in DTX loading to  $3.913 \pm 1.169 \mu\text{g}/1 \times 10^8$  MBs. These results suggest that increasing the DTX content of the lipid film any higher than 5 mg did not provide any significant benefit in terms of resulting DTX loading in the DTX-MB-RB formulation. Therefore, it would appear that the capacity within the acyl chain layer for the hydrophobic incorporation of DTX approaches saturation at concentrations of approximately  $4.0 \pm 1.169 \mu\text{g}/1 \times 10^8$  and adding additional DTX to lipid film in excess of 5mg is not cost effective.

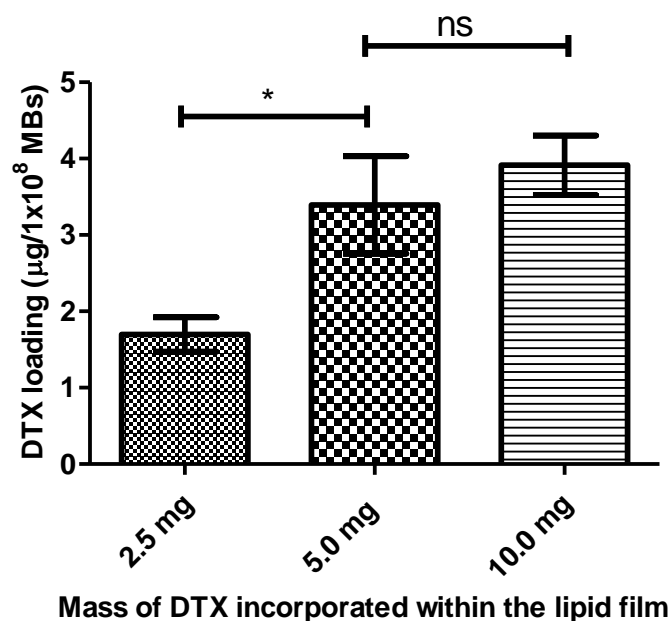


Figure 3.9 DTX loadings for MBs prepared with 2.5, 5.0 or 10.0 mg DTX, determined using HPLC (n=6) nsP>0.05, \*P<0.05.

It was also important to determine whether increasing the DTX content of the MBs would have any effect on the MB number and size. The results from the 2.5, 5.0 and 10.0 mg DTX batches are shown in Table 3.2 and reveal the MB number increased by 8.0% to  $5.965 \times 10^9 \pm 0.638 \times 10^9$  MB/mL from  $5.525 \times 10^9 \pm 0.224 \times 10^9$  on increasing the film DTX content from 2.5 to 5.0mg, with no appreciable difference in the mean MB diameter. The MB number dropped by 3.1% to  $5.785 \times 10^9 \pm 0.380 \times 10^9$  MB/mL when the DTX film content was increased further to 10 mg with no change to the mean MB diameter.

Table 3.2 Mean bubble count (bubbles/mL) and bubble size ( $\mu\text{m}$ ), for MBs prepared with 2.5,

Mass of DTX used in preparation (mg)	Mean bubble number (bubbles/mL)	Mean bubble size ( $\mu\text{m}$ )
2.5	$5.525 \times 10^9 \pm 0.224 \times 10^9$	$0.97 \pm 0.64$
5.0	$5.965 \times 10^9 \pm 0.638 \times 10^9$	$1.00 \pm 0.60$
10.0	$5.785 \times 10^9 \pm 0.380 \times 10^9$	$1.00 \pm 0.61$

5.0 or 10.0 mg of DTX.

### 3.3.2.3 Effect of increasing DTX content on RB loading

Another important parameter to consider was the potential impact increased DTX content had on the ability to load RB-biotin to the surface of the MB. The amount of RB-biotin attached was determined as described in 2.6.1. The results are summarised in Figure 3.10 and reveal no significant difference in RB-biotin loading between the batches prepared with 2.5, 5 and 10mg DTX added to the lipid film. However, the 5 mg DTX batch produced the highest RB-biotin loading at  $12.857 \pm 3.486 \mu\text{g}/1 \times 10^8$  MBs. Combined, these results from the DTX loading, MB number / size and RB-biotin loading experiments, support the use of adding 5mg of DTX to the lipid film during preparation of a standard MB batch equating to 0.64mg of DTX per mg of total lipid content.

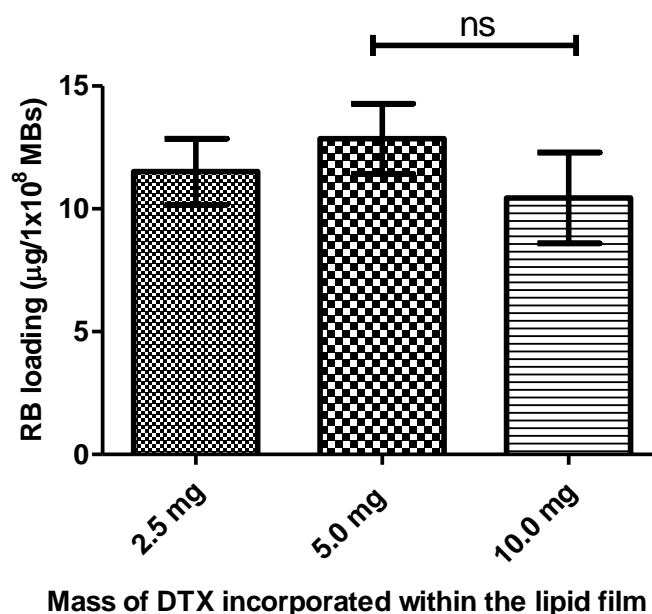


Figure 3.10 RB loadings for MBs prepared with 2.5, 5 or 10mg DTX, determined using UV/vis spectrophotometry (n=4) ns P>0.05

#### 3.3.2.4 Effect of increasing DTX content on stability of DTX-MB-RB at 37°C

The final parameter that required investigation was the effect of different amounts of DTX in the lipid film on MB stability at body temperature (37°C). Samples of DTX-MB-RB prepared from lipid films containing 2.5, 5.0 and 10.0 mg DTX were incubated for 90 min at 37°C and the MB number counted at various intervals throughout. A plot of MB number against time is shown in Figure 3.11 for the 2.5, 5.0 and 10.0 mg DTX batches. No trend was observed when the DTX content of the film was increased with the 5.0 mg batch the most stable with 97.9% of MBs remaining intact after 90 min, suggesting that 5.0 mg of DTX present within the MB shell provides greater stability to the lipids within the MB. However, both the 2.5 mg and 10.0 mg batch were less stable with 73.4% and 62.8% MBs remaining after 90 min. It should be noted that the half-life of contrast agent MBs in the circulation of an adult human is  $1.04 \pm 0.15$  min for SonoVue and  $6.88 \pm 4.88$  min for Definity [210]. Therefore, DTX-MB-RB prepared using 5 mg DTX in the lipid film should have acceptable stability for use in *in vivo* experimentation.

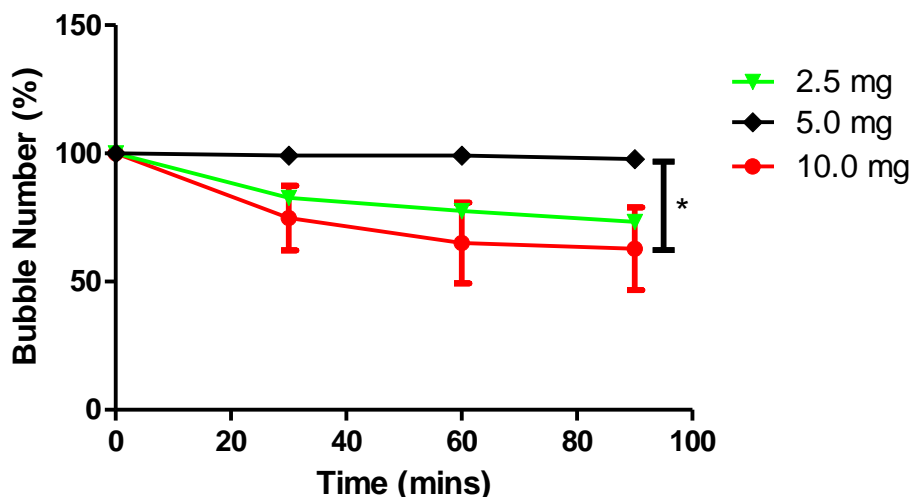


Figure 3.11 Plot of percentage bubble number (%) (calculated as a percentage of starting MB number) of DTX MB RBs prepared with 2.5, 5.0 or 10.0 mg DTX over a period of 90 min.

\* $P > 0.05$ .

### 3.3.4 Efficacy of DTX-MB-RB in Spheroids

As opposed to 2D monolayer culture, when grown in 3D culture systems, cells form aggregates or spheroids within a matrix, on a matrix, or in a suspension medium. In spheroids, cell–cell interactions and cell–extracellular matrix interactions more closely mimic the natural environment found *in vivo*, so that the cell morphology closely resembles its natural shape in the body. In addition, 3D spheroids are comprised of cells in various stages, usually including proliferating, quiescent, apoptotic, hypoxic, and necrotic cells. The outer layers of a spheroid, which is highly exposed to the medium, are mainly comprised of viable, proliferating cells. The core cells receive less oxygen, growth factors, and nutrients from the medium, and tend to be in a quiescent or hypoxic state. Such cellular heterogeneity is very similar to *in vivo* tissues, particularly in tumours. Since the morphology and the interactions of cells grown in 3D culture is more like what occurs *in vivo*, the cellular processes of these cells also closely emulate what is seen *in vivo* [211].

LNCaP cells are an androgen sensitive metastatic prostate carcinoma cell line that were isolated in 1977. They were then transfected with a plasmid containing the genetic material required for the cell to produce the enzyme luciferase present within fireflies, to produce LNCaP-Luc.



When the cells are exposed to D-luciferin, luciferase causes D-luciferin to be converted to oxyluciferin causing luminescence [212]. LNCaP-Luc spheroids were prepared by seeding 1000 cells in ultra-low attachment round bottom 96-well plates. The round bottom of the wells cause cells to aggregate and form spheroids. The LNCaP-Luc cells were incubated at 37°C and 5% CO<sub>2</sub> for 4 days allowing for the spheroids to form. Once the spheroids were formed, they were treated with DTX-MB-RB +/- US. For completeness, MBs were also prepared containing no drugs (blank MB), DTX only (DTX-MB) and Rose Bengal only (RB-MB). Representative optical images, MB number / size and drug are provided for these additional formulations are provided in appendix 9.1 – 9.3. Where US was used, it was applied immediately (1s, 30% DC, 3W) to induce MB inertial cavitation and again after 3 hours (20s, 30% DC, 3W) to trigger SDT (for RB carrying MBs). 48 hours following treatment, the spheroids were imaged and then trypsinised to form a single cell suspension and the MTT assay was used to determine cell viability.

The results from the MTT assay are shown in Figure 3.12 and reveal that exposure to US alone caused no reduction in the viability of cells. Treatment with blank MBs + US caused a moderate reduction in cell viability to 76%, most likely due to the cavitation effects associated with the MB rupturing. The effect of RB-MB alone (i.e., no US) was also minor reducing cell viability to 89% which reduced further to 49% upon the application of US, attributed to a SDT effect. The cell viability for spheroids treated with DTX-MB in the absence of ultrasound (46% viable), was comparable to those treated with DTX-MB+US (49% viable), which was surprising as US induced MB cavitation would be expected to facilitate improved delivery of the DTX deeper into the spheroid structure. Treatment with DTX-MB-RB in the absence of ultrasound produced a cell viability compared to DTX-MB in the absence of ultrasound which was not surprising given the amount of DTX was the same in each case. However, DTX-MB-RB + US treatment resulted in a cell viability of 28%, significantly lower than DTX-MB + US ( $p \leq 0.01$ ), DTX-MB-RB ( $p \leq 0.01$ ) or MB-RB + US ( $p \leq 0.001$ ). This improvement in cytotoxicity can be attributed to the combined effects of DTX chemotherapy and RB mediated SDT. The mechanism of this activation of RB has been proposed to be from the emission of sonoluminescent light emitted during the implosion of MBs, the emission wavelengths of light emitted from sonoluminescence in aqueous medium appears between 250 and 600 nm, which is compatible with the absorption range of RB between 480 and 580 nm. The light absorbed from sonoluminescence activated RB and causes singlet oxygen production [214, 215]. Given

the mechanism of action for both treatments differ (inhibition of microtubular depolymerization versus ROS mediated oxidative stress), it was not surprising both treatments complemented each other.

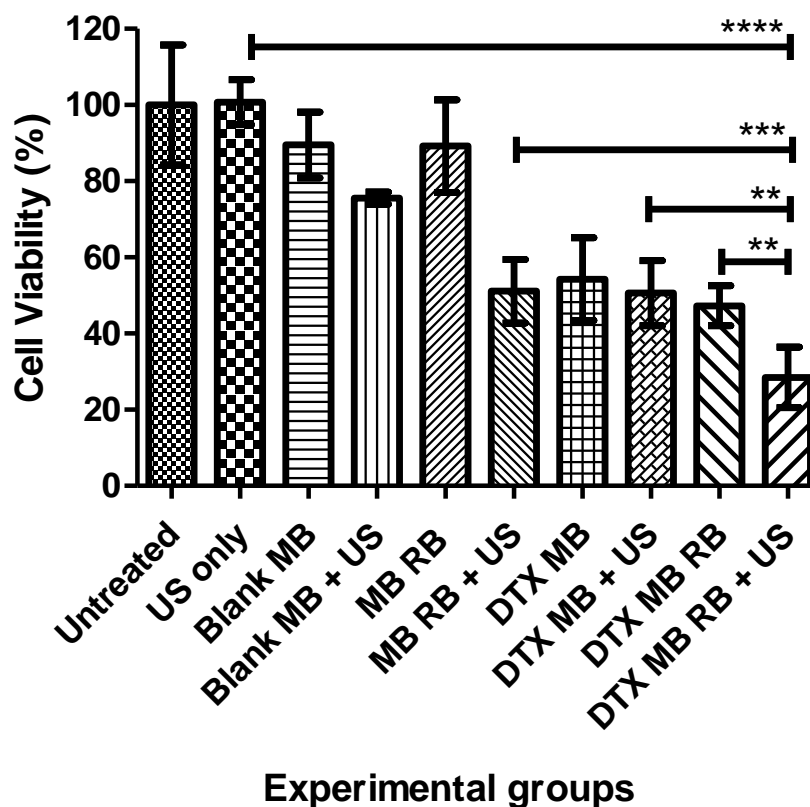


Figure 3.12 Cell viability of LNCaP-Luc spheroids treated with i) Untreated ii) US only (iii) blank MB (iv) blank MB + US (v) MB-RB (vi) MB-RB + US (vii) DTX-MB (viii) DTX-MB + US (ix) DTX-MB-RB (x) DTX-MB-RB + US. [DTX] in all cases is 6.2 $\mu$ M. [RB] in all cases is 30 $\mu$ M. [MB] was 2.88x10<sup>8</sup>/mL. \*\*P<0.01, \*\*\*P<0.001 and \*\*\*\*P<0.0001. Error bars show  $\pm$  SEM (n=4).

### **3.3.5 Efficacy of MB mediated chemo-SDT therapy using the DTX-MB-RB conjugates in mice bearing subcutaneous PC3 tumours.**

Following the encouraging results obtained for the DTX-MB-RB chemo-SDT therapy in the 3D spheroids, the next step was to determine how effective the treatment would be in a murine model of prostate cancer. The PC3 cell line was used to induce subcutaneous tumours in SCID mice. The PC3 cell line is an androgen resistant cell line taken from the bone metastases of a prostatic adenocarcinoma [213]. Once tumours had formed, the animals were separated into 4 groups (n = 4). Group 1 remained untreated, group 2 received a standard systemic dose of DTX (10mg/kg), group 3 received DTX-MB-RB without US and group 4 received DTX-MB-RB with US treatment applied to the tumour during the MB infusion for a total of 3.5 min, with a second US treatment administered 30 mins later. Animals were treated on days 0, 4, 7, 10, 14, 18 and 21 with the tumour volume measured at regular intervals. IP injection was preferred for the administration of DTX (10 mg/kg) rather than IV administration due to the severity of side effects of DTX and the vehicle Taxotere (polysorbate 80 and ethanol) which hadn't been used before in the J. Callan laboratory. It was therefore deemed safer to administer IP in this being the first in vivo experiment for the safety of the mice involved until it was determined that mice could tolerate multiple treatments.

The tumour growth delay plot is shown in Figure 3.13 and reveals that tumours in untreated animals grew by 659.0% 23 days following the initial treatment. The effect of DTX treatment alone and DTX-MB-RB in the absence of ultrasound was similar resulting in tumours that grew by 263.6 and 281.7% respectively by day 23. This was surprising given the amount of DTX used as part of the DTX-MB-RB at 0.28 mg/kg was 35.7 times lower than the DTX group (10 mg/kg). One potential reason for this could be the administration route where the “free” DTX was administered by intraperitoneal (IP) injection and the DTX-MB-RB by intravenous (IV) injection. It has been shown that the rate of absorption following IP administration is one-half to one-quarter as fast as IV administration [216]. However, this reduction would still result in significantly more “free” DTX being available than that contained within the DTX-MB-RB. Another possible explanation could be that the DTX-MB-RB spontaneously degrade over time in circulation. MBs have previously been shown to form nanoparticles such as micelles, liposomes, nanobubbles and nanodroplets when they are destroyed [217]. The spontaneous destruction of the MBs in circulation could result in the production of nanoparticles that

extravasate the vasculature and accumulate in the tumour by the EPR effect [218]. While the DTX-MB-RB showed excellent stability when incubated at 37°C (3.3.2.8), that experiment did not consider other factors such as the shear stress that would be experienced by the particles during capillary circulation and may result in their destruction.

While the “free” DTX and DTX-MB-RB groups provided modest control of tumour growth, the DTX-MB-RB + US group was significantly better with tumours growing by only 97.4% 23 days after their initial treatment relative to the untreated group ( $p < 0.01$ ). Thus, the application of US to the DTX-MB-RB reduces the tumour growth rate by 184.3% indicating that the targeted MB destruction and subsequent activation of SDT provides a marked benefit on tumour control. As was observed in 3D spheroid study, this confirms the benefit of combining SDT and chemotherapy to generate improved efficacy when compared to chemotherapy treatment alone. Importantly, this improved efficacy is obtained using much less toxic chemotherapy which should improve the tolerability of the treatment. Indeed, when the weight of the animals in each group was compared throughout the treatment, it was noticeable that animals in the “free” DTX group were significantly lighter than those in the DTX-MB-RB or DTX-MB-RB + US groups, which matched closely the average weight of animals in the untreated group. This confirms that DTX-MB-RB + US is not only more effective than a much higher dose of DTX chemotherapy, but it is also much better tolerated.

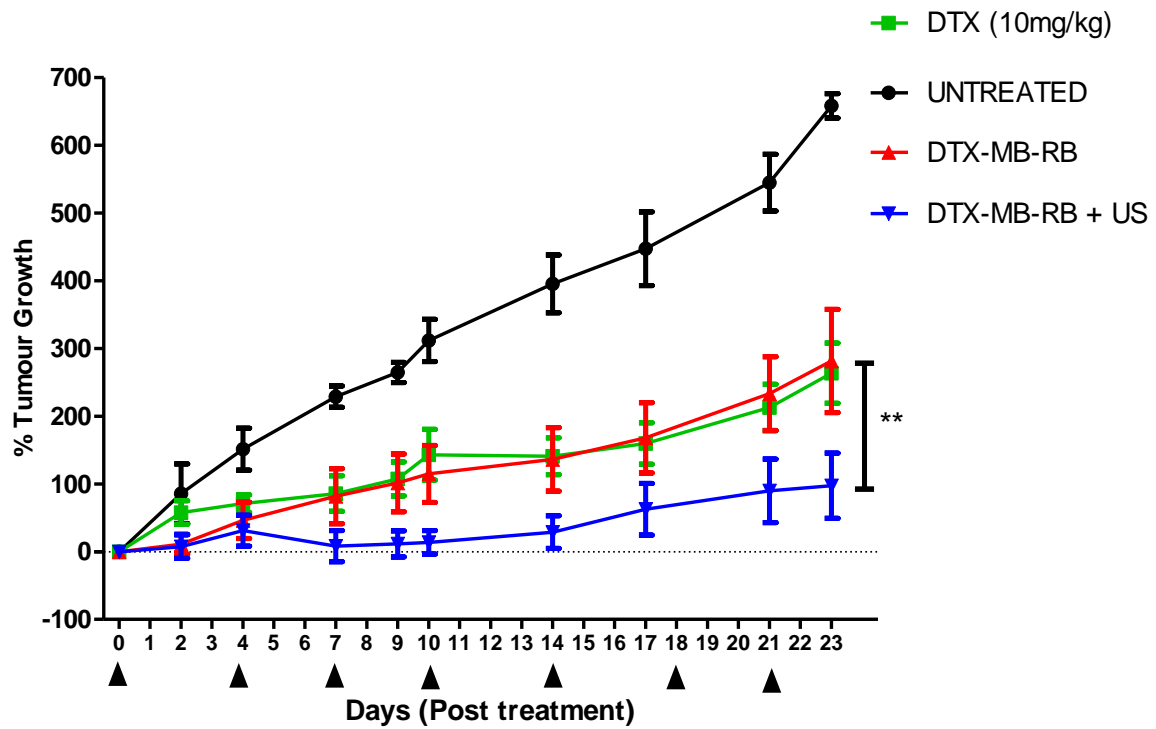


Figure 3.13 Plot of percentage tumour growth in SCID mice bearing PC3 prostate tumours that received (i) no treatment (n=3) (ii) IP injection of DTX (10mg/kg) (n=4) (iii) IV injection of DTX-MB-RB – US (n=4) and (iv) IV injection of DTX-MB-RB + US (n=4). Treated on days 0, 4, 7, 10, 14, 18 and 21 (represented by ▲). \*\*  $P \leq 0.01$ .

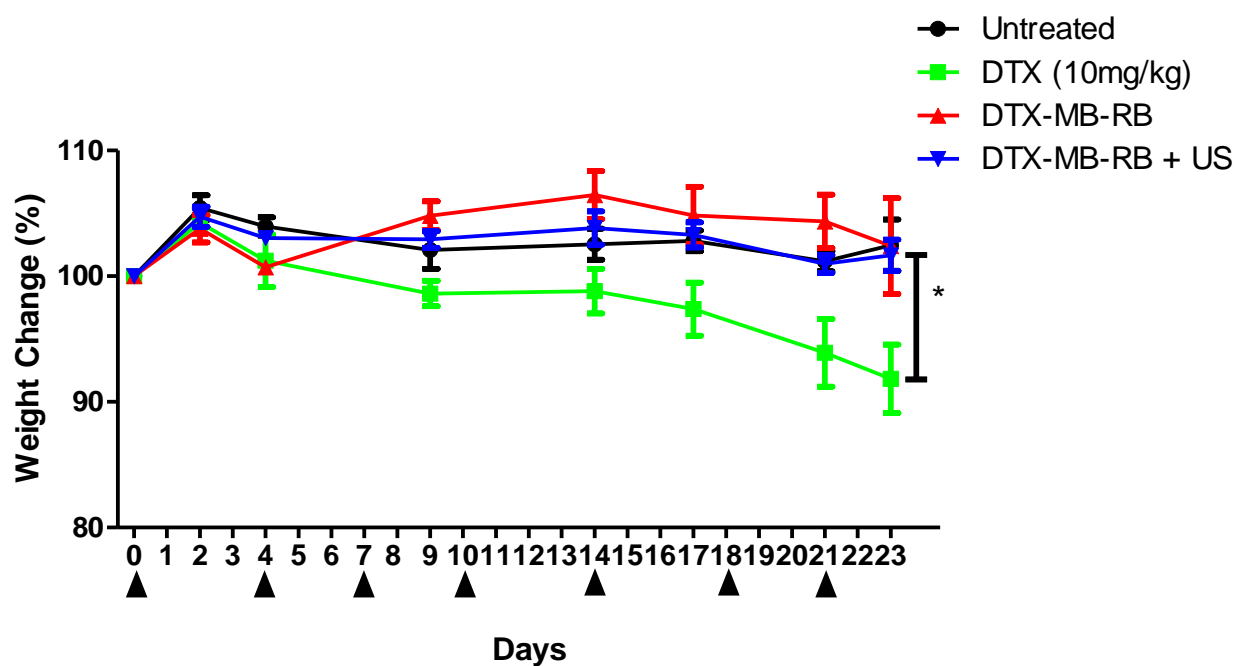


Figure 3.14 Plot of mice weights over 21 days as percentage weight change of day 0 weights. Mice received (i) no treatment (ii) IP injection of DTX (10mg/kg) (iii) IV injection of DTX-MB-RB – US and (iv) IV injection of DTX-MB-RB + US. Treated on days 0, 4, 7, 10, 14, 18 and 21 (represented by ▲). \*P>0.05 (n=4)

### 3.4 Conclusions

Lipid stabilised MBs, loaded with DTX and Rose Bengal were successfully prepared and evaluated for UTMD mediated efficacy in 3D spheroid and murine pre-clinical models of prostate cancer. The DTX-MB-RB were prepared by loading DTX hydrophobically into the phospholipid shell and it was found that the ideal DTX loading was 0.64 mg per mg of lipid. Biotin functionalised RB was synthesised to enable attachment of the sensitiser to the MB surface using the avidin-biotin interaction. UTMD mediated chemo-SDT treatment of 3D LNCaP spheroids using DTX-MB-RB was significantly more efficacious than UTMD mediated chemotherapy using DTX-MB and UTMD mediated SDT treatment using MB-RB. *In vivo*, UTMD mediated chemo-SDT treatment of PC3 tumour bearing mice using DTX-MB-RB was also significantly more effective at controlling tumour growth than a DTX chemotherapy dose some 35.7 times greater. As a result, the DTX-MB-RB chemo-SDT treatment was also well tolerated. These results confirm the potential of UTMD mediated chemo-SDT using DTX-MB-RB as a potential treatment for prostate cancer.

## **Chapter 4:**

### **Development of a Single-Vial, Pre-Microbubble Colloidal Suspension for the Rapid Preparation of Docetaxel and Rose Bengal loaded Microbubbles.**



## 4.1 Introduction

The results presented in Chapter 3 highlight the potential of MB mediated chemo-SDT as a treatment for prostate cancer. However, while useful to determine proof-of-principle, the method used for attachment of Rose Bengal requires several technical steps to be completed after the MBs are generated. With a view toward clinical translation, this would be deemed a manufacturing step by the Medicines and Healthcare Products Regulatory Agency (MHRA) thus requiring a GMP level quality assurance facility within the hospital / clinical trial site. To reduce the complexity of this process, a more straightforward approach is desirable that provides the drug loaded MBs as a single vial that can be re-constituted or activated in a facile manner that is not considered a manufacturing step.

Two main approaches are used to provide MB contrast agents in the clinic. SonoVue® (Bracco) provide a vial of freeze-dried phospholipids under a headspace of SF<sub>6</sub> gas. A vial of saline is also provided which is added using a MiniSpike / syringe that enables the saline to be added without escape of the SF<sub>6</sub> gas while maintaining sterility. (Fig 4.1) The vial contents are then shaken by hand which produces the MB contrast agent that is administered to the patient.



Figure 4.1 SonoVue® (Bracco) vial with powder form MBs (left), MiniSpike (middle) and saline filled syringe (right) (reproduced from [219]).

The second approach adopted by Lantheus for their contrast agent DEFINITY®, provides a pre-MB suspension of the phospholipids in a vial containing an aqueous vehicle under a headspace of PFB gas. Lantheus also provide a Vialmix® device to customers which mechanically agitates the vial for 45s at approximately 4000 rpm generating the MBs, fig 4.2.

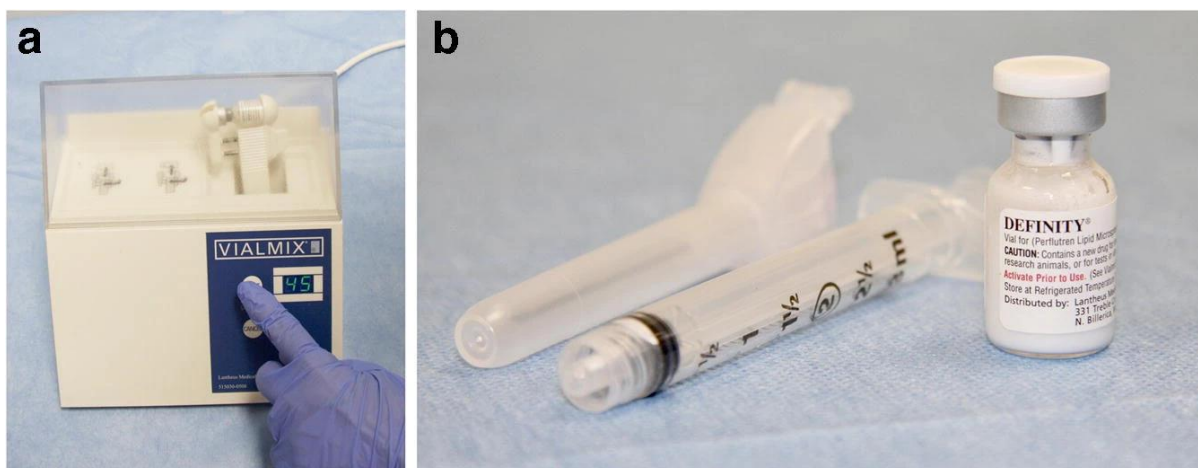


Figure 4.2 a) DEFINITY Vialmix shaker, shakes vial for 45s. b) The MBs are produced within the vial to be removed via a needle for administration (adapted from [220]).

Both approaches involve simple mixing steps that are not considered manufacture steps and therefore can be done at the bedside. The advantage of the DEFINITY® approach is that no liquid addition step is required, and the mixing step is mechanically undertaken guaranteeing consistency. In addition, aseptic manufacture may be required for the freeze-drying and fill-finish steps associated with the SonoVue® which also can be costly when considering scale-up.

Therefore, the focus of the work undertaken in this chapter was to develop a method for the preparation of DTX-MB-RB from a pre-MB suspension of phospholipids using the Vialmix® device. To enable this, the biotin-avidin approach adopted in Chapter 3 for the addition of Rose Bengal to the MB surface was not deemed appropriate as this requires a stepwise approach of adding avidin, washing, then the RB-biotin to avoid cross-linking MBs together. Instead, a Rose Bengal functionalised lipid was synthesised and formulated into the pre-MB suspension with other component lipids, DTX and excipients. A systematic approach was followed until an ideal formulation was identified.

## **4.2 Aims and objectives**

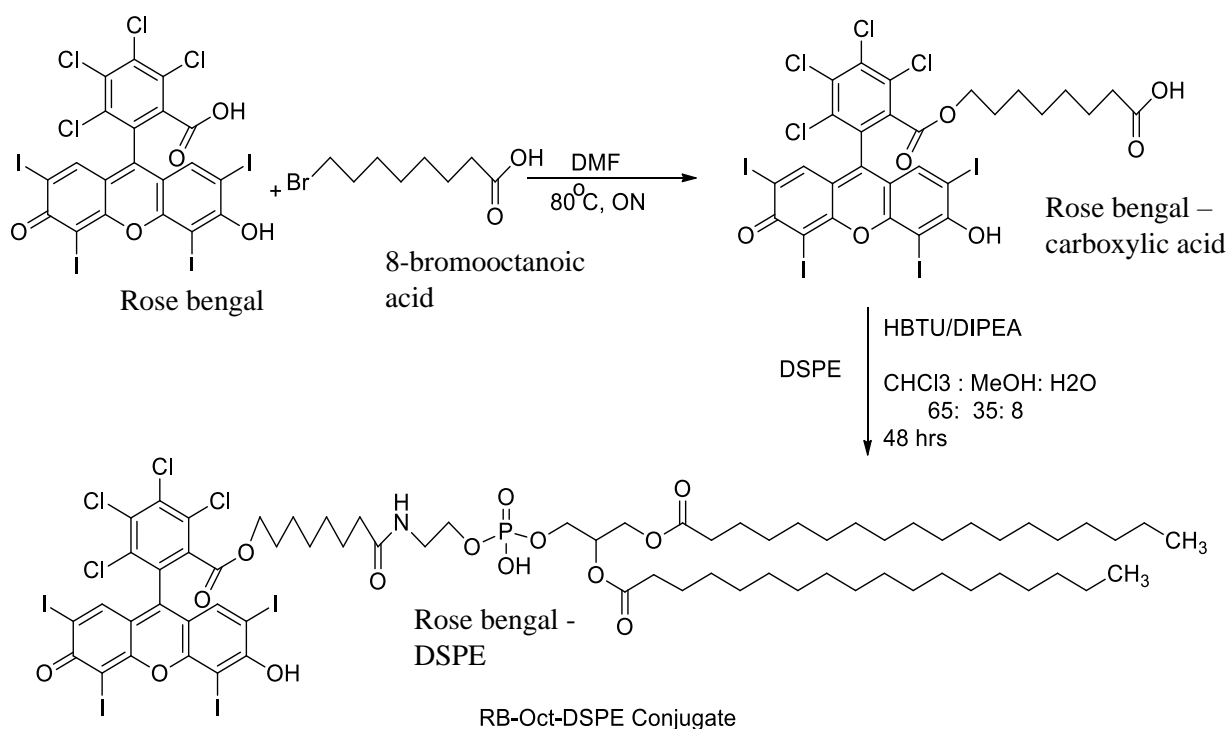
The aim of the work described in this chapter was to develop a pre-MB suspension capable of conversion to DTX-MB-RB in a single step using the Vialmix® device. The specific objectives were:

1. To synthesise and characterise the RB modified phospholipid (RB-DSPE).
2. To develop a pre-MB formulation capable of generating DTX-MB-RB using the Vialmix® device.
3. To scale-up manufacture of the pre-MB formulation.
4. To determine stability of the pre-MB formulation under various storage conditions.

## 4.3 Results and discussion

### 4.3.1 Synthesis and Characterisation of RB-DSPE

Several methods are available for the modification of phospholipids with drug compounds. Logan et al. [221] used an enzymatic catalysed transphosphatidyltion reaction to attach gemcitabine to the lipid DBPC in a single pot approach [221]. Other fluorophore labelled lipids are available commercially such as NBD-DSPE with the fluorophore attached covalently to the amine group of DSPE [222]. A carboxylic functionalised Rose Bengal derivative (RB-COOH) has previously been prepared by Costley et al. [223] and has the capacity to form an amide bond with amine group of DSPE. Therefore, the synthetic protocol shown in Scheme 2 was developed for the preparation of RB-DSPE. This involved the preparation of RB-COOH by the reaction of RB with 8-bromooctanoic. The was then coupled with DSPE using a mixed solvent system ( $\text{CHCl}_3$ , MeOH and  $\text{H}_2\text{O}$  65:35:8) under the assistance of HBTU and DIPEA. Pure RB-DSPE was isolated following column chromatography and analysed using NMR and mass spectroscopy.



Scheme 4.1 Synthetic scheme for the manufacture of RB-DSPE.

The stacked  $^1\text{H}$ -NMR spectra of DSPE, RB-COOH and RB-DSPE are shown in Figure 4.3 in a mixed  $\text{CDCl}_3$  /  $\text{CD}_3\text{OD}$  solvent system to facilitate dissolution of all 3 compounds. Due to

the presence of the CD<sub>3</sub>OD, it was not possible to observe the exchangeable amine and carboxylic protons of DSPE and RB-COOH respectively, that were directly affected during the formation of RB-DSPE. However, the spectrum of RB-DSPE is consistent with its structure comprising resonances from both DSPE and RB-COOH, with some subtle differences in the chemical shifts of protons that were directly impacted by formation of the newly created amide bond. For example, the methylene protons  $\alpha$  to the amine group in DSPE were observed at 3.08 ppm, while the analogous protons in RB-DSPE shifted downfield to 3.40 ppm, because of their new chemical environment. Similarly, the methylene protons  $\alpha$  to the carboxylic acid group in RB-COOH (2.3 ppm) were observed at 2.15 ppm in RB-DSPE, again consistent with their new chemical environment. A resonance for the RB ring protons at 7.45 ppm was also observed in spectrum of RB-DSPE, just upfield of the CHCl<sub>3</sub> signal, that was absent in the spectrum of DSPE. The <sup>13</sup>C-NMR spectra of RB-COOH and RB-DSPE are shown in Figure 4.4 with the most observable structural change being the carbonyl group of the carboxylic acid in RB-COOH converting to an amide in RB-DSPE. This was reflected in the chemical shift of the carboxylic acid carbonyl observed at 163.5 ppm in RB-COOH moving downfield to 175.6 ppm in the spectrum of RB-DSPE. The MALDI-TOF mass spectrum, recorded in the positive mode, also confirmed the formation of RB-DSPE with the base peak at 1844.31 Da consistent with the expected mass of 1845.92 Da for C<sub>69</sub>H<sub>98</sub>NOCL<sub>4</sub>I<sub>4</sub>P. Together, these analyses confirmed the successful synthesis of RB-DSPE.

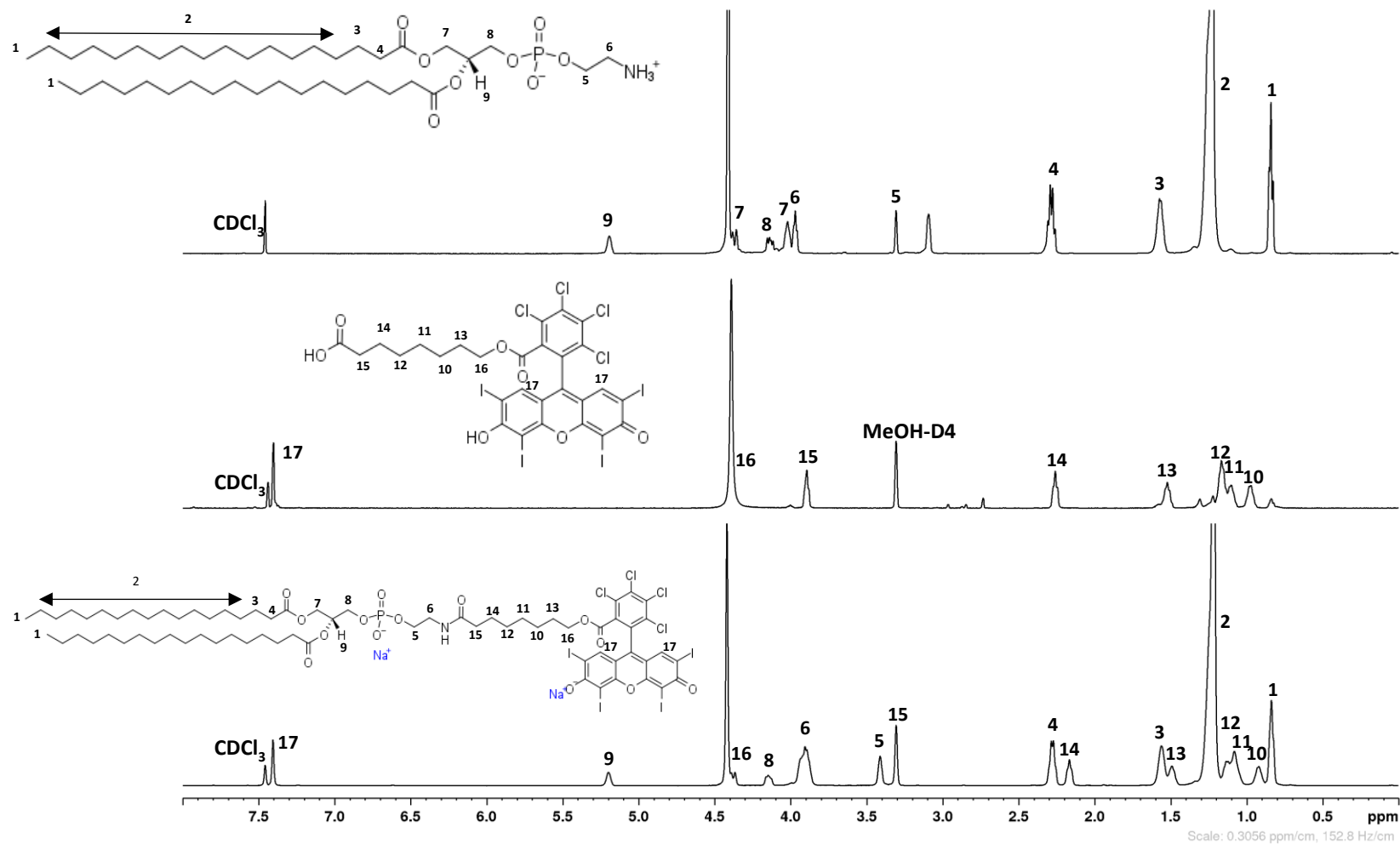


Figure 4.3 Stacked  $^1\text{H}$ -NMR for RB-DSPE.

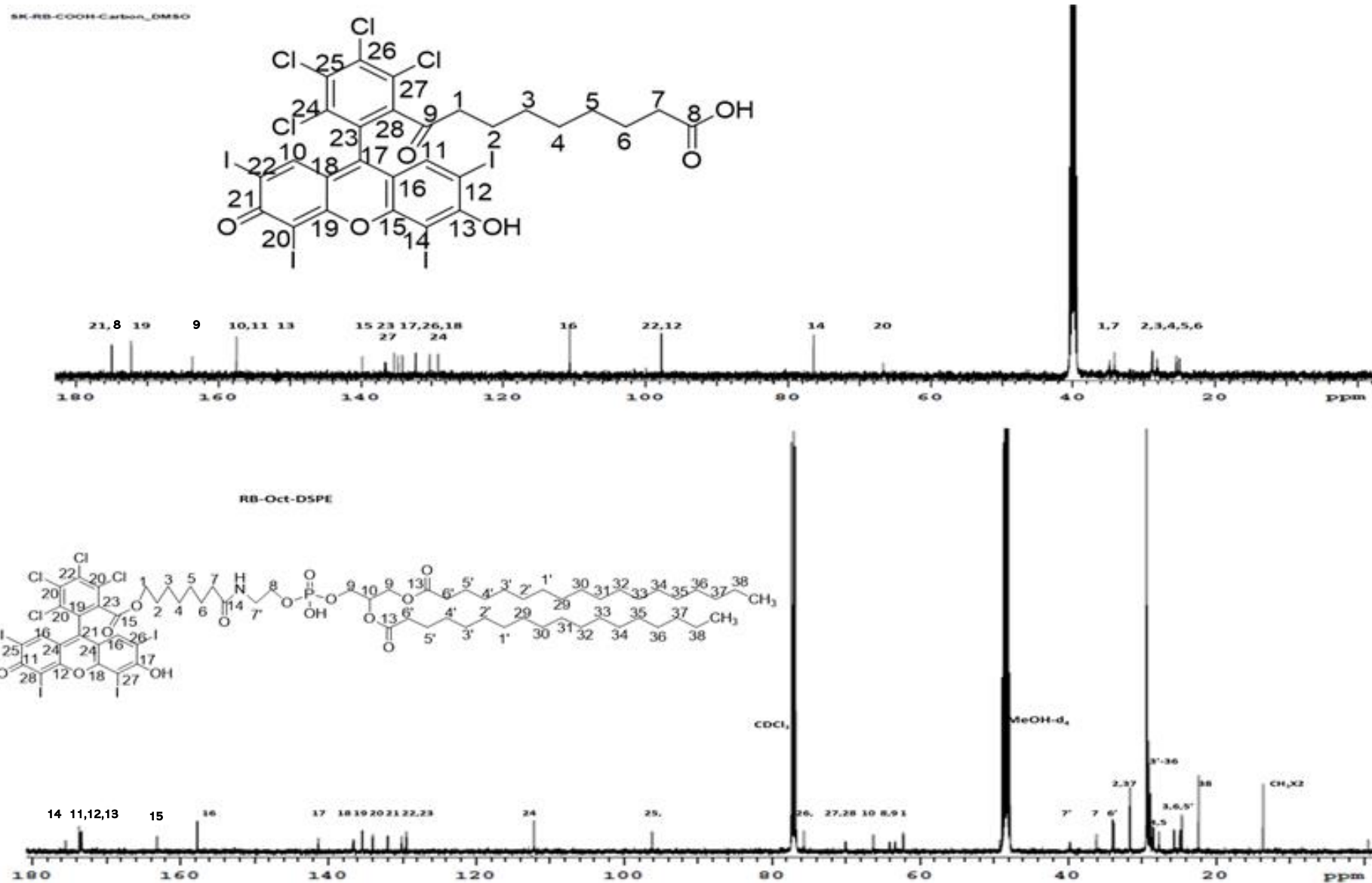


Figure 4.4  $^{13}\text{C}$ -NMR for RB-COOH (top) and RB-DSPE (bottom).



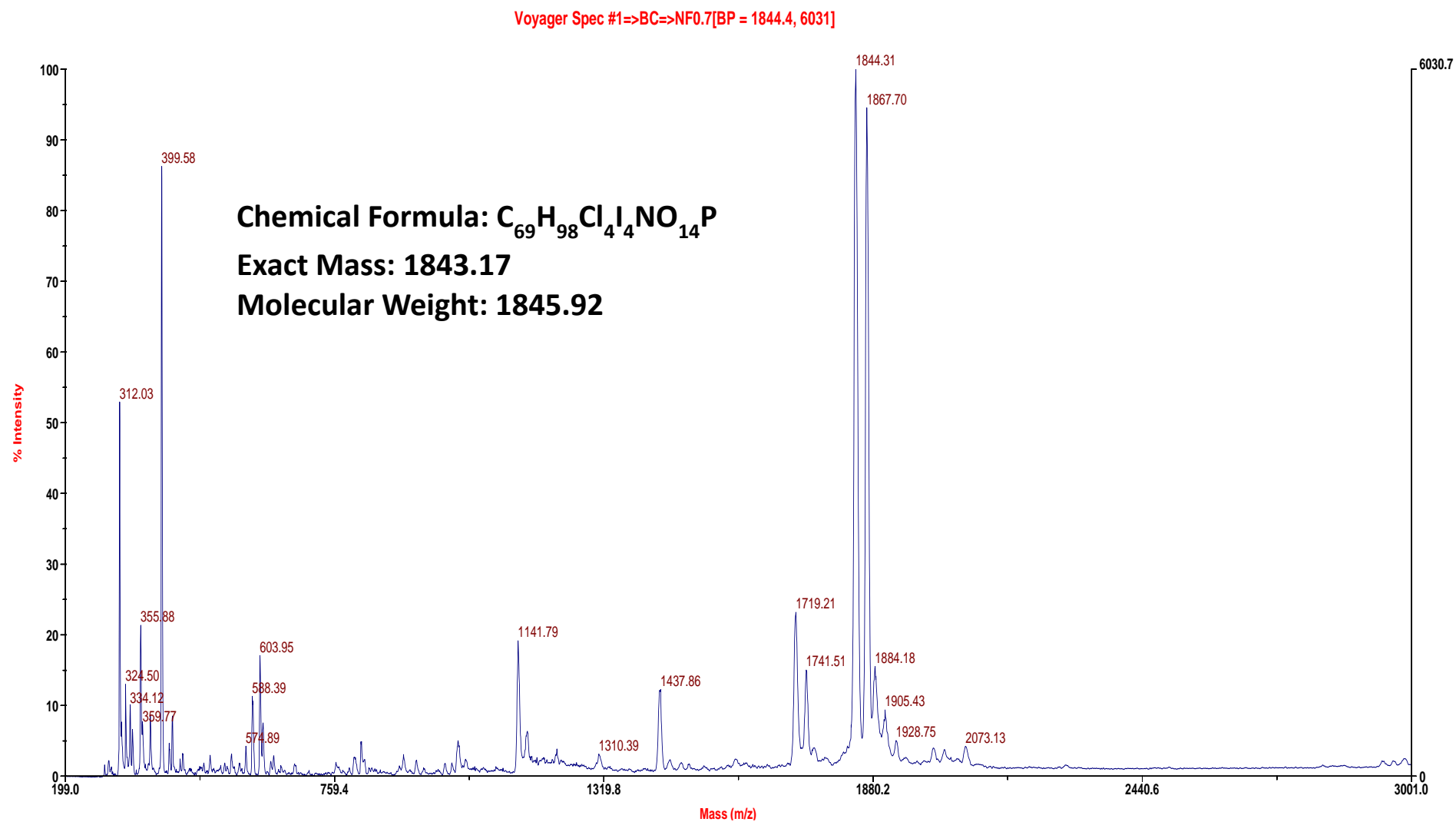


Figure 4.5 The MALDI-TOF spectrum of RB-DSPE.

#### **4.3.2 Preparation of a DTX-MB-RB from a pre-MB suspension**

Having successfully prepared the RB-DSPE lipid, the next step was to develop a method to produce DTX-MB-RB from a pre-MB colloidal suspension containing DTX, DBPC, DSPE-PEG, RB-DSPE and cholesterol. Cholesterol was included in this formulation as it has been shown to improve the lipid stacking within the MB shell [224]. The protocol for preparing the DTX-MB-RB formulation is shown in Figure 4.7 and was the same as that used in Chapter 3 up to the final MB generation step. In chapter 3, this was undertaken using sonication under a constant flow of PFB to generate the non-RB conjugated MBs, with RB added subsequently using the avidin-biotin interaction. Using the revised method, the colloidal suspension (caption 4, Figure 4.7) was transported to a 2mL Vialmix® vial and sealed under an atmosphere of PFB gas. The vials were either stored at fridge temperature or subsequently loaded into a vial mix shaker and shaken for 45 seconds forming DTX-MB-RB. Once the MBs were formed, they were imaged using optical microscopy and the MB size / concentration determined using MATLAB.

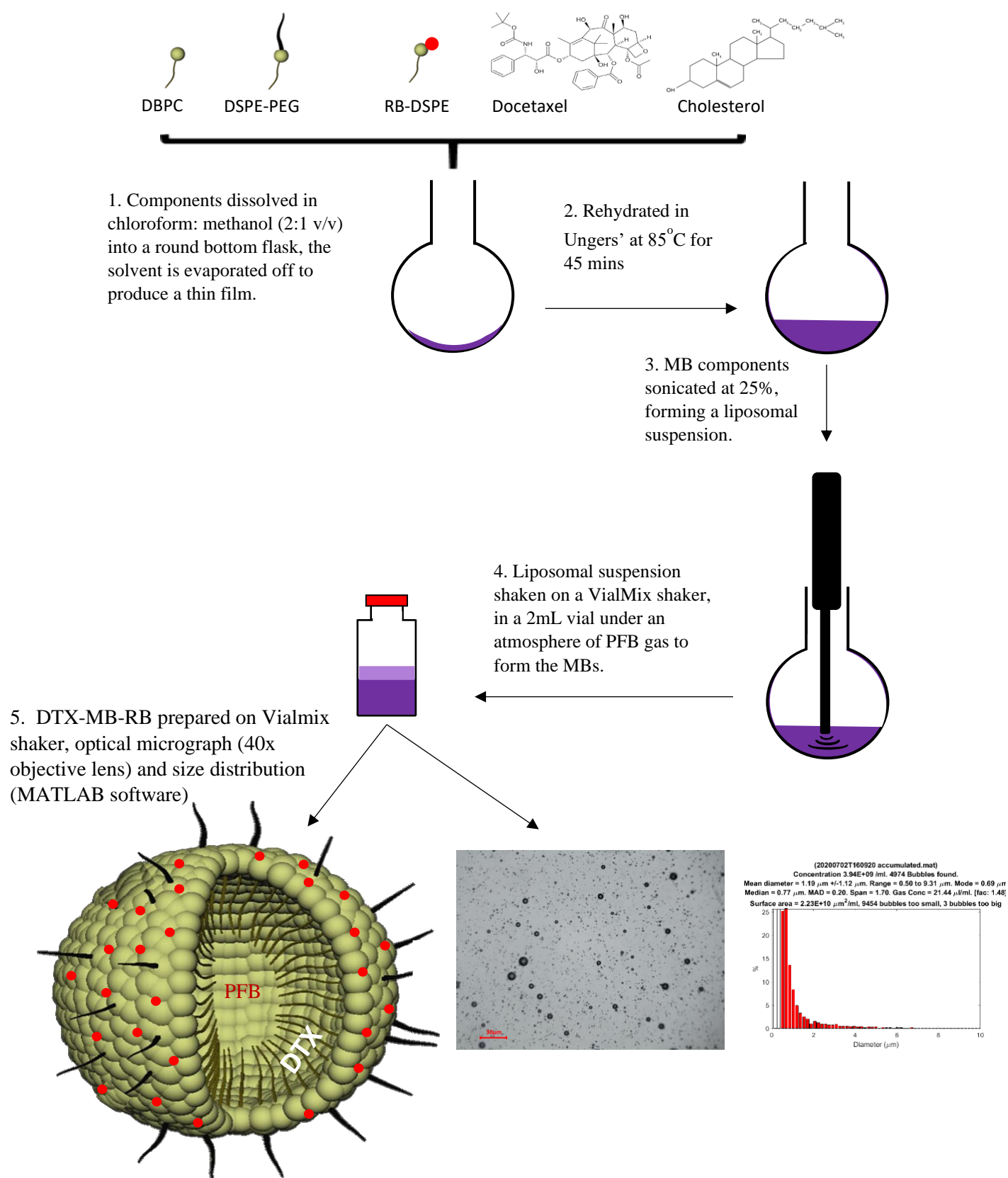


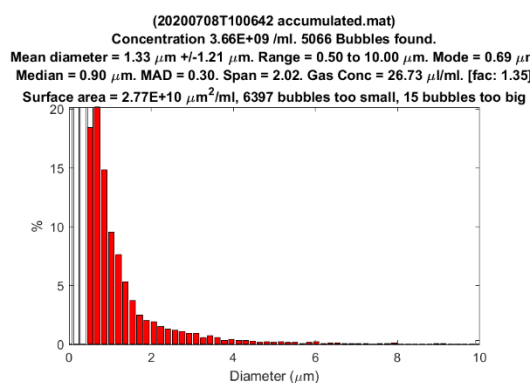
Figure 4.6 Production of DTX-MB-RB using the revised VialMix® method.

The ratio of constituents was varied in an attempt to maximise the amount of the drugs present within the MBs but not to compromise the physical characteristics of the DTX-MB-RB formulation (i.e., flowability, size and MB number). A range of conditions were employed, varying the mol% of RB-DSPE from 25% to 40% and DTX from 10% to 20%. To compensate, the amount of DBPC and DSPE-PEG(2000) was altered. The various formulations tested are shown in Table 4.1 and a representative optical micrograph, size distribution and digital photograph of the DTX-MB-RB formulation provided for each formation shown in Figure 4.7.

Table 4.1 Composition of components (mol%) for formulations a-g.

Formulation	DBPC	RB-DSPE	DTX	DSPE-PEG(2000)	Cholesterol
<b>A</b>	30	40	10	10	10
<b>B</b>	40	20	20	10	10
<b>C</b>	40	25	15	10	10
<b>D</b>	30	30	15	15	10
<b>E</b>	25	35	20	10	10
<b>F</b>	27.5	37.5	15	10	10
<b>G</b>	30	37.5	12.5	10	10

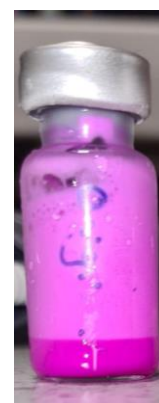
a) i)



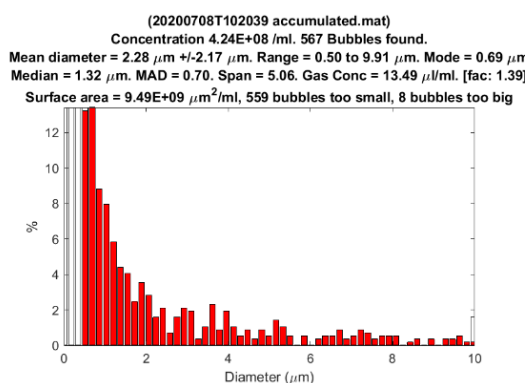
ii)



iii)



b) i)



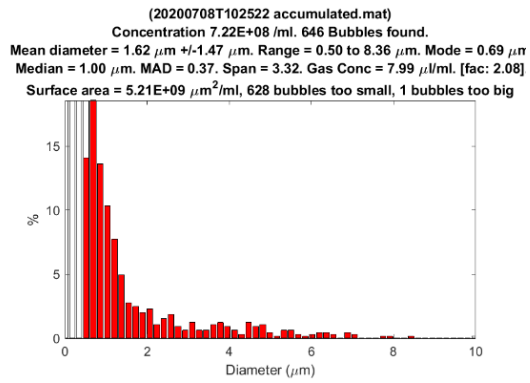
ii)



iii)



c) i)



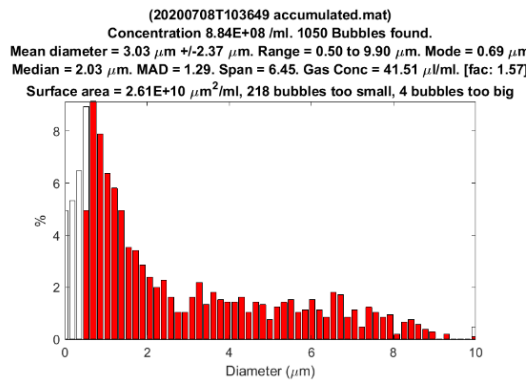
ii)



iii)



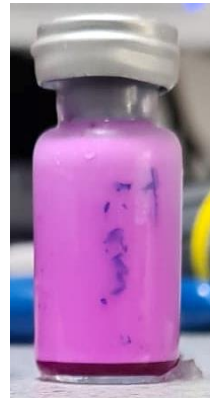
d) i)



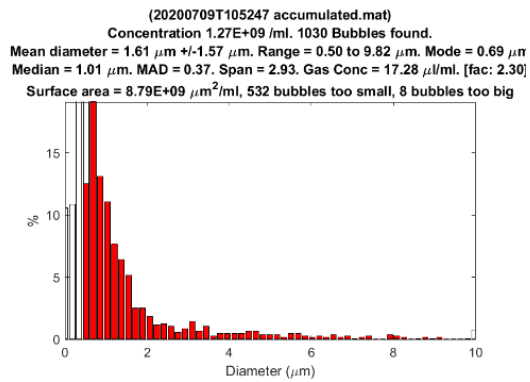
ii)



iii)



e) i)



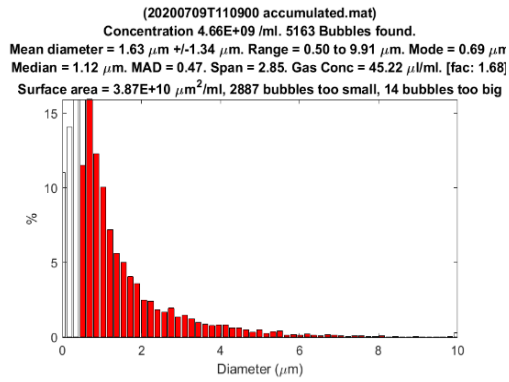
ii)



iii)



f) i)



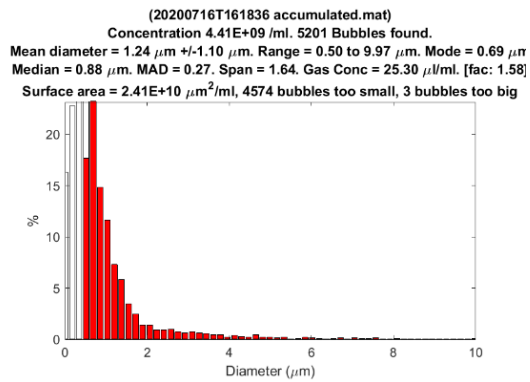
ii)



iii)



g) i)



ii)



iii)



Figure 4.7 Formulations a-g with i) size distribution, b) optical micrograph (40x objective lens) and iii) sample image of MB cake in vial.

A summary of the results are shown in Table 4.2 and indicate that formulations F and G were best in terms of MB number ( $4.476 \times 10^9/\text{mL}$  and  $5.250 \times 10^9/\text{mL}$ ), size ( $1.595 \mu\text{m} \pm 1.41 \mu\text{m}$  and  $1.465 \mu\text{m} \pm 1.24 \mu\text{m}$ ) and both flowed well with little foam evident. However, the pre-MB colloidal suspension for formulation F was observed to be cloudy suggesting some precipitation of the DTX. This was attributed to the higher mol% of DTX (15%) and was not observed for formulation F where the DTX mol% was 12.5%. (Figure 4.8).

Therefore, formulation G was chosen as the preferred pre-MB colloidal formulation as it maximised the DTX loading and produced MBs with physical characteristics suitable for use in subsequent *in vitro* and *in vivo* experiments.

Table 4.2 The bubble size ( $\mu\text{m}$ ), bubble number ( $\times 10^9/\text{mL}$ ) and flowability ranked 1-3. 1 = Static, 2 = moderate flow and 3 = freely flows.

Formulation	Bubble Size ( $\mu\text{m}$ )	Bubble Number ( $\times 10^9/\text{mL}$ )	Flowability
A	$1.325 \pm 1.21$	3.350	2
B	$2.250 \pm 2.15$	0.381	1
C	$1.600 \pm 1.47$	0.450	1
D	$2.890 \pm 2.38$	0.866	1
E	$1.440 \pm 1.35$	2.170	1
F	$1.595 \pm 1.41$	4.476	3
G	$1.465 \pm 1.24$	5.250	3

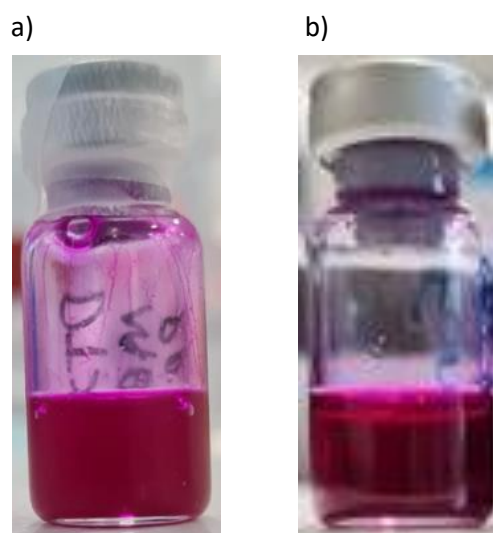


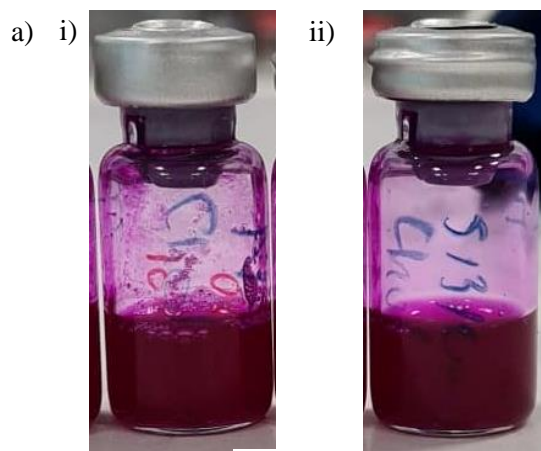
Figure 4.8 Images of pre-MB colloidal formulation a) formulation F and b) formulation G.



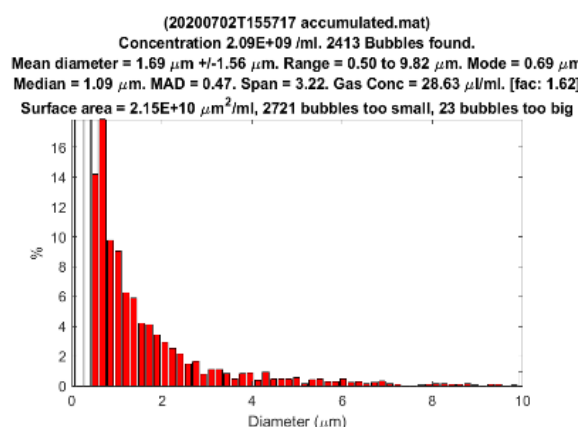
### 4.3.2.1 Determining optimum temperature for storage of the pre-MB colloidal suspension

One of the benefits of using the pre-MB colloidal suspension approach is the potential for the suspension to be prepared well in advance of being needed and activating as and when required. However, it is important to confirm that the quality of the MBs generated is not compromised. Therefore, the quality of DTX-MB-RB were assessed when activated with the Vialmix 1-week following their preparation and storage at either room temperature (20°C) or fridge temperature (5°C).

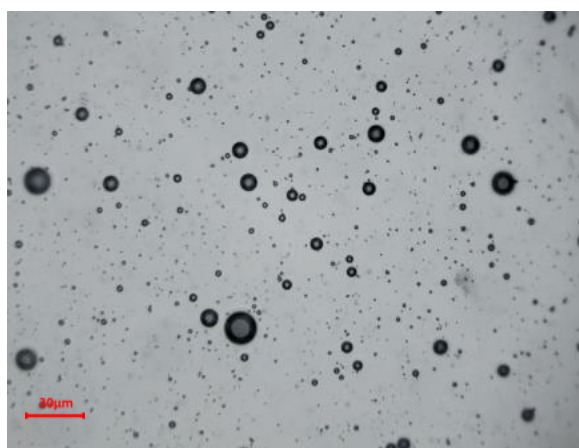
Photographs of the pre-MB colloidal suspension were taken after the week-long storage and are shown in Figure 4.9 a. Storage at room temperature produced a slightly cloudier colloidal suspension than the vial stored in the fridge which was optically transparent. Following activation using the Vialmix, the DTX-MB-RB produced for both storage conditions were acceptable in terms of physical characteristics (Table 4.3). However, the DTX-MB-RB produced from the suspension stored in the fridge were almost twice in number (Figure 4.10). Given the improvement in MB number and optical transparency of the pre-MB suspension, it was concluded that the most optimum storage conditions for the pre-MB colloidal suspension was 5°C.



b) i)



ii)

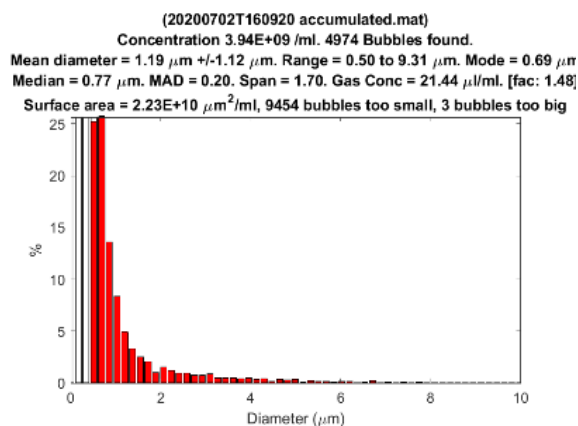


iii)

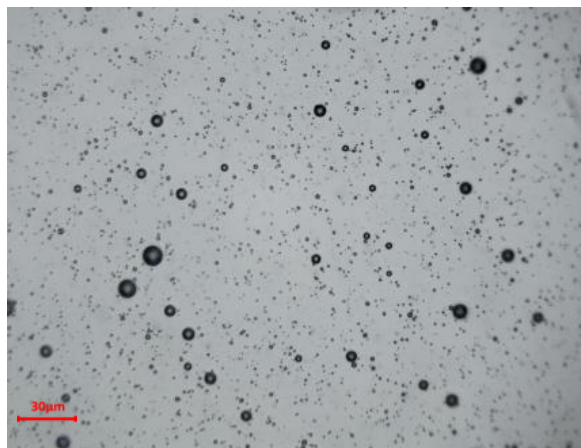




c) i)



ii)



iii)



Figure 4.9 Images of a) pre-MB suspension for vials stored at i) room temperature and ii) in the fridge. The corresponding MB cakes for the pre-MB suspensions stored at b) room temperature and c) in the fridge and i) representative size distribution and ii) 40x optical micrograph and iii) MB cake in the vial.

Table 4.3 The bubble size ( $\mu\text{m}$ ), bubble number ( $\times 10^9/\text{mL}$ ) and flowability ranked 1-3. 1 = Static, 2 = moderate flow and 3 = freely flows.

Storage temperature (°C)	MB number ( $\times 10^9/\text{mL}$ )	MB size ( $\mu\text{m}$ )	Pre-MB suspension clearness	Flowability
20	2.01	$1.48 \pm 1.37$	Clear	3
5	3.62	$1.22 \pm 1.18$	Clear	3

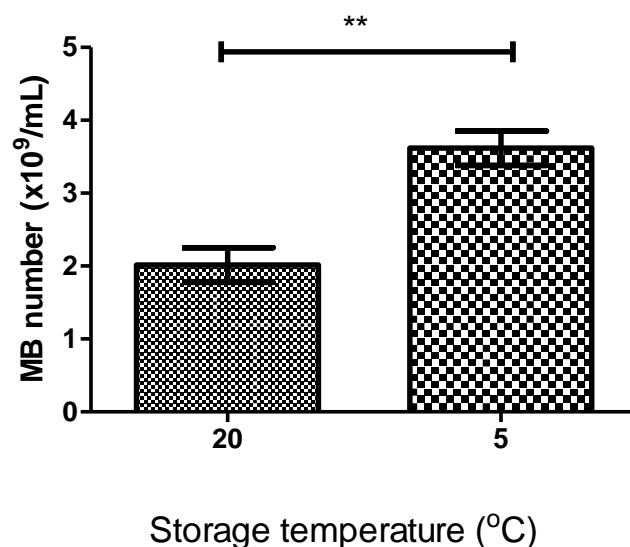


Figure 4.10 The bubble numbers for the batches stored at room temperature and fridge temperature.

#### 4.3.3 Scaling up manufacture of Pre-MB colloidal suspension

Having ensured that the pre-MB colloidal suspension can be stored for at least 1 week and still generate quality DTX-MB-RB, the next step was to determine if manufacture could be scaled up so that enough supply could be prepared well in advance of any planned treatments. Unfortunately, the dimensions of Vialmix vials are fixed and enable a 1 mL volume of MBs to be prepared each time. During the development work described in the preceding sections, 2 mL batches of the pre-MB colloidal suspension were prepared and aliquoted into two 1 mL Vialmix vials.

Instead of producing 2 mL of the pre-MB colloidal suspension, the reaction was scaled up 5-fold to a 10 mL batch size using a 25 mL round-bottomed flask compared to a 5 mL round-bottomed flask. All the other conditions employed for the 2 mL batch were maintained (i.e., temperature, sonication etc) while the Ungers solution vehicle was increased to 10 mL. The pre-MB colloidal suspension generated from this approach is shown in Figure 4.11 and appear much cloudier than observed for the 2 mL batch. To overcome this issue, the process was repeated but due to the increased volume used, the rehydration step was modified by heating at 90°C for 60 min instead of 85°C for 45 min. In addition, the subsequent sonication step was

also increased to 120 sec from 90 sec. These changes were effective and produced a transparent colloidal pre-MB suspension, consistent with the appearance of the 2 mL batch (Figure 4.12). Vials of the suspension were stored at 5°C for 7 days to ensure they were stable for at least 1 week and the appearance remained unchanged. The vials were then converted to DTX-MB-RB using the Vialmix and their physical properties analysed.



Figure 4.11 Image of the pre-MB colloidal suspension vial following scale-up of formulation 6.

The results are shown in Figure 4.13 for the 2 batches and again the parameters were consistent with the 2 mL batch with average MB sizes of  $1.05\mu\text{m} \pm 0.67\mu\text{m}$  and  $1.03\mu\text{m} \pm 0.49\mu\text{m}$  and MB concentrations of  $5.26 \times 10^9/\text{mL}$  and  $4.06 \times 10^9/\text{mL}$ . Therefore, it was deduced that the scale-up method was successful and could produce ten 1 mL vials of pre-MB colloidal suspension with at least 1 week stability that could be used to quickly generate DTX-MB-RB when needed for use in treatments.

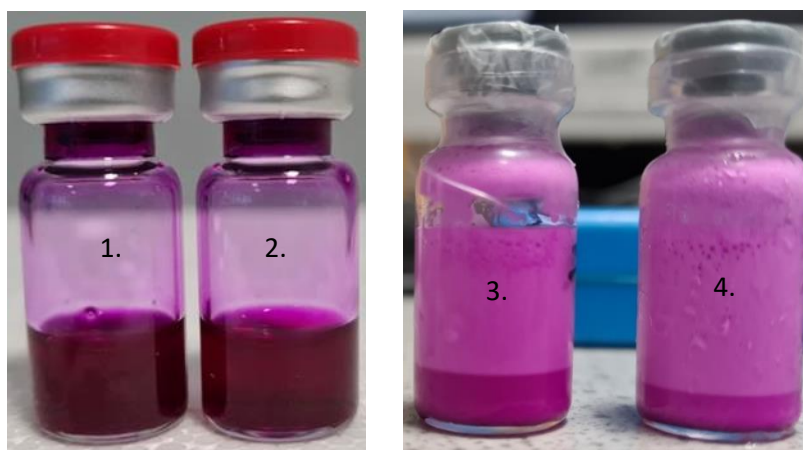


Figure 4.12 Image of vials rehydrated at 90°C for 60 mins. Pre-MB suspension 1 & 2 and the corresponding MB cakes 3 & 4.

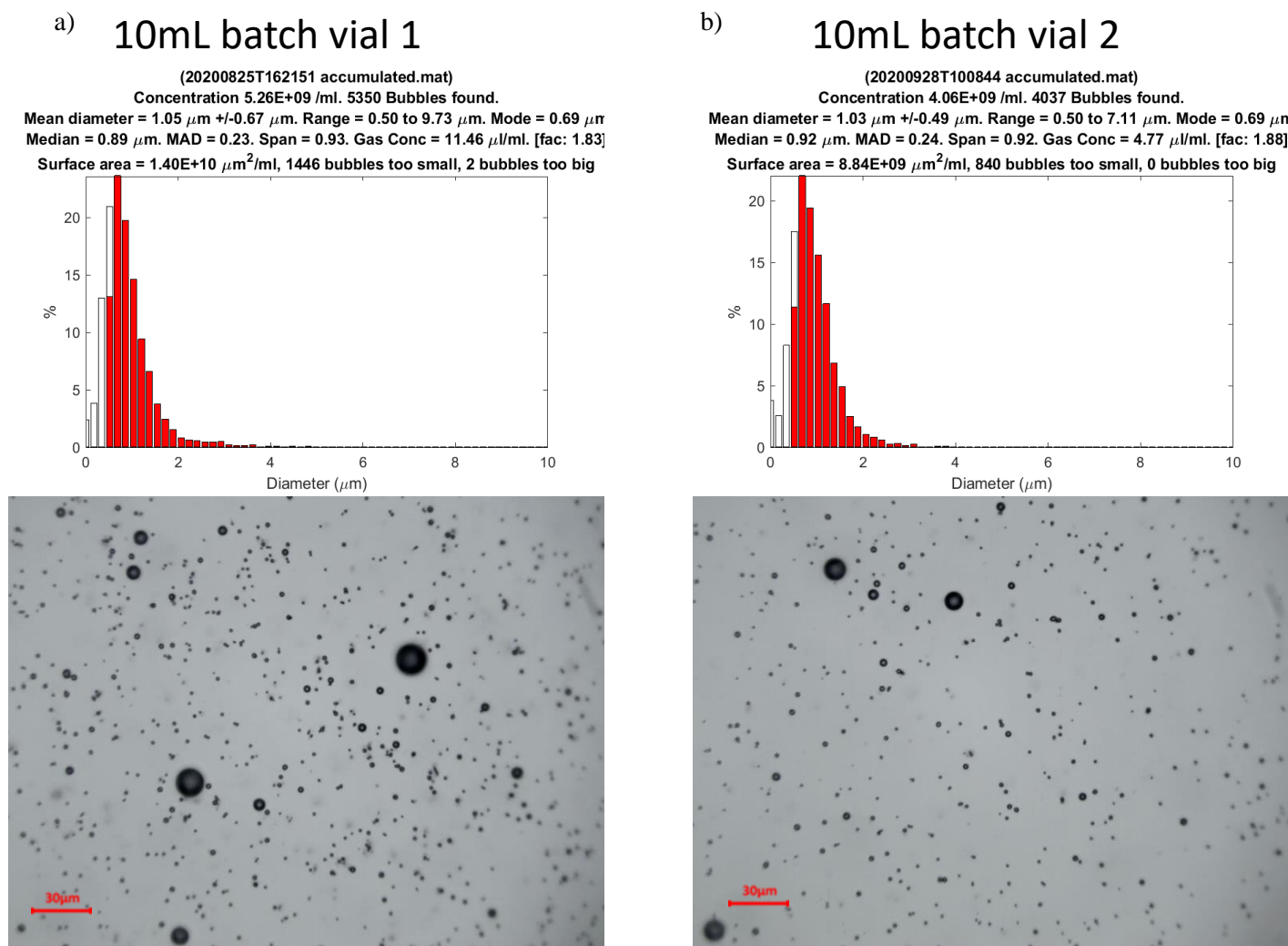


Figure 4.13 Size distributions and optical micrographs for each repeat of the scaled batch.

#### 4.3.4 Extended stability of the Pre-MB colloidal suspension at 5°C.

The commercial contrast agent DEFINITY® has a shelf-life of 24 months enabling the production of bulk quantities of the pre-MB colloidal suspension thereby reducing manufacturing costs. Given the timeline of this PhD project it was not possible to test over such a duration, but 3 months was identified as an appropriate timepoint that would provide a good indication of long-term stability. Using the scale-up protocol discussed in 4.3.3, 15 1mL vials of the DTX-MB-RB pre-MB suspension were prepared and 6-vials each stored for 0, 1, 2 or 3 months. The same 3 vials were sampled and analysed at each time point by DLS to determine if the mean particle diameter of the pre-MB colloidal suspension changed with time. The

remaining 12 vials were converted to MBs using the Vialmix device and the MB concentration, mean MB diameter and physical appearance determined for each storage time point.

DLS traces of the pre-MB colloidal suspensions at the various timepoints are shown in Figure 4.14. There was some heterogeneity in the particle size at all the time points tested with some of the vials showing only one main peak with others displaying several peaks across different size ranges. However, there was no apparent trend in the polydispersity with storage time. This variability in particle size was not unexpected as no size separation or extrusion steps were undertaken with these particles and a range of different vesicle types would be expected. When the mean particle size was calculated for the three batches at each time point, no trend was observed and any differences between the time points were deemed statistically non-significant.

The next step was to determine the quality of MBs generated from the pre-MB colloidal suspensions stored at the various time-points. The mean MB concentration and mean MB diameter were determined for the 3 batches at each timepoint following Vialmix activation. Representative optical micrographs and size distribution plots can be observed in Figure 4.16. The results are plotted in Figures 4.17 and 4.18 and extremely consistent data was observed over the 4 timepoints with a mean MB diameter of approximately 1.2  $\mu\text{m}$  and a mean MB concentration of approximately  $4.5 \times 10^9$  MB/mL. Any minor differences between the different timepoints were deemed statistically non-significant and no difference in the physical appearance was observed.

Therefore, the conclusion from the results of this stability study confirm that the quality of DTX-MB-RB generated from the pre-MB colloidal suspension was of acceptable quality after 3 months storage at 5°C.

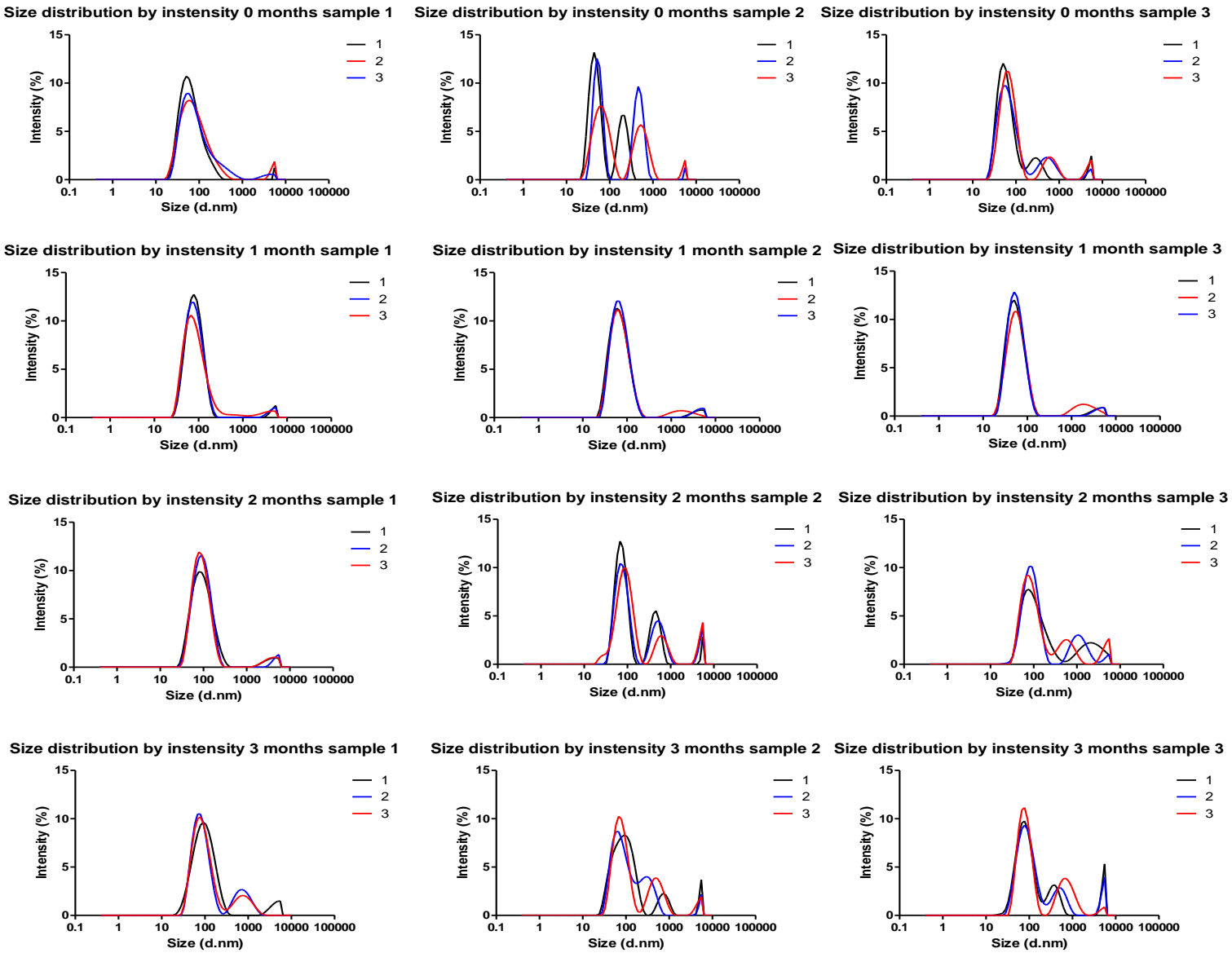


Figure 4.14 Size of liposomes after 3-month fridge storage.

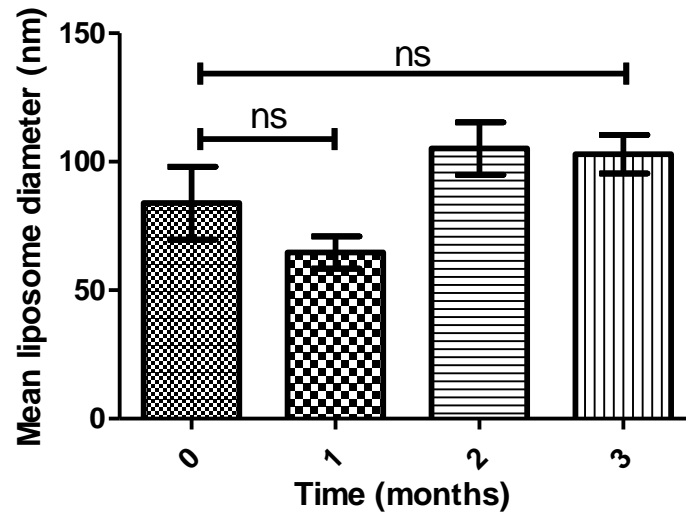


Figure 4.15 Effect on liposome size determined by DLS analysis of the DTX-MB-RB after 3-month fridge storage (n=3).

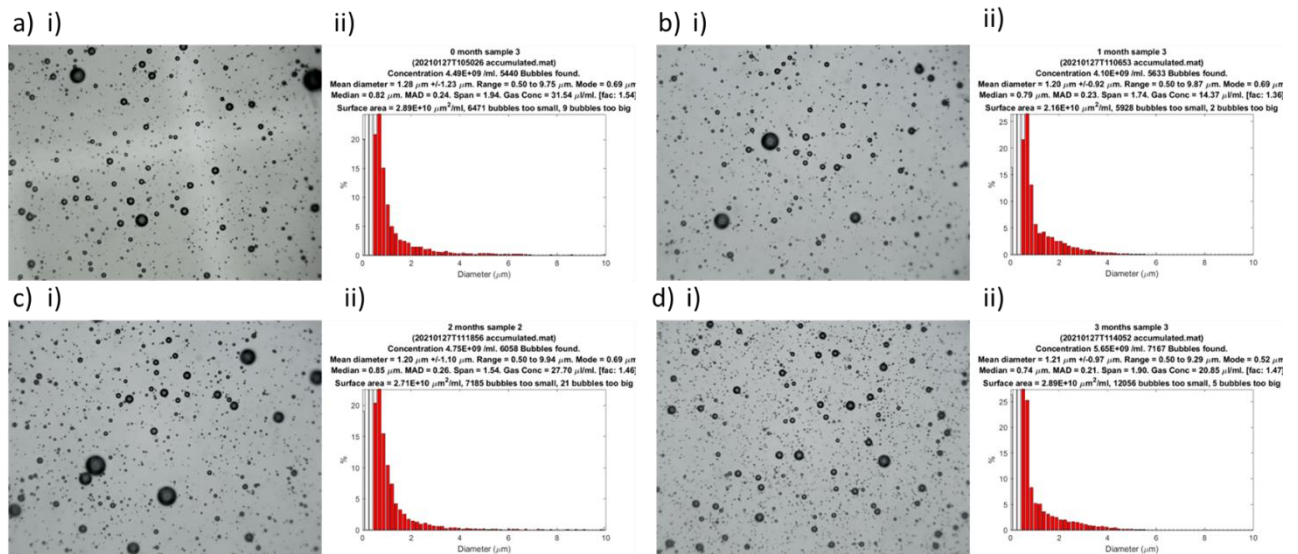


Figure 4.16 Optical micrographs i) and size distribution plots ii) of DTX-MB-RB generated from pre-MB suspensions stored for a) 0 months, b) 1 month, c) 2 months and d) 3 months.

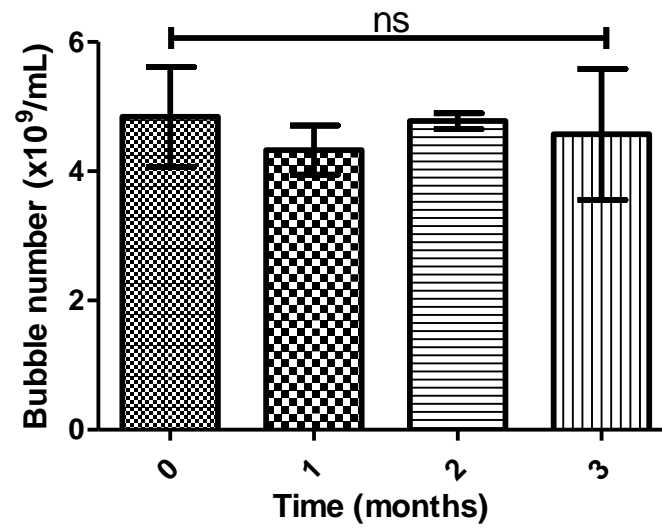


Figure 4.17 The effect on bubble number on DTX-MB-RB after 3-month fridge storage (n=3).

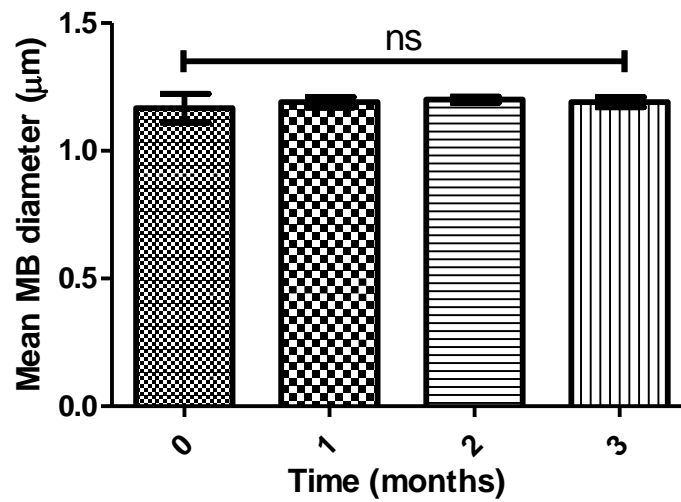


Figure 4.18 The effect on bubble size on DTX-MB-RB after 3-month fridge storage (n=3).



#### 4.3.5 Preparation of Blank MB, DTX-MB, and MB-RB formulations.

To properly evaluate the efficacy of UTMD mediated DTX-MB-RB prepared from the pre-MB colloidal suspension, it is beneficially to assess the relative contribution of each individual component. For example, the use of blank MBs (i.e., no drugs attached) would enable the contribution from MB cavitation to be determined in any efficacy study. Similarly, DTX-MB and MB-RB preparations would enable the individual contribution of UTMB mediated chemotherapy and SDT respectively to be determined.

As these formulations lack one or more of the active components in DTX-MB-RB, the constituents used to prepare the blank MB, DTX-MB and MB-RB were modified accordingly (Table 4.4). The initial attempts at preparing blank MB and DTX-MB involved replacing RB-DSPE with DSPE but the quality of the MBs produced (i.e concentration & size) was unacceptably poor ( $1.41 \times 10^9/\text{mL}$  and  $8.69 \times 10^8/\text{mL}$  respectively) (Figure 4.19). However, substituting RB-DSPE with DSPC improved the quality of blank MB and DTX-MB with MB concentrations of  $1.25 \times 10^{10}/\text{mL}$  and  $6.67 \times 10^9/\text{mL}$  respectively and mean MB diameters of  $1.66 \mu\text{m} \pm 1.40 \mu\text{m}$  and  $1.24 \mu\text{m} \pm 0.99 \mu\text{m}$  respectively (Table 4.4). Representative images of the MB suspension, optical micrograph, and size distribution for the blank-MB and MB-DTX are presented in Figure 4.20. The substitution of DSPC for DSPE in these formulations incorporates a choline headgroup into the MB shell instead of a primary amine. The permanent positive charge on the choline most likely makes the lipid more amphiphilic and may assist with the stability of the MBs, thus producing acceptable MB size and concentrations. Interestingly, Rose Bengal is also charged and using RB-DSPE in place of DSPC was effective in producing MB-RB with a mean MB diameter of  $1.13 \pm 1.06 \mu\text{m}$  and MB concentration of  $7.89 \times 10^9/\text{mL}$  (Figure 4.20)

Table 4.4 Composition of components (mol%) for formulations blank MBs, DTX-MBs and MB-RBs.

Formulation	DBPC (%)	RB-DSPE (%)	DSPC (%)	DTX (%)	DSPE-PEG(2000) (%)	Cholesterol (%)
Blank MBs	33	0	44	0	11.5	11.5
DTX-MBs	28.75	0	38.75	12.5	10	10
MB-RBs	33	44	0	0	11.5	11.5

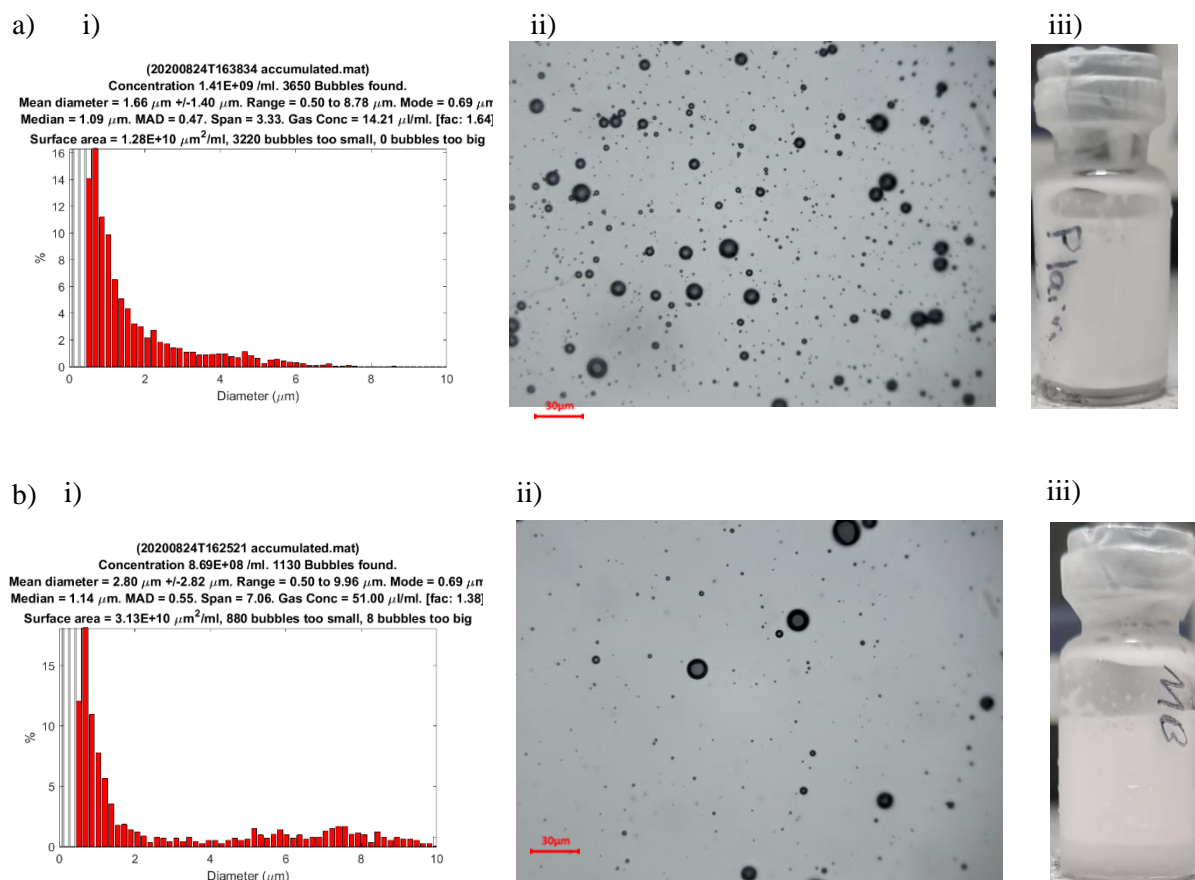


Figure 4.19 Batches of a) blank MBs and b) DTX-MBs made with DSPE as a replacement for DBPC showing i) size distribution, ii) optical micrograph of MBs and iii) image of the vial.

Table 4.5 MB size and MB number for control formulations blank MBs, DTX-MBs and MB-RBs.

Formulation	MB size ( $\mu\text{m}$ )	MB number ( $\times 10^9/\text{mL}$ )
Blank MBs	$1.66 \pm 1.40$	11.25
DTX-MBs	$1.24 \pm 0.99$	6.67
MB-RBs	$1.13 \pm 1.06$	7.68

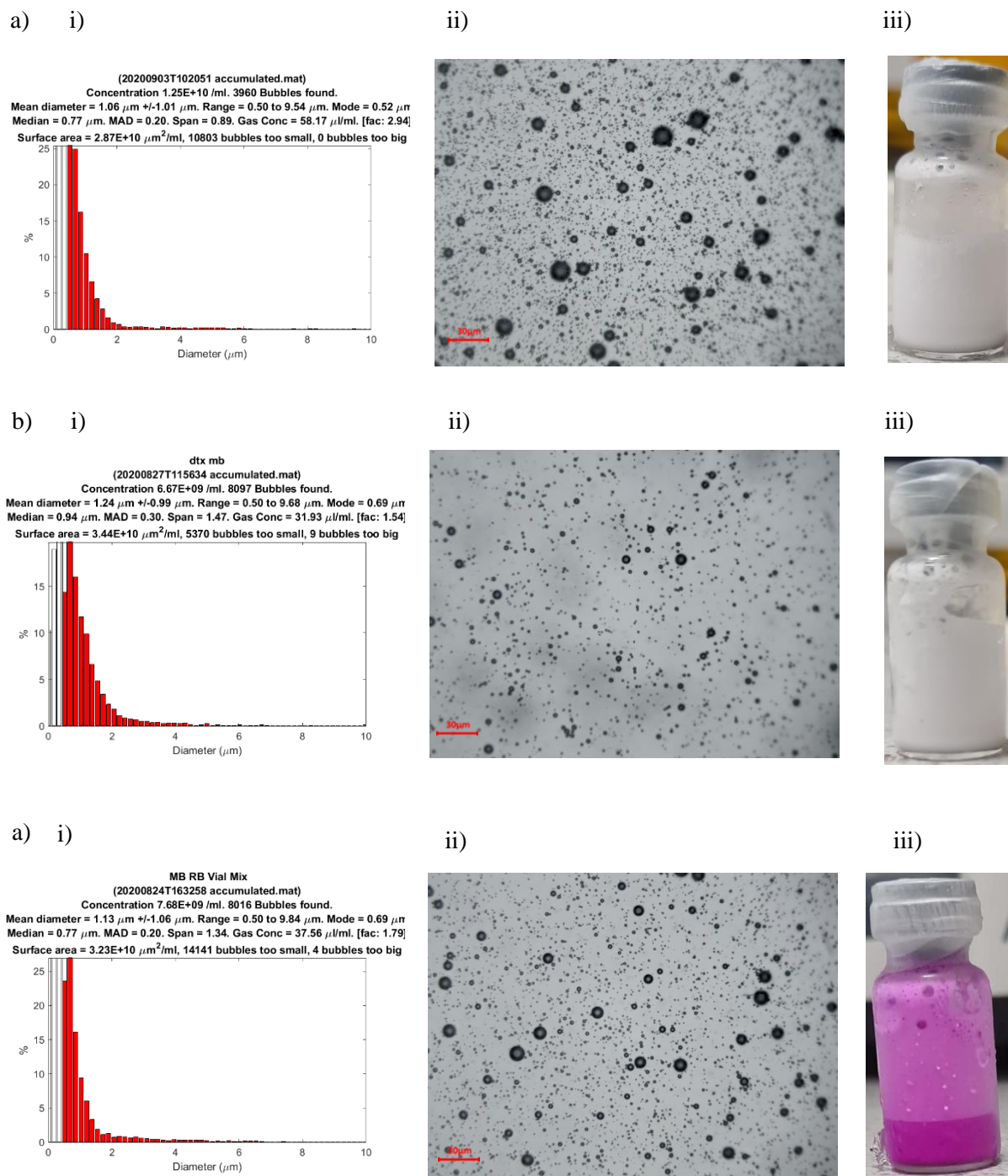


Figure 4.20 Formulations blank MBs, DTX-MBs and MB-RBs with i) size distribution, b) optical micrograph (40x objective lens) and iii) sample image of MB cake in vial.

#### 4.3.6 Stability of Blank MB, DTX MB, MB-RB and DTX-MB-RB at 37°C.

The stability of DTX-MB-RB was assessed alongside the Blank MB, DTX MB, MB-RB formulations at body temperature (37.5°C) using a similar approach as discussed in section 3.3.2.4. The results are shown in Figure 4.21 and reveal the concentration of the DTX-MB-RB decreased steadily to 35.43% after 90 mins. In contrast, Blank MB, DTX MB, MB-RB reduced by 37.4, 8.6 and 64.6% over the same timepoint. This reduction for DTX-MB-RB was significantly greater than for DTX-MB-RB prepared using the biotin-avidin approach in 3.3.2. One potential reason for this may be that the MBs prepared using the biotin-avidin approach are washed several times and this removes a lot of less stable larger MBs. However, while a 64% reduction in MB number may appear a substantial number, from a starting concentration of  $\sim 7.00 \times 10^9$  MB/mL,  $2.52 \times 10^9$  MB/mL would still be remaining after 90 min. In addition, when undertaking UTMD, US is applied during injection to disrupt as many MBs as possible during the first few passes through the circulation. Therefore, the relevance of the 90 min timepoint could be questioned timescales of up to 10 min may be more realistic.

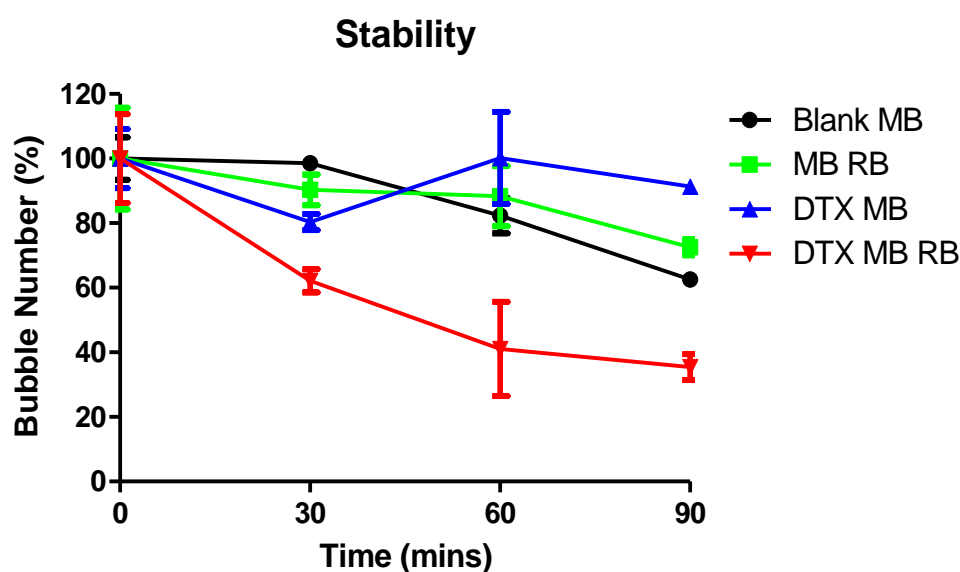


Figure 4.21 Plot of percentage bubble number (%) of blank MBs, MB-RB, DTX-MB, and DTX-MB-RB over 90 min. (N=3)

#### **4.4 Conclusion**

DTX-MB-RB were successfully prepared from a pre-MB colloidal suspension of phospholipids, cholesterol and DTX. This was made possible by the synthesis of the Rose Bengal modified phospholipid RB-DSPE. The inclusion of cholesterol was deemed critical to the stability of the pre-MB colloidal suspension. With careful optimisation of the vessel dimensions, thin film hydration temperature and sonication intensity / time, it was possible to scale the batch size 5-fold from the standard 2 mL to 10 mL. The pre-MB colloidal suspension was deemed stable at 5°C for at least 3 months producing DTX-MB-RB of acceptable quality. While the stability of the DTX-MB-RB at 37°C was reduced when compared to those prepared using the avidin-biotin approach, this should not be detrimental for their use in UTMD applications. Blank MB, DTX-MB and RB-MB formulations were also prepared to enable the efficacy of UTMD mediated chemo-SDT using the DTX-MB-RB to be properly evaluated in chapter 5.

The development of a scalable method to produce stable DTX-MB-RB that are generated at the point of use using the Vialmix device is hugely beneficial when considering potential clinical translation of this technology. Chapter 5 will determine the efficacy of UTMD mediated chemo-SDT treatment using this formulation in pre-clinical models of prostate cancer.

## **Chapter 5:**

**UTMD mediated Chemo-SDT Treatment of Androgen Sensitive and Insensitive Models of Prostate Cancer using DTX-MB-RB Prepared from a Pre-MB Colloidal Suspension.**

## 5.1 Introduction

Having successfully developed a facile method for the preparation of DTX-MB-RB from the corresponding pre-MB colloidal suspension in Chapter 4, the next step was to determine its effectiveness and safety profile when used to treat pre-clinical models of prostate cancer. Patients with recurrent disease following treatment with definitive radiotherapy and / or ADT have been identified as the target group of patients that would most benefit from UTMD mediated DTX-MB-RB treatment. If the treatment proved successful in this group of patients it could also be trialled as first-line therapy in place of radiotherapy. Therefore, both androgen sensitive and resistant pre-clinical prostate cancer models were needed to assess the UTMD mediated DTX-MB-RB treatment.

In this chapter, UTMD mediated DTX-MB-RB treatment was assessed in LNCaP (androgen sensitive) and DU145 (androgen insensitive) 3D spheroids models of prostate cancer. Different cell lines were chosen to establish ectopic tumours for the *in vivo* murine efficacy experiments as it proved difficult to establish LNCaP and DU145 tumours. Therefore, androgen sensitive 22RV1 and androgen insensitive PC3 cell lines were used for the *in vivo* experiments.

The DU145 cell line was derived from a metastatic site on the central nervous system (CNS) of a prostate cancer patient [225]. DU145 is androgen insensitive, like the PC3 cell-line [226]. However, PC3 cells only form loose aggregates rather than compact spheroids without the presence of supplement to enhance the formation of the extracellular matrix. In contrast, DU145 cells are formed easily using 96-well ultra-low attachment (ULA) plates [227]. 22RV1, like LNCaP is also androgen sensitive, the 22Rv1 cell line was propagated in mice from the CWR22 cell line [228. 229].

In addition to the efficacy experiments, an *in vivo* localisation study was also undertaken to determine the effectiveness of UTMD at localising drug payloads at the tumour site. The NIR dye IR780 was incorporated within the MBs as a surrogate payload and whole-body fluorescence imaging used to monitor the relative fluorescence intensity in the murine tumours over time. A safety study was also undertaken in healthy non-tumour bearing animals to establish any potential adverse effects that may occur from administration of the DTX-MB-RB. Collectively, the results from these experiments should serve as a useful pre-clinical data package for the efficacy and safety of the DTX-MB-RB formulation.

## **5.2 Aims and objectives**

The main aim of the work undertaken in this chapter was to establish the efficacy of UTMD mediated chemo-SDT using the DTX-MB-RB prepared from the pre-MB colloidal suspension in androgen sensitive and resistant models of prostate cancer. The ability of UTMD to target delivery of the chemo-SDT to tumours and the tolerability of DTX-MB-RB in healthy animals was also determined.

The specific objectives were:

1. To determine the efficacy of UTMD mediated chemo-SDT using DTX-MB-RB prepared from a pre-MB colloidal suspension in LNCaP and DU145 3D spheroid models.
2. To determine the efficacy of UTMD mediated chemo-SDT using DTX-MB-RB prepared from a pre-MB colloidal suspension in PC3 and 22Rv1 murine models.
3. Identify the effect of chemo-SDT using DTX-MB-RB on the expression of key genes involved in prostate cancer progression.
4. To determine the effectiveness of UTMD to deliver drug payloads to prostate tumours in a murine model.
5. To determine the safety profile of DTX-MB-RB in healthy non tumour bearing mice.



## 5.3 Results and discussion

### 5.3.1 Efficacy of UTMD mediated chemo-SDT using DTX-MB-RB prepared from a pre-MB colloidal suspension in a LNCaP spheroid model of prostate cancer

LNCaP spheroids were prepared as described in section 2.12. Four days after seeding, the spheroids were allocated to groups for treatment as follows: untreated, blank MB + US, MB-RB, MB-RB + US, DTX-MB, DTX-MB + US, DTX-MB-RB, and DTX-MB-RB + US. Two different treatment doses were used: the first involved a DTX / RB dose of 8.33 $\mu$ M and 25 $\mu$ M respectively while in the second experiment the dose was doubled (i.e. [DTX] = 16.67 $\mu$ M and [RB] = 50 $\mu$ M). In the groups where US was applied, the US conditions were the same as those used in the Chapter 3 spheroid experiment. 24h following treatment, spheroids were collected and trypsinised to form a single cell suspension and cell viability determined using a MTT assay.

The results from the lower treatment dose are shown in Figure 5.1 a) and reveal that treatment with the blank MBs caused only a minor, non-statistically significant reduction of 12% in cell viability. The DTX-MB, MB-RB, and DTX-MB-RB treatments in the absence of US also produced minor non-statistically significant reductions of 11, 3 and 13% respectively. Cell viability reduced slightly upon the application of ultrasound with MB-RB + US reducing to 73% as a result of SDT and DTX-MB + US reducing to 76%, most likely due to better dispersion of the DTX into the spheroids. However, when spheroids were treated with DTX-MB-RB + US, cell viability reduced dramatically to 42% ( $p \leq 0.001$ ). This reduction in cell viability was greater than the additive effect of the independent DTX-MB + US and MB-RB + US treatments and suggests the two treatments (SDT and DTX chemotherapy) may be acting synergistically. One reason for this synergy could be that as US is applied soon after the DTX-MB-RB is added, and, as the lifetime and diffusion distance of ROS is short, SDT mediated cytotoxicity would be temporally much faster than DTX mediated damage. Therefore, SDT mediated damage could sensitise the cells to subsequent DTX exposure.

At the higher concentration of DTX and RB, DTX-MB and RB-MB produced no change in cell viability when compared to the untreated spheroids (101 and 100% respectively) in the absence of US. However, the viability of spheroids treated with MB-RB + US decreased significantly to 50% ( $p \leq 0.01$ ), compared to 73% at the lower concentration indicating a dose-dependent SDT effect. The viability of spheroids treated with DTX-MB + US were also

reduced (61%) compared to DTX-MB but the magnitude of reduction was considerably smaller than for MB-RB + US. Again, DTX-MB-RB + US caused the greatest reduction in viability of the spheroids (29% viable) which was also considerably better than at the lower concentration.

Results from both these experiments highlight the benefit of chemo-SDT therapy using DTX-MB-RB in this castrate resistant model of prostate cancer. The results also indicate that in the absence of US, toxicity from DTX-MB-RB was significantly reduced confirming the requirement for US induced cavitation and SDT activation for the treatment to be effective. The reduced toxicity in the absence of US should also enhance the tolerability of the treatment which will be further explored in the *in vivo* experiments.

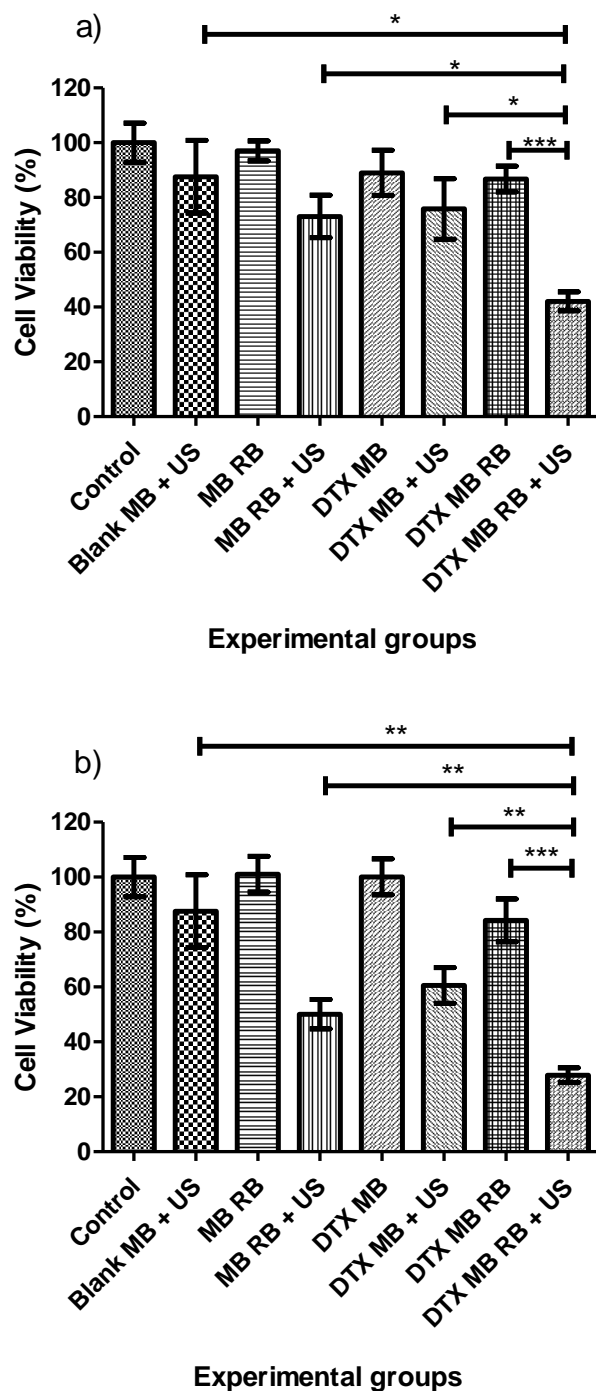


Figure 5.1 Cell viability of LNCaP spheroids treated with i) Untreated ii) blank MBs + US (iii) MB-RB (iv) MB-RB + US (v) DTX-MB (vi) DTX-MB + US (vii) DTX-MB-RB (viii) DTX-MB-RB + US. For experiment a) [DTX] was 8.33  $\mu\text{M}$ , [RB] was 25  $\mu\text{M}$ . For experiment b) [DTX] was 16.67  $\mu\text{M}$ , [RB] was 50  $\mu\text{M}$ . In both cases [MB] was  $3.56 \times 10^8/\text{mL}$ . \* $P < 0.05$ , \*\* $P < 0.01$  and \*\*\* $P < 0.001$ . Error bars show  $\pm$  SEM (n=4).

### **5.3.2 Efficacy of UTMD mediated chemo-SDT using DTX-MB-RB prepared from a pre-MB colloidal suspension in a DU145 spheroid model of prostate cancer**

The experiment described above (5.3.1) was repeated in the androgen insensitive DU145 cell line to determine if any significant changes in treatment efficacy would be apparent between cell lines. Generally, a similar trend was observed with only minor reductions in cell viability observed for DTX-MB and MB-RB in the absence of US. Again, SDT treatment (MB-RB + US) was more also effective than DTX-MB + US at both concentrations tested and at the lower concentration DTX-MB-RB + US was significantly more effective at reducing viability than DTX-MB-RB alone ( $p \leq 0.001$ ), DTX-MB + US ( $p \leq 0.001$ ) or MB-RB + US ( $p \leq 0.001$ ). However, at the higher concentration, chemo-SDT treatment (+ US) was only slightly more effective than the effect of SDT treatment alone (MB-RB + US) and the difference was non-significant. This suggests the DU145 spheroids are more sensitive to the effects of SDT than LNCaP cells. At the higher concentration, given its MOA, the SDT effect may be sufficient on its own to produce a significant cytotoxic effect with little benefit observed from the provision of DTX. In addition, it has previously been shown that DU145 cells are less sensitive to the effects of DTX with a half maximum inhibitory concentration (IC<sub>50</sub>) 3.3-fold greater [230].

Combined, results from both 3D spheroid experiments demonstrate that chemo-SDT is effective at reducing the viability of both castrate sensitive and resistant 3D spheroid models of prostate cancer. The next step was to determine the efficacy of the DTX-MB-RB + US in appropriate animal models of the disease.

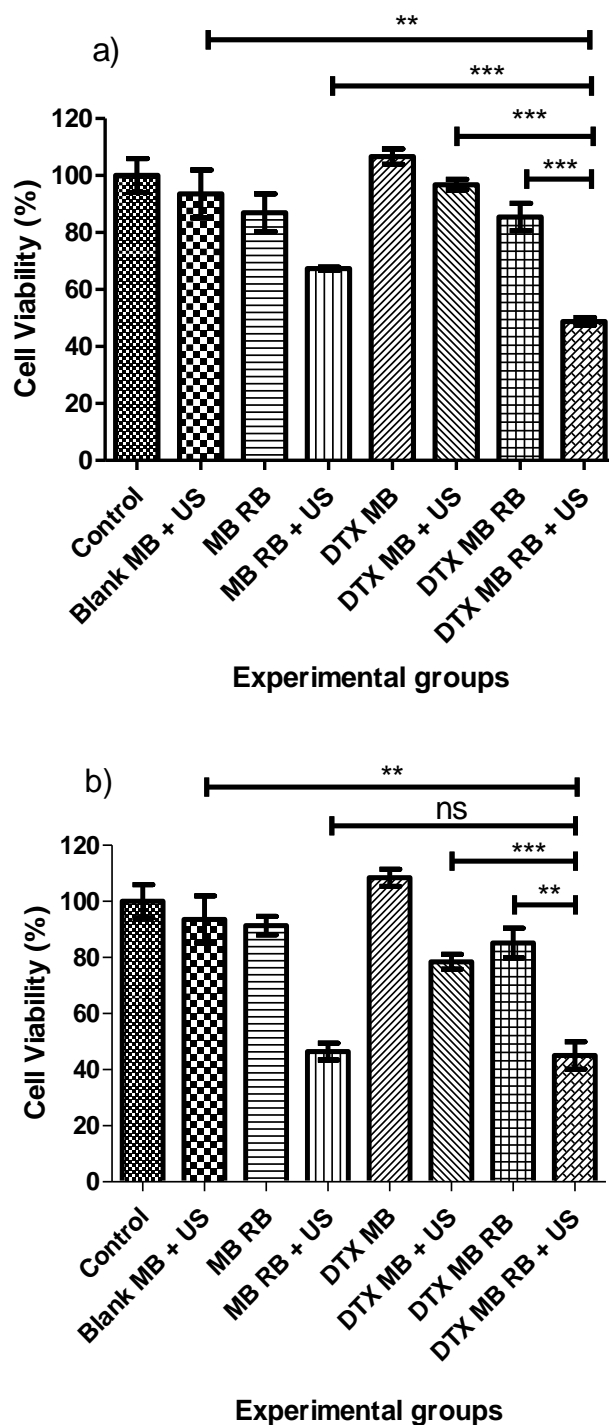


Figure 5.2 Cell viability of DU145 spheroids treated with i) Untreated ii) blank MBs + US (iii) MB-RB (iv) MB-RB + US (v) DTX-MB (vi) DTX-MB + US (vii) DTX-MB-RB (viii) DTX-MB-RB + US. For experiment a) [DTX] was 8.33 $\mu$ M, [RB] was 25 $\mu$ M. For experiment b) [DTX] was 16.67 $\mu$ M, [RB] was 50 $\mu$ M. In both cases [MB] was 4.11x10<sup>8</sup>/mL. \*\*P<0.01 and \*\*\*P<0.001. Error bars show  $\pm$  SEM

### **5.3.3 Efficacy of UTMD mediated chemo-SDT using DTX-MB-RB prepared from a pre-MB colloidal suspension in murine model of prostate cancer bearing ectopic 22Rv1 tumours**

As mentioned in chapter 3, 3D spheroids are an effective model to establish the efficacy of drug-based therapies such as chemo-SDT and reflect the characteristics of solid tumours better than 2D cell models. However, to determine the effectiveness of UTMD as a drug delivery vehicle, *in vivo* experimentation remains the best model available. The androgen sensitive cell line LNCaP was used for the 3D spheroid experiments. Unfortunately, it proved difficult to establish LNCaP tumours in the Balb/c nude SCID mice used and therefore an alternative androgen sensitive cell line was identified. 22Rv1 cells are a prostate carcinoma cell line derived from a parental CWR22 xenograft. The 22RV1 cell line was serially propagated in mice xenografts after castration-induced regression and relapse of the CWR22 parental xenografts. They are an androgen-dependent cell line that also expresses PSA [228, 229].

Male nude balb/c mice were subcutaneously injected with  $5 \times 10^6$  22Rv1 cells in 100 $\mu$ L of Matrigel and serum free media (50:50) and once tumours reached approximately 100 mm<sup>3</sup> the animals were randomly allocated to treatment groups. Group 1 received no treatment. Group 2 received Enzalutamide as an ADT treatment at 10 mg/kg. Group 3 received DTX-MB-RB ([DTX] = 1.11 mg/kg; [RB] = 7.54 mg/kg and [MB] =  $3.12 \times 10^9$  MB/mL) while group 4 received the same DTX-MB-RB dose but also received US treatment applied to the tumour. Group 5 received the same treatment as Group 4 in combination with Enzalutamide treatment. The final group (group 6) received a matched dose of non-MB bound DTX (1.11 mg/kg) i.e. the same concentration as was present on the DTX-MB-RB. Animals were treated on days 0, 4, 6, 8, 10, 12, 14, 16, 18, 20, 22 and 24 unless culled due to tumour size earlier. Tumour volume was recorded daily until the tumours reached the limit of the licence.

The individual growth curves for each mouse in each group is shown in Figure 5.3 (i-vi) with the average for tumour volume for each group shown in Figure 5.4. It is clear from the untreated animals that the 22Rv1 tumours were extremely fast growing and were 821% bigger nine days after the start of the experiment. Treatment with the matched dose of DTX + US provided no real difference to tumour growth compared to untreated animals with tumours growing 838% 9 days after their initial treatment. Similarly, DTX-MB-RB in the absence of US had no impact on tumour growth with tumours on average slightly larger at 1043.1% than untreated animals,

although the difference was not statistically significant. Indeed, review of the individual growth curves for this group indicated that two tumours were extremely fast growing, and this was most likely the reason for the slight increase in average tumour volume compared to the untreated group. DTX-MB-RB + US and Enz treatments provided comparable tumour control with tumours 567 and 514 % larger on Day 9. However, when these two treatments were combined, a significant improvement ( $p \leq 0.01$ ) was observed in tumour growth control with tumours growing only 203% by Day 9. No significant change was observed in the average weight of the animals in any group with the only exception being the DTX + US group where a small 3.3% drop in weight was observed compared to untreated animals on Day 7. The increased efficacy of DTX-MB-RB with US and Enz was not surprising when the context of the phase 3b study: A Randomized, Double Blind, Placebo-Controlled, Phase IIIb Study of the Efficacy and Safety of Continuing Enzalutamide in Chemotherapy Naïve Metastatic Castration Resistant Prostate Cancer Patients Treated With Docetaxel Plus Prednisolone Who Have Progressed on Enzalutamide Alone (PRESIDE). The participants of the PRESIDE trial received daily oral Enz or oral placebo alongside ten cycles of docetaxel every 3 weeks and oral prednisone. The findings showed that median progression-free survival with Enz was 9.5 months versus 8.3 months with placebo [231].

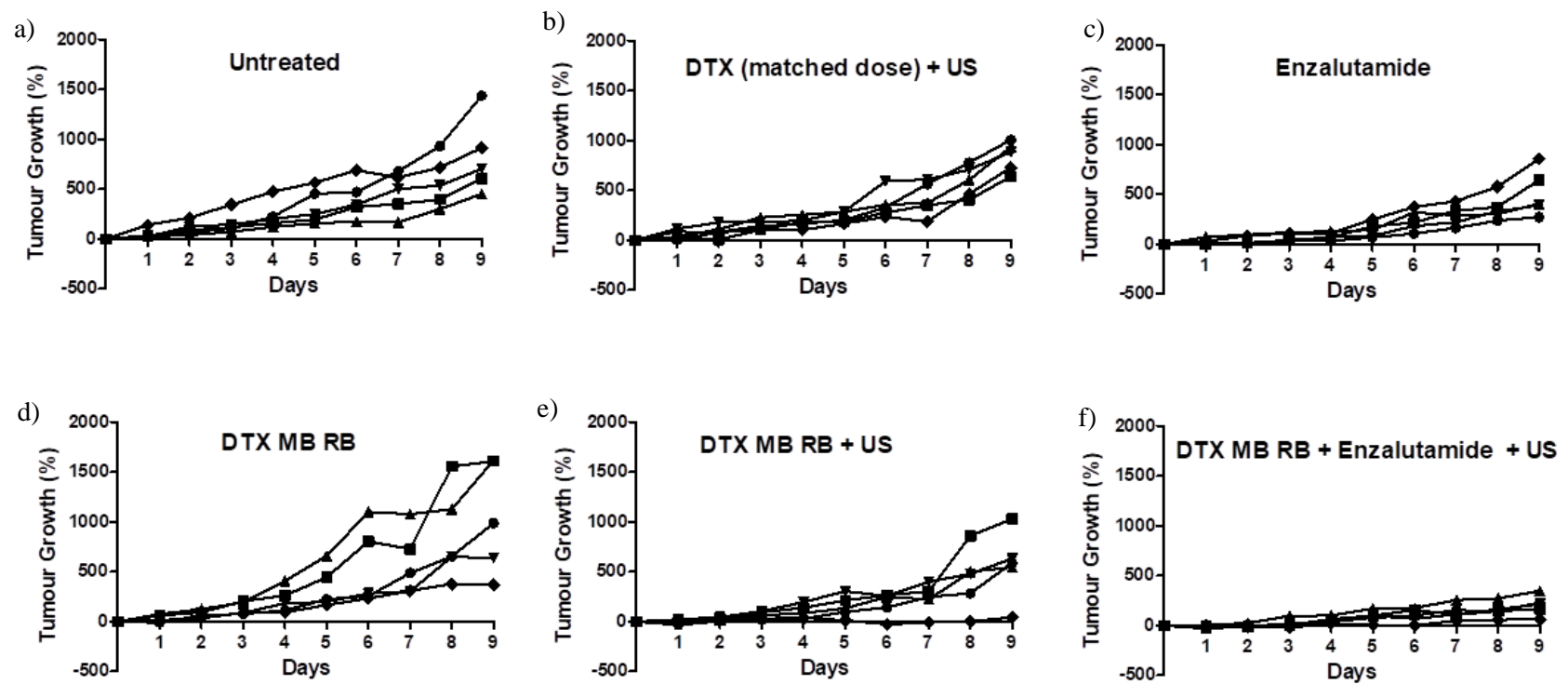


Figure 5.3 Individual tumour growth delay plots for each nude balb/c mice implanted with 22Rv1 tumours, treated with a) untreated, b) DTX (matched dose) + US, c) enzalutamide, d) DTX-MB-RB, e) DTX-MB-RB + US and f) DTX-MB-RB enzalutamide + US.



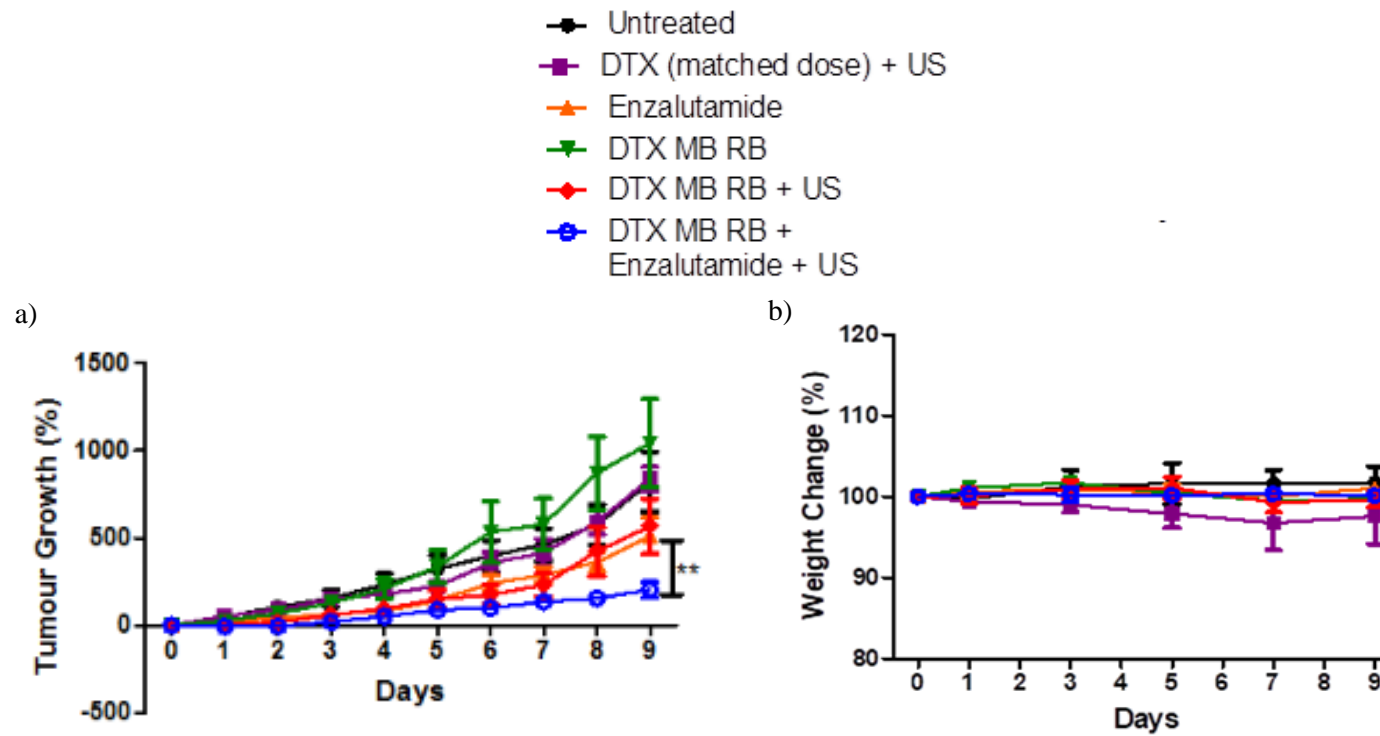


Figure 5.4 Plot of a) percentage tumour growth and b) and b) percentage weight change for nude balb/c mice bearing 22Rv1 tumours. The mice were treated with i) untreated, ii) DTX (matched dose) + US, iii) enzalutamide, iv) DTX-MB-RB, v) DTX-MB-RB + US and vii) DTX-MB-RB enzalutamide + US. \*\* $P < 0.01$  (N=5)

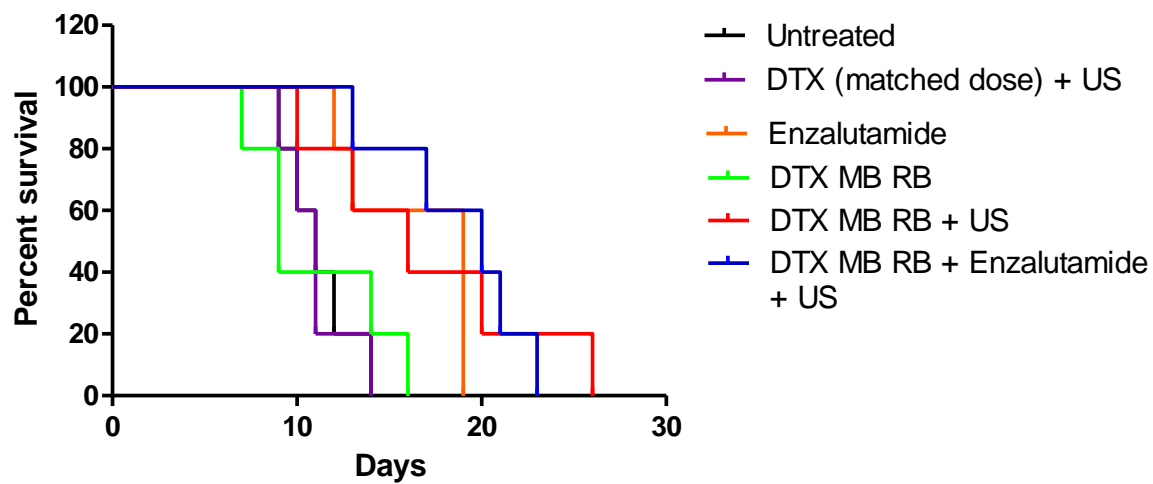


Figure 5.5 Kaplan Meier survival plot for nude balb/c mice bearing 22Rv1 tumours, treated with i) untreated, ii) DTX (matched dose) + US, iii) enzalutamide, iv) DTX-MB-RB, v) DTX-MB-RB + US and vii) DTX-MB-RB enzalutamide + US. (N=5)

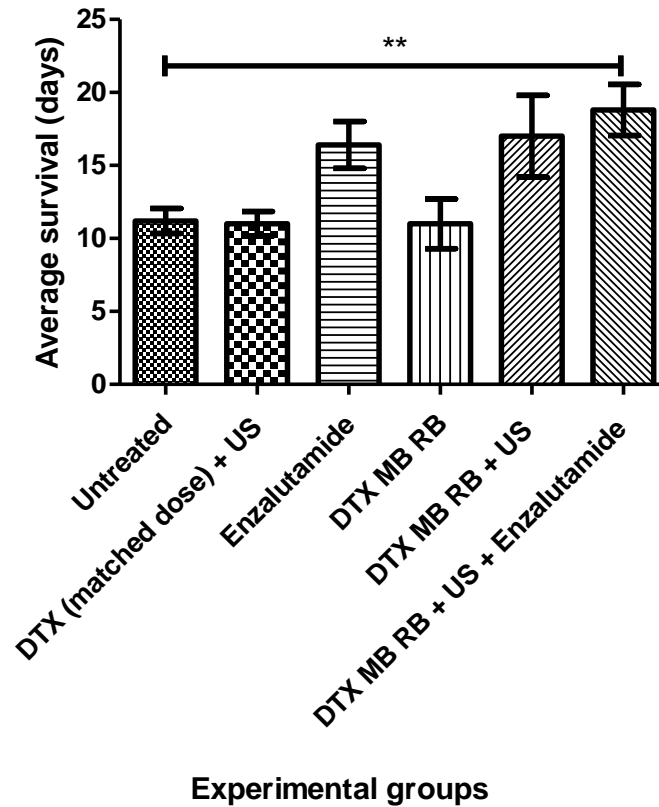


Figure 5.6 Mean survival for nude balb/c mice bearing 22Rv1 tumours, treated with i) untreated, ii) DTX (matched dose) + US, iii) enzalutamide, iv) DTX-MB-RB, v) DTX-MB-RB + US and vii) DTX-MB-RB enzalutamide + US. \*\* $P < 0.01$  (N=5).

The Kaplan Meier plot is shown in Figure 5.5. The endpoint for these mice was indicated by the tumour limit stated within the project license this work was carried out under, this was determined as mice with tumours where the mean size (mm) of the dimensions of the tumour equalled 17 mm. The data in figure 5.5 clearly shows survival benefit for animals in the Enz, DTX-MB-RB + US and DTX-MB-RB + US + Enz groups while DTX-MB-RB and DTX+ US provided no noticeable benefit. This was also reflected in the average survival time of the animals in each group where the untreated, DTX + US and DTX-MB-RB groups had average survivals of  $11.2 \pm 0.9$ ,  $11 \pm 0.8$  and  $11 \pm 1.7$  days (Figure 5.6). Treatment with DTX-MB-RB + US improved the average survival to  $17 \pm 2.8$  days which was slightly better than Enz at  $16.4 \pm 1.6$  days. This was increased to  $18.8 \pm 1.74$  days when DTX-MB-RB + US was combined with Enz.

Combined, these results demonstrate the potential of UTMD mediated chemo-SDT using DTX-MB-RB in this aggressive model of androgen dependent prostate cancer. When combined with Enz, a significant improvement in tumour growth delay was observed and a small improvement in average survival was also evident. The fact that UTMD mediated chemo-SDT using DTX-MB-RB has comparable efficacy as a current standard of care treatment for androgen dependent prostate cancer is encouraging. It would, however, be interesting to compare efficacy against radiotherapy which is also a first line treatment for this form of prostate cancer. Unfortunately, no small animal external beam radiotherapy instrument was accessible during this project.

#### **5.3.4 Efficacy of UTMD mediated chemo-SDT using DTX-MB-RB prepared from a pre-MB colloidal suspension in a murine model of prostate cancer bearing ectopic PC3 tumours**

As discussed in Chapter 3, a PC3 murine tumour model was utilised to determine the efficacy of US mediated DTX-MB-RB treatment against androgen resistant prostate cancer. Mice were treated with either: DTX-MB-RB +/- US; a matched dose of DTX chemotherapy + ultrasound (i.e., same concentration as administered on the DTX-MB-RB = 0.94 mg/kg DTX, RB = 6.35 mg/kg); a standard mouse dose of DTX chemotherapy (10.00 mg/kg); DTX-MB (0.94 mg/kg DTX) + US or MB-RB (6.35 mg/kg DTX) + US. Untreated animals were used for comparative purposes.

Figure 5.8 shows the mean growth of tumours in each group over time. Tumour growth in animals treated with DTX-MB-RB + US were over 195% smaller than the next best group ( $p < 0.05$ ) and over 454% smaller than untreated animals ( $p < 0.01$ ), 29 days after the initial treatment. In comparison, animals treated with DTX-MB + US were 94% smaller than untreated animals and those treated with MB-RB + US were 258% smaller than untreated animals. Therefore, the effect of DTX-MB-RB + US produced 102% smaller tumours than the additive effect of DTX-MB + US and MB-RB + US, indicating synergy. The treatment was also significantly better (228% smaller,  $p < 0.05$ ) than the “standard” dose of DTX which contained > 10-fold more DTX compared to the DTX-MB-RB + US. This represents a very impressive improvement in tumour growth delay when compared to the current standard of care treatment for this form of prostate cancer. The capability of UTMD to enhance the efficacy

of DTX in a PC3 murine model has been highlighted by Goertz et al [232]. Athymic nude mice received a PC3 xenograft and received either i) no treatment, ii) DTX, iii) MBs with US or iv) DTX with MB and US. Tumour histology showed a 2.4-fold increase in necrosis for the DTX alone group relative to the untreated, however, the DTX with MB and US showed a 9.7-fold increase relative to the untreated mice. They also showed greater tumour growth control for mice treated with DTX with MB and US after 5 weeks where mice had average tumour volumes of less than 50mm<sup>3</sup> compared to mice who received only DTX (nearly 500mm<sup>3</sup>) [232].

The Kaplan Meier curve is shown in Figure 5.9 and reveals that DTX-MB-RB + US treatment resulted in improved survival outcome compared to the other groups. The average survival for animals in this group was  $37.8 \pm 0.7$  days, while the next best group was MB-RB + US at  $30.2 \pm 2.3$  days. DTX-MB-RB + US was also significantly better than the standard dose of DTX which had an average survival of  $22.2 \pm 2.6$  days ( $p < 0.001$ ). However, it should be noted, that 2 animals had to be removed from the DTX group for ethical reasons at days 13 and 19 as their weight dropped by more than 20% below the pre-study weight and was attributed to the extreme toxicity of DTX chemotherapy. Nonetheless, as is evident from the Kaplan Meier curve, the animals that remained in this group did not obtain any substantial survival advantage.

Figure 5.8 b) also highlights the toxicity of the DTX standard dose with the average weight of animals dropping significantly following the initial treatment. In contrast, the weight of animals treated with DTX-MB-RB + US remained unchanged over the course of the experiment and was comparable with that of untreated animals indicating that the treatment was well tolerated. These data are key in demonstrating one of the major benefits of this approach, since they demonstrate that the combination of SDT with the highly toxic DTX delivered using MBs affords significant therapeutic benefit without the adverse effects associated with standard doses of DTX.

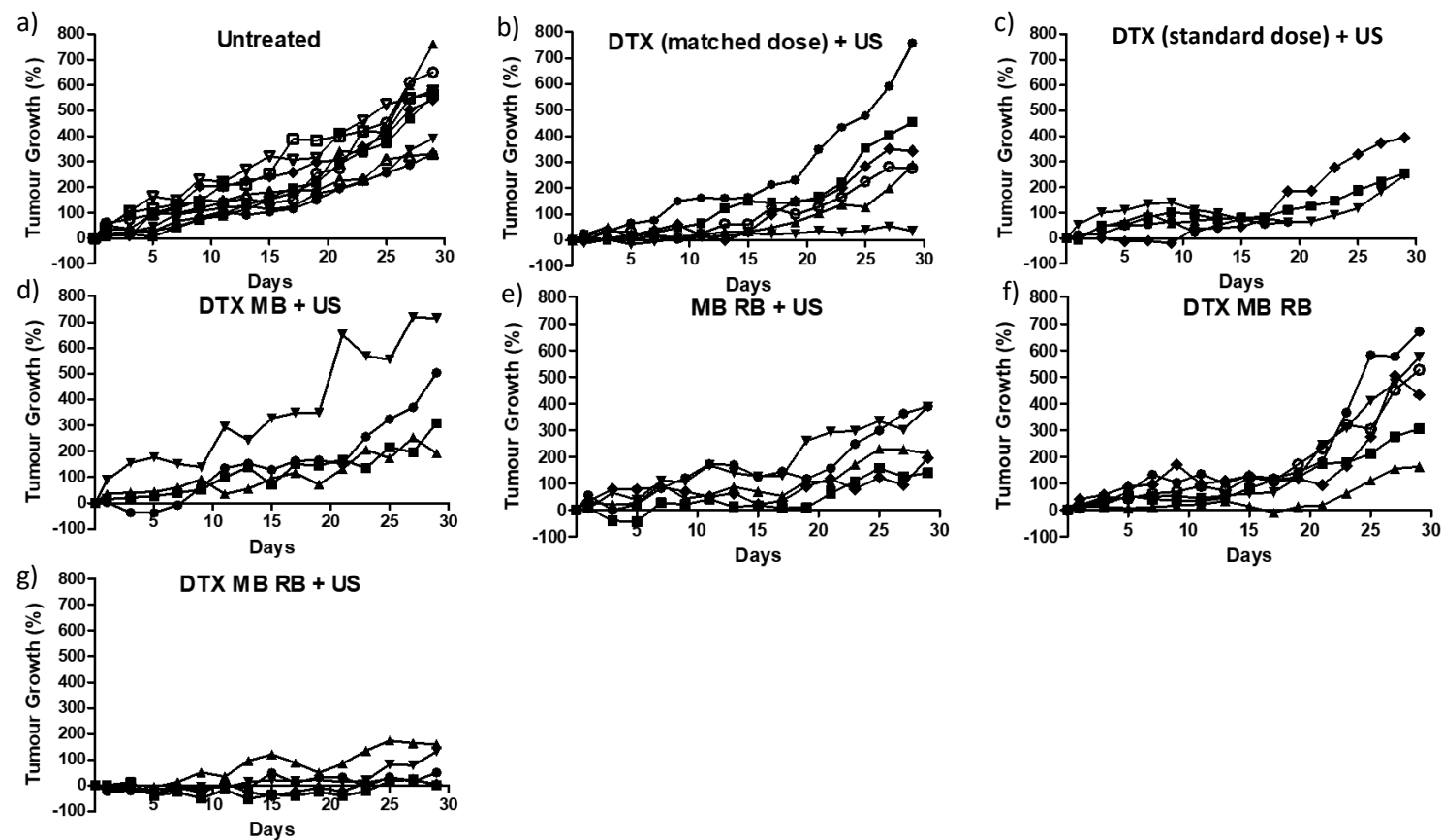


Figure 5.7 Individual tumour growth delay plots for each nude CD-1 mouse implanted with PC3 tumours, treated with a) untreated, b) DTX (matched dose) + US, c) DTX (standard dose + US), d) DTX-MB + US, e) MB-RB + US, f) DTX-MB-RB and g) DTX-MB-RB + US.

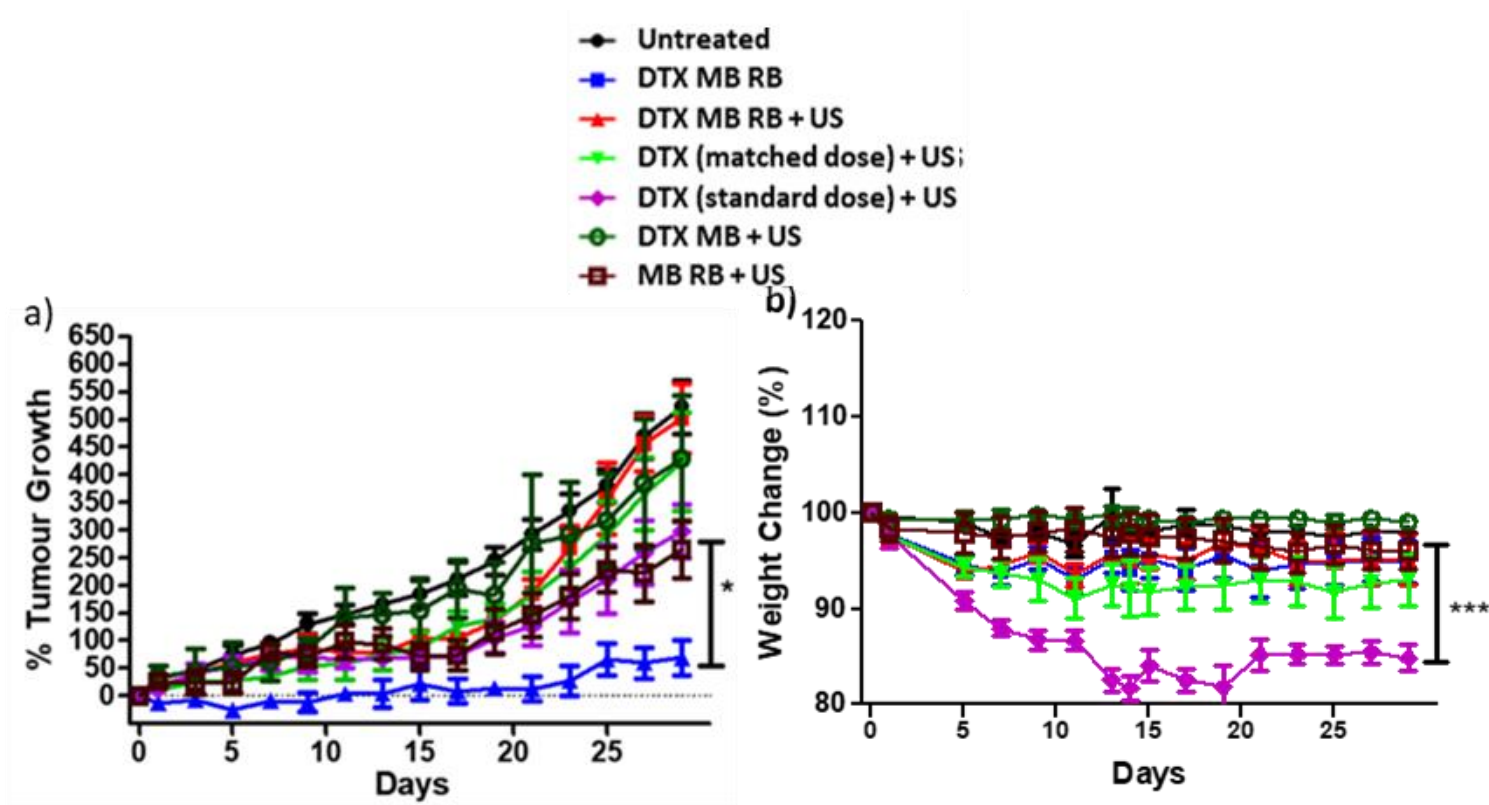


Figure 5.8 Plot of a) percentage tumour growth and b) and b) percentage weight change for nude CD-1 mice bearing PC3 tumours. The mice were treated with i) untreated, ii) DTX (matched dose) + US, iii) DTX standard dose + US), iv) DTX-MB + US, v) MB-RB + US, vi) DTX-MB-RB and vii) DTX-MB-RB + US. \* $P < 0.05$  and \*\* $P < 0.001$  (N=5)

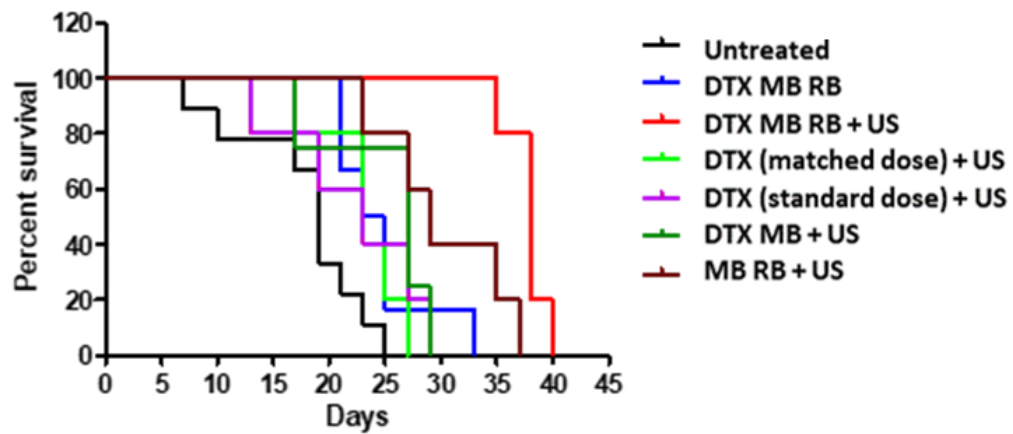


Figure 5.9 Kaplan Meier survival plot for nude CD-1 mice bearing PC3 tumours, treated with i) untreated, ii) DTX (matched dose) + US, iii) DTX (standard dose + US), iv) DTX-MB + US, v) MB-RB + US, vi) DTX-MB-RB and vii) DTX-MB-RB + US. (N=5)



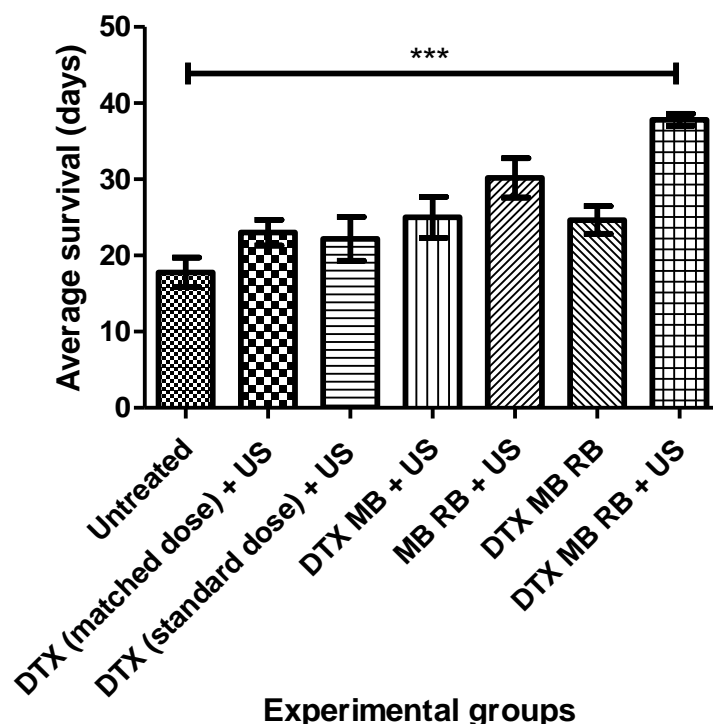


Figure 5.10 Mean survival for nude CD-1 mice bearing PC3 tumours, treated with i) untreated, ii) DTX (matched dose) + US, iii) DTX (standard dose + US), iv) DTX-MB + US, v) MB-RB + US, vi) DTX-MB-RB and vii) DTX-MB-RB + US. \*\*\* $P < 0.001$  (N=5)

### 5.3.5 Safety study of DTX-MB-RB prepared from a pre-MB colloidal suspension in healthy non tumour bearing mice

The efficacy study conducted in mice bearing PC3 tumours demonstrated evidence of acute toxic effects in animals treated with standard DTX chemotherapy. While there was no indication of adverse effects from the DTX-MB-RB chemo-SDT treatment, it was still deemed prudent to undertake an indicative safety study in healthy non-tumour bearing animals. The animals were allocated to three groups: Group 1 were untreated; Group 2 received DTX-MB-RB (I.V., [DTX] = 1.13 mg/kg and [RB] = 7.70 mg/kg) and Group3 received DTX (I.V. [10 mg/kg]). Treatments were administered on days 0, 4, 7, 11 and 14, to mirror the efficacy experiment outlined in section 5.3.4. Blood samples were taken on days 10 and 15 and analysed by an independent laboratory for a range of biochemical markers with the body weight also recorded every other day. Following the final blood sample on Day 15, the animals were

ethanised with the livers and kidneys harvested for independent histopathological examination. It should be noted, however, that in this study, no US was used to focus delivery of the chemotherapy to the tumour meaning in relative terms more was circulating in the systemic circulation and available for sequestration by the liver or kidneys.

As was observed in section 5.3.4, the average weight of animals in the DTX group dropped significantly to 92.1% by Day 15 ( $p \leq 0.01$ ). In contrast, there was no significant change in the average weight of animals in the DTX-MB-RB group (103.6%) which was only slightly different than untreated animals (106.9%). This consistent reduction in body weight between the groups highlights the acute toxicity of DTX chemotherapy at this dose. While the rate and magnitude of weight loss was less than observed in 5.3.4, the slower rate of weight loss may be due to the starting health of the animals i.e., tumour / non-tumour bearing with the latter being better placed to undertake a toxic chemotherapy regimen. In a study conducted by Grudén et al [233] a 10% reduction in body weight was observed in C57bl/6J mice bearing Lewis lung carcinoma (LLC) xenograft tumours after 14 days, which received a higher dose of DTX (25 mg/kg) and were treated 4 times between days 6 and 12. This 10% body weight reduction by day 14 is consistent with the 7.9% body weight reduction seen after 14 days and confirms the toxicity of multiple DTX treatments within various murine models.

Blood smear analysis was carried out by the Veterinary Pathology Group (VPG) (Leeds, UK). Results from the blood analysis are shown in Figure 5.12 c) and reveal no significant differences in the levels of key blood markers. A small rise in ALT level, which can indicate liver damage, was observed for the DTX-MB-RB group at Day 10 but returned to normal (untreated) levels at Day 15. A small reduction in urea levels was also observed for both the DTX-MB-RB and DTX groups when compared to untreated animals but this was not considered problematic as the reduction was minor and elevated urea levels are normally associated with kidney damage. Neutropenia is a common side effect following chemotherapy treatment and while the neutrophil levels were slightly reduced in both the DTX-MB-RB and DTX groups at Day 10, they increased for the DTX-MB-RB by day 15. The lymphocyte level was also slightly reduced in DTX-MB-RB group at Day 15 but against this was minor and not considered a direct effect of the treatment as lymphocyte levels are often found to be elevated following chemotherapy. While there were very minor differences in some of the other

biochemical markers, none were statistically significant or substantial enough to warrant any significant concern.

The histological analysis of tissues was carried out by Paul Kelly and Declan O'Rourke at the Department of Pathology, Belfast Health and Social Care Trust (Belfast, UK). Results from the hepatic histopathological examination are shown in Figure 5.12 and reveal no change in the mean score for lobular inflammation or steatosis. While there was a small increase in the mean portal inflammation score for the DTX-MB-RB and DTX groups, this was below 1.5 and not statistically significant. Indeed, the mean score for the untreated animals was also above 1.0, perhaps indicating the involvement of some other non-treatment related factors. Similarly, renal histopathological examination revealed there was evidence of mild interstitial inflammation in some of the untreated animals which increased further in the DTX-MB-RB and DTX groups, with the magnitude of increase slightly greater for the DTX group. While this increase was statistically different for the DTX group, the mean score was still below 2.0 and deemed mild. The only other difference observed in the kidney analysis was glomerular cellularity where the DTX-MB-RB was slightly elevated (mean score = 1.25) and this was statistically not significant. Toxic effects of DTX in the kidneys was not expected, DTX is commonly used for patients with lung cancer, it has been reported that 20% of lung cancer patients experience chronic kidney disease. In a small study by Anai et al [234]. There was no increase in incidence of DTX associated toxicity between non-small cell lung cancer patients with non-dialysis chronic kidney disease stage 3b or higher [234].

In summary, results from the safety study highlight that any toxic effects associated with the DTX-MB-RB were minor and considered less than mild according to the scoring system used.

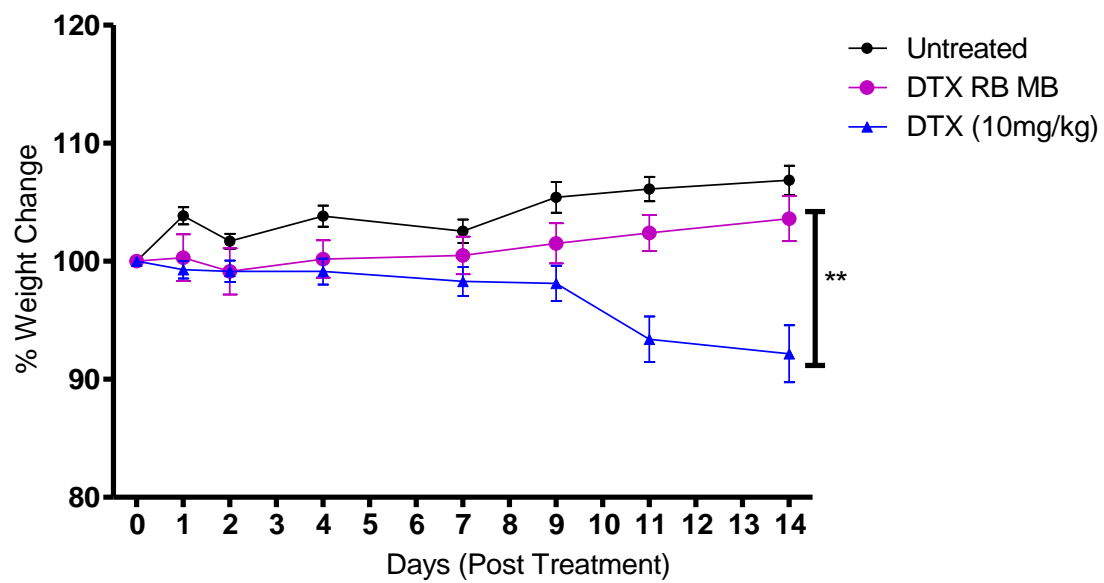


Figure 5.11 Plot of percentage weight change for healthy non tumour bearing mice. The mice were treated with i) untreated, ii) DTX-MB-RB or iii) DTX (10 mg/kg). (N=8)

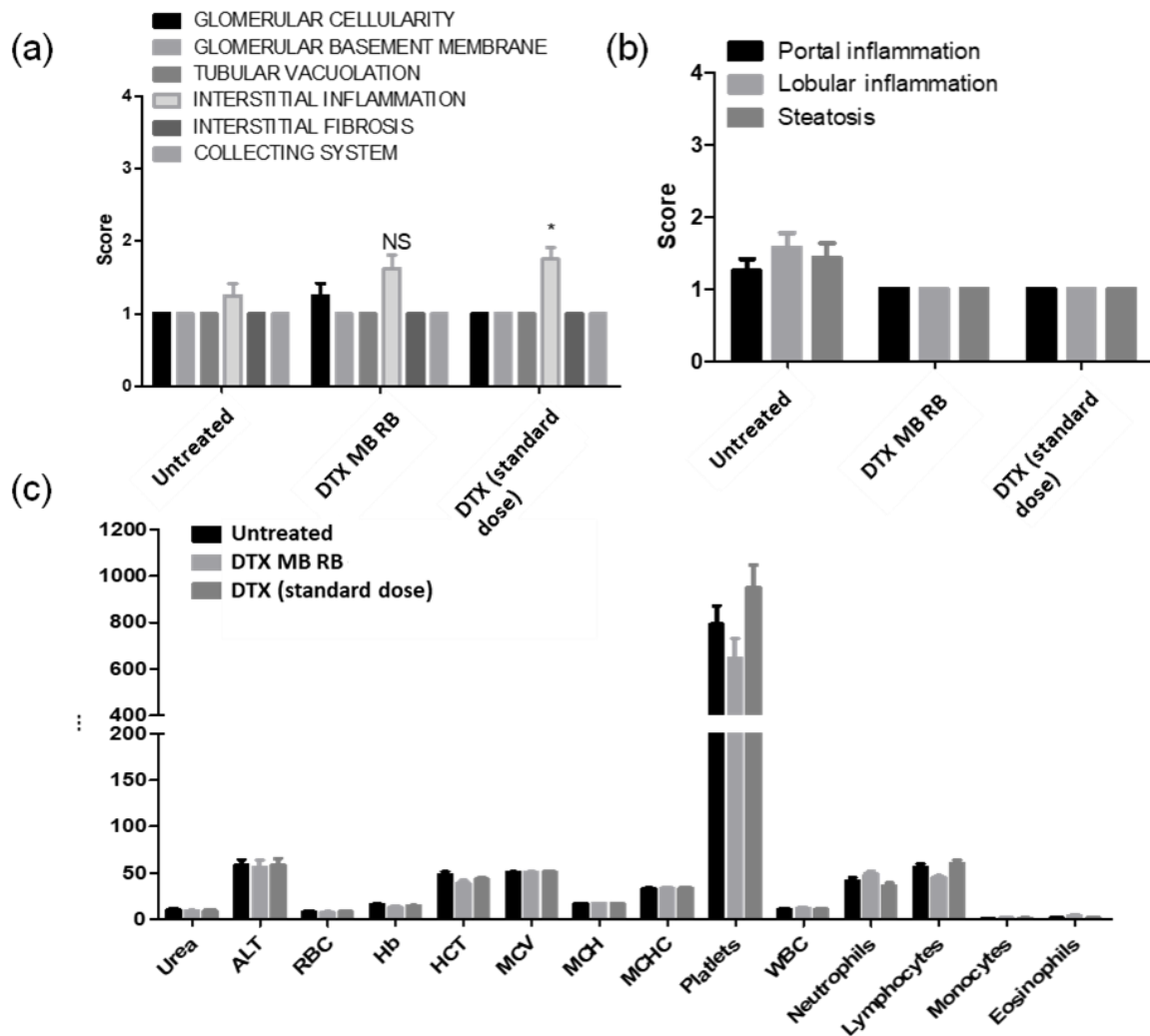


Figure 5.12 Safety study in healthy non tumour bearing mice where mice received i) remained untreated, ii) DTX MB RB or iii) DTX (standard dose). Where biological markers were used to determine the health of mice in a) the kidney (glomerular cellularity, glomerular basement membrane, tubular vacuolation, interstitial inflammation, interstitial fibrosis and collecting system), b) the liver (portal inflammation, lobular inflammation and steatosis) and c) a range of blood biomarkers (urea, ALT, RBC, Hb, HCT, MCV, MCH, MCHC, platelets, WBC, neutrophils, lymphocytes, monocytes and eosinophils). (N=8). (\* $P \leq 0.05$ ).

### **5.3.6 UTMD mediated localisation of MBs loaded with IR780 in a murine model of prostate cancer.**

A previous study by McEwan et al. demonstrated the ability of UTMD to localise NIR dye loaded MBs to tumours in a murine model of pancreatic cancer [235]. This involved attachment of the dye to the MB surface using the biotin-avidin interaction. This approach was warranted as the dye served as a surrogate for the drugs used (Rose Bengal and 5-FU) that were attached using this interaction. However, as DTX was loaded hydrophobically in DTX-MB-RB, it was deemed prudent to examine the UTMD of MBs with a NIR surrogate used in place of DTX which was also incorporated hydrophobically. Therefore, the NIR dye IR780 was incorporated within the MBs in place of DTX to produce the IR780-MB using the method described in 2.19.

Two groups of mice bearing ectopic 22Rv1 tumours received an IV injection of the IR780-MB ( $2.84 \times 10^9$  MB/ml, IR780 0.89 mg/kg) with one group also receiving US treatment using the conditions described in 2.20. The mice were imaged before treatment and 3h after treatment using an IVIS whole body imager. A region of interest (ROI) was circled around the tumour (target) with a second ROI circled on a portion of the back as a non-target reference. The NIR emission associated with each ROI was measured and the ratio of the tumour : back radiance for each group determined. A representative image of an animal from each group at the 0h and 3h timepoints are shown in Figure 5.13 and reveal significant NIR emission from the tumour region of the animal in the IR780-MB + US group when compared to that in the IR780-MB group. When the mean tumour : back radiance was plotted for each group, the IR780-MB + US group was 91% greater than the IR780-MB group. While the difference between these groups was lower than observed for McEwan et al (400% at 30 min,  $P \leq 0.01$ ) and non-significant ( $P = 0.0658$ ), the increase is substantial enough to suggest that UTMD is enhancing tumour delivery of the encapsulated IR780. It must be stressed however, that this experiment was not optimised, and needs repeated with an optimised IR780 loading / MB concentration, as detector saturation was an issue, particularly at the time points soon after administration (i.e. 30 min to 3h). Nonetheless, the results do resemble those obtained by McEwan et al with evidence of enhanced payload localisation in the tumour as a result of UTMD.

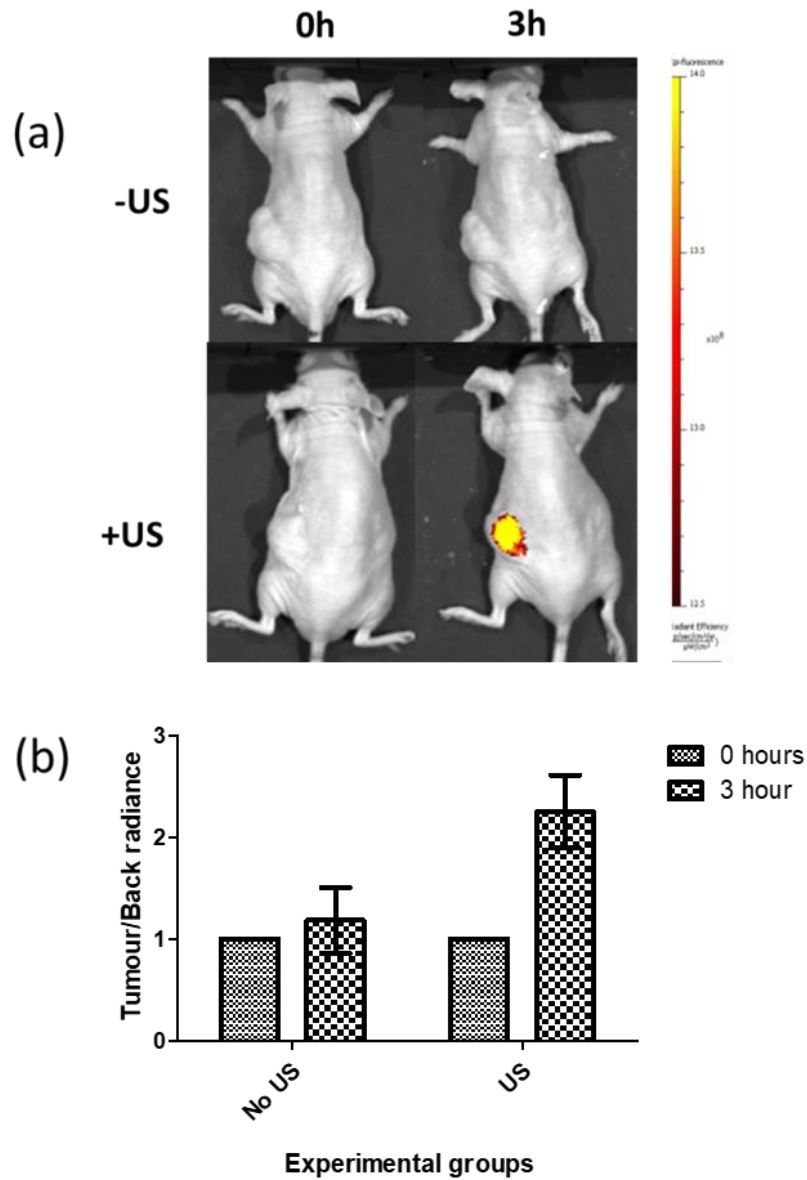


Figure 5.13 a) IVIS images of mice bearing 22Rv1 tumours, that received i) IR780 loaded MBs without US (top images), or ii) IR780 loaded MBs with US (bottom images). The images were taken at 0 hours; before treatment (left images) or 3 hours post treatment; (right images). b) Plot of tumour/back radiance for each treatment and timepoint. (n=3)

## 5.4 Conclusions

UTMD mediated chemo-SDT using DTX-MB-RB, prepared in a single step from its precursor pre-MB colloidal suspension, was evaluated for efficacy in androgen sensitive and resistant 3D spheroid and murine models of prostate cancer. UTMD mediated chemo-SDT was shown to be more effective than either UTMD mediated chemotherapy or SDT in LNCaP and DU145 spheroids at both concentrations tested. However, at the higher concentration the effect of UTMD mediated chemo-SDT was only marginally better than UTMD mediated SDT.

In the androgen dependent 22RV1 murine model, UTMD mediated chemo-SDT using DTX-MB-RB provided a comparable level of tumour control as enzalutamide ADT, and both were more effective than standard DTX treatment. When UTMD mediated chemo-SDT and ADT were combined, a significant improvement in tumour control was observed compared to either individual treatment. In the androgen resistant PC3 murine model, UTMD mediated chemo-SDT was significantly more effective than standard DTX treatment at controlling tumour growth and the average survival was also significantly longer at 23 days compared to 38 days. In addition, the UTMD mediated chemo-SDT was well tolerated while the standard DTX treatment resulted in significant weight loss. A more detailed safety study, investigating the effect of DTX-MB-RB on key blood biochemical markers and liver / kidney pathology, confirmed the treatment did not cause any worrying adverse effects.

Collectively, these results confirm the potential of UTMD mediated chemo-SDT as a treatment for prostate cancer when used alone or in combination or in combination with other clinically approved treatments such as ADT.



## **Chapter 6:**

### **Development of a Single-Vial, Pre-Microbubble Colloidal Suspension Loaded with 5-Fluorouradine and Irinotecan for the Treatment of Prostate Cancer.**

## 6.1 Introduction

FOLFIRINOX is a combination chemotherapy regimen that comprises the non-cytotoxic folinic acid (FOL) alongside 5-fluorouracil (F), irinotecan (IRIN) and oxaliplatin (OX). It is most widely used in the treatment of pancreatic cancer where it is the most effective therapy in terms of OS. FOLFIRINOX was clinically approved in 2010 following the PRODIGE 4/ACCORD 11 study which compared the efficacy of FOLFIRINOX against gemcitabine in patients with metastatic pancreatic cancer [236]. The ACCORD phase III trial showed that FOLFIRINOX had a greater median OS of 11.1 months than gemcitabine (6.8 months) [236]. FOLFIRINOX has shown unparalleled improvement on the OS of patients with metastatic pancreatic cancer than other promising treatment methods such as Abraxane. Abraxane consists of paclitaxel bound albumin nanoparticles, which is used to treat metastatic pancreatic cancer patients alongside gemcitabine. In the MPACT phase III clinical trial an efficacy comparison was made between gemcitabine monotherapy and gemcitabine + Abraxane, the outcomes were recorded by comparing the OS of patients with metastatic pancreatic cancer. Whilst gemcitabine + Abraxane showed a significant increase in OS (9.8 months) than gemcitabine monotherapy (7.5 months) [237]. The increase was not as impressive as that seen in the ACCORD phase III trial in which FOLFIRINOX showed a 63.2% increase in OS vs gemcitabine monotherapy, compared to gemcitabine + Abraxane in the MPACT phase III trial with 30.7% vs gemcitabine monotherapy [238, 239]. However, FOLFIRINOX is associated with significant side effects and is only indicated for patients with a good health performance status (i.e., Eastern Cooperative Oncology Group (ECOG) score  $\leq 2$ ) [240, 241].

The same drug combination as FOLFIRINOX has also been used in the treatment of colorectal cancer where it is termed FOLOXFIRI with the only difference being the rate of 5-fluorouracil infusion. Drug combinations such as FOLFOX and FOLFIRI have been explored in the treatment of colorectal cancer. An analysis study of SEER-Medicare data, it was found that oncologists preferred FOLFOX rather than FOLFIRI with a usage rate of 79.3% compared with 20.7%, despite both treatments showing similar PFS rates of (8 and 8.5 months respectively) [242]. Most patients receiving FOLFOX and FOLFIRI received a monoclonal antibody drug as well such as cetuximab or bevacizumab, and median survival of up to 30 months is achievable in patients with metastatic colorectal cancer. In a phase III randomized

clinical trial titled FIRE-3 it was determined that FOLFIRI + cetuximab had a greater OS (33 months) vs FOLFIRI + bevacizumab (26 months) [243].

5-fluorouracil, irinotecan and oxaliplatin are not current standard of care chemotherapy treatments for prostate cancer. However, a 2018 study has shown that 5-fluorouracil treatment of patient who relapsed following previous ADT, DTX and abiraterone treatment showed a remarkable reduction in PSA level (1,890 ng/mL to <1 ng/mL) [244]. The authors postulated that PSA overexpression may result in prostate cancer cells being uniquely susceptible to antifolate therapies such as 5-FU. A 2018 study also investigated the use of IRIN combined with the hypercholesterolaemia drug simvastatin [244]. Simvastatin downregulates Mcl-1, a highly expressed anti-apoptotic gene in advanced prostate cancer, thereby reducing the effectiveness of apoptotic agents such as IRIN. Therefore, combining simvastatin with IRIN could ameliorate the impact of Mcl-1 expression and improve the effectiveness of IRIN chemotherapy. The results showed that simvastatin enhanced IRIN-induced apoptosis. The percentage of apoptotic cells was 10% for both control PC3 cells and PC3 cells receiving IRIN (10 $\mu$ M), 44% for PC3 cells receiving simvastatin (25 $\mu$ M), however when both IRIN (10 $\mu$ M) and simvastatin (25 $\mu$ M) approximately 68% of cells were apoptotic [245]. An added attraction of this approach is that prostate cancer is most common in elderly men, many of whom are on statins to control their hypercholesterolaemia. However, this age demographic and associated physical wellbeing does limit the potential of using toxic chemotherapy combinations.

The ability to target chemotherapy combinations such as FOLFIRINOX, FOLFOX and FOLFIRIN could help further improve efficacy but reduce the extreme side effects and make them more applicable to a wider range of cancers. Gao et al. [246] has previously designed a MB carrying the three chemotherapy drugs used in FOLFIRINOX for the treatment of pancreatic cancer [246]. Free base IRIN was encapsulated in the MB shell in a manner comparable to DTX in Chapters 3-5. A DBPC lipid derivative of 5-FUR was prepared using an enzyme mediated transphosphatidylation reaction and was a constituent lipid of the MB shell. The MBs were prepared containing IRIN and 5-FUR and then a biotin functionalised oxaliplatin used to attach oxaliplatin using the avidin-biotin interaction. The FIRINOX MBs were administered alongside folinic acid to mice bearing human pancreatic tumours and UTMD mediated treatment was efficacious than standard FOLFIRINOX treatment yet better tolerated.

In this chapter, DSPE derivatives of 5-FUR and IRIN were synthesised and used to prepare 5FUR-MB-IRIN. As with the DTX-MB-RB in chapters 4 and 5, the 5FUR-MB-IRIN will be prepared from a pre-MB colloidal suspension in a single step using the Vial Mix. The efficacy of UTMD mediated 5FUR-MB-IRIN treatment was assessed in a 3D DU145 spheroid model of prostate cancer.

## **6.2 Aims and objectives**

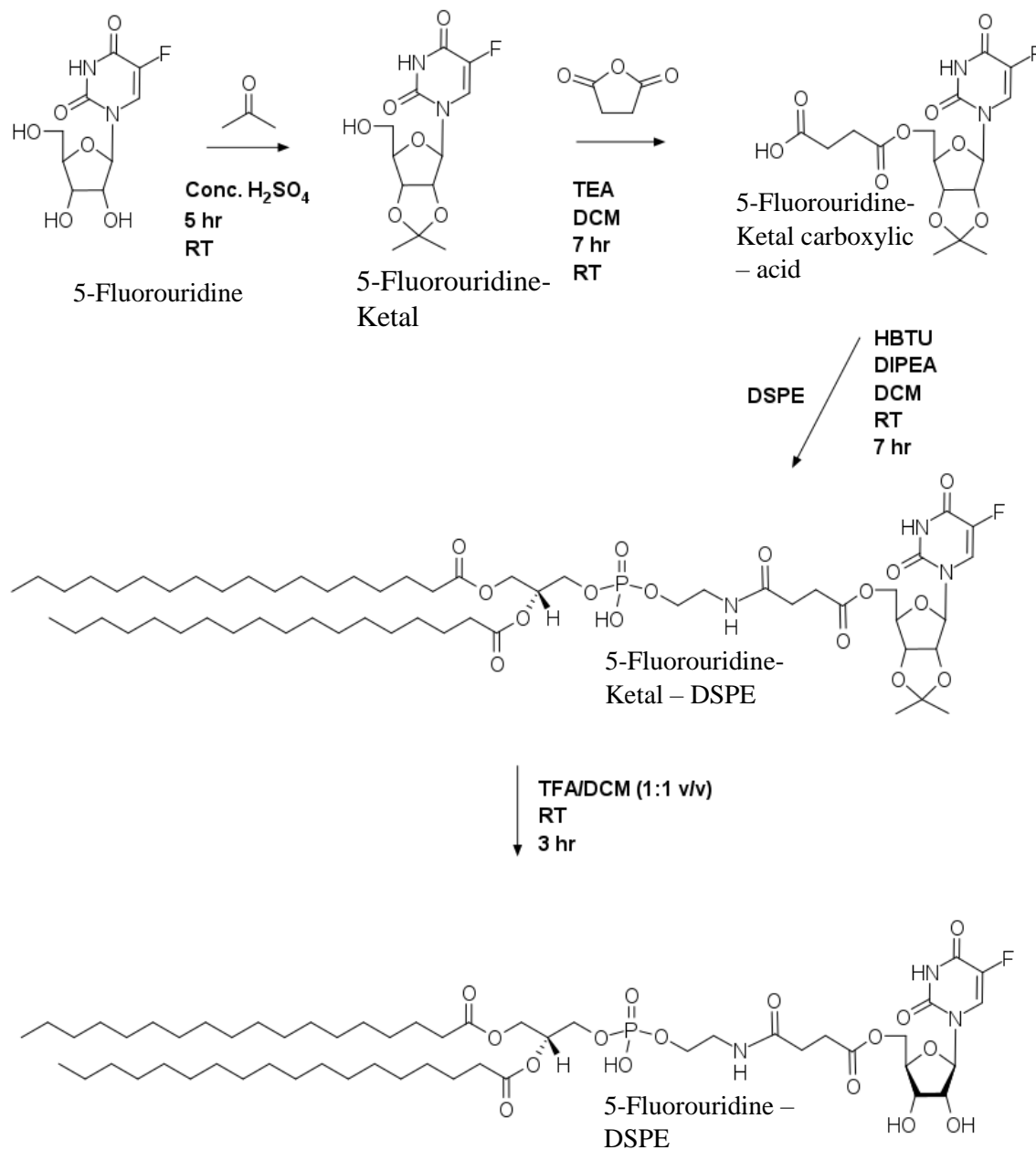
The overall aim of the work undertaken in this chapter was to prepare a 5FUR-MB-IRIN and assess their potential as a treatment for prostate cancer. The specific objectives for this chapter were.

1. Synthesise a 5-FUR modified DSPE phospholipid (5FUR-DSPE) and characterise using NMR and mass spectrometry.
2. Synthesise an IRIN modified DSPE phospholipid (IRIN-DSPE) and characterise using NMR and mass spectrometry.
3. To prepare and characterise 5FUR-MB-IRIN from the drug-loaded lipid conjugates.
4. Determine the efficacy of UTMD mediated of 5FUR-MB-IRIN chemo-SDT therapy using in a DU145 3D spheroid model.

## 6.3 Results and discussion

### 6.3.1 Synthesis of 5FUR-DSPE

5FUR-DSPE was synthesised as outlined in Scheme 6.1.



Scheme 6.1 for synthesis of 5FUR-DSPE.

The first step was to protect the diol on the sugar of the 5-flourouridine by reacting with acetone to form a ketal. The ketal was then reacted with succinic anhydride to form an ester with the primary alcohol and generating the carboxylic acid derivative. The carboxylic acid group of 5-Fluorouridine-Ketal carboxylic – acid was reacted with the primary amine of DSPE linking the

two molecules together through an amide bond producing compound 5-Fluorouridine-Ketal – DSPE. The final step was deprotection of the ketal to produce 5FUR-DSPE.

The structure of 5-fluorouridine – DSPE was confirmed using  $^1\text{H}$ -NMR,  $^{13}\text{C}$ -NMR and ESI-MS. The stacked  $^1\text{H}$ -NMR of DSPE, 5FUR and 5FUR-DSPE are displayed in Figure 6.1. Peaks consistent with 5FUR and DSPE are evident in the spectrum of 5FUR-DSPE except for the methylene protons (**p** and **q**) of the succinic acid linker, which can be found with resonances at 2.30 and 2.70 ppm. Diastereotopic methylene protons (**i**), directly coupled to the primary alcohol in 5FUR and split over two resonances at 3.70 and 3.85 ppm shift upfield to 4.05 ppm in 5FUR-DSPE due to formation of the amide bond. Similarly, DSPE methylene protons (**g** and **h**) observed at 3.80 and 4.15 ppm can be found in 5FUR-DSPE with resonances like that of the NMR spectra for DSPE. Furthermore, the protons of the terminal methyl groups of DSPE (**a**) have resonances between 0.50-0.60 ppm. The methylene protons of the lipid chain (**b**) are found at the large resonances between 1.30-1.60 ppm. Further downfield the methylene protons in the beta position (**c**) and the methylene protons in the alpha position (**d**) to the ester group on the phospholipid chain appear between 1.45-1.55 ppm and 2.45-2.60 ppm. The characteristic glycerol methine proton (**e**) appears as a resonance at 5.30ppm while methylene protons (**f**) were located on a resonance centred at 3.40 ppm. The methine proton of the sugar moiety of the 5-FUR (**k**) observed as a resonance of 5.75 ppm. The methine protons (**m** and **o**) were found with resonances in a complex section of the spectra between 4.00 – 4.15 ppm. The methylene protons (**l**) adjacent to the primary alcohol of the 5-FUR moiety were observed split onto resonances at 3.70 and 3.85 on the 5FUR spectra, the protons (**l**) shift downfield due to the formation of the ester and can be found with resonances within the complex section of the spectra between 4.00 and 4.20 ppm. The Furthest downfield at 7.79-7.80ppm is the methine proton (**j**) found adjacent to the carbon-fluorine bond. The  $^{13}\text{C}$ -NMR spectrum of 5FUR-DSPE is shown in Figure 6.2 and shows the lipid chain (**d**) carbons resonating on a large peak centred at 28.99-31.81 ppm. The carbonyl carbons (**h**), (**i**), (**j**) and (**k**) from the 6 membered ring of the 5FUR component were found furthest downfield at 124.5, 139.6, 141.4 and 149.3 ppm respectively. The amide carbonyl carbon (**l**) was observed at 157.8ppm. while the ester carbonyls (**m**), (**n**) and (**o**) resonate between 172.5-173.8 ppm. The remaining carbon atoms have been assigned as shown in Figure 6.2. The molecular weight of 5-fluorouridine – DSPE was confirmed via ESI-MS (negative mode), with the base peak at 1090.3 Da corresponding to the  $[\text{M-H}]^-$  peak confirming successful synthesis of 5-fluorouridine – DSPE.

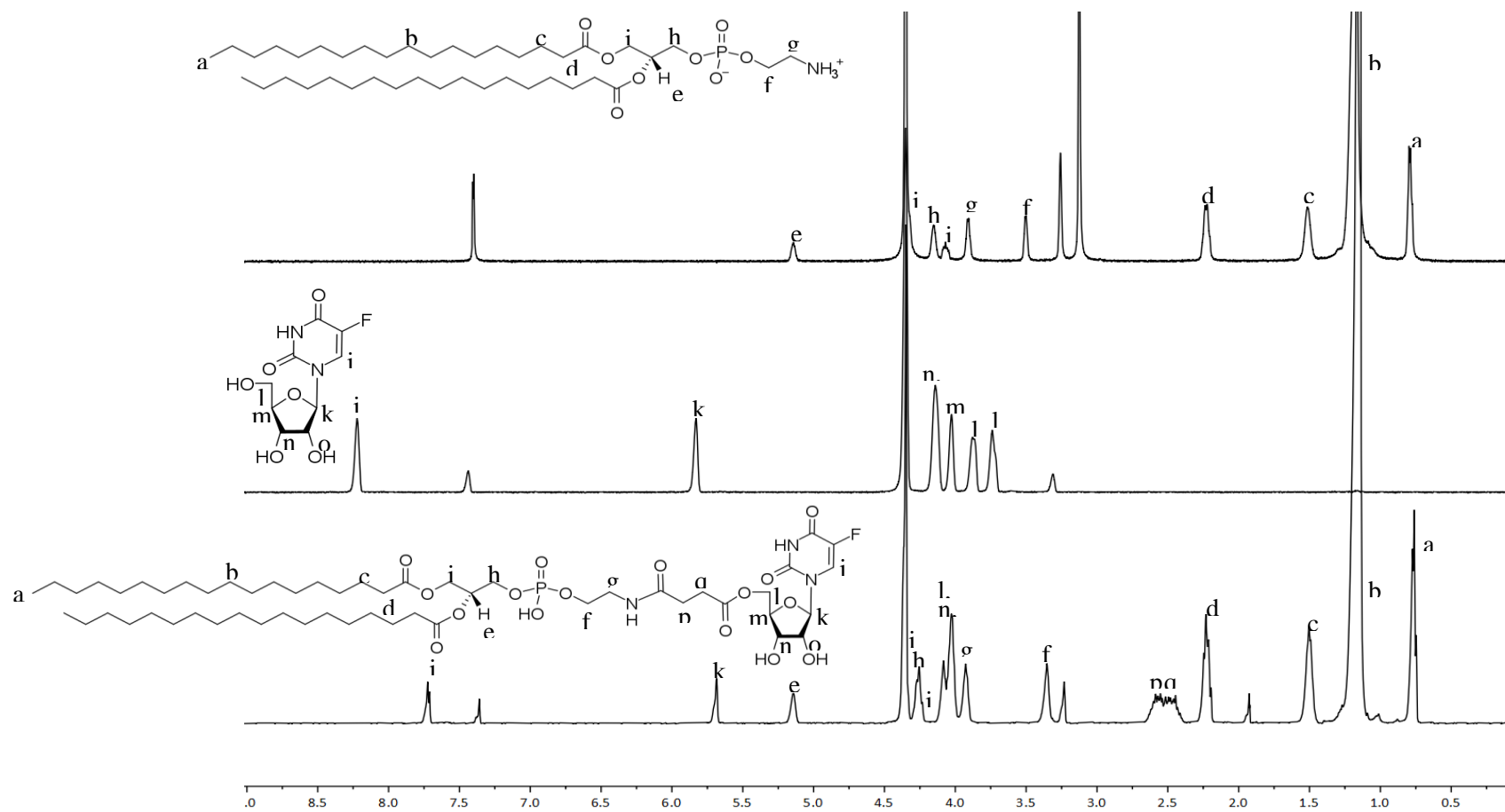


Figure 6.1 Stacked  $^1\text{H}$ -NMR spectra of 5-fluorouridine – DSPE.

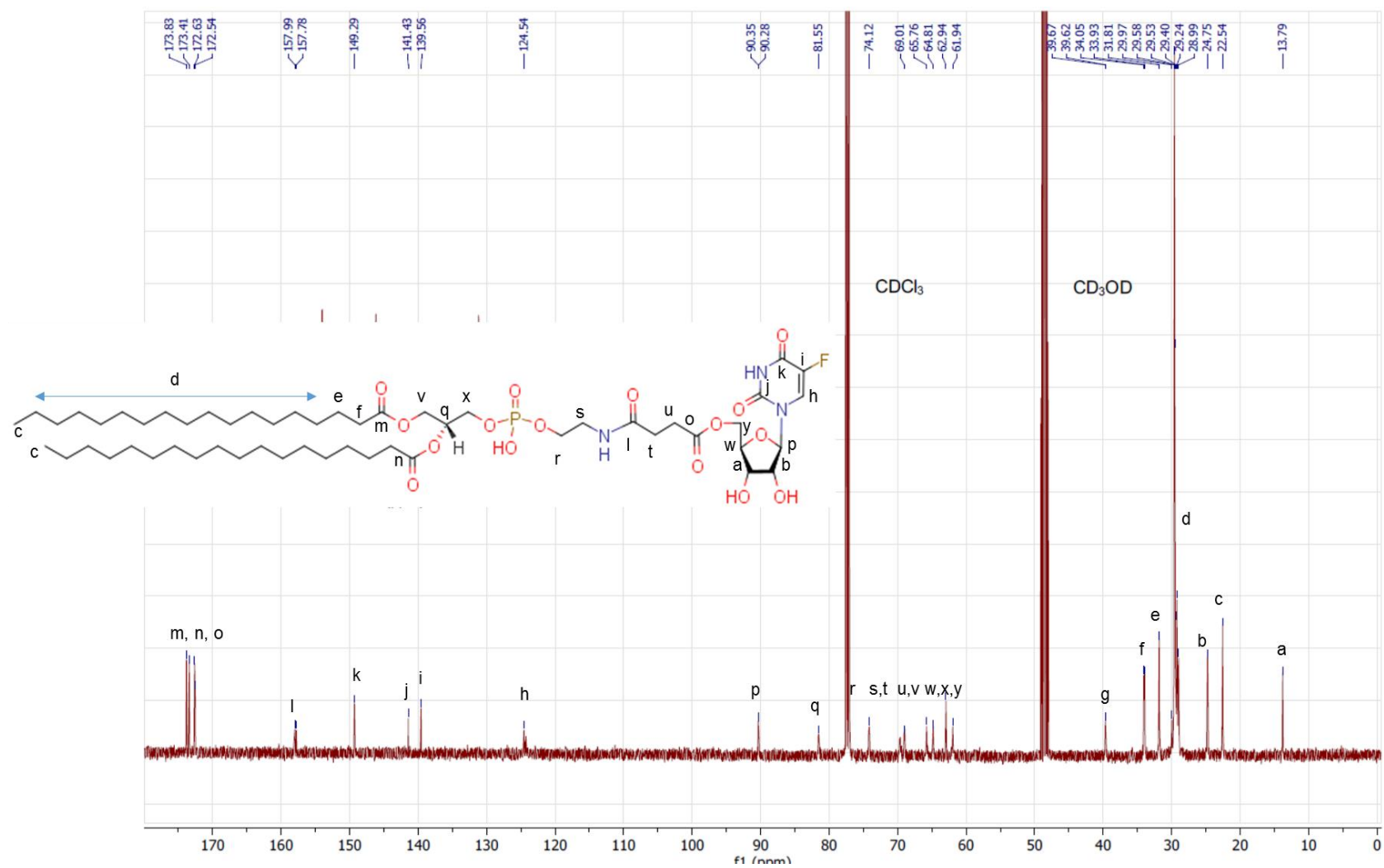


Figure 6.2  $^{13}\text{C}$ -NMR spectra of 5-fluorouridine – DSPE.



KL\_2\_97\_NEG #1-10 RT: 0.01-0.29 AV: 10 NL: 2.61E5  
T: - p ms [ 150.00-2000.00]

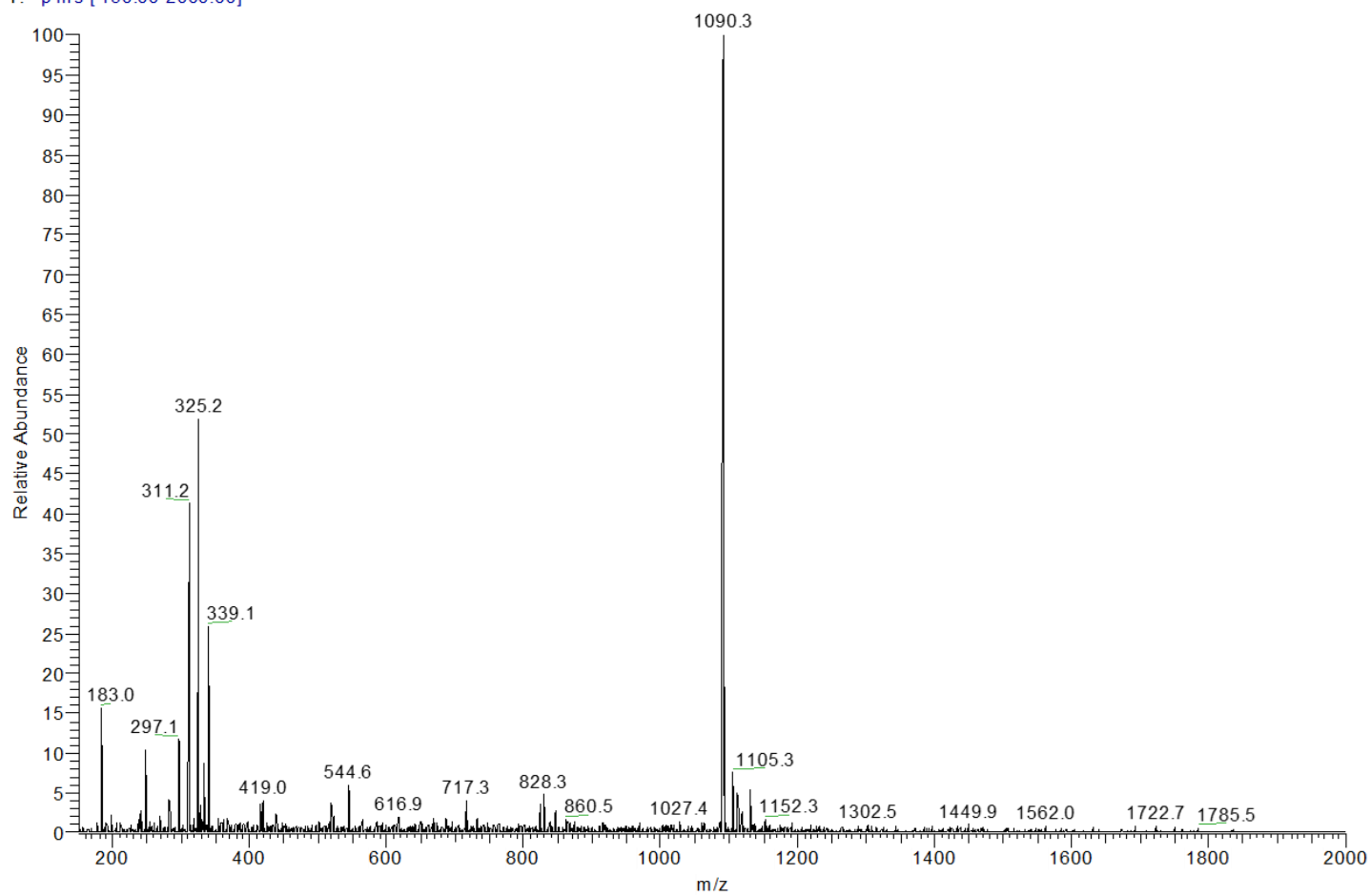
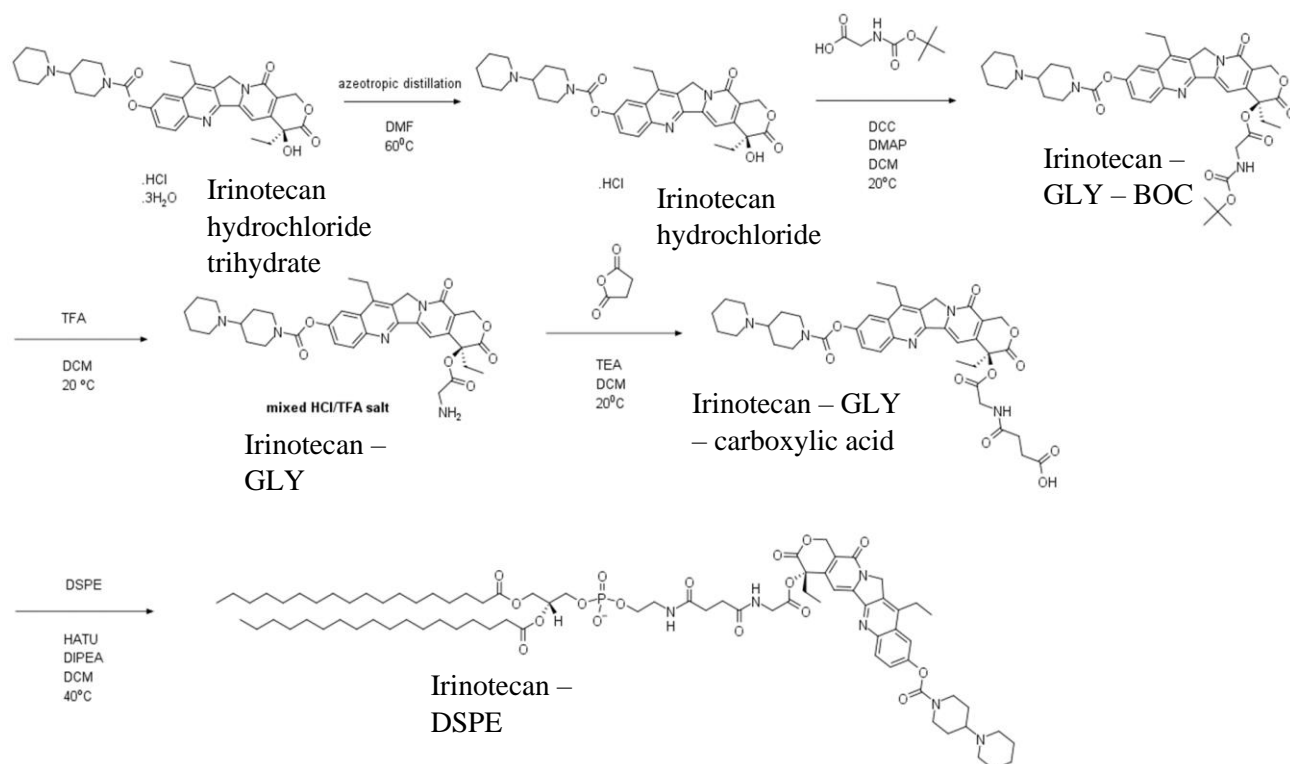


Figure 6.3 ESI-MS spectrum of 5-fluorouridine – DSPE (negative mode).

### 6.3.2 Synthesis of IRIN-DSPE

IRIN-DSPE was synthesised as shown in Scheme 6.2.



Scheme 6.2 for synthesis of IRIN-DSPE.

The first step involved removing the water from IRIN HCL salt trihydrate, by azeotropic distillation using DMF. The carboxylic acid of Boc-protected Glycine (Boc-Gly-OH) was then reacted with the alcohol IRIN to form Irinotecan – GLY – BOC. The Boc group was then removed from the newly introduced glycine component and the resulting primary amine then reacted with succinic anhydride to form carboxylic acid derivative Irinotecan – GLY – carboxylic acid. This carboxylic acid was reacted with the primary amine of the DSPE to produce an amide linkage forming the IRIN-DSPE.

IRIN-DSPE is a large, complicated molecule and assignment by NMR is complex. However, the stacked  $^1\text{H}$ -NMR of DSPE, IRIN and IRIN-DSPE are shown in Figure 6.4 and reveal protons from both the DSPE and IRIN components in the spectrum of IRIN-DSPE,  $^{13}\text{C}$ -NMR and ESI-MS. The NMR spectra for IRIN-DSPE is significantly more complex than 5FUR-DSPE due to the size of the molecule. A large peak at 1.25 ppm represents the protons of the lipid chain (2). The terminal methyl protons of the lipid chain can be found at 0.8 ppm along

with the protons from the methyl group (**1**). The methylene protons on the beta and alpha positions (**3** and **4**) appear as resonances at 1.60 and 2.30 ppm whilst mixed in with other resonances from protons. Some of those protons are from the non-aromatic rings of the IRIN moiety, the protons from the non-aromatic rings that are bonded to carbons not adjacent to the nitrogen atoms have resonances more upfield, the methylene protons at (**22-26**) are found at 2.10 ppm. The remaining protons on these non-aromatic rings adjacent to the nitrogen atom are found further upfield they are labelled as (**16 and 17**) and (**18**) with resonances at 3.30 and 3.10 respectively, the final protons on the non-aromatic rings adjacent to the nitrogen atom are (**20 and 21**) at 3.70 and 3.60 ppm respectively. The characteristic glycerol methine proton has another downfield resonance like what was observed in the  $^1\text{H}$ -NMR for IRIN-DSPE which is labelled (**5**) with a resonance at 5.35 ppm. The other notable resonances are the four signals found furthest downfield. These peaks represent the protons from the aromatic methine protons found on the IRIN moiety, methines (**10-13**) around found between 7.50 and 8.25 ppm. The  $^{13}\text{C}$ -NMR like the  $^1\text{H}$ -NMR for **20** is complex with a large peak at 33.5 ppm reflecting the carbons (**49-62**) that make up the DSPE lipid chain. The terminal methyl carbons are found furthest upfield with a resonance at 18.00 ppm. Carbonyl carbons of the amide (**23**) and the ester (**24**) that are part of the succinic anhydride moiety are found slightly more upfield at 174 and 172 ppm respectively. The remaining carbonyl and aromatic carbons are found on the spectra between 100 and 162 ppm and are labelled accordingly. The remaining carbon atoms are assigned to the corresponding peaks as displayed in Figure 6.5. The molecular weight of IRIN-DSPE was confirmed by ESI-MS (negative mode), the spectrum shown in Figure 6.6 shows there is a major peak at  $m/z$  1471.7 which is representative of the  $(\text{M-H})^-$  peak confirming successful synthesis of IRIN-DSPE.

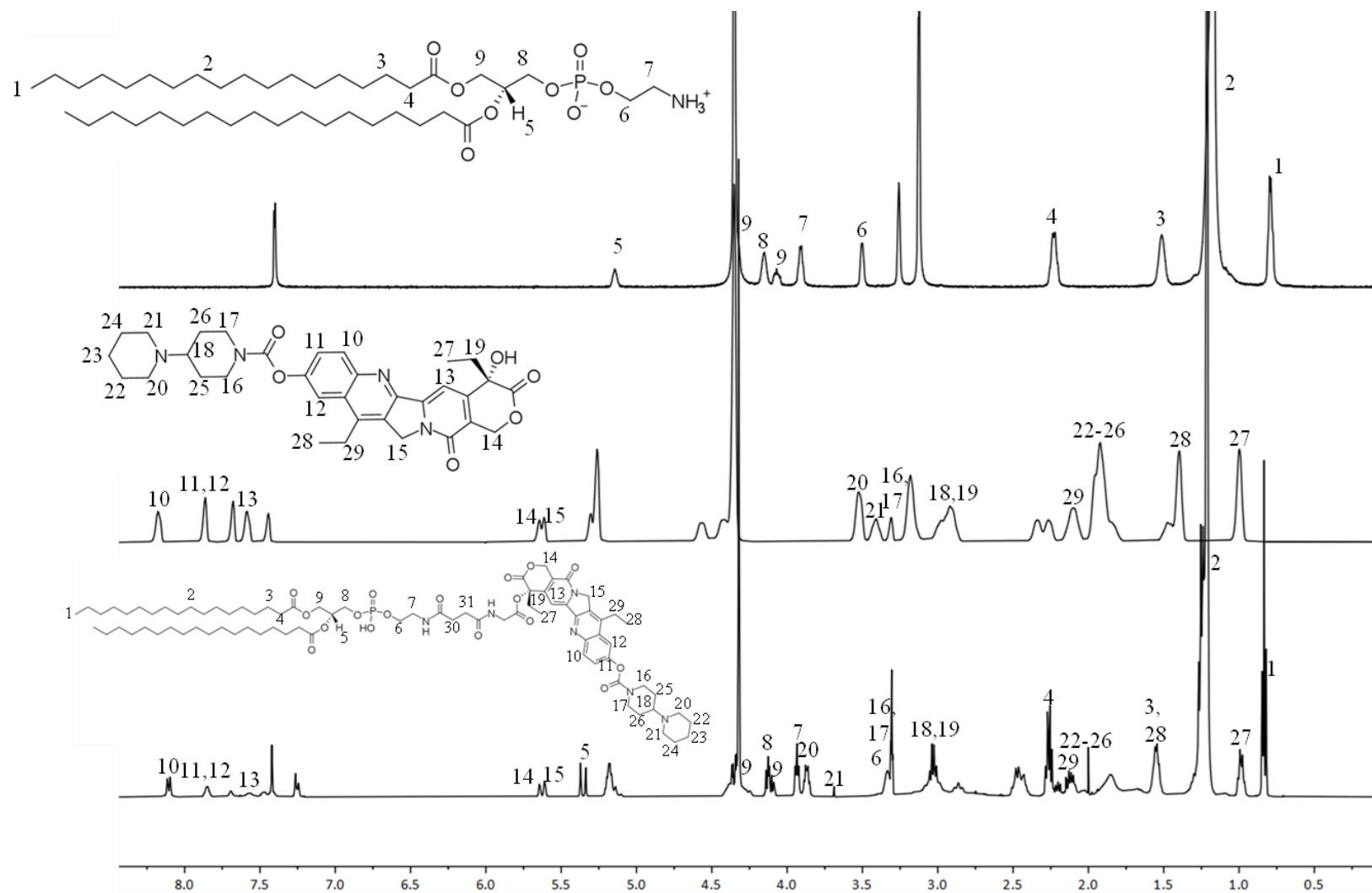


Figure 6.4 Stacked  $^1\text{H}$ -NMR spectra of IRIN-DSPE.

SK-3-133\_Ir-Gly-DSPE\_Pure\_P TLC

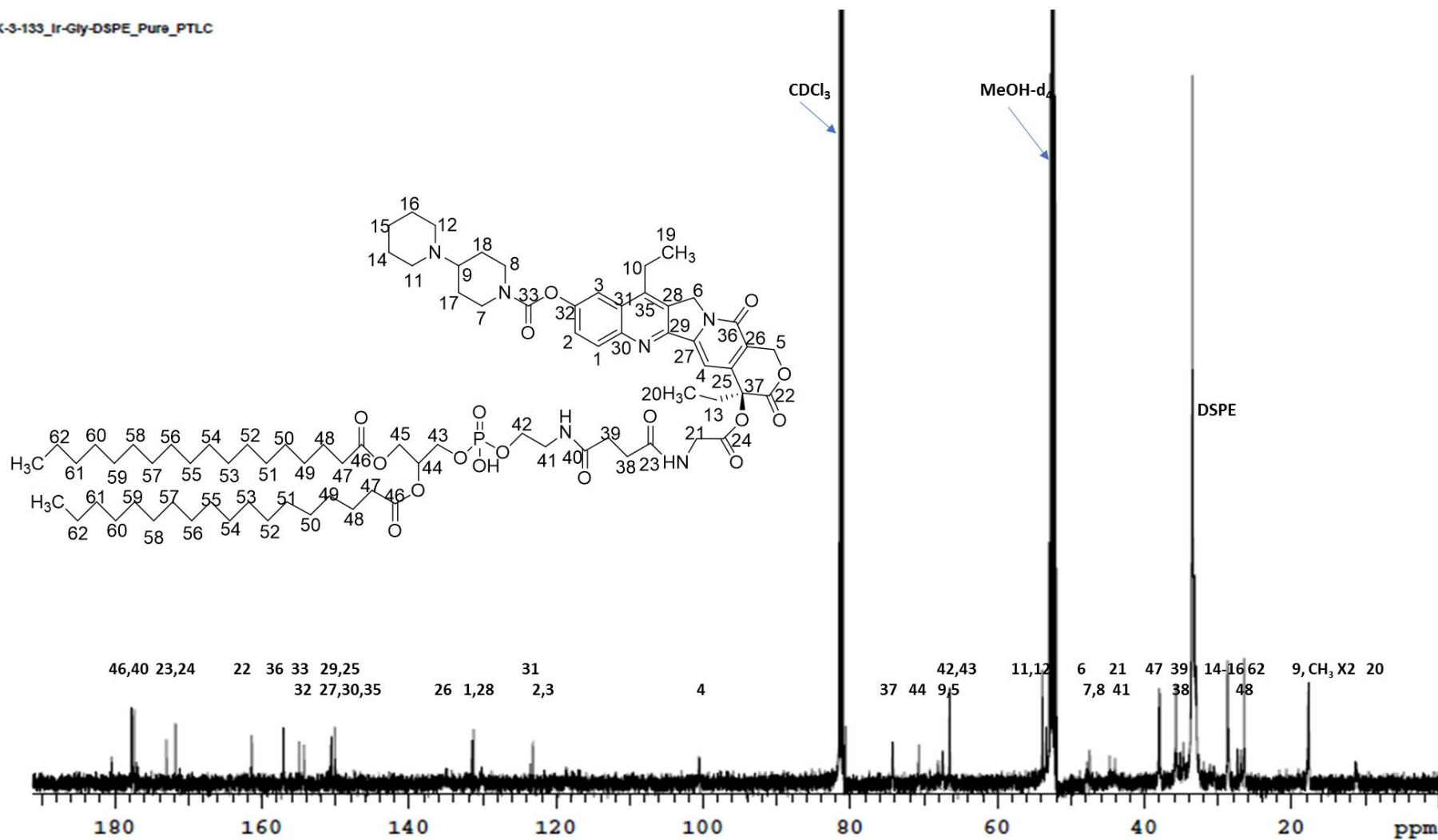


Figure 6.5  $^{13}\text{C}$ -NMR spectra of IRIN-DSPE.

SK-3-133\_A\_NEG#1-10 RT: 0.00-0.18 AV: 10 NL: 6.50E5  
T: - p ms [150.00-2000.00]

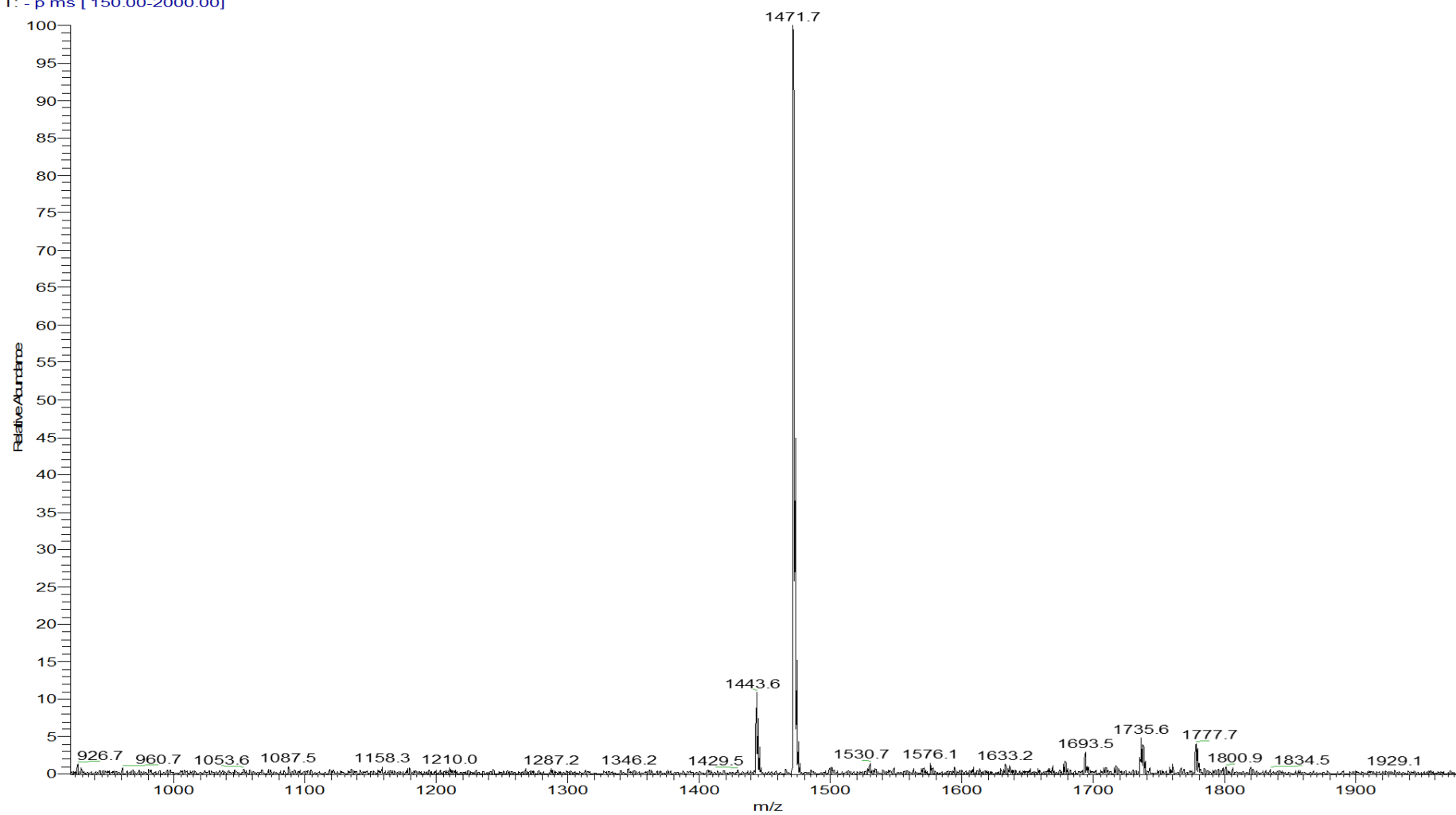


Figure 6.6 ESI-MS spectrum of IRIN-DSPE (negative mode).

### 6.3.3 Preparation of 5FUR-MB-IRIN

The preparation of 5FUR-MB-IRIN was undertaken using a similar method to that used in chapter 4 to produce the DTX-MB-RB but with RB-DSPE and DTX replaced with 5FUR-DSPE and IRIN-DSPE. This means that all drugs will be incorporated within the shell of the MB rather than hydrophobically within the acyl chain layer of the lipids. After a period of development, the 5FUR-DSPE and IRIN-DSPE were incorporated with DBPC, cholesterol and DSPE-PEG(2000) in the ratio described in Table 6.1.

Table 6.1 Formulation for 5FUR-MB-IRIN components.

Components	Mol %	Mass (mg)	Molarity (mM)
DBPC	30	1.0990	1.2188
5FUR-DSPE	25	1.1091	1.0156
IRIN-DSPE	25	1.4959	1.0156
Cholesterol	10	0.1571	0.4063
DSPE-PEG(2000)	10	1.1390	0.4063

#### 6.3.3.1 Characterisation of 5FUR-MB-IRIN

The 5FUR-MB-IRIN pre-MB suspension (Figure 6.7a) was prepared as described in 2.8. and activated by mixing for 45 sec using the VialMix device to produce the 5FUR-MB-IRIN (Figure 6.7b). The MB were imaged using optical microscopy and then analysed using MATLAB software to determine the MB concentration and size (Figure 6.7 c and d). The 5FUR-MB-IRIN pre-MB suspension was slightly cloudy but was similar in appearance to blank MBs (image not shown). After mixing, the 5FUR-MB-IRIN appeared as a white milky suspension that flowed well. Data obtained from MATLAB analysis of the optical microscopic images shows a high yield of MB were produced ( $9.81 \times 10^9$  MB/mL) with a particle size of  $0.98 \mu\text{m} \pm 1.02 \mu\text{m}$ .

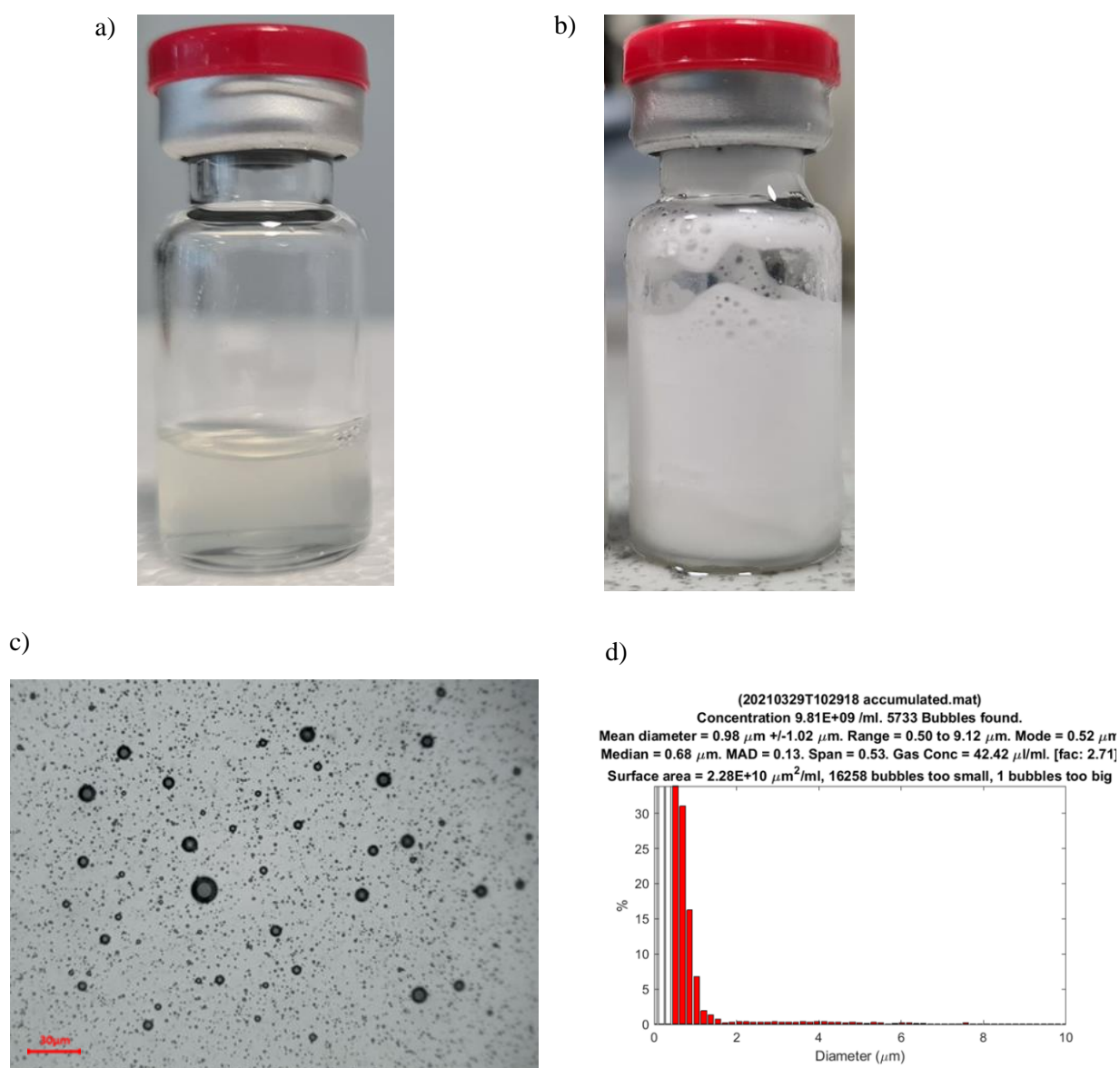


Figure 6.7 5FUR-MB-IRIN produced to determine quality of bubble number and size, a) vial of 5FUR-MB-IRIN liposomes, b) vial of FIRIN MBs, c) 40x optical image of 5FUR-MB-IRIN MBs, d) size distribution of 5FUR-MB-IRIN.



#### 6.3.4 Determination of 37.5°C stability of 5FUR-MB-IRIN

Three batches of 5FUR-MB-IRIN and blank MBs were produced. The MBs were then stored within an incubator for 90 mins at 37.5°C (body temperature). Samples were taken 0, 30, 60, and 90 min, imaged using optical microscopy and subsequently analysed via MATLAB to provide the MB concentration. The results of the study are shown in Figure 6.8 and reveal that while the concentration of the blank MBs reduce to 62.57% after 90 min the 5FUR-MB-IRIN were largely unaffected. This suggests that 5FUR-MB-IRIN are stable at body temperature for durations longer than the half-life of MBs in humans. In addition, it would appear that the incorporation of 5FUR-DSPE and IRIN-DSPE (i.e., in 5FUR-MB-IRIN), in place of DSPC (i.e., in blank MBs), have no adverse effect on MB stability and may even provide additional stability.

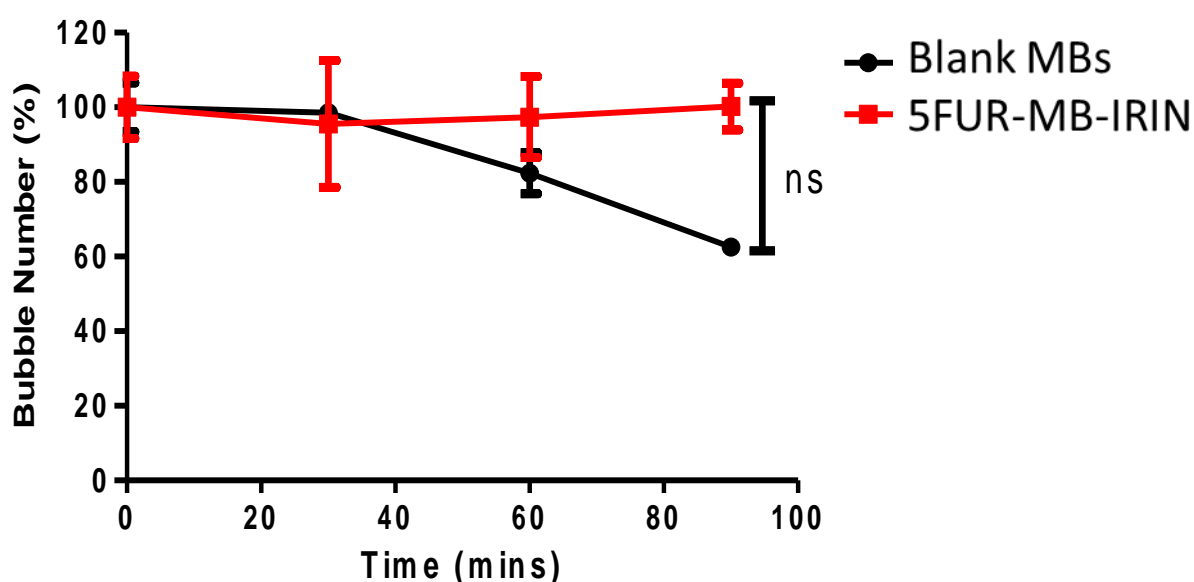


Figure 6.8 Stability of 5FUR-MB-IRIN at 37.5°C. P = ns (n=3).

### **6.3.5 Efficacy determination of 5FUR-MB-IRIN *in vitro* spheroidal DU145 prostate cancer model**

DU145 spheroids were produced in round bottom ultra-low attachment 96 well plates by seeding 5000 cells per well and incubating for 72 hours. At 72 hours the structure of the spheroids was checked and the spheroids were treated. The treatment groups were (i) control, (ii) US only, (iii) blank MBs, (iv) blank MBs + US, (v) 5FUR-MB-IRIN 5 $\mu$ M, (vi) 5FUR-MB-IRIN 5 $\mu$ M + US, (vii) 5FUR-MB-IRIN 10 $\mu$ M, (viii) 5FUR-MB-IRIN 10 $\mu$ M + US, (ix) 5FUR-MB-IRIN 20 $\mu$ M and (x) 5FUR-MB-IRIN 20 $\mu$ M + US. MTT was performed 24 hours later. The US only, blank MBs and blank MBs + US showed small levels of cell viability reduction however they were considered non-significant upon statistical testing. For spheroids treated with MB drug levels at 5 $\mu$ M  $\pm$  US there was a significant reduction in cell viability for the 5FUR-MB-IRIN 5 $\mu$ M + US compared to 5FUR-MB-IRIN 5 $\mu$ M alone (59.9% viable) and (105.9% viable) respectively  $p \geq 0.001$ . An interesting observation was the similarity of the cell viability between 5FUR-MB-IRIN 5 $\mu$ M alone and 5FUR-MB-IRIN 10 $\mu$ M alone 105.9% and 98.1747%, highlighting the impact of US on treatment efficacy. The 5FUR-MB-IRIN 10 $\mu$ M + US showed greater cell viability reduction compared to 5FUR-MB-IRIN 10 $\mu$ M alone 33.6% and 98.2% respectively  $P \geq 0.001$  suggesting that a dose response can be observed, increasing concentration of drug dosage on the spheroids decreases cell viability. When the spheroids were treated with 5FUR-MB-IRIN 20 $\mu$ M alone there is a large reduction in cell viability (34.4% viable), suggesting the toxicity at this concentration can be observed without the penetrative effects of US aiding drug uptake. However, a significant cell viability reduction is observed when US is applied (8.7% viable)  $P \geq 0.01$ . The results of this experiment highlight the efficacy of the 5FUR-MB-IRIN ability to treat DU145 prostate cancer spheroids.

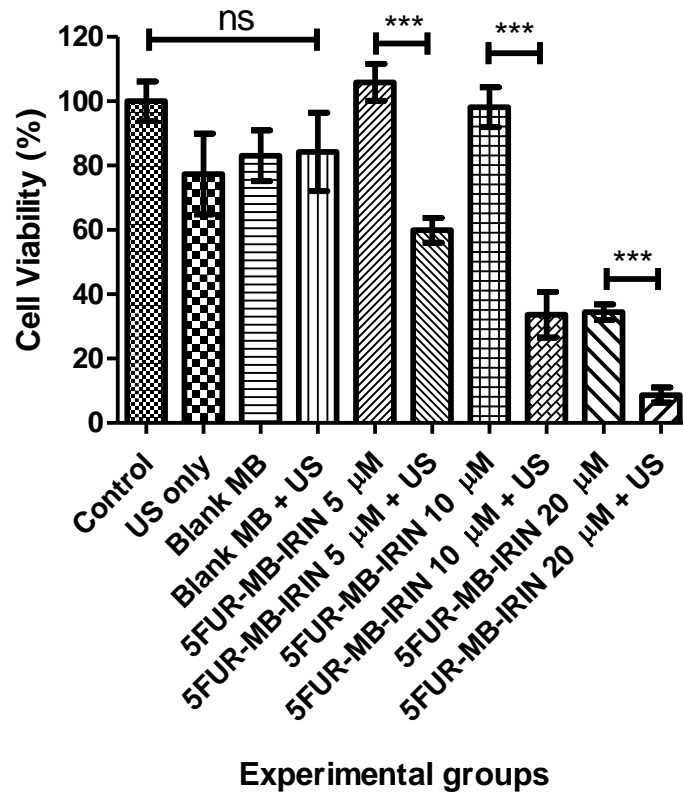


Figure 6.9 DU145 spheroids treated with (i) control, (ii) US only, (iii) blank MB, (iv) blank MB + US, (v) 5FUR-MB-IRIN 5 $\mu$ M, (vi) 5FUR-MB-IRIN 5 $\mu$ M + US, (vii) 5FUR-MB-IRIN 10 $\mu$ M, (viii) 5FUR-MB-IRIN 10 $\mu$ M + US, (ix) 5FUR-MB-IRIN 20 $\mu$ M and (x) 5FUR-MB-IRIN + US. [MB] was  $7.02 \times 10^8$ /mL. N=4. \*\*\* $p \geq 0.001$ .

## 6.4 Conclusion

5FUR and IRIN functionalised DSPE conjugates were prepared and used to successfully prepare a pre-MB suspension that when mixed for 45 sec generated 5FUR-MB-IRIN. These MBs were stable at 37.5°C for 100 min and the efficacy of UTMD mediated treatment was demonstrated in 3D DU145 spheroids. The results show UTMD mediated 5FUR-MB-IRIN treatment to be significantly more effective than 5FUR-MB-IRIN treatment in the absence of ultrasound or UTMD treatment using blank MB. Therefore, the results suggest that inertial cavitation of the 5FUR-MB-IRIN enhance the uptake of the resulting MB shell fragments within the spheroids and the subsequent hydrolysis liberates the 5FUR and IRIN from the lipids. This is important as the functional groups used for attachment of DSPE to the drugs are involved in the ability of the drug to exert its pharmacological effect. 5FUR-MB-IRIN is not a recognised treatment for PCa and this may be in some part to toxic effects associated with this combination. Therefore, targeting delivery of these drugs could provide help reduce systemic side effects. While the results outlined in the 3D spheroid experiment were promising, additional studies are required in murine models to confirm the efficacy and safety of this treatment.

## **Chapter 7:**

### **Conclusions and Future Outlook**

The work in this thesis explored new techniques for incorporating clinically approved cancer therapies and lipid prodrug derivatives of clinically approved cancer therapies, within US-responsive MBs for the treatment of PCa.

Chapter 3 describes the proof of principle for the utility of chemo-SDT mediated UTMD for the treatment of PCa. Synthesis of RB-biotin was carried out to incorporate RB onto the shell of DTX loaded MBs. *In vitro* 3D spheroid model LNCaP-Luc viability determination showed that treatment with DTX-MB-RB + US provided the greatest reduction in cell viability of 72%. DTX-MB-RB + US also showed significantly greater tumour growth control (97.4%) within PC3 tumour bearing mice when compared to mice treated with a standard dose DTX (263.6%) or those animals that were untreated (659.0%). The weights of the mice treated with the DTX-MB-RBs  $\pm$  US showed no significant change whereas those treated with the standard DTX dose showed significant reduction in weight. This is an important observation as the demographic of PCa patients tend to be elderly, many of those patients may have to stop treatment early due to the severity of side effects during treatment.

The main limitation of the work described in chapter 3 was that MB manufacture required the lipid film to be hydrated and MBs to be produced on the day of treatment. This posed logistical issues from a clinical translation perspective. A method where the MBs could be stored or produced in a simpler manner was considered essential for development. An RB-DSPE lipid derivative was synthesised and characterised to directly incorporate RB within the film during the MB preparation. The film was rehydrated producing a solution of MB lipids, RB-DSPE and DTX which was subsequently sonicated to produce a liposomal suspension that could be stored in a vial in a headspace of PFB gas ready for activation. This vial could then be later activated using a VialMix® shaker when required for treatment. The optimal ratio of components was determined with regards to the MB number and size. Successful scale up of the pre-MB liposome suspension was achieved to further improve the clinical suitability of this formulation. The stability of the pre-MB liposome solution was tested over 3 months, no significant difference in liposome size was observed, and the vials produced consistent batches of bubbles once activated over the 3 months.

The results from chapter 5 display the *in vitro* and *in vivo* efficacy of MBs produced using the pre-MB liposome suspension. *In vitro* efficacy was determined using the androgen sensitive cell line LNCaP spheroids which showed that DTX-MB-RB + US had the lowest cell viabilities

at a lower (42%) and higher (29%) treatment concentration of RB and DTX. In the lower concentration treated LNCaP spheroids a synergistic effect was found between SDT and DTX as spheroids treated with DTX-MB reduced to 76% and spheroids treated with MB-RB SDT reduced to 73%. The treatment of the combined DTX-MB-RB + US had a greater reduction in cell viability than the additive effects of the single treatments. A further *in vitro* spheroid model of PCa was tested using the castration resistant cell line DU145 and showed once again that DTX-MB-RB + US was more effective at reducing the cell viability of spheroids at a lower and higher concentration than spheroids treated with other groups. *In vitro* PCa model was used with mice bearing androgen sensitive 22Rv1 tumours. Mice were treated with a combination of DTX-MB-RB and Enz ADT. Mice treated with the combination of DTX-MB-RB + US and Enz showed the greatest tumour growth control of 209%. The combined effect of DTX-MB-RB + US and Enz were greater than the additive effects of mice treated with DTX-MB-RB + US (567%) or mice treated Enz (514%) compared to the untreated mice left untreated (821%). A further *in vivo* experiment carried out in mice bearing PC3 tumours, DTX-MB-RB + US showed further evidence of synergy between SDT and chemotherapy. This was evidenced by the DTX-MB-RB + US producing a 102% greater control than the additive effects of DTX-MB + US and MB-RB + US which were 94% and 258% smaller than the untreated mice, compared to mice treated with DTX-MB-RB + US which were 454% smaller than the untreated mice. Another notable observation was the reduction in mouse weight for those treated with DTX clinical dose, 2 mice had reduced by more than 20% and had to be culled for ethical reasons, whilst the mice treated with DTX-MB-RB + US tolerated their treatment well. A toxicity determination of DTX-MB-RB + US was carried out by treating mice following the same treatment regimen used for the PC3 tumour control experiment. Mice treated with DTX clinical dose once again showed a reduction in weight, however, all groups showed no reduction in UREA or ALT at days 10 and 15. Whole blood and serum analysis at days 10 and 15 showed no difference between mice that were left untreated, or those that received DTX clinical dose or DTX-MB-RB on a wide array of markers. Finally, MBs were produced with the fluorescent tag IR780 replacing DTX to determine the ability of MBs to deliver DTX and RB to mice bearing 22Rv1 tumours. There was an increase in the fluorescence observed on the tumour when compared vs background fluorescence suggesting that MBs in the presence of US can increase the uptake of drugs incorporated within the MBs. To further the work carried out in chapter 3-5 investigations into GMP grade production should be carried out alongside

liaising with a contract development and manufacturing organization (CDMO) in which specialises in micro formulations. The pre-clinical and manufacturing data obtained could then be used to inform a potential clinical trial through contact with a regulatory body such as the MHRA.

The work in chapter 6 was carried out to determine how robust the pre-MB liposomal suspension method is for the incorporation of a wider range of cancer therapies. 5-FUR-DSPE and IRIN-DSPE were successfully synthesised and characterised. MBs were produced using the VialMix® loaded with both 5-FUR and IRIN and showed acceptable MB numbers, size and stability. *In vitro* efficacy was determined in DU145 spheroids. It was observed that at a high and low concentration of drug the 5FUR-MB-IRIN + US provided the greatest reduction in cell viability. Chapter 6 shows the early onset of the ability to load a wider range of cancer therapies, to further this work to inform larger studies several steps could be taken. Firstly, the combination of 5-FUR-DSPE and/or IRIN-DSPE with RB-DSPE to determine chemo-SDT with chemotherapeutic drugs other than Taxanes could show potential for optimising chemo-SDT and to apply it to a wider range of cancers. *In vivo* preclinical studies for both toxicology and efficacy would give a greater insight to the potential capability of reducing the side effects of IRIN and 5-FUR whilst simultaneously improving the efficacy.

The use of MBs has been shown to be highly effective for the treatment of PCa. The clinical translation was improved by developing the pre-MB liposome suspension method, providing a minimum 3-month shelf life. It has been demonstrated that MBs could be formulated with a wide range of drugs, that could be DSPE functionalised or incorporated within the hydrophilic acyl layer of the MB. An outlook from this could be the ability to utilise drugs with serious solubility issues. The ability to use a lower concentration of drug due to the increased uptake with MBs payloads delivered with targeted US could allow for the reintroduction of drugs deemed too potent. To further this work, attempting to DSPE functionalise a wider range of cancer therapies and testing those formulations on a wider range of cancers as well as PCa, to determine the range of applications of the pre-MB liposome suspension activated with VialMix®.



## **Chapter 8:**

## **References**

1. World Health Organization. Cancer [Internet]. 2022 [cited 2022 Nov 05]. Available from: <https://www.who.int/news-room/fact-sheets/detail/cancer>
2. Cancer Research UK. Cancer mortality statistics [Internet]. [cited 2022 Nov 05]. Available from: <https://www.cancerresearchuk.org/health-professional/cancer-statistics/mortality>
3. Macmillan Cancer Support. Causes and risk factors [Internet]. 2018 [cited 2022 Nov 05]. Available from: <https://www.macmillan.org.uk/cancer-information-and-support/worried-about-cancer/causes-and-risk-factors>
4. NHS. Cancer [Internet]. 2022 [cited 2022 Nov 05]. Available from: <https://www.nhs.uk/conditions/cancer/>
5. Cooper GM. The Cell: A Molecular Approach. 2<sup>nd</sup> ed. Sinauer Associates; 2000.
6. Fouad YA, Aanei C. Revisiting the hallmarks of cancer. American Journal of Cancer Research. 2017 May 1; 7(5): 1016-1036.
7. Hanahan D, Weinberg RA. Hallmarks of Cancer: The Next Generation. Cell. 2011 Mar 04; 144(5): 646-674.
8. VanDyke D, Kyriacopulos P, Yassini B, Wright A, Burkhart E, Jacek S, et al. Nanoparticle Based Combination Treatments for Targeting Multiple Hallmarks of Cancer. International Journal of Nano Studies & Technology. 2016 Aug 19: 1-18.
9. Barrueto L, Caminero F, Cash L, Makris C, Lamichhane P, Deshmukh RR. Resistance to Checkpoint Inhibition in Cancer Immunotherapy. Translational Oncology. 2020 Mar; 13(3).
10. Lines JL, Sempere LF, Wang L, Pantazi E, Mak, J, O'Connell S et al. VISTA is an immune checkpoint molecule for human T cells. Cancer Research. 2014 Oct 1; 74(7): 1924-1932.
11. Aaron L, Franco O, Hayward SW. Review of Prostate Anatomy and Embryology and the Etiology of BPH. Urologic Clinics of North America. 2017 Aug 1; 43(3): 279-288.

12. Centers for Disease Control and Prevention. Prostate Cancer [Internet]. 2022 [cited 2022 Nov 05]. Available from: [https://www.cdc.gov/cancer/prostate/basic\\_info/what-is-prostate-cancer.htm](https://www.cdc.gov/cancer/prostate/basic_info/what-is-prostate-cancer.htm)
13. Levin RJ. Prostate-induced orgasms: A concise review illustrated with a highly relevant case study. *Clinical Anatomy*. 2017 Dec 20; 31(1): 81-85.
14. Cancer Research UK. Prostate cancer statistics [Internet]. [cited 2022 Nov 05]. Available from: <https://www.cancerresearchuk.org/health-professional/cancer-statistics/statistics-by-cancer-type/prostate-cancer#heading-Zero>
15. Cancer Research UK. Prostate cancer mortality statistics [Internet]. [cited 2022 Nov 05]. Available from: <https://www.cancerresearchuk.org/health-professional/cancer-statistics/statistics-by-cancer-type/prostate-cancer/mortality>
16. Cancer Research UK. Breast cancer mortality statistics [Internet]. [cited 2022 Nov 05]. Available from: <https://www.cancerresearchuk.org/health-professional/cancer-statistics/statistics-by-cancer-type/breast-cancer/mortality>
17. Prostate Cancer UK. As prostate cancer deaths hit all-time high, we renew our MANifesto [Internet]. 2020 [cited 2022 Nov 05]. Available from: <https://prostatecanceruk.org/about-us/news-and-views/2020/1/as-12-000-men-die-in-one-year-we-renew-our-manifesto>
18. Gann PH. Risk Factors for Prostate Cancer. *Nature Reviews Urology*. 2002; 4.
19. National Institute for Health and Care Excellence. Prostate cancer: diagnosis and management [Internet]. 2021 [cited 2022 Nov 05]. Available from: [https://www.nice.org.uk/guidance/ng131/chapter/Context#:~:text=More%20than%2050%25%20of%20prostate,Ireland%20\(2010%20to%202014\)](https://www.nice.org.uk/guidance/ng131/chapter/Context#:~:text=More%20than%2050%25%20of%20prostate,Ireland%20(2010%20to%202014))
20. Kheirandish P, Chinegwundoh F. Ethnic differences in prostate cancer. *British Journal of Cancer*. 2011 Aug 09; 105(4): 481-485.
21. Guy M, Kote-Jarai Z, Giles GG, Olama AAA, Jugurnauth SK, Mulholland S et al. Identification of new genetic risk factors for prostate cancer. *Asian Journal of Andrology*. 2009 Jan; 11(1): 49-55.

22. Pacheco SOS, Pacheco FJ, Zapata GMJ, Garcia JME, Previale CA, Cura HE et al. Food Habits, Lifestyle Factors, and Risk of Prostate Cancer in Central Argentina: A Case Control Study Involving Self-Motivated Health Behaviour Modifications after Diagnosis. *Nutrients*. 2016 Jul; 8(7): 419.
23. Hughes C, Murphy A, Martin C, Sheils O, O’Leary J. Molecular pathology of prostate cancer. *Journal of Clinical Pathology*. 2005 Jul; 58(7): 673-684.
24. Xu B, Tong N, Li J, Zhang Z, Wu H. ELAC2 polymorphisms and prostate cancer risk: a meta-analysis based on 18 case-control studies. *Prostate Cancer and Prostatic Diseases*. 2010 Sept; 13(3): 270-277.
25. Korver W, Guevara C, Chen Y, Neuteboom S, Bookstein R, Tavtigian S et al. The product of the candidate prostate cancer susceptibility gene ELAC2 interacts with the  $\gamma$ -tubulin complex. *International Journal of Cancer*. 2003 Feb 04; 104(3): 283-288.
26. Korver W, Guevara C, Chen Y, Neuteboom S, Bookstein R, Tavtigian S et al. The product of the candidate prostate cancer susceptibility gene ELAC2 interacts with the  $\gamma$ -tubulin complex. *International Journal of Cancer*. 2003 Feb 04; 104(3): 283-288.
27. Chakrabarti A, Jha BK, Silverman RH. New Insights into the Role of RNase L in Innate Immunity. *Journal of Interferon & Cytokine Research*. 2011 Jan; 31(1): 49-57.
28. Zho L, Ren K, Bai Y, Zhang L, Zou J, Qin X et al. Association of a common genetic variant in RNASEL and prostate cancer susceptibility. *Oncotarget*. 2017 Sept 26; 8(43): 75141-75150.
29. Guo M, Hartlova A, Gierlinski M, Prescott A, Castellvi J, Losa JH et al. Triggering MSR1 promotes JNK-mediated inflammation in IL-4-activated macrophages. *The EMBO Journal*. 2019 Jun 03; 38(11).
30. Chrzanowska KH, Gregorek H, Dembowska-Baginska B, Kalina MA, Digweed M. Nijmegen breakage syndrome (NBS). *Orphanet Journal of Rare Disease*. 2012; 7.
31. Masi A, Antoccia A. NBS1 Heterozygosity and Cancer Risk. *Current Genomics*. 2008 Jun; 9(4): 275-281.

32. Kobayashi J, Antoccia A, Tauchi H, Matsuura S, Komatsu K. NBS1 and its functional role in the DNA damage response. *DNA Repair*. 2004 Aug-Sept; 3(8-9): 855-861.
33. Zilfou JT, Lowe SW. Tumor Suppressive Functions of p53. *Cold Spring Harbor Perspectives in Biology*. 2009 Nov; 1(5).
34. Ozaki T, Nakagawara A. Role of p53 in Cell Death and Human Cancers. *Cancers*. 2011 mar; 3(1): 994-1013.
35. National Library of Medicine. ELAC2 *elaC* ribonuclease Z 2 [*Homo sapiens* (human)] [Internet]. 2022 [cited 2022 Nov 05]. Available from: <https://www.ncbi.nlm.nih.gov/gene/60528>
36. Wang L, McDonnell SK, Elkins DA, Slager SL, Christensen E, Marks AF et al. Role of HPC2/ELAC2 in Hereditary Prostate Cancer. *Cancer Research*. 2001 Sept 01; 61(17), 6494-6499.
37. Chin D, Boyle GM, Parsons PG, Coman WB. What is transforming growth factor-beta (TGF-beta)? *British Journal of Plastic Surgery*. 2004 Apr; 57(3): 215-221.
38. National Library of Medicine. RNASEL ribonuclease L [*Homo sapiens* (human)] [Internet]. 2022 [cited 2022 Nov 05]. Available from: <https://ghr.nlm.nih.gov/gene/RNASEL>
39. Liu X, Zheng D, Lu G, Yang B. The RNASEL – 1385G/A polymorphism is associated with risk of prostate cancer in Africans. *OncoTargets and Therapy*. 2018; 11: 97-102.
40. National Library of Medicine. MSR1 macrophage scavenger receptor 1 [*Homo sapiens* (human)] [Internet]. 2022 [cited 2022 Nov 05]. Available from: <https://ghr.nlm.nih.gov/gene/MSR1>
41. National Library of Medicine. Nijmegen breakage syndrome [Internet]. 2017 [cited 2022 Nov 05]. Available from: <https://medlineplus.gov/genetics/condition/nijmegen-breakage-syndrome>

42. Cybulski C, Gorski B, Debniak T, Gliniewicz B, Mierzejewski M, Masojc B et al. NBS1 Is a Prostate Cancer Susceptibility Gene. *Cancer Research*. 2004 Feb 15; 64(4): 1215-1219.
43. Varon R, Vissinga C, Platzer M, Cerosaletti KM, Chrzanowska KH, Saar K et al. Nibrin, a Novel DNA Double-Strand Break Repair Protein, Is Mutated in Nijmegen Breakage Syndrome. *Cell*. 1998 May 01; 93(3): 467-476.
44. National Library of Medicine. CHEK2 checkpoint kinase 2 [*Homo sapiens* (human)] [Internet]. 2022 [cited 2022 Nov 05]. Available from: <https://www.ncbi.nlm.nih.gov/gene/11200>
45. Mathews LA, Selvaratnam R, Jones DR, Akimoto M, McConkey BJ, Melacini G et al. A Novel Non-canonical Forkhead-associated (FHA) Domain-binding Interface Mediates the Interaction between Rad53 and Dbf4 Proteins. *Journal of Biological Chemistry*. 2014 Jan 31; 289(5): 2589-2599.
46. National Center for Biotechnology Information (US). Genes and Disease [Internet]. Bethesda (MD): National Center for Biotechnology Information (US); 1998-. The p53 tumor suppressor protein.
47. National Library of Medicine. TLR4 toll like receptor 4 [*Homo sapiens* (human)] [Internet]. 2022 [cited 2022 Nov 05]. Available from: <https://www.ncbi.nlm.nih.gov/gene?Db=gene&Cmd=DetailsSearch&Term=7099>
48. Manolakis AC, Kapsoritakis AN, Tiaka EK, Sidiropoulos A, Gerovassili A, Satra M et al. TLR4 gene polymorphisms: evidence for protection against type 2 diabetes but not for diabetes-associated ischaemic heart disease. *European Journal of Endocrinology*. 2001; 165: 261-267.
49. National Library of Medicine. CDKN1B gene [Internet]. 2013 [cited 2022 Nov 05]. Available from: <https://medlineplus.gov/genetics/gene/cdkn1b/>
50. Abbastabar M, Kheyrollah M, Azizian K, Bagherlou N, Tehrani SS, Maniati M et al. Multiple functions of p27 in cell cycle, apoptosis, epigenetic modification, and transcriptional regulation for the control of cell growth: A double-edged sword protein. *DNA Repair*. 2018 Sept; 69: 63-72.

51. National Library of Medicine. AR gene [Internet]. 2015 [cited 2022 Nov 05]. Available from: <https://medlineplus.gov/genetics/gene/ar/>
52. Davey RA, Grossmann M. Androgen Receptor Structure, Function and Biology: From bench to Bedside. *The Clinical Biochemist Reviews*. 2016 Feb; 37(1): 3-15.
53. National Library of Medicine. CYP17A1 gene [Internet]. 2016 [cited 2022 Nov 05]. Available from: <https://medlineplus.gov/genetics/gene/cyp17a1/>
54. Jadvar H. Molecular Imaging of Prostate Cancer: A Concise Synopsis. *Molecular Imaging*. 2009 Mar-Apr; 8(2): 56-64.
55. National Library of Medicine. SRD5A2 gene [Internet]. 2008 [cited 2022 Nov 05]. Available from: <https://medlineplus.gov/genetics/gene/srd5a2/>
56. Hsing AW, Chen C, Chokkalingam AP, Gao Y, Dightman DA, Hguyen HT. Polymorphic Markers in the SRD5A2 Gene and Prostate Cancer Risk: A population-based Case-control Study. *Cancer Epidemiology Biomarkers & Prevention*. 2001 Oct 01; 10(10): 1077-1082.
57. Dunne DW, Shaw A, Bockenstedt LK, Allore HG, Chen S, Malawista SE et al. Increased TLR4 Expression and Downstream Cytokine Production in Immunosuppressed Adults Compared to Non-Immunosuppressed Adults. *PLoS One*. 2010; 5(6).
58. Rakoff-Nahoum S, Medzhitov R. Toll-like receptors and cancer. *Nature Reviews Cancer*. 2008 Dec 04; 9: 57-63.
59. Ou T, Lilly M, Jiang W. The Pathologic Role of Toll-Like Receptor 4 in Prostate Cancer. *Frontiers in Immunology*. 2018; 9: 1188.
60. Hua D, Liu M, Cheng Z, Qin X, Zhang H, Chen Y et al. Small interfering RNA-directed targeting of Toll-like receptor 4 inhibits human prostate cancer cell invasion, survival, and tumorigenicity. *Molecular Immunology*. 2009 Sept; 46(15): 2876-2884.
61. Chiarle R, Pagano M, Inghirami G. The cyclin dependent kinase inhibitor p27 and its prognostic role in breast cancer. 2000 Dec 20; 3(91).

62. Kibel AS, Suarez BK, Belani J, Oh J, Webster R, Brophy-Ebbers M et al. CDKN1A and CDKN1B Polymorphisms and Risk of Advanced Prostate Carcinoma. *Cancer Research*. 2003; 63(9): 2033-2036.
63. Sirma H, Broemel M, Stumm L, Tsourlakis T, Steurer S, Tennstedt P. Loss of CDKN1B/p27Kip1 expression is associated with ERG fusion-negative prostate cancer but is unrelated to patient prognosis. *Oncology Letters*. 2013 Nov; 6(5): 1245-1252.
64. Weng H, Li S, Huang J, He Z, Meng X, Cao Y et al. Androgen receptor gene polymorphisms and risk of prostate cancer: a meta-analysis. *Scientific Reports*. 2017; 7.
65. Tirabassi G, Cignarelli A, Perrini S, Muti ND, Furlani G, Gallo M et al. Influence of CAG Repeat Polymorphism on the Targets of Testosterone Action. *International Journal of Endocrinology*. 2015.
66. Vasaitis TS, Bruno RD, Njar VCO. CYP17 inhibitors for prostate cancer therapy. *The Journal of Steroid Biochemistry and Molecular Biology*. 2011 May; 125(1-2): 23-31.
67. Stanford JL, Noonan EA, Iwasaki L, Kolb S, Chadwick RB, Feng Z et al. A Polymorphism in the CYP17 Gene and Risk of Prostate Cancer. *Cancer Epidemiology Biomarkers & Prevention*. 2002; 11(3): 243-247.
68. Haiman CA, Stampfer MJ, Giovannucci E, Ma J, Decalo NE, Kantoff PW et al. The relationship between a polymorphism in CYP17 with plasma hormone levels and prostate cancer. *Cancer Epidemiology, Biomarkers & Prevention*. 2001 Jul; 10(7): 743-748.
69. Walsh AL, Considine SW, Thomas AZ, Lynch TH, Manecksha RP. Digital rectal examination in primary care is important for early detection of prostate cancer: a retrospective cohort analysis study. *British Journal of General Practice*. 2014 Dec; 64(629): 783-787.
70. Ilic D, Djulbegovic M, Jung JH, Hwang EC, Zhou Q, Cleves A et al. Prostate cancer screening with prostate-specific antigen (PSA) test: a systematic review and meta-analysis. 2018 Sept 05; 362.



71. Magnani CJ, Li K, Seto T, McDonald KM, Blayney DW, Brooks JD et al. Prostate-Specific Antigen Testing Use and Prostate Cancer Diagnostic Stage Following the 2012 USPSTF Guideline Changes. *Journal of the National Comprehensive Cancer Network*. 2019 Jul 01; 17(7): 795-803.
72. Martin RM, Donovan JL, Turner EL, Metcalfe C, Young GJ, Walsh EI et al. Effect of a Low-Intensity PSA-Based Screening Intervention on Prostate Cancer Mortality. 2018 Mar 06; 319(9):883-895.
73. Delahunt B, Miller RJ, Srigley JR, Evans AJ, Samaratunga H. Gleason grading; past, present and future. *Histopathology*. 2012 Jan; 60(1); 75-86.
74. Epstein JI, Zelefsky MJ, Sjoberg DD, Nelson JB, Egevad L, Magi-Galluzzi C et al. A Contemporary Prostate Cancer Grading System: A Validated Alternative to the Gleason Score. *European Urology*. 2016 Mar; 69(3): 428-435.
75. American Cancer Society. Understanding Your Pathology Report: Prostate Cancer [Internet]. 2017 [cited 2022 Nov 05]. Available from: <https://www.cancer.org/treatment/understanding-your-diagnosis/tests/understanding-your-pathology-report/prostate-pathology/prostate-cancer-pathology.html>
76. Stark JR, Perner S, Stampfer MJ, Sinnott JA, Finn S, Eisenstein AS. Gleason Score and Lethal Prostate Cancer: Does  $3 + 4 = 4 + 3$ ? *Journal of Clinical Oncology*. 2009 Jul 20; 27(21): 3459-3464.
77. Prostate Cancer UK. MRI scan [Internet]. 2022 [cited 2022 Nov 05]. Available from: <https://prostatecanceruk.org/prostate-information/prostate-tests/mri-scan>
78. Kumar V, Bora GS, Kumar R, Jagannathan NR. Multiparametric (mp) MRI of prostate cancer. *Progress in Nuclear Magnetic Resonance Spectroscopy*. 2018 Apr; 105: 23-40.
79. Cancer Research UK. TNM staging for prostate cancer [Internet]. 2022 [cited 2022 Nov 05]. Available from: <https://www.cancerresearchuk.org/about-cancer/prostate-cancer/stages/tnm-staging>

80. Saoud R, Heidar NA, Cimadamore A, Paner GP. Incorporating Prognostic Biomarkers into Risk Assessment Models and TNM Staging for Prostate Cancer. *Cells*. 2020 Sept; 9(9); 2116.
81. Roberts MJ, Teloken P, Chambers SK, Williams SG, Yaxley J, Samaratunga H et al. Prostate Cancer Detection. [Updated 2018 Jun 11]. In: Feingold KR, Anawalt B, Boyce A, et al., editors. Endotext [Internet]. Available from: <https://www.ncbi.nlm.nih.gov/books/NBK279042/>
82. Prostate Cancer UK. Watchful waiting [Internet]. 2019 [cited 2022 Nov 05]. Available from: <https://prostatecanceruk.org/prostate-information/treatments/watchful-waiting>
83. Prostate Cancer UK. Active surveillance [Internet]. 2019 [cited 2022 Nov 05]. Available from: <https://prostatecanceruk.org/prostate-information/treatments/active-surveillance>
84. Loeb S, Zhou Q, Siebert U, Rochau U, Jahn B, Muhlberger N et al. Active Surveillance Versus Watchful Waiting for Localized Prostate Cancer: A Model to Inform Decisions. *European Urology*. 2017 Dec; 72(6): 899-907.
85. Wilt TJ, Thompson IM. Clinically localised prostate cancer. *British Medical Journal*. 2006 Nov 25; 333(7578): 1102-1106.
86. Tourinho-Barbosa R, Srougi V, Nunes-Silva I, Baghdadi M, Rembeye G, Eiffel SS et al. Biochemical recurrence after radical prostatectomy: what does it mean? *International Brazilian Journal of Urology*. 2018 Jan-Feb; 44(1): 14-21.
87. American Cancer Society. Surgery for Prostate Cancer [Internet]. 2019 [cited 2022 Nov 05]. Available from: <https://www.cancer.org/cancer/prostate-cancer/treating/surgery.html>
88. Schraudenbach P, Bermejo CE. Management of the complications of radical prostatectomy. *Current Urology Reports*. 2007 May; 8(3): 197-202.
89. Frey AU, Sonksen J, Fode M. Neglected side effects after radical prostatectomy: a systematic review. *Journal of Sexual Medicine*. 2014 Feb; 11(2): 374-385.

90. Baskar R, Lee KA, Yeo R, Yeoh K. Cancer and Radiation Therapy: Current Advances and Future Directions. *International Journal of Medical Sciences*. 2012; 9(3): 193-199.
91. Artibani W, Porcaro AB, De Marco V, Cerruto MA, Siracusano S. Management of Biochemical Recurrence after Primary Curative Treatment for Prostate Cancer: A Review. *Urologia Internationalis*. 2018; 100: 251-262.
92. Prostate Cancer UK. If your prostate cancer comes back [Internet]. 2019 [cited 2022 Nov 05]. Available from: <https://prostatecanceruk.org/prostate-information/treatments/if-your-prostate-cancer-comes-back>
93. Darwish QM, Raj GV. Management of biochemical recurrence after primary localised therapy for prostate cancer. *Frontiers in Oncology*. 2012 May 23; 2(48).
94. Van den Broeck T, Van den Bergh RCN, Briers E, Cornford P, Cumberbatch M, Tilki D et al. Biochemical Recurrence in Prostate Cancer: The European Association of Urology Prostate Cancer Guidelines Panel Recommendations. 2020 Mar 15; 6(2):231-234.
95. National Institute for Health and Care Excellence. Prostate Cancer: Scenario: Management [Internet]. 2022 [cited 2022 Nov 05]. Available from: <https://cks.nice.org.uk/topics/prostate-cancer/management/management/>
96. Westesson KE, Stephenson AJ. Salvage Therapy for Prostate Cancer. *Oncology & Hematology Reviews*. 2013; 9(1): 21-25.
97. Kowalczyk KJ, Gu X, Nguyen PL, Lipsitz SR, Trinh Q, Lynch JH et al. Optimal timing of early versus delayed adjuvant radiotherapy following radical prostatectomy for locally advanced prostate cancer. *Urologic Oncology*. 2014 Apr; 32(3): 303-308.
98. Vogel MME, Kessel KA, Schiller K, Deveck M, Gschwend JE, Weichert W et al. Adjuvant versus early salvage radiotherapy: outcome of patients with prostate cancer treated with postoperative radiotherapy after radical prostatectomy. *Radiation Oncology*. 2019; 14(198).
99. Thompson IM, Tangen CM, Paradelo J, Lucia MS, Miller G, Troyer D et al. Adjuvant Radiotherapy for Pathologic T3N0M0 Prostate Cancer Significantly Reduces Risk of

- Metastases and Improves Survival: Long-term Follow up of a Randomized Clinical Trial. *Journal of Urology*. 2009 Mar; 181(3); 956-962.
100. Thompson IM, Tangen CM, Paradelo J, Lucis S, Miller G, Troyer D et al. Adjuvant Radiotherapy for Pathologically Advanced Prostate Cancer: A Randomized Clinical Trial. *Journal of the American Medical Association*. 2006 Nov 15; 296(19): 2329-2335.
  101. Bolla M, Van Poppel H, Tombal B, Vekemans K, Da Pozzo L, De Reijke TM et al. Postoperative radiotherapy after radical prostatectomy for high risk prostate cancer: long-term results of a randomised controlled trial (EORTC trial 22911). *The Lancet*. 2012; 380(9858): 2018-2027.
  102. Chargari C, Deutsch E, Blanchard P, Gouy S, Martelli, H, Guerin F et al. Brachytherapy: An overview for clinicians. *CA: A Cancer Journal for Clinicians*. 2019 Jul 30; 69(5): 386-401.
  103. Park DS. Current Status of Brachytherapy for Prostate Cancer. *Korean Journal of Urology*. 2012 Nov 14; 53(11): 743-749.
  104. Gray C, Campbell K. High Dose Rate Brachytherapy versus Low Dose Rate Brachytherapy for the Treatment of Prostate Cancer: A Review of Clinical Effectiveness and Cost-Effectiveness. *CADTH Rapid Response Report: Summary with Critical Appraisal*. 2019 Feb 14.
  105. Zhong J, Slevin F, Scarsbrook AF, Serra M, Choudhury A, Hoskin PJ et al. Salvage Reirradiation Options for Locally Recurrent Prostate Cancer: A Systematic Review. *Frontiers in Oncology*. 2021 Sept 09; 11.
  106. American Cancer Society. Cryotherapy for Prostate Cancer [Internet]. 2019 [cited 2022 Nov 05]. Available from: <https://www.cancer.org/cancer/prostate-cancer/treating/cryosurgery.html>
  107. Cytron S, Greene D, Witzsch U, Nylund P, Johansen TEB. Cryoablation of the prostate: technical recommendations. *Prostate Cancer and Prostatic Diseases*. 2009 Sept 01; 12: 339-346.

108. Jones JS, Rewcastle JC, Donnelly BJ, Lugnani FM, Pisters LL, Katz AE. Whole gland primary prostate cryoablation: initial results from the cryo on-line data registry. *Journal of Urology*. 2008 Aug; 180(2): 554-558.
109. Tan WP, ElShafei A, Aminsharifi A, Khalifa AO, Polascik TJ. Salvage Focal Cryotherapy Offers Similar Short-term Oncological Control and Improved Urinary Function Compared to Salvage Whole Gland Cryotherapy for Radiation Resistant/Recurrent Prostate Cancer. *Clinical Genitourinary Cancer*. 2020 Jun; 18(3): 260-265.
110. Prostate Cancer UK. High-intensity focused ultrasound (HIFU) [Internet]. 2020 [cited 2022 Nov 05]. Available from: <https://prostatecanceruk.org/prostate-information/treatments/hifu>
111. Maestroni U, Morandin F, Ferretti S, Dinale F, Ziglioli F. Recurrence of prostate cancer after HIFU. Proposal of a novel predictive index. *ACTA Biomedica*. 2018; 89(2): 220-226.
112. National Institute for Health and Care Excellence. High-intensity focused ultrasound for prostate cancer [Internet]. 2005 [cited 2022 Nov 05]. Available from: <https://www.nice.org.uk/guidance/ipg118>
113. Blana A, Murat FJ, Walter B, Thuroff S, Wieland WF, Chaussy C et al. First Analysis of the Long-Term Results with Transrectal HIFU in Patients with Localised Prostate Cancer. *European Urology*. 2008 Jun; 53(6): 1194-1203.
114. Chalasani V, Martinez CH, Lim D, Chin J. Salvage HIFU for recurrent prostate cancer after radiotherapy. *Prostate Cancer and Prostatic Disease*. 2008 Oct 14; 12: 124-129.
115. Mauri G, Nicosia L, Xu, Z, Di Pietro S, Monfardini L, Bonomo G et al. Focused ultrasound: tumour ablation and its potential to enhance immunological therapy to cancer. *The British Journal of Radiology*. 2018 Mar; 91(1083).
116. Ng J, Dai T. Radiation therapy and the abscopal effect: a concept comes of age. *Annals of Translational Medicine*. 2016 Mar; 4(6): 118.

117. Eranki A, Srinivasan P, Ries M, Kim A, Lazarski CA, Rossi CT et al. High-Intensity Focused Ultrasound (HIFU) Triggers Immune Sensitization of Refractory Murine Neuroblastoma to Checkpoint Inhibitor Therapy. *Clinical Cancer Research*. 2020 March 1; 26(5): 1152-1161.
118. Orrason AW, Westerberg M, Garmo H, Lissbrant IF, Robinson D, Stattin P. Changes in treatment and mortality in men with locally advanced prostate cancer between 2000 and 2016: a nationwide, population-based study in Sweden. *Urological Oncology*. 2020 Apr 10; 126(1): 142-151.
119. Prostate Cancer UK. Locally advanced prostate cancer [Internet]. 2022 [cited 2022 Nov 05]. Available from: <https://prostatecanceruk.org/prostate-information/just-diagnosed/locally-advanced-prostate-cancer>
120. Payne H. Management of locally advanced prostate cancer. *Asian Journal of Andrology*. 2008 Dec 01; 11(1): 81-87.
121. Kent EC, Hussain MHA. Neoadjuvant Therapy for Prostate Cancer: An Oncologist's Perspective. *Reviews in Urology*. 2009; 5.
122. Gandaglia G, Abdollah F, Schiffmann J, Trudeau V, Shariat SF, Kim SP et al. Distribution of metastatic sites in patients with prostate cancer: A population-based analysis. *Prostate*. 2014 Feb; 74(2): 210-216.
123. Park JC, Eisenberger MA. Advances in the Treatment of Metastatic Prostate Cancer. *Mayo Clinic Proceedings*. 2015 Dec 01; 90(12), 1719-1733.
124. Yamada Y, Beltran H. The treatment landscape of metastatic prostate cancer. *Cancer Letters*. 2021 Oct 28; 519: 20-29.
125. Sweeney CJ, Chen Y, Carducci M, Liu G, Jarrard DF, Eisenberger M. Chemohormonal Therapy in Metastatic Hormone-Sensitive Prostate Cancer. *The New England Journal of Medicine*. 2015 Aug 20; 373: 737-746.
126. James ND, Sydes MR, Clarke NW, Mason MD, Dearnaley DP, Spears MR et al. Addition of docetaxel, zoledronic acid, or both to first-line long-term hormone therapy in prostate cancer (STAMPEDE): survival results from an adaptive, multiarm,

- multistage, platform randomised controlled trial. *The Lancet*. 2016 Mar; 387(10024): 1163-1177.
127. Sharifi N, Gulley JL, Dahut WL. Androgen Deprivation Therapy for Prostate Cancer. *The Journal of the American Medicine Association*. 2005 July 13; 294(2): 238-244.
  128. Crawford ED. Hormonal Therapy in Prostate Cancer: Historical Approaches. *Reviews in Urology*. 2004; 6.
  129. Schroder F, Crawford ED, Axcrone K, Payne H, Keane TE. Androgen deprivation therapy: past, present, and future. 2012 Jun 04.
  130. Rice MA, Malhotra SV, Stoyanova T. Second-Generation Antiandrogens: From Discovery to Standard of Care in Castration Resistant Prostate Cancer. *Frontiers in Oncology*. 2019 Aug 28; 9: 801.
  131. National Institute for Health and Care Excellence. Bicalutamide [Internet]. 2022 [cited 2022 Nov 05]. Available from: <https://bnf.nice.org.uk/drugs/bicalutamide/>
  132. Penson DF, Armstrong AJ, Concepcion R, Agarwal N, Olsson C, Dunshee LK et al. Enzalutamide Versus Bicalutamide in Castration-Resistant Prostate Cancer: The STRIVE Trial. *Journal of Clinical Oncology*. 2016 Jun 20; 34(18): 2098-2106.
  133. National Library of Medicine. Compound Summary - Docetaxel [Internet]. [cited 2022 Nov 05]. Available from: <https://pubchem.ncbi.nlm.nih.gov/compound/Docetaxel>
  134. Kenmotsu H, Tanigawara Y. Pharmacokinetics, dynamics, and toxicity of docetaxel: Why the Japanese dose differs from the Western dose. *Cancer Science*. 2015 May; 106(5): 497-504.
  135. Dagher R, Li N, Abraham S, Rahman A, Sridhara R, Pazdur R. Docetaxel in Combination with Prednisone for the Treatment of Androgen-Independent Hormone-Refractory Prostate Cancer. *Clinical Cancer Research*. 2004 Dec 15; 10(24): 8147-8151.

136. Cancer Research UK. Yew clippings to make chemotherapy [Internet]. 2020 [cited 2022 Nov 05]. Available from: <https://www.cancerresearchuk.org/about-cancer/cancer-in-general/treatment/chemotherapy/yew-clippings>
137. Yared JA, Tkaczuk KHR. Update on taxane development: new analogs and new formulations. *Drug Design, Development and Therapy*. 2012; 6: 371-384.
138. Ohi R, Zanic M. Ahead of the Curve: New Insights into Microtubule Dynamics. *F1000 Research*. 2016; 5.
139. National Institute for Health and Care Excellence. Docetaxel [Internet]. [cited 2022 Nov 05]. Available from: <https://bnf.nice.org.uk/drugs/docetaxel/>
140. Wang Y, Yu Y, Li G, Li S, Wu C, Gigant B. Mechanism of microtubule stabilization by taccalonolide AJ. *Nature Communications*. 2017 Jun 06; 8.
141. Maahs L, Sanchez BE, Gupta N, Van Harn M, Barrack ER, Reddy P et al. Class III  $\beta$ -tubulin expression as a predictor of docetaxel-resistance in metastatic castration-resistant prostate cancer. *PLoS One*. 2019 Oct 28; 14(10).
142. Stanton RA, Gernert KM, Nettles JH, Aneja R. Drugs That Target Dynamic Microtubules: A New Molecular Perspective. *Medicinal Research Reviews*. 2011 May; 31(3): 443-481.
143. Hardwick JM, Soane L. Multiple Functions of BCL-2 Family Proteins. *Cold Spring Harbor Perspectives in Biology*. 2013 Feb; 5(2).
144. Ruvoilo PP, Deng X, May WS. Phosphorylation of Bcl2 and regulation of apoptosis. *Leukemia*. 2001 May 01; 15: 515-522.
145. Lin Y, Fukuchi J, Hiipakka RA, Kokontis JM, Xiang J. Up-regulation of Bcl-2 is required for the progression of prostate cancer cells from an androgen-dependent to an androgen-independent growth stage. *Cell Research*. 2007 Apr 03; 17: 531-536.
146. Van Tellingen O, Beijnen JH, Verwij J, Scherrenburg EJ, Nooijen WJ, Sparreboom A. Rapid Esterase-sensitive Breakdown of Polysorbate 80 and its Impact on the Plasma Pharmacokinetics of Docetaxel and Metabolites in Mice. *Clinical Cancer Research*. 1999 Oct; 5(10): 2918-2924.



147. Sibaud V, Leboeuf NR, Roche H, Belum VR, Gladieff L, Deslandres M et al. Dermatological adverse events with taxane chemotherapy. *European Journal of Dermatology*. 2016 Oct 1; 26(5): 427-443.
148. Cancer Research UK. Paclitaxel (Taxol) [Internet]. 2019 [cited 2022 Nov 05]. Available from: <https://www.cancerresearchuk.org/about-cancer/cancer-in-general/treatment/cancer-drugs/drugs/paclitaxel>
149. Cancer Research UK. Docetaxel (Taxotere) [Internet]. 2019 [cited 2022 Nov 05]. Available from: <https://www.cancerresearchuk.org/about-cancer/cancer-in-general/treatment/cancer-drugs/drugs/docetaxel>
150. Zhong L, Li Y, Xiong L, Wang W, Wu M, Yuan T. Small molecules in targeted cancer therapy: advances, challenges, and future perspectives. 2021 May 31; 6.
151. Quirke VM. Tamoxifen from Failed Contraceptive Pill to Best-Selling Breast Cancer Medicine: A Case-Study in Pharmaceutical Innovation. *Frontiers in Pharmacology*. 2017 Sept 12; 8.
152. Joo WD, Visintin I, Mor G. Targeted cancer therapy – Are the days of systemic chemotherapy numbered? *Maturitas*. 2013 Dec; 76(4): 308-314.
153. National Cancer Institute. Targeted Therapy to Treat Cancer [Internet]. 2022 [cited 2022 Nov 05]. Available from: <https://www.cancer.gov/about-cancer/treatment/types/targeted-therapies>
154. Student S, Hejmo T, Poteręła-Hejmo A, Lesniak A, Bułdak R. Anti-androgen hormonal therapy for cancer and other diseases. *European Journal of Pharmacology*. 2020 Jan 05; 866.
155. McCubrey JA, Steelman LS, Chappell WH, Sun L, Davis NM, Abrams SL. Advances in Targeting Signal Transduction Pathways. *Oncotarget*. 2012 Dec; 3(12): 1505-1521.
156. Babur O, Demir E, Gonen M, Sander C, Dogrusoz U. Discovering modulators of gene expression. *Nucleic Acids Research*. 2010 Sept; 38(17): 5648-5656.

157. Kasibhatla S, Gourdeau H, Meerovitch K, Drewe J, Reddy S, Qiu L et al. Discovery and mechanism of action of novel series of apoptosis inducers with potential vascular targeting activity. *Molecular Cancer Therapeutics*. 2004 Nov; 3(11): 1365-1374.
158. Cook KM, Figg WD. Angiogenesis Inhibitors – Current Strategies and Future Prospects. *CA: A Cancer Journal for Clinicians*. 2010 Jul-Aug; 60(4): 222-243.
159. Esfahani K, Roudaia L, Buhlaiga N, Del Rincon SV, Papneja N, Miller Jr WH. A review of cancer immunotherapy: from the past, to the present, to the future. *Current Oncology*. 2020 Apr; 27.
160. Chau CH, Steeg PS, Figg WD. Antibody-drug conjugates for cancer. *The Lancet*. 2019 Aug 31; 394(10200): 793-804.
161. Allison RR, Moghissi K. Photodynamic Therapy (PDT): PDT Mechanisms. *Clinical Endoscopy*. 2013 Jan; 46(1): 24-29.
162. Ash C, Dubec M, Donne K, Bashford T. Effect of wavelength and beam width on penetration in light-tissue interaction using computational methods. *Lasers in Medical Science*. 2017; 32(8): 1909-1918.
163. Sugimoto H, Hasebe H, Furuyama T, Fujii M. Direct Excitation of Triplet State of Molecule by Enhanced Magnetic Field of Dielectric Metasurfaces. *Nano Micro Small*. 2021 Oct 13.
164. Kwiatkowski S, Knap B, Przystupski D, Saczko J, Kedzierska E, Knap-Czop K. Photodynamic therapy – mechanisms, photosensitizers and combinations. *Biomedicine & Pharmacotherapy*. 2018 Oct; 106: 1098-1107.
165. Schieber M, Chandel NS. ROS Function in Redox Signaling and Oxidative Stress. *Current Biology*. 2014 May 19; 24(10): 453-462.
166. Zhang W, Xiao S, Ahn DU. Protein oxidation: basic principles and implications for meat quality. *Clinical Reviews in Food Science and Nutrition*. 2013; 53(11): 1191-1201.
167. Auten RL, Davis JM. Oxygen Toxicity and Reactive Oxygen Species: The Devil is in the Details. *Pediatric Research*. 2009 Aug; 66: 121-127.

168. Qiang Y, Yow CMN, Huang Z. Combination of photodynamic therapy and immunomodulation – current status and future trends. *Medicinal Research Reviews*. 2008 Jul; 28(4): 632-644.
169. Brown SG, Rogowska AZ, Whitelaw DE, Lees WR, Lovat LB, Ripley P et al. Photodynamic therapy for cancer of the pancreas. *Gut*. 2002 Apr; 50(4): 549-557.
170. Speed CA. Therapeutic ultrasound in soft tissue lesions. *Rheumatology*. 2001 Dec; 40(12): 1331-1336.
171. Yan P, Liu L, Wang P. Sonodynamic Therapy (SDT) for Cancer Treatment: Advanced Sensitizers by Ultrasound Activation to Injury Tumor. *Applied Bio Materials*. 2020 May 07; 3(6): 3456-3475.
172. Liu Y, Kon T, Li C, Zhong P. High intensity focused ultrasound-induced gene activation in sublethally injured tumor cells *in vitro*. *The Journal of the Acoustical Society of America*. 2005 Nov; 118(5): 3328-3336.
173. Costly D, McEwan C, Fowley C, McHale AP, Atchison J, Nomikou N et al. Treating cancer with sonodynamic therapy: A review. *International Journal of Hyperthermia*. 2015 Jan 13; 31(2).
174. Misik V, Riesz P. Free Radical Intermediates in Sonodynamic Therapy. *Annals of the New York Academy of Sciences*. 2006 Jan 25; 899(1): 335-348.
175. Wan G, Liu Y, Chen B, Liu Y, Wang Y, Zhang N. Recent advances of sonodynamic therapy in cancer treatment. *Cancer Biology & Medicine*. 2016 Sept; 13(3): 325-338.
176. Giuntini F, Foglietta F, Marucco AM, Troia A, Dezhkunov NV, Pozzoli et al. Insight into ultrasound-mediated reactive oxygen species generation by various metal-porphyrin complexes. *Free Radical Biology and Medicine*. 2018 Jun; 121: 190-201.
177. Umemura S, Yumita N, Nishigaki R, Umemura K. Mechanism of Cell Damage by Ultrasound in Combination with Hematoporphyrin. *Japanese Journal of Cancer Research*. 1990 Sept; 81(9): 962-966.
178. Beguin E, Shrivastava S, Dezhkunov NV, McHale AP, Callan JF, Stride E. Direct Evidence of Multibubble Sonoluminescence Using Therapeutic Ultrasound and

- Microbubbles. *ACS Applied Materials & Interfaces*. 2019 Jun 05; 11(22): 19913-19919.
179. National Library of Medicine. Compound Summary – 2,3,4,5-Tetrachloro-6-(3-hydroxy-2,4,5,7-tetraiodo-6-oxo-xanthen-9-yl)benzoic acid [Internet]. [cited 2022 Nov 05]. Available from: <https://pubchem.ncbi.nlm.nih.gov/compound/25474>
  180. Doughty MJ. Rose Bengal staining as an assessment of ocular surface damage and recovery in dry eye disease – A review. *Contact Lens and Anterior Eye*. 2013 Dec; 36(6): 272-280.
  181. Chang C, Yang Y, Yang J, Wu H, Tsai T. Absorption, and emission spectral shifts of rose Bengal associated with DMPC liposomes. *Dyes and Pigments*. 2008 Nov; 79(2): 170-175.
  182. McEwan C, Nesbitt H, Nicholas D, Kavanagh ON, McKenna K, Loan P et al. Comparing the efficacy of photodynamic and sonodynamic therapy in non-melanoma and melanoma skin cancer. *Bioorganic & Medicinal Chemistry*. 2016 Jul 01; 24(13): 3023-3028.
  183. Sirsi S, Borden M. Microbubble Compositions, Properties and Biomedical Applications. *Bubble Science, Engineering & Technology*. 2009 Nov; 1(1-2): 3-17.
  184. Xu Q, Nakajima M, Ichikawa S, Nakamura N, Shiina T. A comparative study of microbubble generation by mechanical agitation and sonication. *Innovative Food Science & Emerging Technologies*. 2008 Oct; 9(4): 489-494.
  185. Wilson SR, Barr RG. Contrast-Enhanced Ultrasonography of the Abdomen: Ready for Prime Time! *Advances in Clinical Radiology*. 2020 Sept; 2: 213-233.
  186. Unger EC, Matsunaga TO, McCreery T, Schumann P, Sweitzer R, Quigley R. Therapeutic applications of microbubbles. *European Journal of Radiology*. 2002 May; 42(2): 160-168.
  187. Martin KH, Dayton PA. Current Status and Prospects for Microbubbles in Ultrasound Theranostics. *Wiley Interdisciplinary Reviews Nanomedicine and Nanobiotechnology*. 2013 Jul-Aug; 5(4).

188. Lee H, Kim H, Han H, Lee M, Lee S, Yoo H, Chang JH et al. Microbubbles used for contrast enhanced ultrasound and theragnosis: a review of principles to applications. *Biomedical Engineering Letters*. 2017 May; 7(2): 59-69.
189. Sirsi S, Borden M. Microbubble Compositions, Properties and Biomedical Applications. *Bubble Science, Engineering & Technology*. 2009 Nov; 1(1-2): 3-17.
190. Carovac A, Smajlovic F, Junuzovic D. Application of Ultrasound in Medicine. *ACTA Informatica Medica*. 2011 Sept; 19(3): 168-171.
191. Kossoff G. Basic Physics and Imaging Characteristics of Ultrasound. *World Journal of Surgery*. 2014 Feb 14; 24: 134-142.
192. O'Brien WD. Ultrasound – biophysics mechanisms. *Progress in Biophysics and Molecular Biology*. 2007; 93(1-3): 212-255.
193. Pinton G, Aubry J, Bossy E, Muller M, Pernot M, Tanter M. Attenuation, scattering, and absorption of ultrasound in the skull bone. *American Association of Physicists in Medicine*. 2011; 39(1): 299-307.
194. Patey SJ, Corcoran JP. Physics of ultrasound. *Anaesthesia and Intensive Care Medicine*. 2020 Dec 06; 22(1): 58-63.
195. Yamaguchi T, Kitahara S, Kusuda K, Okamoto J, Horise Y, Masamune J et al. Current Landscape of Sonodynamic Therapy for Treating Cancer. *Cancers*. 2021 Dec; 13(24): 6184.
196. Wang M, Zhang Y, Cai C, Tu J, Guo X, Zhang D. Sonoporation-induced cell membrane permeabilization and cytoskeleton disassembly at varied acoustic and microbubble-cell parameters. *Scientific Reports*. 2018 Mar 01; 8.
197. Brujan EA, Ikeda T, Matsumoto Y. Jet formation and shock wave emission during collapse of ultrasound-induced cavitation bubbles and their role in the therapeutic applications of high-intensity focused ultrasound. *Physics in medicine & Biology*. 2005 Sept 28; 50(20).

198. Yang Y, Li Q, Guo X, Tu J, Zhang D. Mechanisms underlying sonoporation: Interaction between microbubbles and cells. *Ultrasonics Sonochemistry*. 2020 Oct; 67.
199. Tomizawa M, Shinozaki F, Motoyoshi Y, Sugiyama T, Yamamoto S, Sueishi M. Sonoporation: Gene transfer using ultrasound. *World Journal of Methodology*. 2013 Dec 26; 3(4): 39-44.
200. Chowdhury SM, Abou-Elkacem L, Lee T, Dahl J, Lutz AM. Ultrasound and microbubble mediated therapeutic delivery: Underlying mechanisms and future outlook. *Journal of Controlled Release*. 2020 Oct 10; 326: 75-90.
201. Nesbitt H, Sheng Y, Kamila S, Logan K, Thomas K, Callan B et al. Gemcitabine loaded microbubbles for targeted chemo-sonodynamic therapy of pancreatic cancer. *Journal of Controlled Release*. 2018 Jun 10; 279: 8-16.
202. McEwan C, Kamila S, Owen J, Nesbitt H, Callan B, Borden M et al. Combined sonodynamic and antimetabolite therapy for the improved treatment of pancreatic cancer using oxygen loaded microbubbles as a delivery vehicle. *Biomaterials*. 2016 Feb; 80: 20-32.
203. Logan K, Foglietta F, Nesbitt H, Sheng Y, McKaig T, Kamila S et al. Targeted chemo-sonodynamic therapy treatment of breast tumours using ultrasound responsive microbubbles loaded with paclitaxel, doxorubicin and Rose Bengal. *European Journal of Pharmaceutics and Biopharmaceutics*. 2019 Jun; 139: 224-231.
204. Lee HJ, Yoon YI, Bae YJ. Theragnostic ultrasound using microbubbles in the treatment of prostate cancer. *Ultrasonography*. 2016 Oct; 35(4): 309-317.
205. Sennoga CA, Mahue V, Loughran J, Casey J, Seddon JM, Tang M, et al. On sizing and counting of microbubbles using optical microscopy. *Ultrasound Med Biol*. 2010 Dec;36(12):2093–6.
206. O'Brien J, Hayder H, Zayed Y, Peng C. Overview of MicroRNA Biogenesis, Mechanisms of Actions, and Circulation. *Frontiers in Endocrinology*. 2018 Aug 03; 9(402).

207. Qin D, Li H, Xie H. Ultrasound-targeted microbubble destruction-mediated miR-205 enhances cisplatin cytotoxicity in prostate cancer cells. *Molecular Medicine Reports*. 2018 Sep; 18(3): 3242-3250.
208. Nomikou N, Fowley C, Byrne NM, McCaughan B, McHale AP, Callan JF. Microbubble-sonosensitizer conjugates as therapeutics in sonodynamic therapy. *Chemical Communications*. 2012 Jun 21; 48, 8332-8334
209. Haugland RP, Bhalgat MK. Preparation of avidin conjugates. *Methods in Molecular Biology*. 2008; 418: 1-12.
210. Wu S, Chu P, Chai W, Kang S, Tsai C, Fan C, Yeh C, Liu H. Characterization of Different Microbubbles in Assisting Focused Ultrasound-Induced Blood-Brain Barrier Opening. *Scientific Reports*. 2017 Apr 20; 7(46689): 1-11.
211. Edmondson R, Broglie JJ, Adcock AF, Yang L. Three-Dimensional Cell Culture Systems and Their Applications in Drug Discovery and Cell- Based Biosensors. *Assay and Drug Development Technologies*. 2014 May 1; 12(4): 207-2018
212. Kuzuya A, Pieters RJ, Terai T, Yavin E, Samhan-Arias A, Kii I. Molecular Design of D-Luciferin-Based Bioluminescence and 1,2-Dioxetane-Based Chemiluminescence Substrates for Altered Output Wavelength and Detecting Various Molecules. *Molecules*. 2021 Mar; 26(6): 1618.
213. Buchanan G, Craft PS, Yang M, Cheong A, Prescott J, Jia L, Coetzee GA, Tilley WD. PC-3 cells with enhanced androgen receptor signalling: A model for clonal selection in prostate cancer. *The Prostate*. 2004 Mar 04; 60(4): 352-366.
214. Nakonechny F, Barel M, David A, Korte S, Litvak B, Ragozin E, Etinger A, Livne O, Phinhasi Y, Gellerman, Nisnevitch M. Dark Antibacterial Activity of Rose Bengal. *International Journal of Molecular Sciences*. 2019 Jun 29; 20(13): 3196.
215. Abrahamse H, Hamblin MR. New photosensitizers for photodynamic therapy. *Biochemical Journal*. 2016 Feb 15; 473(4): 347-364.
216. Shoyaib AA, Archie SR, Karamyan VT. Intraperitoneal Route of Drug Administration: Should it Be Used in Experimental Animal Studies? *Pharmaceutical Research*. 2019 Dec 23; 37(1): 12.

217. Blum NT, Yildirim A, Chattaraj R, Goodwin AP. Nanoparticles Formed by Acoustic Destruction of Microbubbles and Their Utilization for Imaging and Effects on Therapy by High Intensity Focused Ultrasound. *Theranostics*. 2017; 7(3): 694-702.
218. Duan L, Yang L, Jin J, Yang F, Liu D, Hu K, Wang Q et al. Micro/nano-bubble-assisted ultrasound to enhance the EPR effect and potential theranostic applications. *Theranostics*. 2020; 10(2): 462-483.
219. Weinstein S, Jordan E, Goldstein R, Yee J, Morgan T. How to set up a contrast-enhanced ultrasound service. *Abdominal Radiology*. 2017 Aug 04; 43: 808-818.
220. Hwang M, Back SJ, Didier RA, Lorenz N, Morgan TA, Poznick L, Steffgen L et al. Pediatric contrast-enhanced ultrasound: optimization of techniques and dosing. *Pediatric Radiology*. 2021; 51: 2147-2160.
221. Logan KA, Nesbitt H, Callan B, Gao J, McKaig T, Taylor M, Love M et al. Synthesis of a gemcitabine-modified phospholipid and its subsequent incorporation into a single microbubble formulation loaded with paclitaxel for the treatment of pancreatic cancer using ultrasound-targeted microbubble destruction. *European Journal of Pharmaceutics and Biopharmaceutics*. 2021 Aug; 165: 374-382.
222. Merck. 18:0 NBD PE (NBD-DSPE) [Internet]. 2022 [cited 2022 Nov 05]. Available from:  
[https://www.sigmaaldrich.com/GB/en/product/avanti/810141p?gclid=Cj0KCQiAmpyRBhC-ARIsABs2EAps1VTJkzbWlinAl2VIOfm5a8oIh-IX9TK\\_PNp1FakpuznEBkR6F3QaAj8yEALw\\_wcB](https://www.sigmaaldrich.com/GB/en/product/avanti/810141p?gclid=Cj0KCQiAmpyRBhC-ARIsABs2EAps1VTJkzbWlinAl2VIOfm5a8oIh-IX9TK_PNp1FakpuznEBkR6F3QaAj8yEALw_wcB)
223. Costley D, Nesbitt H, Ternan N, Dooley J. Huang Y, Hamblin MR, McHale AP et al. Sonodynamic inactivation of Gram-positive and Gram-negative bacteria using a Rose Bengal-antimicrobial peptide conjugate. *International Journal of Antimicrobial Agents*. 2017 Jan; 49(1): 31-36.
224. Langeveld SAG, Beekers I, Collado-Lara G, van der Steen AFW, de Jong N, Kooiman K. The Impact of Lipid Handling and Phase Distribution on the Acoustic Behavior of Microbubbles. *Pharmaceutics*. 2021 Jan; 13(1): 119.



225. Tan Z, Lam WW, Oakden W, Murray L, Koletar MM, Liu SK, Stanisz GJ. Saturation transfer properties of tumour xenografts derived from prostate cancer cell lines 22Rv1 and DU145. *Scientific Reports*. 2020 Dec 04; 10(21315).
226. Marchiani S, Tamburrino L, Nesi G, Paglierani M, Gelmini S, Orlando C, Maggi M et al. Androgen-responsive and -unresponsive prostate cancer cell lines respond differently to stimuli inducing neuroendocrine differentiation. *International Journal of Andrology*. 2010 Dec; 33(6): 784-793.
227. Grayson KA, Jyotsana N, Ortiz-Otero N, King MR. Overcoming TRAIL-resistance by sensitizing prostate cancer 3D spheroids with taxanes. *PLOS One*. 2021 Mar 04; 16(3).
228. Lee C, Sutkowski DM, Sensibar JA, Zelner D, Kim I, Amsel I, Shaw N et al. Regulation of proliferation and production of prostate-specific antigen in androgen-sensitive prostatic cancer cells, LNCaP, by dihydrotestosterone. *Endocrinology*. 1995 Feb; 136(2): 796-803.
229. Sramkoski RM, Pretlow II TG, Giaconia JM, Pretlow TP, Schwartz S, Sy M, Marengo SR et al. A new human prostate carcinoma cell line, 22Rv1. 1999 Jul, 35, 403-409.
230. Yang C, Zhang W, Wang J, Chen P, Jin J. Effect of docetaxel on the regulation of proliferation and apoptosis of human prostate cancer cells. *Molecular Medicine Reports*. 2019 Mar; 19(5): 3864-3870.
231. Merseburger AS, Attard G, Astrom L, Matveev VB, Bracarda S, Esen A, Feyerabend S, Senkus E, Piqueras ML, Boysen G, Gourgioti G, Martins K, Chowdhury S. Continuous enzalutamide after progression of metastatic castration resistant prostate cancer treated with docetaxel (PRESIDE): an international, randomised, phase 3b study.
232. Goertz DE, Todorova M, Omid M, Agache V, Chen B, Karshafian R, Hynynen K. Antitumour Effects of Combining Docetaxel (Taxotere) with the Antivascular Action of Ultrasound Stimulated Microbubbles. *PLoS One*. 2012; 7(12).
233. Gruden S, Sandelin M, Rasanen V, Micke P, Hedeland M, Axen N, Jeansson M. Antitumoral effect and reduced systemic toxicity in mice after intra tumoral injection

- of an in vivo solidifying calcium sulfate formulation with docetaxel. *European Journal of Pharmaceutics and Biopharmaceutics*. 2017 May; 114: 186-193.
234. Anai S, Ibusuki R, Takao T, Sakurai Y, Hisasue J, Takaki Y, Hara N. Retrospective cohort study on the safety and efficacy of docetaxel in Japanese non-small cell lung cancer patients with nondialysis chronic kidney disease stage 3b or higher. *Thoracic Cancer*. 2019 Dec; 10(12): 2282-2288.
  235. McEwan C, Kamila S, Owen J, Nesbitt H, Callan B, Borden M, Nomikou N et al. Combined sonodynamic and antimetabolite therapy for the improved treatment of pancreatic cancer using oxygen loaded microbubbles as a delivery vehicle. *Biomaterials*. 2016 Feb; 80: 20-32.
  236. Gourgou-Bourgade S, Bascoul-Mollevi C, Desseigne F, Ychou M, Bouche O, Guimbaud R, Becouarn Y et al. Impact of FOLFIRINOX compared with gemcitabine on quality of life in patients with metastatic pancreatic cancer: results from the PRODIGE 4/ACCORD 11 randomized trial. *Journal of Clinical Oncology*. 2013 Jan 01; 31(1): 23-29.
  237. Conroy T, Desseigne F, Ychou M, Bouche O, Guimbaud R, Becouarn Y, Adenis A et al. FOLFIRINOX versus Gemcitabine for Metastatic Pancreatic Cancer. *The New England Journal of Medicine*. 2011 May 12; 364(19): 1817-1825.
  238. Von Hoff DD, Ervin T, Arena FP, Chiorean G, Infante J, Moore M, Seay T et al. Increased Survival in Pancreatic Cancer with nab-Paclitaxel plus Gemcitabine. *The New England Journal of Medicine*. 2013 Oct 31; 369(18): 1691-1703.
  239. Vogel A, Rommler-Zehrer J, Li JS, McGovern D, Romano A, Stahl M. Efficacy and safety profile of nab-paclitaxel plus gemcitabine in patients with metastatic pancreatic cancer treated to disease progression: a subanalysis from a phase 3 trial (MPACT). *BMC Cancer*. 2016; 16: 817.
  240. Wang Z, Zhang F, Deng T, Zhang L, Feng F, Wang F, Wang W et al. The efficacy and safety of modified FOLFIRINOX as first-line chemotherapy for Chinese patients with metastatic pancreatic cancer. *Cancer Communications*. 2019; 39(26).

241. Conroy T, Desseigne F, Ychou M, Bouche O, Guimbaud R, Becouarn Y, Adenis A, Raoul J, Gourgou-Bourgade S, de la Fouchardiere C, Bennouna J, Bachet J, Khemissa-Akouz F, Pere-Verge D, Delbaldo C, Assenat E, Chauffert B, Michel P, Montoto-Grillot C, Ducreux M. FOLFIRINOX versus Gemcitabine for Metastatic Pancreatic Cancer. *The New England Journal of Medicine*. 2011 May 12; 364: 1817-1825.
242. Neugut AI, Lin A, Raab GT, Hillyer GC, Keller D, O'Neil DS, Accordino MK et al. FOLFOX and FOLFIRI use in Stage IV Colon Cancer: Analysis of SEER-Medicare Data. *Clinical Colorectal Cancer*. 2019 Jun; 18(2): 133-140.
243. Heinemann V, von Weikersthal LF, Decker T, Kiani A, Kaiser F, Al-Batran S, Heintges T et al. FOLFIRI plus cetuximab or bevacizumab for advanced colorectal cancer: final survival and per-protocol analysis of FIRE-3, a randomised clinical trial. *British Journal of Cancer*. 2020 Nov 06; 124: 587-594.
244. Manogue C, Ledet E, Guddati AK, Lewis B, Sartor O. Extreme Prostate-Specific Antigen Response to Infusional 5-Fluorouracil in Castrate-Resistant Prostate Cancer. *The Oncologist*. 2018 Mar; 23(3): 383-385.
245. Alqudah MAY, Mansour HT, Mhaidat N. Simvastatin enhances irinotecan-induced apoptosis in prostate in prostate cancer via inhibition of MCL-1. *Saudi Pharmaceutical Journal*. 2018 Feb; 26(2): 191-197.
246. Gao J, Logan KA, Nesbitt H, Callan B, McKaig T, Taylor M, Love M et al. A single microbubble formulation carrying 5-fluorouridine, Irinotecan and oxaliplatin to enable FOLFIRINOX treatment of pancreatic and colon cancer using ultrasound targeted microbubble destruction. 2021 Oct 10; 338: 358-366.

## **Chapter 9:**

## **Appendices**

## 9.1 Control formulations - blank MBs

The next step of the process was to produce the control batches of the DTX-MB-RBs. The control batches to be produced were blank MBs, MB-RBs and DTX-MBs, therefore providing the opportunity to determine the effect of DTX and RB within a single MB vs a batch loaded with just one of those drugs, on stability and *in vitro* efficacy. Three batches of blank MBs were manufactured following the method described in 3.2.0 with no DTX in the film and only conjugating avidin to the MB shell. The MB number and size were determined using optical microscopy and micrographs were taken at 40x objective lens magnification. The images were then analysed through the MATLAB algorithm giving the size distribution shown in Figure 9.1 (b). A representative micrograph of the blank MBs are shown in Figure 9.1 (a). The mean MB numbers and sizes for three batches are shown in Table 9.1 and show a mean blank MB number of  $6.553 \times 10^9/\text{mL} \pm 1.112 \times 10^9/\text{mL}$ , and a mean diameter of  $1.233 \mu\text{m} \pm 0.090 \mu\text{m}$ .

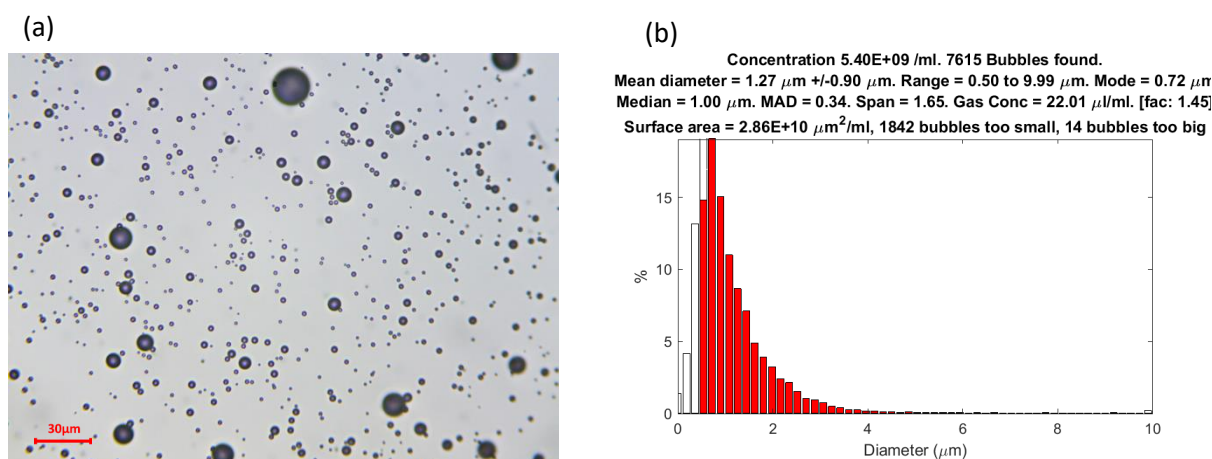


Figure 9.1 (a) Optical microscope image at 40x objective lens magnification of blank MBs after 1 in 25 dilution in Unger's solution. (b) size distribution of blank MBs obtained from optical microscope images through MATLAB software.

Table 9.1 Mean bubble count (number/mL), bubble size ( $\mu\text{m}$ ) for blank bubbles (n=3)

	Bubble Count (Number/mL) $\pm$ SD	Bubble Size ( $\mu\text{m}$ ) $\pm$ SD	RB Loading ( $\mu\text{g}/1 \times 10^8$ bubbles) $\pm$ SD
Mean	$6.240 \times 10^9 \pm 2.161 \times 10^9$	$1.130 \pm 0.020$	$12.485 \pm 1.520$

## 9.2 Control formulations - MB-RB

After preparation of the blank MB formulations the next control batch were MBs with only RB-biotin incorporated onto the shell. The MB-RB were prepared following the method in 3.2.0 without DTX in the MB film. 3 batches of MB-RB were prepared. The RB loading was determined by UV-vis spectrophotometry using the calibration curve displayed in 3.2.1. Optical micrographs of the 3 batches were also taken and the bubble number and sizes were determined, representative images of MB-RB and size distribution curve is displayed in Figure 9.2. The data in displayed in Table 9.2 shows an average bubble number of  $6.240 \times 10^9/\text{mL} \pm 2.161 \times 10^9/\text{mL}$ , bubble size of  $1.130 \text{ nm} \pm 0.020 \text{ nm}$ , and RB loading of  $12.485 \pm 1.520 \mu\text{g}/1 \times 10^8$  MBs.

Table 9.2 Mean bubble count (number/mL), bubble size ( $\mu\text{m}$ ), Rose Bengal loading

	Bubble Count (Number/mL) $\pm$ SD	Bubble Size ( $\mu\text{m}$ ) $\pm$ SD
Mean	$6.553 \times 10^9 \pm 1.112 \times 10^9$	$1.233 \pm 0.090$

concentration ( $\mu\text{M}$ )  
batches of MB-RB  
(n=3).

### 9.3 Control formulations - DTX-MB

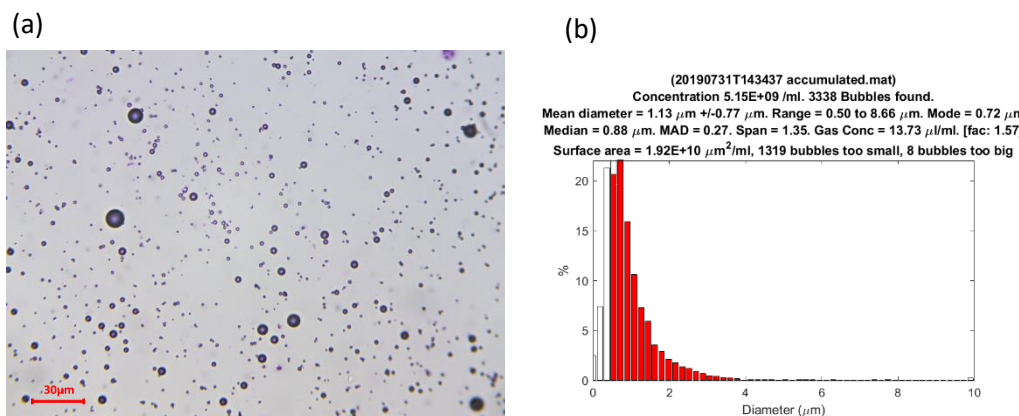


Figure 9.2 (a) Optical microscope image at 40x objective lens magnification of MB-RB after 1 in 25 dilution in Unger's solution. (b) size distribution of DTX-MB-RB obtained from optical microscope images through MATLAB software.

The final control formulation was DTX-MB, the DTX-MBs were produced following the method described in 3.2.0 without RB-biotin added. 3 batches of DTX-MB were produced 5mg of DTX present in the film. The DTX-MB bubble numbers, sizes and DTX loading was determined. To do this the 3 batches of DTX-MB produced were sampled and optical micrographs of the DTX-MB were taken and analysed via the MATLAB software, providing a size distribution which is displayed in Figure. The DTX loading was determined using the method and calibration curve displayed in 3.2.1. The bubble numbers / size, RB and DTX loadings are displayed in Table 9.3, showing an average bubble number of  $7.187 \times 10^9/\text{mL} \pm 2.161 \times 10^9/\text{mL}$ , bubble size of  $1.103 \text{ nm} \pm 0.070 \text{ nm}$ , and DTX loading of  $3.521 \pm 0.669 \mu\text{g}/1 \times 10^8 \text{ MBs}$ .

Table 9.3 Mean bubble count (number/mL), bubble size ( $\mu\text{m}$ ), DTX loading concentration ( $\text{mg/mL}$ ) batches of DTX-MB ( $n=3$ ).

	Bubble Count (Number/mL) $\pm$ SD	Bubble Size ( $\mu\text{m}$ ) $\pm$ SD	DTX Loading ( $\mu\text{g}/1 \times 10^8$ bubbles) $\pm$ SD
Mean	$7.187 \times 10 \pm$ $2.161 \times 10^9$	$1.103 \pm 0.070$	$3.521 \pm 0.669$

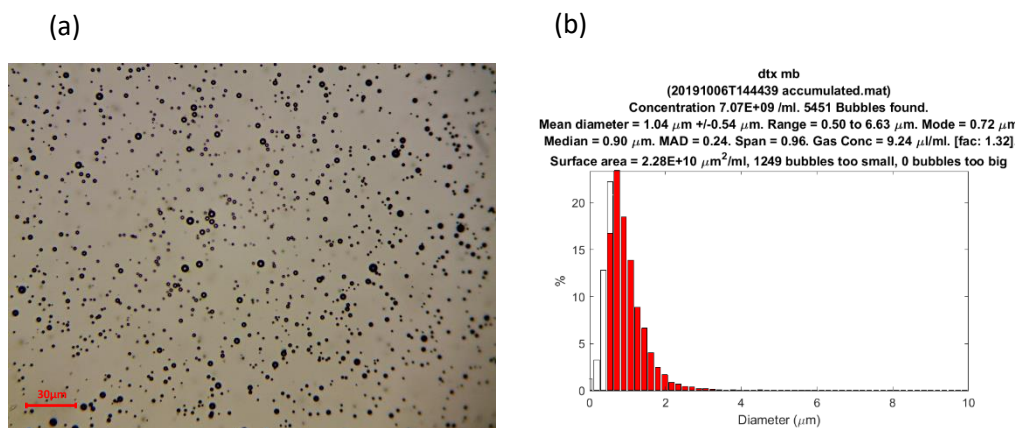


Figure 9.3 (a) Optical microscope image at 40x objective lens magnification of DTX-MB after 1 in 25 dilution in Unger's solution. (b) size distribution of DTX-MB obtained from optical microscope images through MATLAB software.



## 9.4 Publications and conferences

### 9.4.1 Publications

Logan K, Foglietta F, Nesbitt H, Sheng Y, McKaig T, Kamila S, Gao J, Nomikou N, Callan B, McHale AP, Callan JF. Targeted chemo-sonodynamic therapy treatment of breast tumours using ultrasound responsive microbubbles loaded with paclitaxel, doxorubicin and Rose Bengal. *Biopharmaceutics*. 2019 June; 139: 224-331.

Nesbitt H, Logan K, Thomas K, Callan B, Gao J, McKaig T, Taylor M, Love M, Stride E, McHale AP, Callan JF. Sonodynamic therapy complements PD-L1 immune checkpoint inhibition in a murine model of pancreatic cancer. *Cancer Letters*. 2012 Oct; 517: 88-95.

Dhillon SK, Porter SL, Rizk N, Sheng Y, McKaig T, Burnett K, White B, Nesbitt H, Matin RN, McHale AP, Callan B, Callan JF. Rose Bengal-Amphiphilic Peptide Conjugate for Enhanced Photodynamic Therapy of Malignant Melanoma. *Journal of Medicinal Chemistry*. 2020; 63(3): 1328-1336.

Logan KA, Nesbitt H, Callan B, Gao J, McKaig T, Taylor M, Love M, McHale AP, Callan JF. Synthesis of a gemcitabine-modified phospholipid and its subsequent incorporation into a single microbubble formulation loaded with paclitaxel for the treatment of pancreatic cancer using ultrasound targeted microbubble destruction. *European Journal of Pharmaceutics and Biopharmaceutics*. 2012 Aug; 165, 374-382.

Gao J, Logan KA, Nesbitt H, Callan B, McKaig T, Taylor M, Love M, McHale AP, Griffith DM, Callan JF. A single microbubble formation carrying 5-fluorouridine, Irinotecan and oxaliplatin to enable FOLFIRINOX treatment of pancreatic and colon cancer using ultrasound targeted microbubble destruction. *Journal of Controlled Release*. 2012 Oct 10; 338: 358-366.

#### 9.4.2 Publications resulting from thesis – under review

McKaig T, Logan K, Nesbitt H, Callan B, McKeown S, O’Sullivan J, Kelly P, O’Rourke D, McHale AP, Callan JF. Docetaxel and Rose Bengal Loaded Microbubbles for Target Chemo-Sonodynamic Therapy Treatment of Prostate Cancer. *Journal of Controlled Release*. 2023.

#### 9.4.3 Conferences

Poster at Young Cancer Researchers Networking (YCRN) in Cork (2018)

Presentation at 19<sup>th</sup> International Symposium for Therapeutic Ultrasound in Barcelona (2019)

Presentation at the 41<sup>st</sup> All-Ireland School of Pharmacy Conference in Dublin (2019)